

**The Design, Synthesis, and Radiosynthesis
Optimization of Novel Approaches towards the *In Vivo*
PET Imaging of Beta Cell Mass**

Dissertation

der Mathematisch-Naturwissenschaftlichen Fakultät
der Eberhard Karls Universität Tübingen
zur Erlangung des Grades eines
Doktors der Naturwissenschaften
(Dr. rer. nat.)

vorgelegt von
Gregory David Bowden
Johannesburg, Südafrika

Tübingen
2020

Gedruckt mit Genehmigung der Mathematisch-Naturwissenschaftlichen Fakultät der Eberhard Karls
Universität Tübingen.

Tag der mündlichen Qualifikation:

09.06.2021

Dekan:

Prof. Dr. Thilo Stehle

1. Berichterstatter:

Prof. Dr. rer. nat. Bernd J. Pichler

2. Berichterstatter:

Prof. Dr. rer. nat. Stefan Laufer

Plagiarism Declaration

Ich erkläre hiermit, dass ich die Promotion eingereichte Arbeit selbständig verfasst, nur die angegebenen Quellen und Hilfsmittel benutzt und wörtlich oder inhaltlich übernommene Stellen als solche gekennzeichnet habe. Ich erkläre, dass die Richtlinien zur Sicherung guter wissenschaftlicher Praxis der Universität Tübingen (Beschluss des Senats vom 25.5.2000) beachtet wurden. Ich versichere an Eides statt, dass diese Angaben wahr sind und dass ich nichts verschwiegen habe. Mir ist bekannt, dass die falsche Abgabe einer Versicherung an Eides statt mit Freiheitsstrafe bis zu drei Jahren oder Geldstrafe bestraft wird.

Tübingen, September 2020

Gregory David Bowden

Contributions and Collaborations

Gregory Bowden (GB) wrote the thesis presented below in its entirety.

Chapters 6 and 11:

GB performed all organic synthesis and radiolabeling experiments. *In vitro* experiments were designed and performed by GB with the assistance of Lieke Claessens-Joosten and Desirée Bos at the Department of Nuclear Medicine at Radboud University Medical Center (RUMC) in The Netherlands under the guidance of Prof. Dr. Martin Gotthardt. The *In vivo* experiments in this chapter were designed by GB and Filippo Michelotti (FM) under the guidance of Prof. Bernd Pichler (BP), Dr. Andreas Maurer (AM), and Dr. Andreas Schmidt. FM performed the imaging experiments and analyzed the data.

Chapters 7 and 12:

Parts of the work in chapters 4, 7, and 12 were published in a peer-reviewed journal: Bowden, G. D., Pichler, B. J., & Maurer, A. *Sci. Rep.* **9**, 11370 (2019). All experiments were designed by GB. All organic synthesis, radiosynthesis, compound characterization, DoE studies, and data analysis was carried out by GB. Select DoE experiments were carried out by Nantanat Chailanger under the practical supervision of GB as part of her Masters thesis studies.

Chapters 8 and 13:

All organic synthesis, radiosynthesis, compound characterization, and data analysis was carried out by GB. The *in vitro* experiments were designed by GB and Sophie Stotz (SS). The *in vitro* experiments were carried out by SS. GB and SS analyzed and interpreted the data.

Acknowledgments

First and foremost, I would like to thank Prof. Dr. Bernd Pichler for his generosity, supervision, advice, constant encouragement, and confidence in me. There are no words to describe the gratitude I feel for the opportunities afforded me at the Werner Siemens Imaging Center (WSIC). You have given me the time and space to learn and grow into my own as an independent scientist, develop my ideas, and forge my way forward. Bernd, thank you.

I would also like to thank Prof. Stefan Laufer for acting as my second supervisor. Thank you for the advice and support in preparing for my defense and in finalizing this dissertation.

This completion of this work could not have been achieved without the inspiring support, leadership, and friendship of Dr. Andreas Maurer. Thank you, Andi, for your help and guidance in all aspects of scientific research over the years. Under your mentorship, I have learned so much from the practical aspects of planning and conducting elegant experiments, writing manuscripts, and dealing with the peer review process. You have also inspired me to learn and implement new skills, such how to program microcontrollers for building open-source lab equipment, which have ultimately contributed to the success of various scientific projects. Moreover, I have learned from you the importance of compassion and kindness in scientific leadership, virtues I can only hope to instill in others one day. Thank you for being there for me, both in and out of the lab, when I needed it most.

Thanks to all the members and colleagues within the Beta-Train Consortium. Specifically, I would like to thank Prof. Dr. Martin Gotthard for his passion, advice, and leadership. I want to give special thanks to my colleagues in beta-cell imaging, Filippo Michelotti and Dr. Andreas Schmid, for their help in translating some of my ideas from the chemistry bench to the imaging lab.

To the members of the WSIC radiochemistry group, past and present: I would especially like to thank the technical assistants: Ramona Stumm, Katharina Wolf, Elena Kimmerle, Johannes Kinzler, Natalie Herman, and Ramona Stremme for their direct and indirect support in making it a true pleasure to work the lab. Thanks to my friend Dominik Seyfried for putting up with me in the office and for the help with German translations. I would also like to thank Sophie Stotz for her friendship, help, and enthusiastic support with the testing of new tracers in both *in vitro* and *in vivo* models. Finally, I would like to thank Dr. Jonathan Cotton for his support and friendship over the years and for sharing that Ph.D. position advertisement with me many years ago.

Kind thanks to Dr. Gerald Reischl and the rest of the radiopharmacy team at the WSIC for their scientific and technical support. I would especially like to thank Marko Matijevic for his help in the cyclotron control room and the countless last-minute deliveries of ^{18}F target washes.

I would also like to thank my friends and colleagues, past and present, at the WSIC for their friendship and the creative and constant exchange of new ideas. It has been an honor to work in such a multidisciplinary environment with a diverse and vibrant group of people from all over the world.

To my South African family, specifically my dad, Dave; my brother, Nick; and my mom, Lyn: Thank you for all for always being present despite the distances between us. I am incredibly thankful for the strength, wisdom, and unwavering support of my mother, Lyn, especially when things got really tough. Mom, thank you for your unshakeable belief in me. I know the last years have been tough, but I couldn't have gotten to this point without it.

There are so many people who, over the years, have made thousands of more intangible yet equally important contributions to the completion of this thesis. Through friendship, caring, compassion, kind words, and general moral support, (often over a few very needed beers at the Boulanger) they have helped me get through the quagmires of broken bones and hard times, both in- and outside the lab. To my army of best friends from all over the world, thank you from the bottom of my heart.

This thesis is dedicated to the loving memory of

Grandpa Reg and Granny Maureen

Who helped me find the pleasure in figuring things out.

Table of Contents

TABLE OF CONTENTS.....	I
ABSTRACT	V
ZUSAMMENFASSUNG	VII
TABLE OF ABBREVIATIONS	IX
INTRODUCTION AND LITERATURE REVIEW	1
Chapter 1: Introduction and Thesis Outline	1
Chapter 2: Beta Cell Imaging: Quantifying Mass and Function	3
2.1 The Rationale Behind Beta Cell Mass Imaging	3
2.2 The Challenges and Limitations Affecting <i>In Vivo</i> Beta Cell Mass Imaging	3
2.3 Imaging Modalities for <i>In Vivo</i> Beta Cell Detection.....	5
2.3.1 Nuclear Medical Imaging for β Cell Quantification (PET and SPECT)	5
2.3.1.1 <i>The Tracer Principle</i>	5
2.3.1.2 <i>SPECT Imaging</i>	6
2.3.1.3 <i>PET Imaging</i>	7
2.3.1 Magnetic Resonance Imaging (MRI)	8
2.3.2 Multimodal Imaging for β Cell Imaging.....	10
Chapter 3: Radiochemistry and Tracer Synthesis	11
3.1 Radionuclides for Nuclear Medical Imaging	11
3.1.1 The Selection of Radionuclides for the PET imaging of β Cells.	11
3.1.2 Production of PET isotopes.....	13
3.1.3 The PET Tracer Production Workflow	15
3.2 The Chemistry of [^{18}F]Fluorine	16
3.2.1 Electrophilic ^{18}F Chemistry.....	17
3.2.2 Nucleophilic ^{18}F chemistry	18
3.2.2.1 [^{18}F]Fluoride Processing.....	18
3.2.2.2 <i>Nucleophilic Alkyl Radiofluorination</i>	19
3.2.2.3 <i>Nucleophilic Aryl Radiofluorination</i>	20
3.3 New Advances in Late-Stage Aromatic Nucleophilic Radiofluorination.....	21
3.3.1 Copper Mediated Radiofluorinations (CMRFs).....	22
3.3.2 [^{18}F]Trifluoromethylation Reactions	26
3.4 The Radiolabeling of Biomolecules with Radiometals	27
Chapter 4: Design of Experiments: The Optimization of Chemical Processes.....	31
4.1 Reaction Optimization and Experimental Design (OVAT Vs DoE).....	31
4.2 DoE: Experimental Matrices in Multivariable Studies.....	32
4.2.1 Factor Screening Designs	33
4.2.2 Experimental Designs for Response Surface Optimization (RSO)	35
4.3 Model Construction and Data Interpretation	37
4.4 DoE in Practice.....	38
Chapter 5: Biomarkers and Probes for Beta Cell Imaging	39
5.1 Pharmacological Criteria for Probes and Biomarkers for BCI	39
5.2 Biomarkers and Probes for β Cell Imaging.....	39

5.3	The Glucagon-Like Peptide-1 Receptor (GLP-1R)	40
5.3.1	Radiolabeled GLP-1R Ligands for BCMI.....	41
5.3.2	Allosteric Modulation of GLP-1R Activity and Ligand Binding	43
5.3.2.1	<i>“Compound 2” (C2): an Ago-Allosteric Affinity Modulator of GLP-1R</i>	44
5.3.2.2	<i>BETP: A Covalent Modifier of GLP-1R</i>	45
RESULTS AND DISCUSSION		47
Chapter 6:	Allosteric Affinity Modulators as GLP-1R Tracer Uptake Enhancers	47
6.1	Aims and Objective	47
6.2	Synthesis of the Quinoxaline Derivative “Compound 2”	48
6.3	<i>In vitro</i> Uptake Enhancement Experiments	49
6.3.1	Establishment of Dose-Response Curve of Tracer Uptake Enhancement	49
6.3.2	Receptor Binding Experiments	50
6.4	<i>In vivo</i> Uptake Enhancement Experiments	52
6.4.1	[⁶⁴ Cu]Ex-4 <i>in vivo</i> GLP-1R Specificity and Binding	53
6.4.2	The Effect of C2 on the Uptake of [⁶⁴ Cu]Ex-4 into INS-1 Xenografts	53
6.4.3	Dynamic PET Imaging of Native and Transplanted Pancreatic Islets	54
6.5	Summary and Discussion	55
6.6	Conclusion and Future Work	57
Chapter 7:	The Use of DoE for the Optimization of Copper-Mediated Radiofluorinations (CMRFs)	59
7.1	Aims and Objectives	59
7.2	DoE vs OVAT Efficiency Estimation	60
7.3	DoE Optimization of the CMRF of Arylstannanes	61
7.3.1	Factor Screening DoE Study Using 4-Tributyltinbiphenyl	61
7.3.2	Response Surface Optimization of [¹⁸ F]pFBC ([¹⁸ F]8).....	64
7.3.3	Response Surface Optimization of [¹⁸ F]pFBnOH ([¹⁸ F]10).....	68
7.4	The Development of Improved ¹⁸F Processing Conditions for CMRF Reactions	70
7.5	DoE Optimization of the CMRF of Arylboronic Acid Pinacol Esters	74
7.6	Summary and Discussion	77
7.7	Conclusions and Future Work	80
Chapter 8:	The Synthesis of ¹⁸F labeled BETP Derivatives	83
8.1	Aims and Objectives	83
8.2	Synthesis of BETP and FBETP Standards by Literature Published Routes	83
8.3	The Synthesis of Isotopically Labeled [¹⁸F]BETP	88
8.3.1	Precursor Synthesis.....	88
8.3.2	Radiosynthesis of [¹⁸ F]BETP via Radiotrifluoromethylation.....	90
8.4	The Synthesis of [¹⁸F]F-BETP	91
8.4.1	The Synthesis of Diverse Precursors of [¹⁸ F]F-BETP	91
8.4.2	Radiosynthesis of 4-[¹⁸ F]F-BETP from Arylstannane and Arylboronate Precursors.....	94
8.4.3	Automated Radiosynthesis	98
8.5	[¹⁸F]F-BETP <i>In vitro</i> Experiments	102
8.6	Summary and Conclusion	103
Chapter 9:	General Conclusion	105
EXPERIMENTAL		107
Chapter 10:	General Information Pertaining to Materials and Methods	107
10.1	General Organic Chemistry Information	107

10.2	General Radiochemistry Information	108
10.3	General <i>In vivo</i> Information	109
10.4	Ethics Disclaimer.....	109
Chapter 11:	Allosteric Affinity Modulators as GLP-1R Tracer Uptake Enhancers	111
11.1	Organic Synthesis	111
11.2	C2 Formulation	113
11.3	Radiolabeling of Exendin Derivatives for BCMI	113
11.3.1	(Lys ⁴⁰ -[¹¹¹ In]In-DTPA)Exendin-3 and (Lys ⁴⁰ -[¹¹¹ In]In-DTPA)exendin(9-39) for <i>In vitro</i> Studies ¹³⁶	113
11.3.2	(Lys ⁴⁰ -[⁶⁴ Cu]Cu-NODAGA)Exendin-4 ([⁶⁴ Cu]Ex-4) ¹³⁸	114
11.4	<i>In Vitro</i> Studies	114
11.4.1	Cell Culture	114
11.4.2	C2 Dose Calibration Experiments.....	115
11.4.3	Receptor Binding Experiments	115
11.5	<i>In Vivo</i> Studies	116
11.5.1	<i>In vivo</i> Experiments to Validate Tracer Specificity	116
11.5.2	C2 Enhanced Tumor Uptake	116
11.5.3	Tracer Infusion with a C2 Bolus Challenge in Transplanted Islets.....	117
11.5.4	Tracer Infusion with C2 Infusion in Native Pancreatic Islets.....	118
Chapter 12:	The Use of DoE for the Optimization of Copper-Mediated Radiofluorinations (CMRFs)	119
12.1	Organic Synthesis	119
12.2	General Procedure for DoE Design and Data Analysis	122
12.3	Development of Base-Free ¹⁸ F Processing Conditions.....	122
12.4	General Radiochemistry Procedures for DoE Studies	123
12.4.1	General CMRF Procedure 1 ⁸⁶	123
12.4.2	General CMRF Procedure 2	123
12.5	DoE Optimization of the CMRF of Arylstannanes	124
12.5.1	DoE Factor Screening Study Using Precursor 5 ⁸⁶	124
12.5.2	DoE Factor Response Surface Optimization of [¹⁸ F]pFBC ([¹⁸ F]8) ⁸⁶	124
12.5.3	DoE Factor Response Surface Optimization of [¹⁸ F]pFBnOH ([¹⁸ F]10) ⁸⁶	125
12.6	D-Optimal Response Surface Optimization of [¹⁸ F]10 from Arylboronic Acid Pinacol Esters.....	125
12.7	Automated Radiosynthesis	125
Chapter 13:	The Synthesis of ¹⁸F Labeled BETP Derivatives	127
13.1	Organic Synthesis	127
13.2	Manual Radiosynthesis Experiments.....	143
13.2.1	Radiosynthetic Studies Towards [¹⁸ F]BETP	143
13.2.2	Radiosynthetic Studies Towards [¹⁸ F]F-BETP	143
13.3	Automated Radiosynthesis	144
13.3.1	General Information	144
13.3.2	¹⁸ F Processing on the Elixys FLEX/CHEM Synthesizer	144
13.3.3	Automated Synthesis of [¹⁸ F]F-BETP (Two-Pot)	144
13.4	<i>In Vitro</i> Studies	145
13.4.1	Cell Culture	145
13.4.2	Tracer Uptake Experiments	146
13.4.3	SDS-PAGE experiments	146
13.4.4	Autoradiography.....	146
13.4.5	Coomassie Staining.....	147
REFERENCES:	149

Abstract

This work details the investigation of new approaches for *in vivo* diabetes imaging, including the optimization of the required radiochemical syntheses.

Diabetes mellitus is a group of metabolic disorders characterized by impaired glucose homeostasis that arises from the loss or improper functioning of insulin-producing beta cells (β cells). Despite significant advances in diabetes medicine, the changes that occur to the number of viable β cells, the β cell mass (BCM), over the course of the illness, are poorly understood in both forms of the disease. This is in large part due to the lack of an effective non-invasive method for localizing and quantifying the BCM *in vivo*. The development of such a method could potentially pave the way for a paradigm shift in diabetological research, as it would allow for the longitudinal tracking of the BCM in affected patients as the disease progresses. Nuclear medical imaging techniques, such as positron emission tomography (PET), have come to the forefront of this development; however, these methods rely on the development of highly specific radiotracers that target β cell-specific biomarkers.

The glucagon-like peptide-1 receptor (GLP-1R) is an excellent biomarker for *in vivo* β cell quantification. Radiolabeled derivatives of the GLP-1R orthosteric agonist exendin have been developed as specific GLP-1R targeting radiotracers; however, these compounds suffer from several drawbacks. Small molecule drug discovery programs have revealed several allosteric modulators of GLP-1R, such as the quinoxaline “compound 2” (**C2**) and **BETP**, which may present alternative approaches for β cell targeting. **C2** has been shown to enhance the affinity of several GLP-1R orthosteric ligands and could serve as a “tracer uptake enhancer” for GLP-1R radioligands. Alternatively, radiolabeled **BETP** derivatives may be of interest as GLP-1R targeting radiotracers, as **BETP** has been shown to covalently bind to an allosteric site on GLP-1R. This would slow the clearance of the tracer from GLP-1R expressing tissue and may ultimately enhance the target-to-background ratio of the resulting PET image. The investigation of these alternative approaches to β cell imaging represents one of the main aims of this thesis.

The automated radiosynthesis of any novel imaging probe relies on the availability of a well-established and optimized radiochemical toolbox. Many novel probes, such as **BETP**, present no obvious site for ^{18}F radiolabeling using traditional late-stage radiochemical methodologies; however, the recent disclosure of copper-mediated radiofluorination (CMRF) chemistry has allowed unprecedented access to ^{18}F -labeled electron-rich and -neutral aromatic compounds. These multicomponent reactions are, however, complex and depend on several interacting experimental factors for success. We thus investigated several variations of the CMRF reaction using “design of experiments” (DoE), a statistical approach to reaction optimization, to glean new insights into the behavior of CMRF chemistry. This work reports on the successful optimization of CMRF chemistry for the automated synthesis of [^{18}F]-**BETP** and several other novel tracers.

Zusammenfassung

Diese Arbeit beschreibt die Erforschung neuer Ansätze für die *in vivo* Bildgebung von Diabetes inklusive der Optimierung der dafür benötigten radiochemischen Synthesen.

Der Begriff *Diabetes mellitus* umfasst mehrere metabolische Störungen mit beeinträchtigter Glucose-Homöostase, die durch den Verlust oder die beeinträchtigte Funktion der insulinproduzierenden Betazellen ausgelöst werden. Trotz erheblicher Fortschritte bei der Behandlung von Diabetes ist die pathologische Reduktion der Anzahl der verfügbaren Betazellen (*beta cell mass*, BCM) während des Krankheitsverlaufs für beide Ausprägungen der Krankheit nur ansatzweise verstanden. Dies liegt zu einem großen Teil am Fehlen einer effektiven nichtinvasiven Methode zur Lokalisierung und Quantifizierung der BCM *in vivo*. Die Entwicklung einer solchen Methode zur krankheitsbegleitenden Überwachung der BCM in betroffenen Patienten könnte dementsprechend zu einem Paradigmenwechsel im Bereich der Diabetesforschung führen. Nuklearmedizinische Bildgebungstechniken wie die Positronenemissionstomographie (PET) bieten enormes Potenzial für diese Anwendung, beruhen allerdings auf der Entwicklung hochspezifischer Radiotracer, die eine Affinität zu betazellspezifischen Biomarkern aufweisen.

Der Glucagon-like-Peptide-1-Rezeptor (GLP-1R) ist ein hervorragender Biomarker für die *in vivo* Quantifizierung von Betazellen. Radiomarkierte Derivate von Exendin, einem orthosterischen Agonisten von GLP-1R, wurden bereits als spezifische Radiotracer für GLP-1R entwickelt, besitzen allerdings mehrere Nachteile. Screeningprogramme für niedermolekulare Arzneistoffe ergaben mehrere allosterische Modulatoren für GLP-1R wie zum Beispiel Quinoxalin „Compound 2“ (**C2**) und **BETP**, die möglicherweise alternative Ansätze zur Quantifizierung von Betazellen ermöglichen. Für **C2** wurde gezeigt, dass es die Affinität von mehreren orthosterischen Liganden für GLP-1R erhöht, wodurch es als „Aufnahmeverstärker“ für GLP-1R Radioliganden dienen könnte. Alternativ dazu könnten radiomarkierte **BETP**-Derivate als auf GLP-1R abzielende Radiotracer von Bedeutung sein, da **BETP** nachweislich kovalent an ein allosterisches Zentrum von GLP-1R bindet. Dies würde die Ausscheidung des Tracers aus GLP-1R-exprimierendem Gewebe verlangsamen und könnte letztendlich das Verhältnis des Signals von Zielstrukturen zum Hintergrund bei der folgenden PET Bildgebung verbessern. Die Untersuchung dieser alternativen Ansätze für die Bildgebung von Betazellen ist eines der Hauptziele dieser Doktorarbeit.

Zur Automatisierung der Radiosynthese von neuartigen Substanzen zur Bildgebung sind etablierte und optimierte radiochemische Methoden essentiell. Viele dieser Substanzen, wie auch **BETP**, besitzen keine offensichtliche Position für eine praktikable Radiomarkierung mit ^{18}F durch herkömmliche radiochemische Methoden. Allerdings hat das Aufkommen der kupfervermittelten Radiofluorierung (*copper-mediated radiofluorination*, CMRF) bahnbrechende Möglichkeiten zur Synthese ^{18}F -markierter elektronenreicher und –neutraler aromatischer Verbindungen generiert. Der Erfolg dieser komplexen Mehrstoffreaktionen hängt jedoch von der präzisen Abstimmung zahlreicher, untereinander interagierender Reaktionsfaktoren ab. Um

neue Erkenntnisse über die unterschiedlichen Einflüsse dieser Faktoren auf die CMRF-Reaktionen zu erhalten, haben wir mehrere Varianten der Reaktion mittels der „*Design of Experiments*“ (DoE) Methode, einem statistischen Ansatz zur Reaktionsoptimierung, untersucht. Die vorliegende Arbeit fasst die erfolgreiche Optimierung der automatisierten Synthese von [^{18}F]**F-BETP** und weiterer neuartiger Tracer unter Einsatz von CMRF-Chemie zusammen.

Table of Abbreviations

AcOH	Acetic Acid
ADME	Absorption, Distribution, Metabolism, Excretion
AM	Allosteric Modulator
B ₂ Pin ₂	Bis(pinacolato)diboron
BBD	Box-Behnken Design
BCF	Beta Cell Function
BCM	Beta Cell Mass
BCMI	Beta Cell Mass Imaging
BETP	4-(3-Benzyloxyphenyl)-2-ethylsulfinyl-6-(trifluoromethyl)pyrimidine
BSA	Bovine Serum Albumin
C2	6,7-Dichloro-2-methylsulfonyl-3- N-tert-butylaminoquinoxaline
Cat.	Catalyst Loading
CCD	Central Composite Design
CCCD	Circumscribed Central Composite Design
cGMP	Current Good Manufacturing Practice
CHI	Congenital Hyperinsulinism
CHL	Chinese Hamster Lung Carcinoma
ClF ₂ CCO ₂ Me	Methyl Chlorodifluoroacetate
CMRF	Copper-Mediated Radiofluorination
CP	Centerpoints
CT	Computed Tomography
Cu(OTf) ₂	Cu(II) Triflate
DCM	Dichloromethane
DFO	Desferrioxamine
DIAD	Diisopropyl Azodicarboxylate
DMA	Dimethylacetamide
DME	Dimethoxyethane
DMF	Dimethylformamide
DMSO	Dimethyl Sulfoxide
DoE	Design of Experiments
DPPIV	Dipeptidyl Peptidase IV
DTPA	Diethylenetriaminepentaacetic Acid
ECD	Extracellular Domain
EDTA	Ethylenediaminetetraacetic Acid
EOB	End of Bombardment

ESI	Electro Spray Ionization
Et ₂ O	Diethyl Ether
Et ₃ N	Triethylamine
EtOAc	Ethyl Acetate
EtOH	Ethanol
EWG	Electron-Withdrawing Groups
Ex(9-39)	Exendin(9-39)
Ex-3	Exendin-3
Ex-4	Exendin-4
[¹⁸ F]FDG	2-[¹⁸ F]Fluoro-2-deoxy-D-glucose
FCCD	Face-Centered Central Composite Design
FID	Free Induction Decay
GLP-1	Glucagon-Like Peptide-1
GLP-1R	Glucagonlike Peptide-1 Receptor
GPCR	G-Protein Coupled Receptor
HEK	Human Embryonic Kidney
HPLC	High-Performance Liquid Chromatography
HPLC-MS	HPLC-Mass Spectroscopy
IBX	2-Iodoxybenzoic acid
K ₂₂₂	[2.2.2]Kryptofix
KOAc	Potassium Acetate
LOR	Line of Response
<i>m</i> -CPBA	<i>meta</i> -Chloroperoxybenzoic Acid
MeCN	Acetonitrile
MEMRI	Manganese-Enhanced MRI
MeOH	Methanol
MLR	Multiple Linear Regression
MOMCl	Methoxymethyl Chloride
MRI	Magnetic Resonance Imaging
MS	Mass Spectrometry
NAM	Negative Allosteric Modulator
NaOEt	Sodium Ethoxide
NaSEt	Sodium Ethylthiolate
<i>n</i> -BuLi	<i>n</i> -Butyllithium
<i>n</i> -BuOH	<i>n</i> -Butanol
NEt ₃	Triethylamine

NLE	Norleucine
NMI	Nuclear Medical Imaging
NMR	Nuclear Magnetic Resonance
NODAGA	1,4,7-Triazacyclononane,1-gluteric acid-4,7-acetic acid
NOTA	1,4,7-Triazacyclononane-1,4,7-triacetic Acid
OCCD	Orthogonal Central Composite Design
OL	Orthosteric Ligand
OPT	Optical Projection Tomography
OTf	Trifluoromethanesulfonate (Triflate)
OVAT	One Variable at a Time
OXM	Oxyntomodulin
PAM	Positive Allosteric Modulator
Pd(dppf)Cl ₂	[1,1'-Bis(diphenylphosphino)ferrocene]dichloropalladium(II)
Pd(PPh ₃) ₄	Tetrakis(triphenylphosphine)palladium(0)
PET	Positron Emission Tomography
POCl ₃	Phosphoryl Chloride
PTC	Phase-Transfer Catalyst
PVE	Partial Volume Effect
Py	Pyridine
QMA	Quaternary Methylammonium
RCC	Radiochemical Conversion
RCY	Radiochemical Yield
RCP	Radiochemical Purity
RES	Resolution
RSM	Response Surface Modeling
RSO	Response Surface Optimization
RF	Radiofrequency
ROI	Region of Interest
SDS-PAGE	Sodium Dodecyl Sulfate-Polyacrylamide Gel Electrophoresis
SET	Single Electron Transfer
SPE	Solid-Phase Extraction
SPECT	Single-Photon Emission Computed Tomography
Sub	Substrate/Precursor loading
T1DM	Type 1 Diabetes
T2DM	Type 2 Diabetes
TAC	Time-Activity Curve

TBAF	Tetrabutylammonium Fluoride
TBAOTf	Tetrabutylammonium Triflate
TEAB	Tetraethylammonium Bicarbonate
THF	Tetrahydrofuran
TLC	Thin-layer Chromatography
7TMD	7-Membered Transmembrane Domain
TMEDA	N,N,N',N'-tetramethylethylenediamine
UV	Ultraviolet

Introduction and Literature Review

Chapter 1: Introduction and Thesis Outline

Diabetes mellitus is a group of metabolic diseases that are characterized by disrupted glucose homeostasis brought about by either an individual's inability to produce sufficient insulin or through insulin resistance. Insulin is the peptide hormone primarily involved in regulating glucose uptake and thus the glucose level in the bloodstream (Figure 1).¹ Diabetes is the direct cause of potentially fatal or maiming complications associated with the eyes, kidneys, central nervous system, and circulatory system.² The epidemic affects more than 340 million people globally, a number which is expected to grow by approximately 20% by 2030.³ The increasing burden of diabetes is set to put a further financial strain on the world's healthcare systems, potentially having significant direct and indirect economic consequences, particularly in large low- to middle-income developing countries, such as South Africa, China, and India.³ The need for the development of new medications and treatments is thus more important than ever.

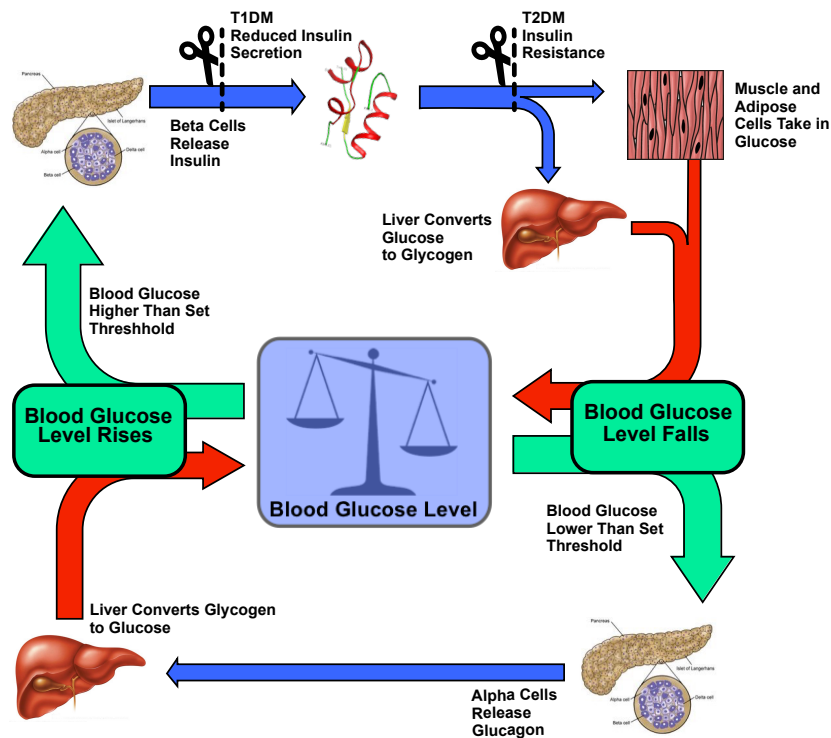


Figure 1: Glucose Homeostasis is mediated by a feedback loop controlled by the beta and alpha cells of the endocrine pancreas. T1DM disrupts this loop by impairing the secretion of insulin. T2DM stems from a resistance to the effects of the insulin molecule itself. The diagram has been adapted from Riaz.⁴

Diabetes occurs primarily in two forms: Type 1 diabetes (T1DM) results from autoimmune destruction of the insulin-producing beta cells (found in the pancreatic islets of Langerhans), ultimately leading to hyperglycemia.¹ Type 2 diabetes (T2DM), the most prevalent form of the disease in adult patients, occurs as a result of insulin resistance that results in hyperglycemia. This causes the β cells to over-secrete insulin in an attempt to compensate for the insulin resistance, which leads to β cell metabolic exhaustion and a disruption of normal β cell function (BCF) (Figure 1).¹ Changes to the function and quantity of viable β cells

(β cell mass or BCM) are highly important factors in both T1DM and T2DM; however, the implications of these changes during disease progression are poorly characterized and inadequately understood in all forms of the illness.^{5,6} This is in large part due to the absence of an accurate and reliable method for the *in vivo* quantification of the BCM and the changes that it undergoes.^{7,8}

Currently, the only data available to accurately study the BCM in humans has been obtained via biopsy, pancreatectomy, and autopsy, which are ineffective at providing immediately useful longitudinal information to clinicians and their patients.^{6,7,9} Due to their sensitivity and their ability to provide researchers with detailed biochemical information, molecular imaging techniques, such as positron emission tomography (PET), single-photon emission computed tomography (SPECT), and magnetic resonance imaging (MRI), may serve as effective methods for *in vivo* BCM and BCF quantification.¹ However, these techniques rely heavily on the use of well-defined biomarkers, and thus, novel BCM and BCF tracers or contrast agents need to be developed and translated into routine clinical use.⁵

A non-invasive *in vivo* imaging technique to accurately assess how both BCM and BCF change over time would be a revolutionary tool for future diabetes research and the evaluation of new treatments against the disease, potentially opening the door to a paradigm shift in our understanding and treatment of the illness.^{6,7} Moreover, the development of a method to quantify, localize, and target β cell-derived tissues would also be of great benefit to the diagnosis and treatment of potentially fatal hyperinsulinemic disorders such as insulinoma (insulin-secreting tumors derived from pancreatic β cells)¹⁰ and congenital hyperinsulinism in infants (CHI, a disorder that results from an over-secretion of insulin resulting in hypoglycemia.)^{11,12} This work aims to explore and discuss the development, design, synthesis, radiosynthesis, and radiosynthesis optimization of novel tracers for BCM quantification. Additionally, it will discuss potential new ways of enhancing the specificity, uptake, and pharmacokinetics of existing BCM tracers using small molecule allosteric modulators to improve *in vivo* PET BCM imaging.

The review presented below aims to discuss the aspirations, rationale, and challenges associated with β cell mass imaging (BCMI). It will also discuss potential new approaches to image the BCM brought about through the development of novel β cell-specific radiotracers and the chemistry used to synthesize them. An introduction into molecular imaging techniques, probe discovery, and biomarker development for BCMI, with a particular focus on PET imaging, will be presented throughout chapters 2 and 5.

The development of novel PET tracers for any application relies on the availability of an adequate radiochemical toolbox. New radiochemical methodologies are being developed and optimized to help meet some of the synthetic challenges of novel radiotracer design and development. Chapters 3 and 4 will respectively discuss the current state of the art of synthetic radiochemistry (with a focus on radiofluorine chemistry) and the optimization of radiochemical processes using a “design of experiments” (DoE) approach.

Chapter 2: Beta Cell Imaging: Quantifying Mass and Function

2.1 The Rationale Behind Beta Cell Mass Imaging

The decay of the BCM, as well as the suppression of normal BCF, are central yet poorly characterized events in diabetes pathogenesis in both forms of the disease.^{1,6} The relationship between these two factors is, however, not well understood, in part due to the fact that the two factors are coupled and are difficult to distinguish by the currently available assays. While it runs true that diabetic patients (both T1 and T2) tend to display a lower BCM, they may have significantly varying levels of insulin secretion, the primary metric of BCF.⁶ In T2DM, the BCM is not static and can change considerably throughout the illness, even increasing to offset increased insulin resistance and reduced BCF.¹³ Up until now, accurate and direct quantification of the BCM has only been obtainable from autopsy results.⁶ While non-invasive biomarkers for BCM and BCF do exist, the measurement of these biomarkers are usually indirect, relatively insensitive and often unreliable (e.g., C-peptide measurement).^{8,14–16}

New diabetological research continues to reveal that the relationship between BCM and BCF is complex and that it is often difficult to distinguish and qualify changes between them.¹⁷ In order to further our understanding of this relationship, an accurately quantifiable method to assess the BCM of individuals would be a powerful tool for both clinical and pre-clinical diabetologists and could pave the way for the personalized management of diabetes.⁶ Specifically, new research into treatments that either replace the BCM (through β cell transplantation) or combat autoimmune inflammation in the pancreatic islets, promote β cell proliferation, and restore β cell function, would benefit significantly from accurate *in vivo* BCM quantification.^{15,18}

For approximately the last 20 years, researchers across the globe have attempted to solve this problem. The ultimate goal being the development of non-invasive methods to reliably and reproducibly measure and correlate the BCM and BCF *in vivo*.⁹ This task has, however, proved to be non-trivial as the challenges facing BCI are significant and numerous (*vide 2.2*). Molecular imaging techniques have come to the forefront of this endeavor, and the state of the art of BCMI is reviewed in detail below (*vide 2.3*).

2.2 The Challenges and Limitations Affecting *In Vivo* Beta Cell Mass Imaging

The field of β cell imaging suffers from many significant obstacles, making it a particularly challenging area of research.⁹ The *in vivo* imaging of different islet/ β cell animal models yield different challenges depending on the structures being studied, whether they be native islets, transplanted islets, or tumor-derived β cell models. The native β cells of the endocrine pancreas are arranged within tiny clusters of cells known as the *Islets of Langerhans*. These structures, which are typically between 100-300 μm in diameter, are distributed unevenly throughout the pancreas, and make up only 0.3-3% of the total pancreatic mass (Figure 2, A).^{6,8} Moreover, human islets themselves do not consist entirely of β cells ($\approx 60\%$) but also contain other endocrine

cells such as α -cells ($\approx 30\%$), δ -cell ($<10\%$), and PP cells ($<5\%$) arranged in a complex cytoarchitecture (Figure 2, B).¹⁹ The small size and low abundance of β cells in the pancreas thus makes any *in vivo* analysis of their volume and number incredibly challenging. Additionally, in most diabetes disease models, the number of β cells and the biomarkers of their mass and function are diminished, thus requiring an exceptionally high level of sensitivity in the analytical method used to detect them.⁶

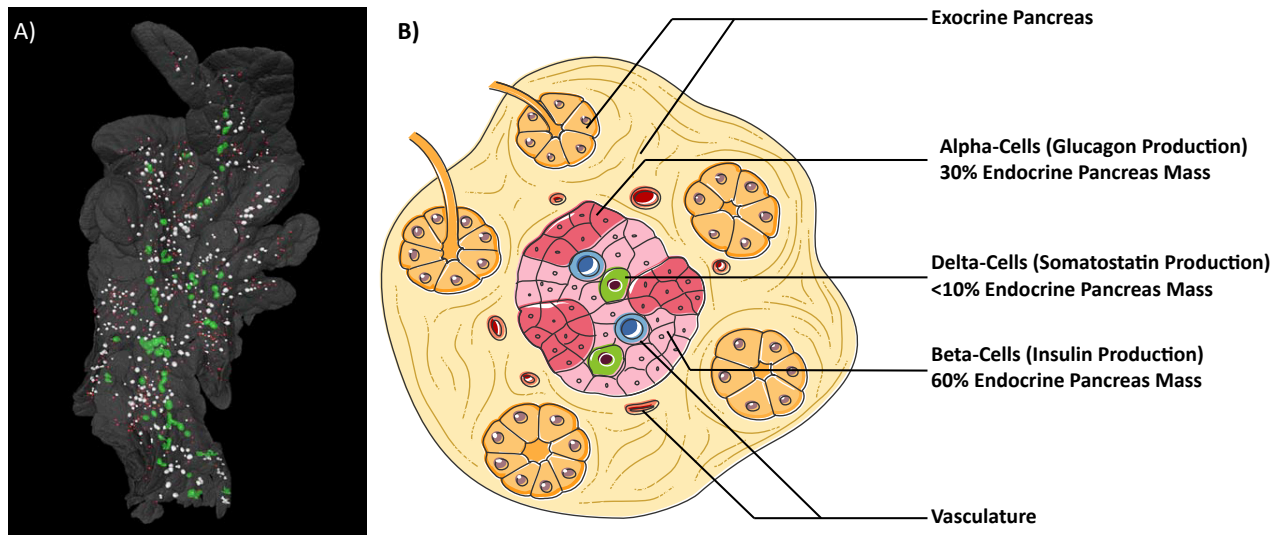


Figure 2: A) Optical projection tomography (OPT) imaging of a NOD mouse pancreas. The pancreatic islets (highlighted in red, green, and white) have been labeled with an insulin specific antibody. The exocrine pancreas is outlined using background fluorescence, highlighting the uneven distribution of the islets throughout the pancreas. The image has been taken and modified from the publication by Holmberg and Ahlgren.²⁰ B) A schematic diagram of the endocrine pancreas (Islet of Langerhans)¹⁹. The diagram ART was adapted from CC-BY SMART Servier, <https://smart.servier.com/>, under CC-BY 3.0 license.

As discussed by Laurent *et al.*, the BCM and the distribution of the β cells throughout the pancreas can vary widely between individuals, regardless of their disease state (or lack of), making comparative studies among large cohorts of individuals inherently difficult.⁸ These variances, in all likelihood, will be a significant limitation when it comes to the use of *in vivo* BCMI as a predictive or diagnostic tool in a clinical setting. BCMI would find more use as a tool for longitudinal studies over multiple time points and as such, would be of high importance for the assessment of new treatments and in the monitoring of clinical trials within individuals.⁸

Another problem affecting BCMI is the introduction of motion artifacts through breathing or through the irregular motion of organs in the abdomen (e.g., peristalsis). While motion is a problem to molecular imaging in general due to the temporal resolution⁹ of most imaging modalities, the small size, quantity, and irregular distribution of the islets throughout the pancreas exacerbate this issue when imaging techniques are applied to quantify β cells.

Ultimately, due to the relatively low quantity and irregular distribution of islets throughout the pancreas, the core practical issues affecting BCMI are those of sensitivity and resolution. Nuclear molecular imaging methods, such as PET and SPECT, possess the exceptional sensitivity to make *in vivo* BCM quantification a

⁹ Temporal resolution: The precision of a measurement with respect to time. In molecular imaging, the time scales of experiments can change dramatically depending on the modality being used and the processes being observed.

possibility; however, due to the low spatial resolution^a of these techniques, it is unlikely that *in vivo* imaging of individual islets will be possible any time in the near future.⁸ However, with well-designed, β cell-specific probes, PET and SPECT imaging could achieve the chemical resolution^b necessary to quantify the BCM accurately.

PET and SPECT probe development for BCMI has since received a fair amount of attention, and there is an ever-growing body of work exploring the use of radiotracers for BCM quantification. While much progress has been made, there is currently still no tracer for BCMI in use in clinical routine.¹⁷ There is, therefore, a need for the continuing discovery and development of novel β cell-specific probes and biomarkers. Despite the challenges listed and discussed above, PET and SPECT (and their use in combination with other non-invasive *in vivo* imaging techniques such as magnetic resonance imaging (MRI) and X-ray computed tomography (CT)) hold high promise as viable solutions for the problem of *in vivo* BCMI.¹

2.3 Imaging Modalities for *In Vivo* Beta Cell Detection

2.3.1 Nuclear Medical Imaging for β Cell Quantification (PET and SPECT)

Nuclear medical imaging (NMI) is a branch of nuclear medicine concerned with the use of radioactive isotopes to image structures and processes within the body. While modalities such as X-ray and CT both use external radiation sources to image “through” their subjects, the main NMI techniques of PET and SPECT both rely on the use of administered radiopharmaceuticals carrying radioactive isotopes (radiotracers), which enrich in target tissues and can be detected upon their decay.

2.3.1.1 The Tracer Principle

The invention of the tracer method and the tracer principle was a breakthrough in the field of chemical biology, and in 1943, George de Hevesy was awarded the Nobel prize “for his work on the use of isotopes as tracers in the study of chemical processes.”²¹ The tracer principle relies on two fundamental premises: i) That the chemical properties (and thus biological behavior) of a radioactive isotope of any given element will be identical to those of its non-radioactive counterpart. ii) Radioactive decay is a highly energetic event (much more energetic than any chemical assay) and thus has a low detection threshold. Therefore, radiochemical assays are highly sensitive, and radioactive probes may thus be used in very low (trace) molar quantities. With good radiochemical “tracers,” one can directly target and quantify chemical or biochemical processes with a level of sensitivity high enough as not to disrupt, interfere or alter the process being observed (Figure 3, A).

^a Spatial resolution: The spatial resolution of an imaging modality refers to its ability to differentiate structures separated by distance. A modality with a low spatial resolution will thus not be able to effectively distinguish between structures that are close together.¹⁸³

^b Chemical resolution: The specificity of a molecular imaging probe and thus its ability to distinguish between one (bio)chemical process or target from another.

In addition to “tracing” the path of the tracer through the subjects’ anatomy, one is also able to observe the metabolic fate of the labeled moiety of the tracer compound. As with any chemical entity in an *in vivo* setting, tracers undergo metabolism and modification through physiological or pathological biochemical processes. It is vital and often useful to attempt to design tracers around such possible metabolic pathways, either to avoid unwanted metabolism as a tracer makes its way to a non-enzymatic target (such as a receptor or antigen) or to observe a metabolic pathway of interest. In the case of the former, to achieve uptake and enrichment of a tracer into a target tissue, the tracer must be highly specific and have a high affinity to its target. In the case of the latter, the tracer can be designed to be modified by a metabolic pathway so that it cannot leave the tissue where that process is taking place, either by blocking its continued metabolism or by biosynthetic incorporation. This process is known as metabolic trapping and is a key concept behind the use of important clinical tracers such as 2- ^{18}F fluorodeoxyglucose (^{18}F FDG), 9-(4- ^{18}F fluoro-3-[hydroxymethyl]butyl) guanine (^{18}F FHBG) and ^{18}F fluoromisonidazole (^{18}F FMISO) (Figure 3, B).

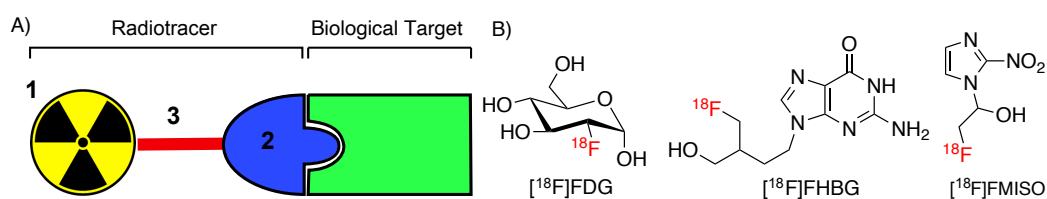


Figure 3: A) PET tracers usually consist of three parts: 1: A radioactive atom such as fluorine 18 (^{18}F), carbon 11 (^{11}C), or indium 111 (^{111}In), which contains the energy necessary for detection. 2: A “targeting moiety,” which typically makes up most of the mass of the tracer molecule and contains the chemical information required to selectively hit its target. 3: A stable linking group or chemical bond that joins the “targeting group” to the radioactive atom. B) Examples of (^{18}F) PET tracers.

The tracer principle and the concepts of metabolic trapping and targeted enrichment are cornerstones of both PET and SPECT imaging modalities. In the case of PET and SPECT BCMI, careful tracer development is required to achieve the high target specificities and specific activities (*vide infra* 3.1.1) and thus chemical resolution required to quantify the BCM *in vivo*. The stability of the tracer, how selectively it interacts with its intended target, and how it is ultimately metabolized and excreted (cleared), all result in the overall chemical resolution of the information obtained from imaging.

2.3.1.2 SPECT Imaging

SPECT imaging relies on the detection of single gamma photons emitted through decay pathways such as electron capture (^{111}In and ^{123}I) or isomeric transition ($^{99\text{m}}\text{Tc}$). The emitted gamma photons are detected and registered as a 2D projection by two or three detector blocks that rotate around the subject. Each detector block is fitted with a lead collimator that only allows gamma photons traveling in specific directions to enter the detector. The angular information from the position of the detector and collimator is then used to reconstruct the 2D projections into a 3D image. As gamma photons are detected directly from the decaying atom, the spatial resolution of SPECT imaging is predominantly limited by the technological factors, and the development of new detectors and collimators has resulted in preclinical SPECT scanners capable of sub-millimeter spatial resolution; a significant advantage for preclinical BCMI.²² However, many of these advances

have resulted in reduced sensitivity, which can be 3 to 4 orders of magnitude lower than that of PET.²² Several important studies featuring SPECT tracers for BCMI have nonetheless been published (*vide* chapter 5); however, the low sensitivity of SPECT remains a significant challenge to its role in the field of BCMI.

2.3.1.3 PET Imaging

The sensitivity afforded by PET imaging has secured it as a vital tool in several preclinical research areas, including BCMI. PET requires the use of positron-emitting (neutron deficient) radionuclides, where a proton decays into a neutron by the emission of a positron and a neutrino. The emitted positron travels through the surrounding matter over a distance that is dependent on the energy of decay (termed the “positron range”). The moving positron undergoes random and often drastic changes in course due to its interaction with the coulombic fields present in the matter it passes through. The positron eventually finds an electron in the surrounding matter and forms a positronium atom ($e^+ + e^-$), that annihilates to release two 511 keV gamma photons that travel outward at a 180° angle to each other (Figure 4, A). The PET camera takes the form of a detector ring made up of multiple scintillator detector blocks that encircle the subject. The emitted pair of γ -photons reach the detectors on opposite sides of the ring, which is registered and recorded as a coincidence^a that is used to define a line of response (LOR, the space between two detector blocks). The data can then be reconstructed to form an image (Figure 4, B).

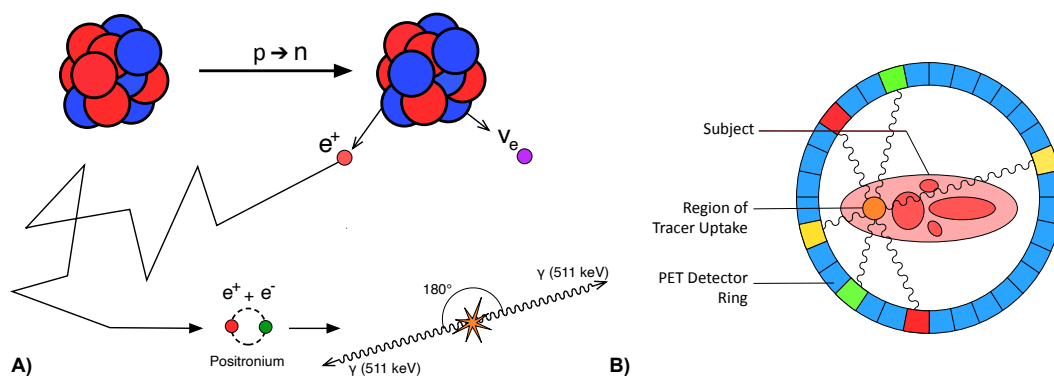


Figure 4: A) The mechanism of decay for a β^+ emitting isotope. B) A subject in the field of view of a PET detector ring. The gamma photons emitted by the tracer taken up into the target organ travel outward and interact with the scintillators in the detector block. The colored detector blocks represent true coincidences, i.e., from the same nuclear decay, and the space between the two blocks is termed the line of response (LOR). The LORs are used to reconstruct a 3D image of the activity distribution throughout the subject.

As PET detectors do not require collimators and all co-registered decay events are collected and used for reconstruction of the final image, the sensitivity of PET is much higher compared to that of SPECT. However, where technological and sensitivity factors broadly limit SPECT spatial resolution, PET spatial resolution is also limited by the physics of positron decay (specifically the positron range), non-collinearities^b in the

^a A true coincidence defined as two detection events from a single annihilation.

^b PET image reconstruction assumes that the two annihilation photons travel at 180° angle to each other, and any deviation from this angle will result in a false LOR reducing the spatial resolution and adding noise to the image. False LORs can occur due to: i) Scattered coincidences, where one of the annihilation photons is deflected by Compton scattering on its way to the detector, or ii) a random coincidence, where two photos from different annihilation events are registered simultaneously.

gamma photon pair, and the physics of gamma photon detection in scintillator^a crystal detectors.²² Thus, most modern preclinical PET scanners have a maximum spatial resolution of 1-2 mm.²³

Given the small physical size of pancreatic islets, transplanted islet clusters, and other β cell and diabetes models, another important factor that needs to be considered in the context of BCI is the partial volume effect (PVE). The PVE arises from the limited spatial resolution of the scanner and the way the images are sampled during quantification. The outcome of the PVE on PET image analysis is: i) a blurring of the region of interest (ROI) as “spill-out” and ii) an underestimation of the apparent activity within the ROI. The PVE can also occur when an excessively high background noise (higher than the ROI) is observed, which can be due, for example, from spill-over from other organs. This results in a “spill-in” effect whereby the activity in the ROI is overestimated. Both of these effects can be corrected for by modern image reconstruction algorithms; however, as pancreatic islets and other β cell models are typically small in size (well below the voxel size for a typical preclinical PET scanner), the partial volume effect can often be profound and adds an extra level of complexity when considering BCM image analysis and signal quantification.

Nonetheless, the sensitivity afforded by PET may allow for the quantification specific tracer uptake at β cell-specific biomarkers. However, due to the limitations of PET spatial resolution and the PVE, the development of a quantifiable PET BCMI method using current clinical and preclinical PET scanners depends almost entirely on probe development (*vide* chapter 5).

2.3.1 Magnetic Resonance Imaging (MRI)

Magnetic resonance imaging (MRI) has become one of the most widely used clinical and preclinical imaging modalities as it does not use ionizing radiation, has a high spatial resolution, excellent soft-tissue contrast, and can identify labeled tissues through the use of appropriate contrast agents.²⁴ However, of all the dominant molecular imaging modalities, MRI is one of the least sensitive with a sensitivity that is many orders of magnitude lower than that of PET.²⁵ MRI makes use of nuclear magnetism and the nuclear magnetic resonance (NMR) principle, as discovered and developed by Bloch and Purcell,^{26,27} to detect the density, chemical, and magnetic environments of spin-active nuclei (predominantly protons in water or lipid molecules) through the use of high-strength magnetic fields and radiofrequency (RF) pulses.

The placement of a population of spin-active atomic nuclei, such as ^1H , into a strong magnetic field splits the population of “magnetic” or “spin-active” nuclei into a “low energy” level (nuclei aligned with the magnetic field) and a “high energy” level (nuclei aligned against the magnetic field.) The population of protons in the lower energy level is larger than that of the higher energy level. This difference increases proportionally with the energy difference between the two energy levels, which is dependent on the strength of the magnetic

^a The interaction of a γ -photon with a scintillator crystal produces visible light which can be detected and amplified by the detector electronics. However, the crystal must have the correct properties (geometry, chemistry, density, etc.) for this effect to take place. The limitations imposed by these crystal properties are also major contributors to the scanner spatial resolution.

field. However, the ratio between these populations is small (as calculated by the Boltzmann distribution: $\frac{N_{\text{antiparallel}}}{N_{\text{parallel}}} = e^{\left(\frac{-\Delta E}{kT}\right)} = e^{\left(\frac{-\gamma \hbar B_0}{2\pi kT}\right)}$) and this accounts for the low sensitivity of MR methods in general. The protons in the lower energy level are excited with a pulse of electromagnetic radiation with a frequency (in the RF band) in resonance with the “precession” of the nuclei in question. The effect is a “flipping” of the net nuclear spins of the proton populations to a higher net energy or “excited” state. The relaxation^a of the excited population of protons back to the ground state releases energy in the form of RF radiation that is received as a free induction decay (FID) waveform by an RF receiver coil, which can then be further processed into a spectrum (in the case of NMR spectroscopy) or, with spatial encoding provided by the gradient coils of an MRI scanner, an image of the subject.²⁴

The high spatial resolution of MRI and its excellent soft-tissue contrast make it an important tool for abdominal imaging in general as well as for β cell imaging.⁵ However, due to the low volume and irregular distribution of the pancreatic islets, an islet-specific MRI contrast agent or islet labeling is required to visualize pancreatic islets and the BCM.^b Contrast agent free indirect methods such as blood oxygen level dependent (BOLD) and arterial spin labeling (ASL) MRI have been applied to the problems of BCM and BCF imaging preclinically but have not thus far been successfully translated into a clinical setting.⁹ Additionally, the low sensitivity of NMR methods mean that relatively high concentrations of contrast agent need to be taken into or onto the target cells before a significant signal change can be detected. This means that MRI contrasts and probes need to have limited toxicity and high selectivity for their targets.⁹

The development of safe, effective and β cell-specific MRI contrast agents is thus an important branch of β cell imaging research. Novel MR probes and contrast agents, which take the form of free metals, metal complexes, nanoparticles, and various bioconjugates of the former, have found application not only towards the imaging and quantification of the BCM but also BCF. One potential method of the *in vivo* measurement of BCF is manganese-enhanced MRI (MEMRI), which uses paramagnetic manganese (Mn^{2+}) as a calcium (Ca^{2+}) analog. When β cells are stimulated, there is an influx of Ca^{2+} through voltage-gated Ca^{2+} ion channels (VGCC). Mn^{2+} ions are also taken up through these channels and thus accumulate in the stimulated β cells, showing a glucose-dependent uptake signal and a diminished signal in diabetes models.^{28–33} However, given the cyto- and neuro-toxicity of Mn^{2+} , especially at the concentrations required to achieve a good MR contrast in

^a The relaxation (the loss of energy) of a nucleus from an excited spin state to the ground spin state can occur through two main modes i) Spin-lattice relaxation or thermal relaxation occurs as the excited state nuclei lose their energy as thermal motion to atoms and electrons in their immediate environment (the lattice) and is characterized by the spin-lattice relaxation time (T_1). ii) Spin-spin relaxation (T_2) occurs due to a loss of magnetic moment phase coherence with other nearby protons, as all magnetically (chemically) non-equivalent protons precess at slightly different rates. Protons in different magnetic environments will shorten each other's spin-spin relaxation time. The different chemical/magnetic environments (which occur in different tissues) effect both T_1 and T_2 in a given magnetic field and this results in image contrast between different tissues and regions.²⁴

^b An MRI contrast agent will change the relaxation time (T_1 and T_2) experienced by protons in the region of uptake and will enhance the contrast with the surrounding tissue.²⁴

pancreatic islets, more work is needed to determine the safety and feasibility of this method in a clinical setting.^{8,17}

2.3.2 Multimodal Imaging for β Cell Imaging

Each molecular imaging modality discussed above has its strengths and weaknesses that contribute to its usefulness as a modality for β cell imaging. However, given the challenges to BCMI as discussed above (*vide supra* 2.2), no modality can provide a “one size fits all” solution. By using other modalities such as MRI, OI, and CT in combination with PET or SPECT, either sequentially or simultaneously, one can begin to answer biological questions that would be difficult to address with a single stand-alone modality. Another important use of multimodal techniques is the cross-validation of BCI imaging protocols and experiments against each other and other imaging platforms. One such example is the report by Eter *et al.*, where the authors used optical projection tomography (OPT, an *ex-vivo* optical imaging technique) to accurately assess, cross-validate, and correlate stereological information about BCM (from OPT) with the volume of uptake of a β cell-specific SPECT radiotracer in a rat pancreas diabetes model. In this case, all imaging experiments were sequentially performed *ex vivo* (in separate facilities), and separate radio-probes/stains were used.³⁴

One combination of modalities with potential clinical importance for β cell imaging is the combination of PET and MRI. As discussed above, PET with the use of appropriate β cell-specific tracers has the sensitivity to quantify BCM, while MRI presents several avenues for exploring BCF. Despite the methods thus far developed to study the BCM and BCF, a tool to investigate and track the relationship between BCM and BCF is still lacking. Simultaneous PET/MEMRI is a multimodal approach that has the potential to address these questions.

Chapter 3: Radiochemistry and Tracer Synthesis

3.1 Radionuclides for Nuclear Medical Imaging

How one designs, synthesizes, and characterizes radiotracers for any application is in itself a non-trivial exercise. While the specific design criteria for BCM tracers will be discussed in chapter 5, the core concepts of PET radiochemistry and their implications on isotope selection, PET tracer design, and synthesis will be the focus of this chapter. This chapter will also aim to review a number of ground-breaking advances in radiochemical methodology that are expanding the accessibility and chemical diversity of novel PET tracers, especially where the use of ^{18}F is concerned.

3.1.1 The Selection of Radionuclides for the PET imaging of β Cells.

The diverse range of positron-emitting isotopes can be broadly categorized into two groups, each characterized by their chemical properties: i) The “main-group” elements, which include isotopes such as ^{11}C , ^{15}O , and ^{18}F , and ii) the “radiometals”, which feature heavier metallic atoms such as ^{64}Cu , ^{68}Ga , and ^{89}Zr (Table 1).³⁵ The large selection of radioisotopes available to radiochemists and imaging scientists for a particular imaging application needs to be carefully considered in terms of both their chemical and physical properties.³⁶

Table 1: Important commonly used positron emitting isotopes for the development of novel PET tracers. Data taken from Conti et al.³⁷ and Machulla et al.³⁵

Labeling Chemistry	Isotope	Half-life	Decay Mode	E max of β^+ (MeV)	Positron Range in Water	
					R_{max} (mm)	R_{mean} (mm)
Main-Group Elements (Covalent)	^{11}C	20,4 (min)	β^+ (99.8 %)	0,386	4,20	1,20
	^{13}N	9,97 (min)	β^+ (99.8 %)	0,492	5,50	1,80
	^{15}O	2,04 (min)	β^+ (99.9%)	0,735	8,40	3,00
	^{18}F	109,8 (min)	β^+ (97 %); EC (3%)	0,25	2,40	0,60
Transition Metals (Chelation)	^{68}Ga	67,7 (min)	β^+ (88.9%); EC (11.1%)	1,899	9,20	3,50
	^{64}Cu	12,7 (hr)	β^+ (17.5 %); β^- (39 %); EC (43 %)	0,653	2,50	0,70
	^{89}Zr	78,4 (hr)	β^+ (22.7%)	0,902	3,80	1,30

The chemistry of the radioisotope dictates not only how and where it can be attached to a molecule of interest (either covalently or through chelation (radiometals)) but also the overall ADME (absorption, distribution, metabolism, excretion) behavior of the final tracer. The main-group radioisotopes are typically used to label small molecules and prosthetic groups through the formation of strong covalent bonds. This often requires harsh reagents and reaction conditions that are not suitable for large biomolecules (such as peptides, hormones, and antibodies). Biomolecules are more often conjugated with a chelator and labeled with radiometals; a process, which due to its thermodynamic favorability, can be carried out under relatively mild reaction conditions. The pharmacological behavior of a large biomolecule will not be significantly

affected by the addition of a radiometal-chelator complex; however, such a complex would likely have a significant effect on the pharmacokinetic behavior of small lipophilic molecules.

The physical properties of the isotope used for labeling, including its decay mode, decay energy, positron range in tissue, and half-life, must be carefully considered (Table 1). For PET isotopes, decay by positron emission is essential, but many common PET isotopes also decay by other pathways. ^{64}Cu , for example, also decays by electron capture, which can introduce noise into the image, as well as β^- and byproduct Auger electron emission, which are biologically destructive and carry implications for radiotoxicity (or theranostic approaches).³⁶ The energy of decay and the positron range of a radioisotope can also have major implications on image resolution (*vide supra* 2.3.1.3). Tracers that feature isotopes with long positron ranges result in lower spatial resolutions as the positron will travel further from the decay event in the target tissue.

Of particular importance is the half-life of the isotope, which is not only of direct practical concern when considering the synthesis, handling, and use of the final radiotracer, but should also match the biological half-life of the intended tracer. Small molecules typically reach their targets and are subsequently cleared relatively quickly (minutes to hours), while larger biomolecules may take many hours or days to become sufficiently enriched at their targets to provide a suitable target to background contrast for imaging. A long-lived isotope conjugated to a rapidly cleared molecule may thus show an unwanted accumulation of radio-metabolites in off-target/excretory tissues (such as the gut, liver or urinary tract system), which is of consequence to patient dosimetry. A short-lived isotope conjugated to a large molecule with slow pharmacokinetics may decay entirely by the time the tracer shows sufficient uptake at its target.

Additionally, the half-life of a particular isotope is also related to the specific activity^a of the tracer. A radionuclide's maximum theoretical specific activity can be calculated by:

$$a = \frac{N_A \ln 2}{T_{\frac{1}{2}} \cdot m}$$

Short-lived isotopes can, therefore, theoretically, be produced with much higher specific activities while longer-lived isotopes have much lower maximum specific activities.^b The implications of tracer specific activity on the sensitivity of a PET assay are particularly important to BCMI due to the small size of the pancreatic islets and the low binding capacities of the established imaging biomarkers. It is thus essential to maximize the specific activity of the tracer, both by choice of isotope and during the production procedure, to achieve maximal sensitivity of the PET experiment. This is especially important where receptor imaging is concerned as many high-affinity receptors (such as GLP-1R for BCI (*vide Chapter 5*)) have a relatively low

^a The SI unit of the radioactivity of a substance is the Becquerel (Bq), which is defined by the number of nuclear decays per second. The specific activity of any radioactive material is defined as the activity per unit mass (Bq/g), but in biomedical and radiochemical literature, it is often given as activity per mole (Bq/mol).

^b In practice, the specific activities achieved in a laboratory are typically much lower than those theoretically possible as stable isotopic impurities are easily introduced when producing and working with radiochemicals. The mass of a given amount of a radioactive substance is typically very low, and impurities are often in large excess (by mass) relative to the radionuclide.

binding capacity. Tracers with high specific activities should be used to prevent saturation of the target with non-labeled carrier^a or pseudo-carrier^b, which may result in a violation of the conditions of the tracer principle. Thus, the choice of isotope for BCMI is a critical factor in this regard.

3.1.2 Production of PET isotopes

Due to their neutron deficient nature, PET isotopes for medical imaging are typically produced by the proton or deuteron bombardment of a target material using small medical cyclotrons, which usually have beam energies between 10-20 MeV.^{36,38} Initially invented and developed by Ernest Lawrence,^c the cyclotron is a particle accelerator that uses a static homogeneous magnetic field and an alternating electrostatic field to accelerate a continuous beam of charged ions to sufficiently high energies to perform nuclear reactions.³⁹⁻⁴¹

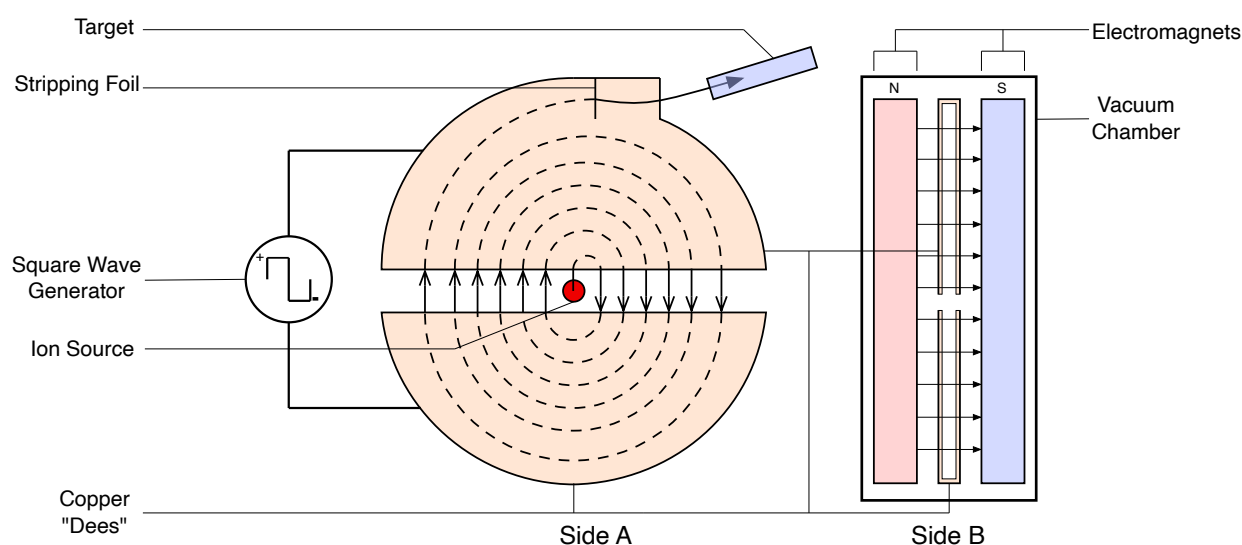


Figure 5: A schematic diagram showing the structure and function of a typical medical cyclotron.

A cyclotron typically consists of two hollow D-shaped copper electrodes (termed “Dees”) that are situated in a vacuum chamber between two electromagnetic poles.⁴¹ At the center of the cyclotron is an ion source which is able to provide a constant flow of charged ions, usually hydride (H^-) or deuteride (D^-) (from hydrogen or deuterium gas), which are accelerated by an oscillating electrostatic field between the two Dees^d (Figure 5). By adjusting the frequency of the oscillating electrostatic field and the magnetic field strength, the operator can adjust the beam current, flux, and energy to account for the type of particle being accelerated, the nuclear reaction cross-section, and the nuclide being produced. The accelerated particles travel outward along an expanding spiral path due to the Lorentz force they experience by moving through a strong external

^a Such isotopic impurities are termed “carrier” if they are of the same element as the radionuclide of interest.

^b Such chemical impurities are termed “pseudo-carrier” if they are from another element with only slightly different chemical properties.

^c Ernest Lawrence was awarded the 1939 Nobel Prize in physics for “the invention and development of the cyclotron and for results obtained with it, especially with regard to artificial radioactive elements.”³⁹

^d The cyclotron resonance frequency is the frequency required so that the accelerating particle makes a circuit of the cyclotron during one cycle of the oscillation of the electrical field. It is given as $f = \frac{qB}{2\pi m}$ where q is the charge of the particle, B is the magnetic field strength, and m is the relativistic mass of the moving particle.⁴¹

magnetic field. Once the beam of negatively charged particles reaches the outer edge of the spiral, it passes through a “stripping foil” that removes the electrons from the atomic nuclei, thus reversing their polarities ($H^- \rightarrow H^+$).^{40,41} This causes the particle beam to leave the spiral as it then experiences an inverted Lorentz force. The beam of protons or deuterons is thus directed into a target containing the required material to produce the desired radionuclide (Table 2).

By adjusting the location of the stripping foil along the other edge of the beam path, one can deviate and focus the beam onto different cyclotron targets. Modern medical cyclotrons can perform several different nuclear reactions and can be fitted with multiple targets that are capable of holding either solid, liquid, or gas materials. The classical nuclear reactions performed in most radiopharmacies on a day-to-day basis are those to produce ^{18}F and ^{11}C (Table 2). Typically, the proton beam passes through the foil window (made from either Havar, aluminum, niobium, or titanium)⁴² of the water-cooled target housing that contains the material to be transmuted. [^{18}F]fluoride (*vide infra*) is, for example, synthesized by the $^{18}\text{O}(p,n)^{18}\text{F}$ nuclear reaction whereby [^{18}O]H₂O is irradiated with a beam of protons producing high specific activity [^{18}F]HF with the expulsion of a neutron (Figure 6). ^{18}F and ^{11}C are synthesized in liquid and gas targets respectively, and the product of these nuclear reactions can easily be transferred to an automated synthesizer or collection vial with pressure from a carrier gas (such as helium) at the end of bombardment (EOB).³⁶ In the case of ^{64}Cu and ^{89}Zr , solid targets are used that need to be manually removed from the target and processed in order to isolate the desired radionuclide.

Table 2: Common nuclear reactions performed on medical cyclotrons.

Isotope	Half-life	Production Reaction
^{11}C	20,4 (min)	$^{14}\text{N}(p,\alpha)^{11}\text{C}$
^{13}N	9,97 (min)	$^{16}\text{O}(p,\alpha)^{13}\text{N}$
^{15}O	2,04 (min)	$^{14}\text{N}(d,\alpha)^{15}\text{O}$
^{18}F	109,8 (min)	$^{18}\text{O}(p,n)^{18}\text{F}$
^{68}Ga	67,7 (min)	$^{68}\text{Ge} \rightarrow ^{68}\text{Ga}$ (generator)
^{64}Cu	12,7 (hr)	$^{64}\text{Ni}(p,n)^{64}\text{Cu}$
^{89}Zr	78,4 (hr)	$^{89}\text{Y}(p,n)^{89}\text{Zr}$

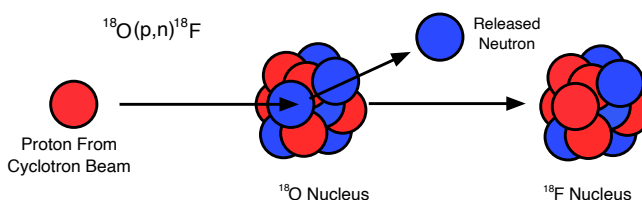


Figure 6: The mechanism of the $^{18}\text{O}(p,n)^{18}\text{F}$ nuclear reaction whereby [^{18}O]H₂O is transmuted in [^{18}F]fluoride by the addition of an accelerated proton and the expulsion of a neutron.

In addition to cyclotron production, radioisotopes can also be produced by radionuclide generators. ^{68}Ga is a notable example of such an isotope and is used ubiquitously as a short-lived PET isotope in nuclear imaging facilities that do not have easy access to cyclotron-produced radionuclides. This is due to the fact that it can be produced easily and relatively cheaply (when compared to the large and expensive infrastructure required for cyclotron facilities) with an isotope generator, which can be easily set up and operated out of a suitable laboratory.³⁶ Germanium-68/gallium-68 generators contain ^{68}Ge ($T_{1/2} = 271$ days) that is adsorbed onto a stationary phase and decays via electron capture to produce $^{68}\text{Ga}^{3+}$ ions. The ^{68}Ga can then be periodically eluted, typically with dilute (0.05 – 0.1 M) hydrochloric acid as [^{68}Ga]Gallium (III) chloride, after which it is further processed and concentrated for radiosynthesis. Due to the long half-life of the ^{68}Ge parent isotope,

the generator has a long shelf-life and can be used to generate ^{68}Ga regularly for many months. As such, ^{68}Ga has become an important isotope in BCMI research due to its easy accessibility. Several ^{68}Ga based BCM probes have been published (*vide* 5.3.1). However, due to the chemical nature of the isotope extraction and isolation, generators such as these are not capable of reaching the high specific activities achievable by most medical cyclotrons.

3.1.3 The PET Tracer Production Workflow

Once produced, the required radionuclide can be collected and processed (for manual synthesis) or transferred to an automated synthesizer for tracer production. Due to the high radioactivities required for the production of PET tracers using short-lived isotopes like ^{11}C and ^{18}F , radiosyntheses are typically carried out in lead chambers (hot cells) by pre-programmed automatic synthesizers (or synthesis modules) in order to limit the radiation exposure to the personnel performing the synthesis. Once delivered to the module, the isotope is processed (converted into a reactive chemical species), purified, and reacted with the necessary tracer precursor to form the desired tracer. Upon completion, the reaction is quenched, diluted, and subjected to a purification step, after which it can then be concentrated and formulated for injection. Given the short half-lives of most clinical PET tracers, delivery of the tracer usually occurs immediately after the synthesis is complete. Samples are then taken from the final product for quality control, after which the tracer can be released for use^a (Figure 7).

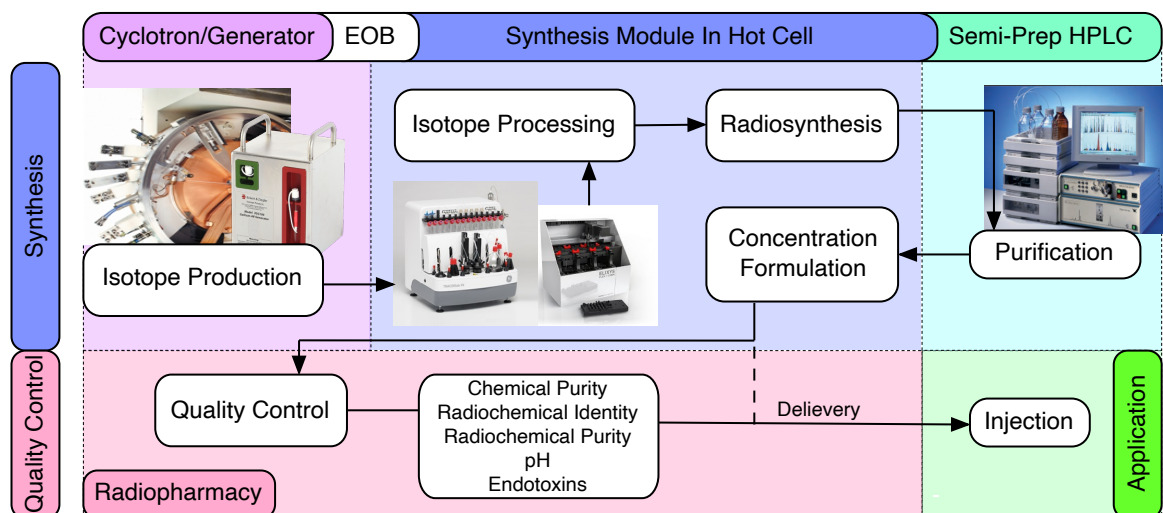


Figure 7: The typical workflow of a tracer production, from nuclide production to injection into an animal or patient.

When low amounts of radioactivity are used, the radiosynthesis can be carried out manually behind appropriate shielding (lead for PET and γ -emitting isotopes, plexiglass for β^- and α emitters). Manual syntheses are frequently applied to tracer and radiochemical methodology development but are seldomly performed for routine tracer productions. However, the translation of a manual radiosynthesis onto an

^a The rigorous quality and safety standards required for clinical tracer production mean that highly standardized synthesis, handling, and quality control procedures need to be defined according to the rules of good manufacturing practice (GMP).

automated synthesizer is often non-trivial due to many complex factors, and the chemistry often requires careful optimization. The optimization of radiochemical processes through a design of experiments (DoE) approach, for improved tracer production and to facilitate the automation of new radiochemical methodologies, is a central topic of this thesis and will be discussed in detail (*vide Chapter 7*. The core concepts of DoE are discussed below in **Chapter 4**).

3.2 The Chemistry of [¹⁸F]Fluorine

Due to its outstanding imaging properties, practical half-life, and “clean” decay pathway (97 % β^+ decay) (*vide supra*), [¹⁸F]fluorine has become arguably the most important isotope available for PET Imaging. Fluorine is the element with the highest electronegativity on the Pauling scale (3.98) and as such, has a high reduction potential, small ionic radius (1.33 Å), and is strongly electron-withdrawing.⁴³ Elemental fluorine (F₂) is thus extremely reactive and only exists in nature in its reduced form, the fluoride (F⁻) ion.^{38,44} C-F bonds are the strongest in organic chemistry due to fluorine’s small size and electronic configuration, which are also responsible for the unique pharmacodynamic and pharmacokinetic properties fluorine imparts on small drug-like molecules. This has driven the pharmaceutical industry to invest in the development of organofluorine chemistry and C-¹⁹F bond formation methodologies.⁴⁵ However, despite these advances, the chemical toolbox available to radiochemists is somewhat limited as most ¹⁹F-fluorination reactions are not easily adapted for use as late-stage radiofluorination reactions^a on functionally complex precursors. This is because ¹⁸F is short-lived and is produced in sub-stoichiometric quantities (relative to precursors and reagents), even at high radioactivity concentrations.^{43,46} Thus far, the synthesis of the ¹⁸F labeled “work-horse” tracers used for clinical PET has relied on a well-established yet small set of radiofluorination methodologies.

In their 2017 commentary in *Nature Chemistry*, Campbell *et al.* discussed the gaps that currently exist in the PET tracer development pipeline, specifically citing the value of fundamental radiochemical method development to both the fields of radiochemistry and molecular imaging.⁴⁶ The authors argued that lack of diverse radiochemical methodologies lead to a lack of chemical diversity in the molecules that were chosen for evaluation as novel tracers and that the expansion and development of “the ¹⁸F radiochemical space” available to radiochemists was thus a necessity. The development of new ¹⁸F-fluorinations and the adaption of ¹⁹F-fluorinations for use with [¹⁸F]fluoride expands the radiochemical toolbox available to developmental radiochemists and imaging scientists, allowing access to more molecular diversity in novel ¹⁸F tracers. At the same time, more work, with a focus on bringing newly developed radiochemical methods into routine use, is required to facilitate the translation of new tracers from concepts to clinically useful tools.⁴⁶ Moreover, poor labeling performance often results in compromises to the tracer’s final structure. Novel tracer

^a A “late-stage radiofluorination” aims to incorporate the radioisotope as late as possible in the synthetic sequence. This usually allows for shorter synthesis times and higher overall radiochemical yields over fewer steps.

precursors are often designed with structural modifications (such as the addition of prosthetic groups or chelators), which may affect the tracer's *in vivo* behavior and performance, in order to accommodate easier and more reliable labeling chemistry.

The current challenges of ^{18}F fluorination stem from the availability and reactivity of the two dominant ^{18}F sources:⁴³ i) as electrophilic, highly reactive and unspecific $^{18}\text{F}\text{F}_2$ gas, or ii) as nucleophilic, relatively unreactive aqueous hydrogen fluoride ($^{18}\text{F}\text{HF}$) (Table 3).⁴⁷

Table 3: The three most common methods for producing ^{18}F and their advantages in terms of specific activity and Fluorine reactivity. Data taken from the review by Preshlock et al.⁴⁷

Production Reaction	Target material	Target Type	Product	Reactivity	Max molar activity (GBq/ μmol)
$^{20}\text{Ne}(d,\alpha)^{18}\text{F}$	^{20}Ne (gas) (200 μmol $^{19}\text{F}\text{F}_2$)	Gas	$^{18}\text{F}\text{F}_{2(g)}$	electrophilic (high)	0.04-0.4
$^{18}\text{O}(p,n)^{18}\text{F}$	$^{18}\text{O}_2$, Kr (gas) (50 μmol $^{19}\text{F}\text{F}_2$)	Gas	$^{18}\text{F}\text{F}_{2(g)}$	electrophilic (high)	0.35-2.00
$^{18}\text{O}(p,n)^{18}\text{F}$	$^{18}\text{O}\text{H}_2\text{O}_{(l)}$	Liquid	$^{18}\text{F}\text{HF}$ (F^-) _(aq)	nucleophilic (low)	40000

3.2.1 Electrophilic ^{18}F Chemistry

$^{18}\text{F}\text{F}_2$ is produced by using either $^{20}\text{Ne}/^{19}\text{F}$ or $^{18}\text{O}_2/\text{Kr}/^{19}\text{F}_2$ gas targets. Gaseous $^{19}\text{F}_2$ must be added as a carrier gas to pick up any ^{18}F formed by the nuclear reaction, forming $^{18}\text{F}\text{-}^{19}\text{F}$ gas as the final product.⁴⁷ The radionuclide is thus diluted by the presence of $^{19}\text{F}\text{F}_2$ resulting in a final product of low specific activity. The reaction of electrophilic $^{18}\text{F}\text{-}^{19}\text{F}$, which can be attacked by a nucleophilic labeling precursor at either atom, further reduces the specific activity of the final tracer (Figure 8: A). Additionally, $^{18}\text{F}\text{F}_2$ gas is highly reactive and often chemically non-specific, and thus, difficult to handle. However, its reactivity means that it can be used to synthesize several powerful electrophilic fluorinating reagents to be used as $^{18}\text{F}\text{F}^+$ sources for various radiolabeling strategies.⁴⁷ Due to $^{18}\text{F}\text{F}_2$'s low specific activity and relative inaccessibility (compared to ^{18}F fluoride), it will not be discussed further here.

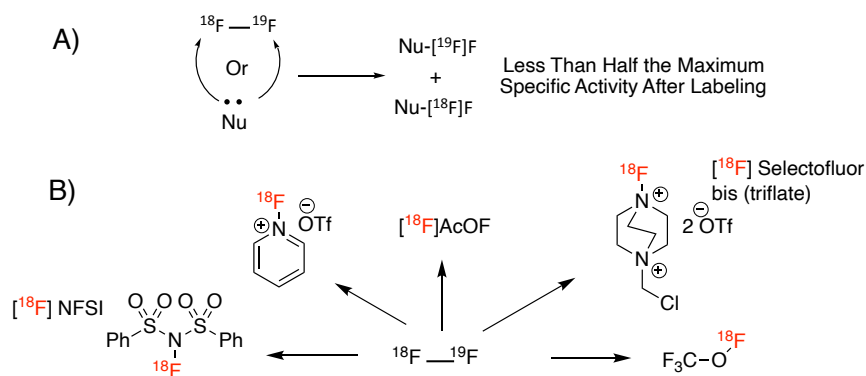


Figure 8: A) The mechanism by which $^{18}\text{F}\text{-}^{19}\text{F}$ reacts results (in the optimum case) in a 50% reduction in the specific activity of the final tracer/fluorinating reagent. B) A selection of several common " F^+ " sources that can be synthesized from $^{18}\text{F}\text{F}_2$ (Scheme modified from review by Preshlock et al.)⁴⁷

3.2.2 Nucleophilic ^{18}F chemistry

^{18}F Fluoride ($^{18}\text{F}^-$), the most commonly used form of ^{18}F , is easily handled in aqueous solution. It is easily produced as ^{18}F HF in large quantities and high specific activities by medical cyclotrons through the $^{18}\text{O}(\text{p},\text{n})^{18}\text{F}$ nuclear reaction of $^{18}\text{O}\text{H}_2\text{O}$ (*vide supra* 3.1.2).⁴⁷ Due to its high electronegativity, F^- is the smallest anion, has a high ionization energy, and strongly polarizes any bond in which it participates. However, due to its small atomic radius, C-F and H-F bonds are short and unexpectedly strong.⁴⁸ HF is thus, somewhat unintuitively, the weakest hydrohalic acid and possesses a high hydration energy, with unsolvated F^- being a Bronsted base. HF, the main species of F^- in water, is a weak nucleophile unless all hydrogen bond donors can be excluded. By de-solvating the F^- anion and introducing “softening” counter ions and phase transfer catalysts (PTCs) in organic solvents, the strength of the ionic interaction between the F^- anion and its counter cation can be reduced, increasing the effective nucleophilicity of F^- (Figure 9, A).^{47,48} In radiochemical experiments, this is typically achieved by processing and drying the fluoride before the reaction, freeing the reactive lone pair of electrons on F^- for nucleophilic substitution reactions.⁴⁹ However, due to its strong Bronsted basicity, a key challenge when using unsolvated (anhydrous) $^{18}\text{F}^-$ is limiting unwanted side reactions.⁴³

3.2.2.1 ^{18}F Fluoride Processing

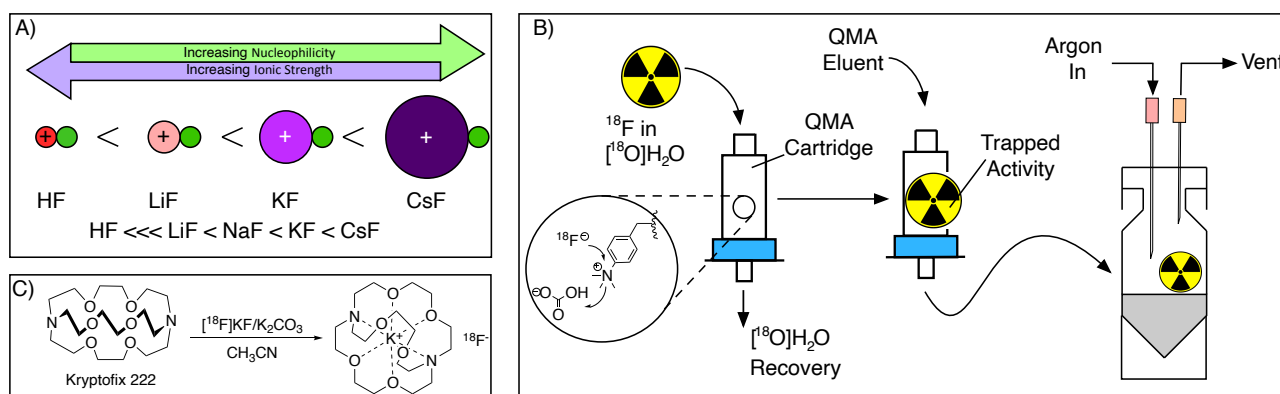


Figure 9:A) The alkali fluorides in the sequence of increasing nucleophilicity. B) The general procedure for fluoride processing by QMA ion exchange and azeotropic drying. C) The inclusion of the potassium cation into a [2.2.2]kryptofix (K_{222}) phase transfer catalyst to further “soften” the cation by distributing the charge over a large surface and by increasing the cation charge volume.

In the majority of established radiofluorinations, ^{18}F fluoride in $^{18}\text{O}\text{H}_2\text{O}$ is delivered from the cyclotron, after which it is trapped on a cartridge containing a resin rich in positively charged quaternary methylammonium (QMA) moieties paired with an appropriate counterion, usually hydrogen carbonate. The fluoride displaces the counterions through ion exchange, becoming trapped on the resin while the valuable $^{18}\text{O}\text{H}_2\text{O}$ water passes through the cartridge and is collected for recycling. The ^{18}F fluoride is then eluted from the cartridge using a suitable eluent (Figure 9, B).⁴⁷ Often, this is a mixture of potassium carbonate (K_2CO_3) providing a counter ion (a weakly nucleophilic mild base to prevent the formation of volatile ^{18}F HF)⁴⁹ and a PTC, most often [2.2.2]kryptofix[®] (K_{222}), in solution of water and an organic solvent such as acetonitrile. K_{222} is a bowl-shaped molecule that wraps around the potassium counter ion and serves to decrease the

cation's charge density, weakening the interaction between the [^{18}F]fluoride and the counterion, and thus increasing the [^{18}F]fluoride's nucleophilicity (Figure 9 C).^{49,50} Once the [^{18}F]fluoride has been eluted into a reaction vessel, the water is removed via azeotropic drying whereby the solution is boiled under a stream of argon in the presence of an organic solvent, usually acetonitrile, which can form an azeotrope^a with water (Figure 9 B). Multiple additions of the solvent are added to ensure complete dryness.⁴⁷ Once dry, the fluoride can be taken up in the necessary solvent and subjected to the desired reaction conditions.

3.2.2.2 Nucleophilic Alkyl Radiofluorination

The simplest and most prevalent reaction in ^{18}F radiochemistry is the $\text{S}_{\text{N}}2$ [^{18}F]fluoride substitution of a leaving group (such as alkyl halides and sulfonic esters) on sp^3 hybridized carbons, formally known as the Finkelstein reaction (Figure 10). These reactions are typically carried out in polar aprotic organic solvents (such as acetonitrile (MeCN) or dimethyl sulfoxide (DMSO)) using protected (non-acidic, non-nucleophilic) precursors.⁴⁹ This chemistry is responsible for the production of most clinically and preclinically relevant tracers currently in routine use, including [^{18}F]FDG, [^{18}F]FMISO, [^{18}F]FHBG (*vide supra*, Figure 3), [^{18}F]FLT, and [^{18}F]FET (Figure 10, inset).

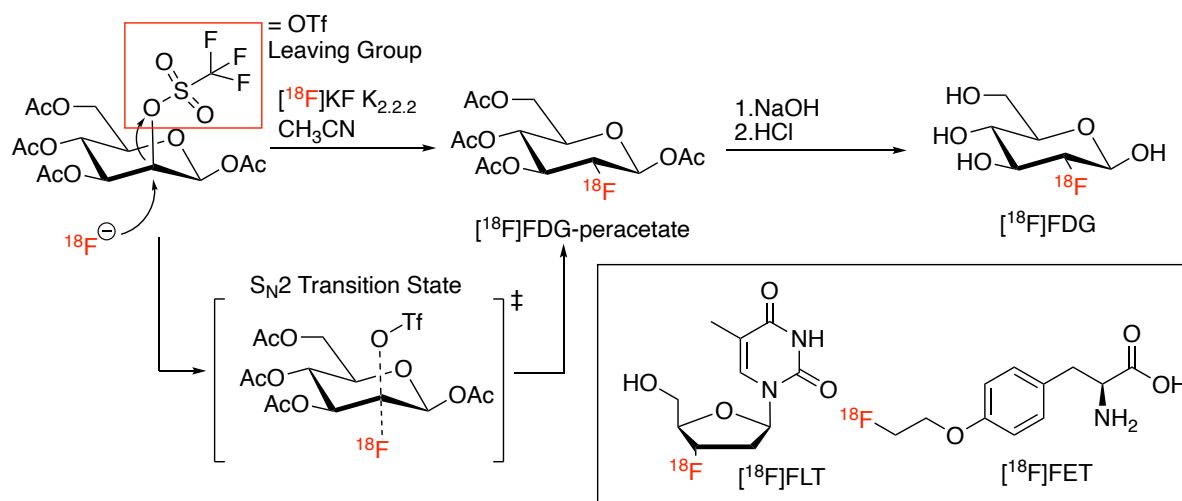


Figure 10: The mechanism of the $\text{S}_{\text{N}}2$ reaction in the context of the radiosynthesis of [^{18}F]FDG. The reaction transition state is marked with a double dagger. Inset: the structures of [^{18}F]FLT and [^{18}F]FET.

The $\text{S}_{\text{N}}2$ substitution occurs when a nucleophile is introduced to an electrophilic sp^3 carbon center possessing a suitable leaving group. The key feature of the $\text{S}_{\text{N}}2$ mechanism (as opposed to the $\text{S}_{\text{N}}1$) is that the new bond between the incoming nucleophile and carbon center forms as the old bond between the carbon and the leaving group breaks and thus the stereochemistry of the carbon center is specifically inverted.⁵¹ There is no carbocation intermediate (as with $\text{S}_{\text{N}}1$) and thus no possibility to form a racemic product. This inversion of

^a An azeotrope is a mixture of two liquids that has a constant composition throughout distillation. Practically, this effect is used to efficiently remove water from solutions with azeotrope-forming organic solvents such as acetonitrile or toluene.

stereochemistry is a vital feature of the synthesis of [^{18}F]FDG and allows the efficient stereospecific conversion of 2-mannose triflate to 2-[^{18}F]fluorodeoxyglucose, its diastereomer.⁵⁰

These simple aliphatic substitutions are of vital importance to the field of ^{18}F radiochemistry as they are robust and reliable; however, they are limited to stable aliphatic carbon centers. Thus, this prevalent chemistry is limited in scope, which limits the chemical diversity that could otherwise be achieved in tracer design. Many ^{18}F tracers are designed with a suitable aliphatic chain included for labeling (such as a fluoroethyl (as in [^{18}F]FET (Figure 10)), which can alter the tracer's bioavailability and ADME properties.

3.2.2.3 Nucleophilic Aryl Radiofluorination

As the prevalence of novel tracers based on drug-like aromatic core structures has begun to rise, radiochemists have had to develop methods for the labeling of aromatic (sp^2) carbon centers using ^{18}F -fluoride. The most obvious way by which this can be achieved is a nucleophilic aromatic substitution, which primarily occurs through the "addition-elimination" ($\text{S}_{\text{N}}\text{Ar}$) mechanism.⁵² A limitation of the $\text{S}_{\text{N}}\text{Ar}$ is that it is limited to aromatic rings that contain electron-withdrawing groups (EWG) such as a carbonyl, nitro, or electronegative atoms within the ring itself (e.g., pyridine) (Figure 11, A). The position of the EWG relative to the site of substitution is also vital to maximize reactivity. EWGs either in the *ortho*- (*o*-) or *para* (*p*-) positions can better stabilize the molecular orbital of the transition state arenium ion^a formed as a result of nucleophilic addition (Figure 11, B).^{47,52} The more electron-withdrawn the aromatic ring is, the more reactive it is to aromatic substitution with ^{18}F . Nucleophilic aromatic substitutions are robust and reliable, yet the structural requirements and harsh reaction conditions for an efficient $\text{S}_{\text{N}}\text{Ar}$ to take place often pose constraints on the design and synthesis of novel radiotracers. Nonetheless, several widely used tracers and prosthetic groups are labeled using nucleophilic aromatic substitution conditions.

The Balz-Schiemann reaction, which proceeds through the formation and elimination of diazonium salts (aromatic $\text{S}_{\text{N}}1$ mechanism), was one of the first reactions to be investigated for the radiofluorination of electron-rich and -neutral aromatic rings (Figure 11, C). However, the reaction, which uses [^{18}F]BF₄⁻ as the fluorinating agent, suffered from low specific activities due to the competing fluorination with ^{19}F ⁻ and thus never found application as a viable methodology for tracer synthesis.⁴⁷ The Wallach reaction, which also follows an $\text{S}_{\text{N}}1$ type mechanism, was also investigated as a method to access electron-rich/-neutral fluoroarenes (Figure 11, D). While it did circumvent the low specific activities and radiochemical yields (RCYs) obtained by the Balz-Schiemann reaction, the stability of the precursor and the tendency of the aryl cation transition state to form byproducts also prevented the widespread adoption of this method.

^a The electrons are delocalized through the aromatic ring and can also be represented by the Meisenheimer complex resonance structures.

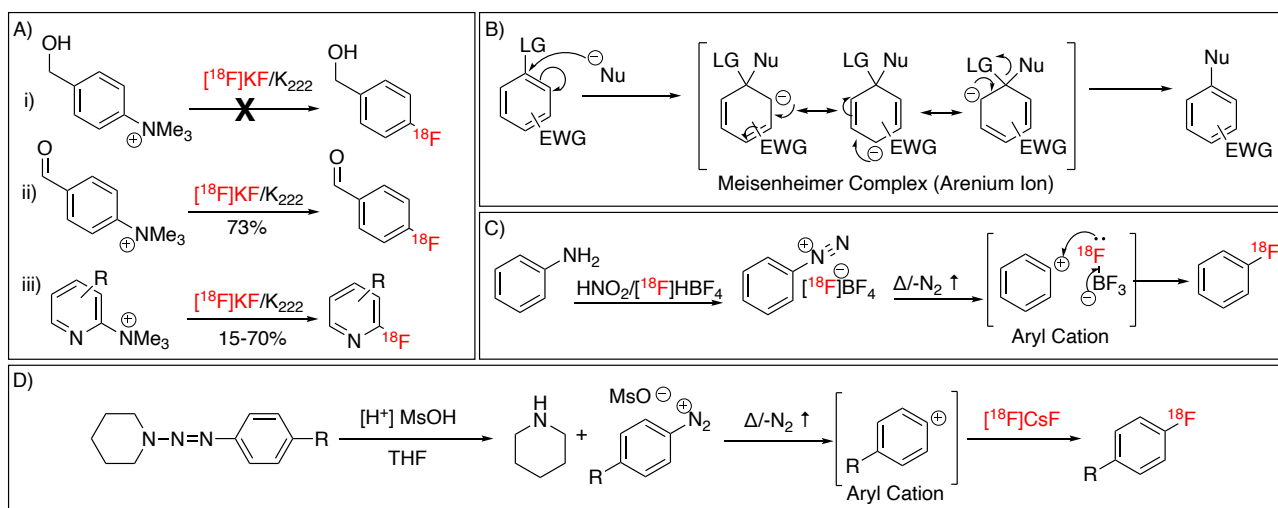


Figure 11: A) A selection of S_NAr radiofluorinations: i) the benzyl alcohol is not electron withdrawn and cannot accept electrons from the nucleophile, while ii) and iii) are well-known radiofluorination strategies.⁴⁷ B) The mechanism of the nucleophilic aromatic substitution reaction (S_NAr).⁵² C) The mechanism of the Balz-Schiemann radiofluorination reaction.⁵³ D) The Wallach reaction adapted for radiofluorination.⁴⁷

3.3 New Advances in Late-Stage Aromatic Nucleophilic Radiofluorination

As discussed above, the radiochemical toolbox has specifically lacked methodologies for the labeling of electron-rich and -neutral aromatic rings that cannot be effectively labeled with S_N2 and S_NAr type reactions. However, the last half-decade has seen a surge in the number of published methodologies for the radiofluorination of a wide scope of aromatic and heteroaromatic precursors, and these new methods are being adapted for tracer development with increasing frequency.^{47,54} Notable, among these methodologies, are the chemoselective radiofluorinations of diaryliodonium salts and ylides^a (*vide infra*),^{47,54–57} the palladium and nickel complex-mediated radiofluorinations or electron-rich arenes,^{58–60} and the ^{18}F -deoxyfluorination of phenols via ruthenium metallocenes (Figure 12).^{61,62} These reactions were demonstrated through the synthesis of several clinically relevant molecules. However, many did not fulfill the requirements for widespread application as they were often difficult to carry out, featured difficult and complex precursor syntheses, unstable precursors with limited shelf-lives, afforded multiple byproducts that demanded complex purification strategies, and required specialist equipment not present most production radiopharmacies (e.g., gloveboxes). These and the other methodologies discussed below have nonetheless been important steps on the way to scalable, cost-effective, and operationally simple late-stage nucleophilic radiofluorination strategies.

^a A ylide is an uncharged compound that features a negatively charged carbon center bonded directly to a positively charged heteroatom, such as sulfur, phosphorus, or iodine.

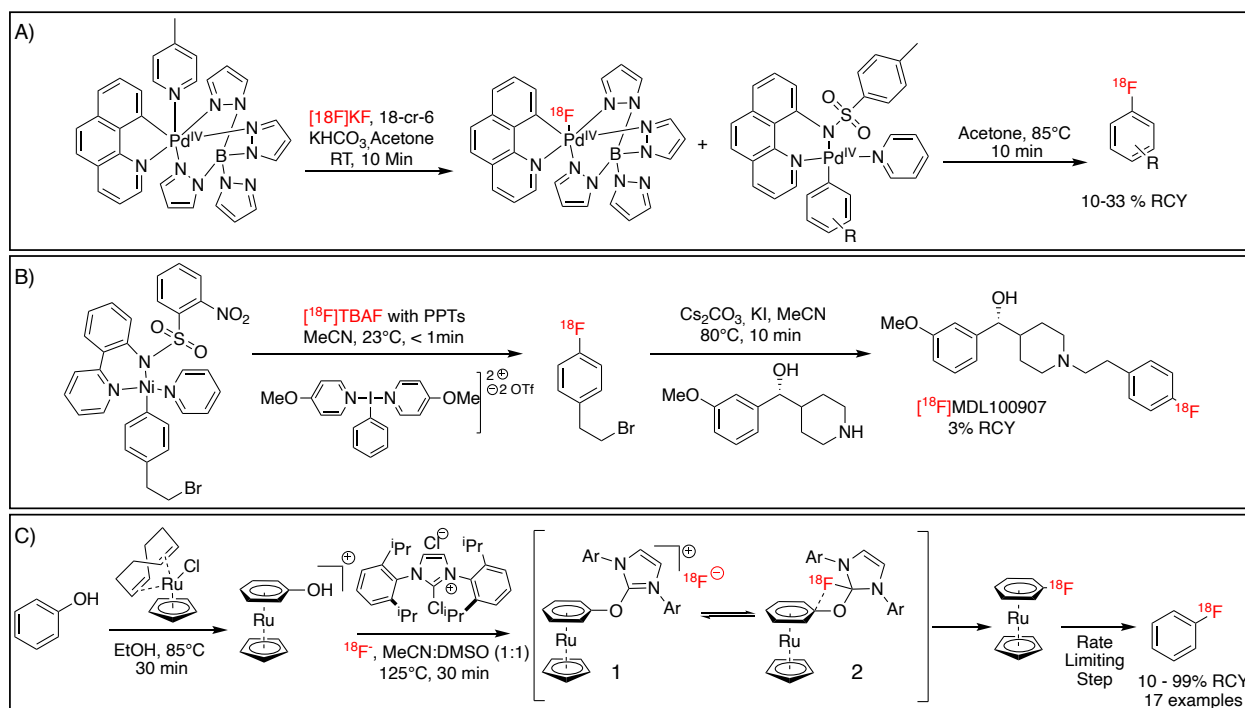


Figure 12: A) Palladium mediated radiofluorination.⁵⁸ B) Nickel mediated radiofluorination and synthesis.⁵⁹ C) Deoxyradiofluorination of ruthenium complexes via a concerted aromatic substitution (cS_NAr) mediated by a chlorimidazolium chloride salt.^{61,62}

3.3.1 Copper Mediated Radiofluorinations (CMRFs)

Arguably the most important and thus far widely adopted advance in radiofluorine chemistry has been the development of copper-mediated radiofluorinations (CMRFs).⁶³ Building upon the work on the radiofluorination of diaryliodonium salts mentioned above, Sanford *et al.* discovered that the nucleophilic [¹⁹F]fluorination of asymmetric (mesityl)(aryl)iodonium salts (*vide supra*) could be catalyzed with Cu(I) and Cu(II) salts to yield aryl fluorides in low to good yields under mild conditions.⁵⁵ Ichiishi, Scott, and coworkers later adapted Sanford's initial conditions for use with [¹⁸F]fluoride; the bulky mesityl group directs the radiofluorination reaction toward the less sterically hindered aromatic ring (Figure 13, A).⁵⁶ The reaction makes use of air- and moisture-stable commercially available catalysts with long shelf lives; however, the synthesis and storage of the iodonium precursors containing sensitive functional groups can be challenging. McCamant, Scott, and Sanford *et al.* later addressed this shortcoming and expanded the scope of this methodology by disclosing a related two-step, one-pot procedure for the radiofluorination of unfunctionalized electron-rich aromatic rings (Figure 13, B).⁵⁷ This methodology employed an umpolung approach^a to activate a nucleophilic aromatic ring by functionalizing it *in-situ* through an S_EAr (electrophilic aromatic substitution) reaction with an electrophilic iodine (III) reagent. The resulting electron-rich $Ar^{III}X_2$ ((mesityl)(aryl)iodonium) salts can then be labeled with [¹⁸F]KF in the presence of a Cu(I) catalyst. A limitation of

^a An umpolung approach involves any reaction that activates a functional group by inverting the polarity of that group, in this case, from a nucleophile to an electrophile.

this procedure is that the first step is air- and moisture-sensitive and can take up to 18 hours to reach completion.

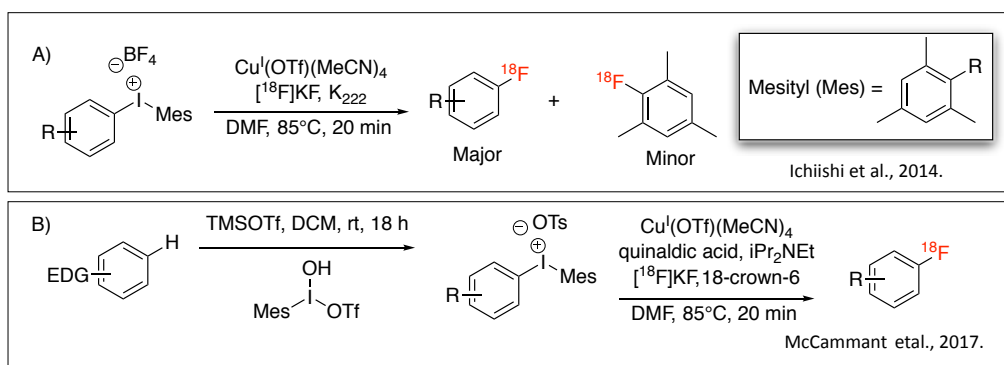


Figure 13: A) The CMRF of (mesityl)(aryl)iodonium salts. B) The one-pot CMRF of unfunctionalized aryl rings via the in-situ generation of (mesityl)(aryl)iodonium salts

Ye and Sanford then reported the Cu(II) triflate ($\text{Cu}(\text{OTf})_2$, 4 eq) mediated fluorination of trifluoroborates using KF (4 eq, non-radioactive) as a nucleophilic fluorine source.⁶⁴ This reaction was proposed to work through a similar mechanism to the well-known and versatile Chan-Lam cross-coupling. The Chan-Lam (Cham-Evans-Lam) reaction is the copper-mediated oxidative cross-coupling of nucleophilic heteroatoms with arylboronates.⁶⁵ According to the proposed mechanism (Figure 14, B), a Cu(II) center in complex with triflate and appropriate ligands such as acetate or pyridine, accepts a nucleophilic atom or group. A transmetalation step then takes place where the aryl precursor is transferred to the metal center through the exchange of the boron atom, and this has been shown to be the rate-limiting step.⁶⁶ The resulting Cu(II) complex is then oxidized to a Cu(III) complex through disproportionation via a single electron transfer (SET) by excess strongly oxidative Cu(II)(OTf)₂.⁶⁶ The reactive Cu(III) complex then reductively eliminates the aryl fluoride product to release the metal promoter as Cu(I)OTf.⁶⁴ By this mechanism, the reaction converts two equivalents of Cu(II) to unreactive Cu(I) for every equivalent of product produced. If the reaction is performed under an atmosphere of air, O₂ re-oxidizes the resulting Cu(I)OTf to Cu(II)(OTf)₂, regenerating the active metal promoter species, thus allowing the reaction to be run under true catalytic conditions.^{64,66}

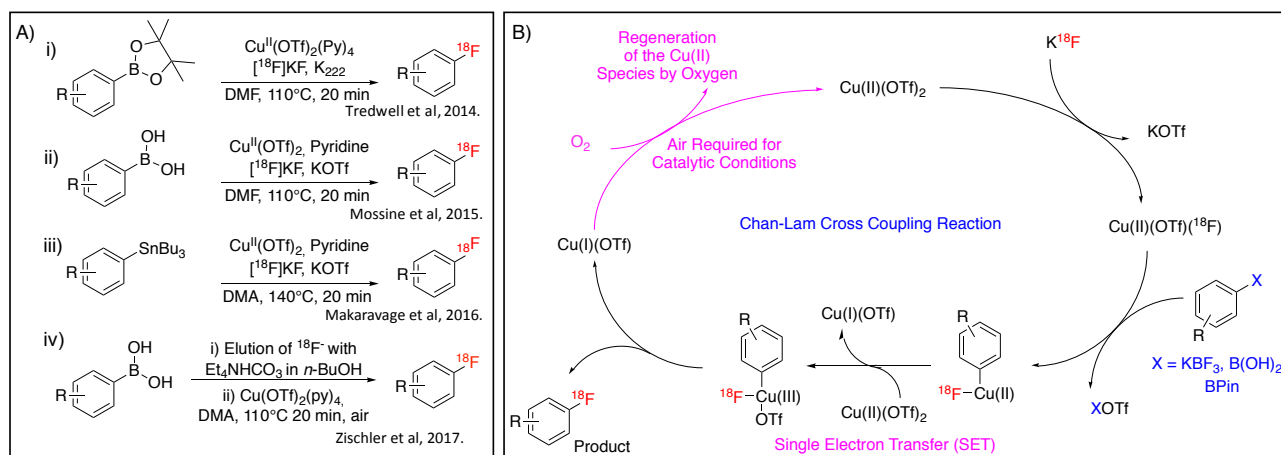


Figure 14: A) Recent Cu-mediated radiofluorination conditions: B) The proposed generalized mechanism of the CMRF of arylboronates. Cu can be used catalytically if oxygen is present to regenerate the Cu(I) species back to Cu(II). Diagram adapted from the work by King et al⁶⁶ and Ye et al.⁶⁴

Building from this knowledge, Tredwell and Gouverneur *et al.* disclosed a general copper-mediated nucleophilic ^{18}F -fluorination of arylboronate esters, which made use of small aliquots (30-40 MBq) of activated nucleophilic $^{18}\text{F}[\text{K}]/\text{K}_{222}$ that was dried and activated by standard ^{18}F fluoride processing protocols (Figure 14, A i)).⁶⁷ The operationally simple reaction displayed a broad scope; used cheap, commercially available, and easily prepared reagents (arylboronic esters) and catalysts (Tetrakis(pyridine)copper(II) triflate, 10 mol%); was carried out under air (as an oxidant) under mild catalytic conditions; and proved to be moisture tolerant. However, Zlatopolskiy, Zischler and Neumaier *et al.* (later acknowledged by Preshlock and Gouverneur *et al.*) discovered that the Cu catalyst was intolerant to strongly basic conditions, being particularly sensitive to the amount of K_{222} and K_2CO_3 present in large scale QMA elutions. This limited the reaction's performance and reproducibility on larger automated scales.^{68,69}

Mossine, Scott, and coworkers reported alternative conditions for the radiofluorination of arylboronic acids, which were developed with the specific goals of addressing the issues of scalability, reproducibility, and automation (Figure 14, A ii)).⁷⁰ They too cited the use of large quantities of strongly basic K_2CO_3 used in standard fluoride processing protocols as detrimental to the performance of the reaction and investigated the use of alternative salts for QMA cartridge elution. The authors examined the use of a weakly basic aqueous solution of potassium triflate (KOTf) and K_2CO_3 (73:1 molar ratio) with which they were able to elute 80% of the ^{18}F from the QMA cartridge. Azeotropic drying with acetonitrile in the usual way afforded K_{222} free ^{18}F with no activity loss caused by evaporation, however, as would be later noted by Zischler and Zlatopolskiy *et al.*, in some instances the resulting poorly soluble fluoride could be lost due to etching on the reaction vessel wall.^{68,71} The authors went on to investigate the copper mediator and determined that Cu(I) catalysts do not promote radiofluorination (in line with the proposed mechanism) and that $\text{Cu}(\text{OTf})_2$ was an excellent catalyst due to a combination of its reactivity, availability, and low cost. They also determined pyridine (in substituted or unsubstituted forms) to be an essential reaction component with a significant effect on the reaction's performance, a fact later confirmed and elaborated upon by Antuganov *et al.*⁷² Unlike Gouverneur *et al.*, Scott *et al.* used pyridine as an additive and not as part of a preformed copper/pyridine complex. Another notable departure from the protocol by Gouverneur *et al.* was the use of $\text{Cu}(\text{OTf})_2$ as a reagent (5 eq) and not a catalyst, performing the reaction under inert gas. This allowed for an easier transfer of the methodology to automatic synthesis modules which typically operate using argon, nitrogen, or helium; however, it was initially noted by Gouverneur *et al.* that performing the reaction under inert gas can lead to increased rates of the competing protodeborylation side reaction.⁶⁷

Scott and coworkers continued to expand on their mild CMRF conditions by disclosing the CMRF of stannylated compounds (easily synthesized with long shelf-lives) in dimethylacetamide (DMA), including electron-rich and neutral aryl-, heteroaryl-, and vinyl-stannanes, further extending the scope and versatility of the reaction (Figure 14, iii)).⁷³ They were able to demonstrate the accessibility and translatability of this chemistry by applying their reaction conditions to the automated radiosynthesis of several clinically relevant

tracers, ensuring that levels of copper and tin analytes were below the prescribed limits for radiopharmaceuticals.

Throughout the development of CMRFs, the improvement of fluoride processing techniques and the development of CMRF specific QMA eluents was determined by several groups to be critical to scalable CMRF reaction performance. The Neumaier group first reported reasonable RCCs when they applied a “low base” QMA eluent using 0.06 mg K_2CO_3 and 0.27 mg K_{222} in 80% MeCN vs. the usual 2.8 mg K_2CO_3 and 13 mg K_{222} in 80% MeCN used in standard QMA elution and azeotropic drying protocols.⁶⁸ The Gouverneur group also modified their original reaction conditions using a QMA eluent consisting of potassium oxalate ($K_2C_2O_4$) and minimal quantities of K_2CO_3 , a 1:1.5 ratio of substrate to catalyst, and DMA as the reaction solvent.⁶⁹ They were also able to automate the radiosynthesis of eight “difficult to synthesize” clinically relevant tracers using these conditions on several different synthesis modules, in different laboratories, demonstrating a significant step towards the reproducibility and scalability required for routine tracer production.

Zischler and Zlatopolskiy investigated the use of quaternary ammonium, iodonium or sulfonium salts in volatile alcoholic solutions for a direct “azeotropic-drying-free” QMA elution protocol for the CMRF of iodonium and sulfonium salts (*vide supra*).⁶⁸ They expanded on this development by reporting that $^{18}F^-$ could be eluted from a QMA cartridge using tetraethylammonium hydrogen carbonate (TEAB) in alcoholic solvents, namely methanol and *n*-butanol (*n*-BuOH), resulting in the development of an azeotropic drying free CMRF of arylboronic esters and acids (Figure 14, A iv)).⁷¹ Their new “minimalist” protocol involved both trapping and eluting the $^{18}F^-$ from the output end of the QMA cartridge, which was claimed to recover more $^{18}F^-$ without the need for azeotropic drying. Interestingly, they discovered that, under their conditions, the presence of protic *n*-BuOH as a co-solvent with DMA enhanced the RCC of the reaction, possibly by reducing the basicity of the $^{18}F^-$ ion and/or by stabilizing the transition state which occurs during the transmetalation step of the catalytic cycle through hydrogen bonding effects with the boronate precursors.^{66,74} In a later paper, Zarrad *et al.* demonstrated that the enhancing effect of *n*-BuOH on the CMRF of arylstannanes was marginal, although the protocol could also be used to efficiently label arylstannanes at production scales.⁷⁴

Mossine and Scott reported their work into the development and optimization of custom CMRF $^{18}F^-$ processing protocols that eliminated the use of ionic bases and problematic additives (such as K_{222}).⁷⁵ They rigorously investigated the use of different QMA cartridge conditioning methods, QMA counterions, and organic bases (in place of K_2CO_3) in order to provide a framework that could be used to tailor the QMA eluent to the CMRF (and overall synthesis) in question. They also reported on the importance of the “order of addition” of reagents into the reaction vessel with a focus on reducing the competing protodeboronation, a prominent side reaction that occurs during the CMRF of arylboronate substrates.⁷⁶

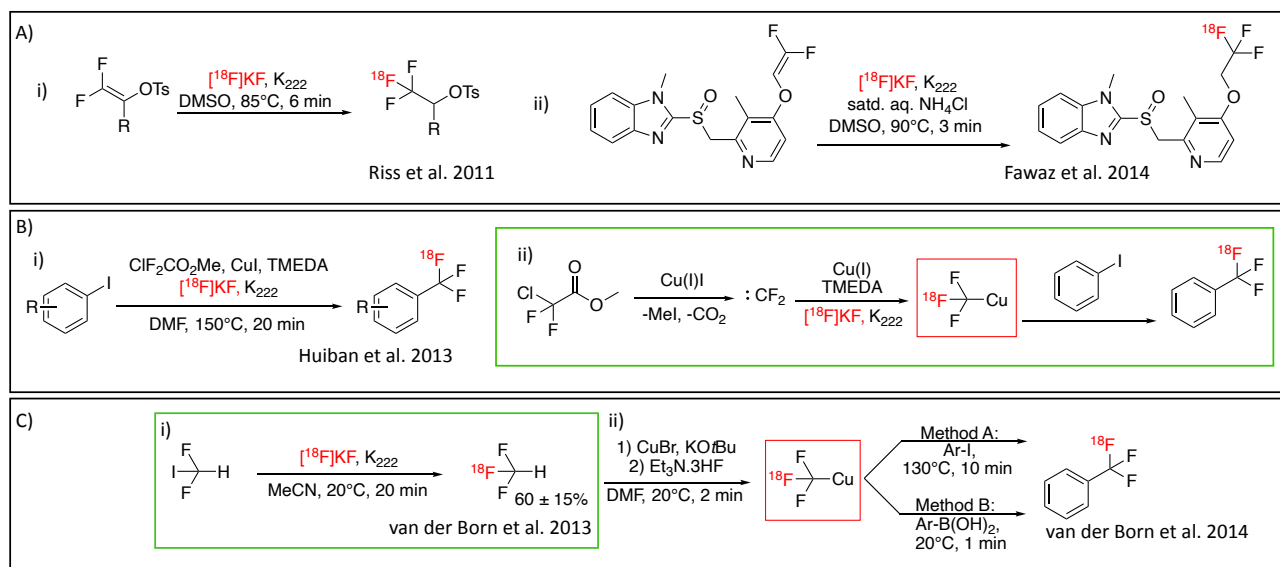
3.3.2 [^{18}F]Trifluoromethylation Reactions

Figure 15: A) The synthesis of alkyl [^{18}F]trifluoromethyl functional groups. Schemes taken from Riss et al.⁷⁷ and Fawaz et al.⁷⁸ B) Copper mediated [^{18}F]trifluoromethyl of aryl iodides by Huiban et al.⁷⁹ C) i) The synthesis of [^{18}F]trifluoromethane⁸⁰ and ii) its subsequent use to synthesize [^{18}F]trifluoromethyl arenes from arylboronic acids and iodides.⁸¹

Another area where CMRFs have received attention is in the synthesis of isotopically labeled Trifluoromethyl groups. Trifluoromethyl groups are ubiquitous in drug-like molecules due to their favorable steric, electronic, and lipophilic properties.⁶³ As PET imaging is used more frequently as a tool to evaluate the *in vivo* behavior of new drug candidates, [^{18}F]alkyl- and [^{18}F]aryl-trifluoromethyl groups serve as attractive sites for the isotopic radiolabeling of new drug candidates with ^{18}F .⁴⁷ In the past, [^{18}F]alkyl-trifluoromethyl groups have been synthesized using $\text{R}-\text{CF}_2\text{Br}$ and, more recently, in higher specific activities, from *gem*-difluoro enol ether precursors (Figure 15, A) (initially reported by Riss et al.^{77,82} and later refined and automated by Fawaz et al.)^{63,78} Newer methods towards the synthesis of [^{18}F]aryl-trifluoromethyl groups have also been recently disclosed.^{47,63} These protocols generally involve the *in situ* formation of [^{18}F]Cu(I)CF₃, which can undergo cross-coupling reactions with several leaving groups. Huiban et al. first published an operationally simple [^{18}F]trifluoromethylation (Figure 15, B i)) of aryl and heteroaryl iodides using [^{18}F]Cu(I)CF₃ generated through the reaction of $^{18}\text{F}^-$ and difluorocarbene, which is formed *in situ* from methyl chlorodifluoroacetate (Figure 15, B ii), inset in green).⁷⁹ However, the resulting highly reactive trifluoromethide (CF_3^-) is unstable and can undergo fluorination side reactions with itself, incorporating ^{19}F and reducing the specific activity of the product.⁸¹ Van der Born, Vugts, and coworkers refined the production of high specific activity [^{18}F]fluoroform ([^{18}F]HCF₃) (Figure 15, C i), inset in green),⁸⁰ and applied this protocol to the copper-mediated [^{18}F]trifluoromethylation of aryl and heteroaryl iodides and boronic acids to produce trifluoromethylation products with improved specific activities (Figure 15, C ii)).⁸¹

The methodologies discussed above are but a few notable additions to the radiochemical toolbox, and while they do have their limitations, they have nonetheless dramatically expanded the scope and chemical diversity of novel radiotracers that can now be considered for development. Methodology development for the

synthesis of ^{18}F radiotracers remains an exciting field; future developments and broader synthetic tools will no doubt help drive the development of PET as both a preclinical research tool and as a tool for drug development.⁸³ In order for these methods to begin making an impact on the synthesis of tracers produced under GMP conditions for clinical use, they still require extensive optimization in terms of both the synthesis performance and in the robustness and reliability of the production process.

3.4 The Radiolabeling of Biomolecules with Radiometals

Biomolecules are typically too sensitive to survive the harsh reaction (thermal and chemical) conditions required for the late-stage covalent radiolabeling with isotopes such as ^{18}F and ^{11}C . Additionally, the short half-life times of these isotopes are not suited to the slow pharmacokinetics and long *in vivo* half-lives of antibody and large peptide tracers. ^{18}F is, in certain circumstances, still an attractive isotope for the radiolabeling of some peptide tracers, and this is typically achieved by reacting the peptide of interest with an activated prosthetic group. However, most large biomolecules tracers and radiotherapeutics are most often covalently conjugated to a chelator, which can complex a radiometal.

There is a multitude of easily accessible radiometals that can be applied to a range of nuclear medicine applications. Some of the most popular radiometal isotopes for nuclear medicine include $^{99\text{m}}\text{Tc}$ and ^{111}In for SPECT; ^{68}Ga , ^{64}Cu , ^{44}Sc , ^{89}Zr , and ^{86}Y for PET; and ^{177}Lu , ^{90}Y , and ^{225}Ac for radionuclide therapy/theranostics.⁸⁴ These radiometals are typically supplied in nM to pM concentrations (as is the case for most medical radionuclides) and are not capable of forming formal covalent bonds^a due to their large atomic size and low ionization energy. Radiometals must, therefore, be sequestered from very dilute solutions using chelators.⁸⁴ The chelator/radiometal combination for radiolabeling should be carefully matched in terms of the metal's donor atom preferences (N,O,S,P; hard/soft donor atoms), the optimum coordination number (the maximum number of coordination bonds the metal can accept), the optimum coordination geometry of the complex, and the chemistry of the reaction solution (optimal pH and counter ion composition for metal complex formation), so that the affinity of the radiometal-chelator interaction is maximized.⁸⁴

^a Most transition radiometals can accept electron density through a co-ordinate bond (also known as a dative covalent bond) with a donor atom carrying a free lone pair of electrons (such as NH_3 or PPh_3 .)

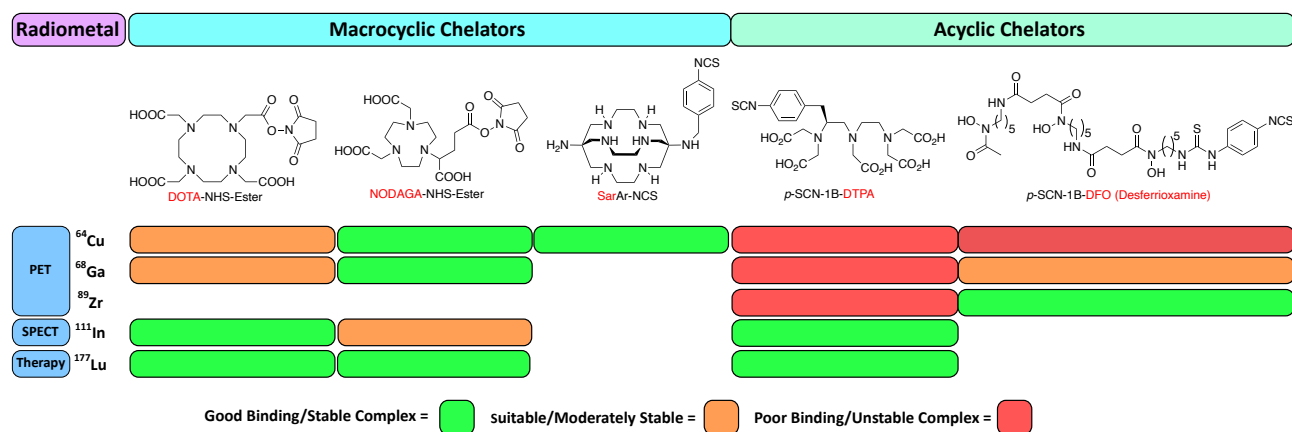


Figure 16: A selection of commonly used functionalized macrocyclic and acyclic chelators (the name of chelator is highlighted in red and the radiometals with which they are commonly paired). The suitability of the metal-chelator complex for in vivo imaging is shown by the colored boxes (absence of a box indicates a lack of data). The binding data and chelator structures have been obtained and adapted from the review by Price and Orvig.⁸⁴

The stability of such a complex is dependent on the combination of the chosen ligands (groups that able to donate electron pairs into the metal's empty *d*-orbitals), the specific radiometal ion, and the solvent conditions of the free metal ion. Chelators are large organic groups that feature multiple (4-8) electron-donating atoms (C, the coordination number) which are arranged in such a way as to donate electron density to a metal ion center and thus bind the metal center into a highly stable complex from which it cannot easily escape (Figure 16). The high thermodynamic stability and rapid formation of metal-chelator complexes arises from the "chelate effect" which is due to favorable enthalpic (ΔH , the heat of reaction) and entropic (ΔS) changes that occur relative to metal complexes with lower order^a ligands.^{84,85}

Chelators can be divided into two families: i) acyclic chelators, which are linear or branched molecules, and ii) macrocyclic chelators, which feature at least one closed ring (Figure 16). Acyclic chelators must undergo large conformational changes to assume an optimal metal-binding geometry, while macrocycles, which feature more constrained geometries and are thus more "preorganized," suffer from a lower loss of entropy and thus typically form more stable coordination complexes than acyclic chelators (the macrocycle effect).⁸⁴ However, acyclic chelators require lower activation energies to include the metal center than macrocycles and thus demonstrate faster reaction kinetics at lower temperatures, a significant advantage when labeling heat-sensitive proteins or using very short-lived radiometals.⁸⁴

There is an extensive body of published literature that has identified metal-chelator pairs with stabilities and reaction kinetics appropriate for radiochemical and nuclear medical applications (this work has been summarized and reviewed in detail by Price and Orvig).⁸⁴ Of particular interest is NOTA (1,4,7-triazacyclononane-1,4,7-triacetic acid; C = 6) which is often used in the NODAGA form (Figure 16). NODAGA

^a The inclusion of a solvated metal ion into any complex is a reversible process that behaves as a thermodynamic equilibrium. A metal coordinating ligand can be classified by the number of coordination bonds it can form with a metal center. Ligands with a single electron-pair donating atom are termed monodentate ligands (monodentate means "single toothed"; thus, the prefix to the word "dentate" indicates the number of coordinating atoms); two donor atoms are termed bidentate; three, tridentate; etc. Higher-order ligands are termed chelators and can form multiple (4-8) coordination bonds with the metal center.

is often used to chelate $^{64}\text{Cu}^{2+}$ and $^{68}\text{Ga}^{3+}$, forming stable complexes with reasonable reaction rates and temperatures for heat-sensitive biomolecules (25 °C, 30-60 min). DTPA (diethylenetriaminepentaacetic acid; C = 8), is used to rapidly form $^{111}\text{In}^{3+}$ and $^{117}\text{Lu}^{3+}$ complexes at low temperatures (25 °C, 5-20 min), while DFO (desferrioxamine; C = 6) is the “gold standard” chelator for tracers with $^{89}\text{Zr}^{4+}$.

Chapter 4: Design of Experiments: The Optimization of Chemical Processes

Parts of this review have been published: Bowden, G. D. *et al. Sci. Rep.* **9**, 11370 (2019).⁸⁶

The adoption of new radiochemical methods into routine research workflows and tracer productions is heavily dependent on how easy it is to adapt the general reaction conditions to a specific tracer synthesis problem. Upon discovering new reactions, chemists typically perform extensive optimization studies to thoroughly explore the effects of experimental variables such as concentration, temperature, reaction time, reagent amounts, etc.⁸⁷ These studies serve two purposes: i) Revealing the contributions of the various experimental factors to the behavior of the process, which may provide mechanistic information; a measure of the reactions performance, scope, and functional group tolerance; and a better understanding of how the process can be manipulated. And ii) optimizing the general conditions of the method so that it may be quickly applied to a specific synthesis to give a desirable outcome (a high RCY or RCC).

Before a new tracer can be made available for imaging studies, it must be produced efficiently and reliably in a way that is both practical and safe; this is usually achieved by automating the synthesis on a robotic synthesis module. To facilitate the automation of a radiosynthesis, the synthesis and purification of the product tracer should be well understood and optimized for performance (high RCY and molar radioactivity) and robustness (reproducibility). The optimization of a novel tracer synthesis can often be a frustrating and time-consuming endeavor that is further hindered by the practical constraints of handling large quantities of radioactivity. Thus, the synthesis optimization of new tracers often represents a significant part of the bottleneck in the tracer development pipeline that slows a tracer's progress from conception to routine preclinical (and clinical) use.⁴⁶

4.1 Reaction Optimization and Experimental Design (OVAT Vs DoE)

Typically, new radiochemical reactions and novel tracer syntheses are optimized through a "one variable at a time" (OVAT) approach, where all the controllable variables that affect the reaction yield or conversion (Response, Y_i) are held constant except for the variable under investigation (X_1).^{88,89} That variable is adjusted through its range until a maximum is observed. The optimal setting of X_1 is then used in a new set of experiments to investigate the next variable (X_2), and this process is repeated until all experimental variables have been individually optimized.⁸⁸ This process, while intuitive, is laborious and time-consuming,^a and when performed over many variables, often results in a large number of individual experimental runs.⁹⁰ The results of these experiments are often not intuitively interpretable due to the large numbers of interacting experimental variables (also known as factors).⁹¹ A factor interaction occurs when the setting of one variable affects the behavior of another, and as the OVAT approach only looks at one variable at a time, it is unable to detect and quantify any factor interactions.⁸⁸ As a result, the outcome of an OVAT study is heavily

^a In the context of radiochemistry, an inflated experimental effort often translates to more use of expensive reagents, chemicals, kits, cartridges, and time, as well as a larger radiation dose to the radiochemist!

dependent on the starting conditions (which are often arbitrarily chosen), and as such, the OVAT approach is prone to finding local optima, failing to predict the actual set of optimal conditions (Figure 17, A).⁹⁰

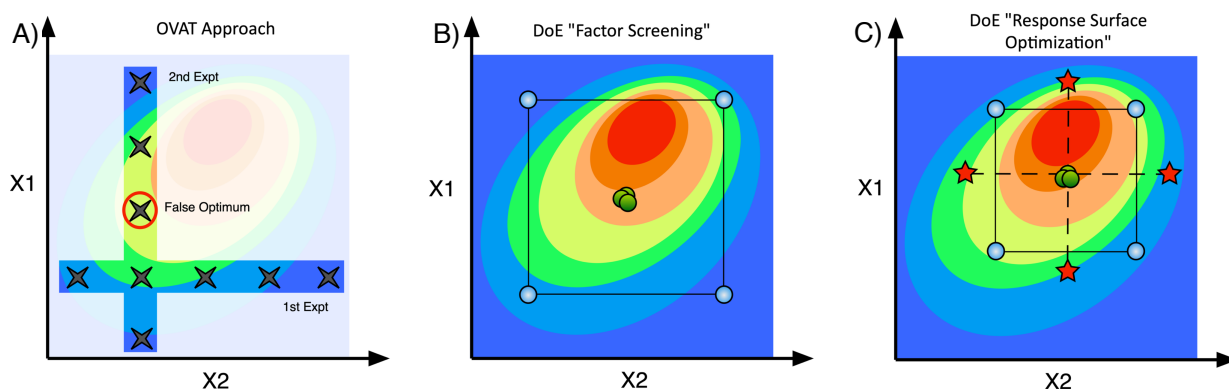


Figure 17: A) The OVAT approach is only able to resolve slices of experimental space at a time. The DoE approach builds an experimental matrix that models the effect of all experimental factors simultaneously, either B) for low resolution “factor screening” or C) for higher resolution and more focused “response surface modeling” studies. The color grading represents the magnitude of the response value (Y, blue low, red high). This figure was originally adapted from Murray et al.^{89,92} and is taken from Bowden et al.⁸⁶

“Factorial experimental design” or “Design of experiments” (DoE), as it is more commonly known as, is an alternative systematic approach to process optimization (Figure 17, B and C).^{86,89,91} It has been widely employed by process chemists and engineers across a wide range of industries to maximize process output and profitability, yet it has only seen limited use in academic laboratories.^{89,90,93} DoE involves the construction of predefined experimental matrices that are designed to maximize the amount of information that can be extracted from as few experimental runs as possible by varying all experimental variables simultaneously. The DoE process then uses multivariate analysis to map and model reaction space (*vide infra*), providing a predictive model that determines the effect of each controllable variable on the response and can resolve and quantify factor interactions when they occur.⁹¹ Additionally, uncontrollable factors (such as day-to-day variances in laboratory conditions, and reagent batch differences) can be accounted for by arranging the experiments in blocks, measuring the variation between the blocks, and including these results into the final model as so-called “blocking factors”.^{86,94}

In order to estimate experimental error and variance, each run in an OVAT study needs to be conducted multiple to times (typically in triplicate), which further increases the experimental effort. As DoE studies use statistical methods to construct and fit a model to the acquired experimental data set, the experimental error can be estimated across the whole regression model.⁹³ The pure error is calculated through the inclusion of replicate “centerpoint” experiments.⁸⁹ Experimental outliers can thus be easily identified and either excluded from the model or repeated to ensure model validity without the need for replicate experiments at every experimental point.

4.2 DoE: Experimental Matrices in Multivariable Studies

The combination of the maximum and minimum investigated ranges across all of the investigated factors is termed “reaction space.”⁸⁷ DoE studies are designed with experimental points at critical locations (defined

by the design type) throughout the investigated reaction space.⁸⁹ More detailed information about a process usually comes at the cost of greater experimental effort. Thus, the choice of experimental design is usually made to balance the amount and quality of information obtained against the number of experiments.⁹³ There are a large number of established DoE design types that can be applied in different situations to answer specific questions about the process of interest.⁹¹ Most DoE studies are typically carried out in three phases:⁹³ i) Initially, a broad range of different experimental factors are screened for their contribution to the process outcome (Figure 17, B). ii) Once the most important (significant over their investigated ranges) experimental variables have been identified, a “response surface optimization” (RSO)^a study can be carried out (Figure 17, C) Finally, iii) the model must be validated by performing experiments to confirm the model prediction. Once confirmed, the information afforded by higher-resolution RSO studies can suggest what the optimal conditions may be or, at the very least, aid in further decision making.

4.2.1 Factor Screening Designs

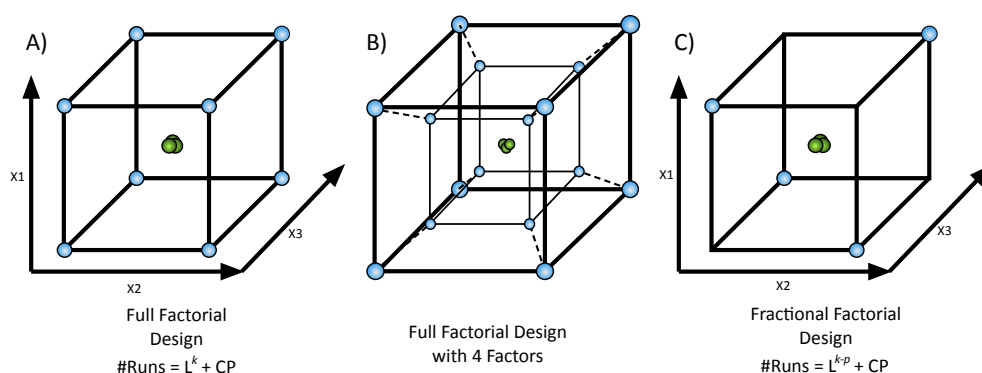


Figure 18: Graphical representations of factorial experimental matrices: A) A 3-factor full factorial experimental matrix, B) a 4-factor full factorial experimental matrix, and C) a 2_{III}^{3-1} fractional factorial experimental design. All representations feature three centerpoint runs (green) in addition to the main experimental runs (blue).⁹³

The full factorial design forms the mathematical basis for most DoE design types.^{91,94} In a typical 2-setting full factorial design, experimental runs are performed at both the high and low settings for each factor in combination with all the other factors of interest. Graphically, this can be represented as a hypercube^b with an experimental run on each of its vertices with several centerpoint runs (typically 3-5) at the center of the hypercube to estimate experimental reproducibility (Figure 18, A and B). This generates a model where all the main effects on the response are determined, all factor interactions can be resolved, and curvature in the response surface (quadratic terms) can be estimated. The number of runs = L^k , where L is the number of settings,^c and k is the number of factors under investigation.⁹⁴ This design type works well for studies with a

^a The response surface is a modeled surface that represents how the response variable (Y) changes concerning the various input factors.

^b The term hypercube is a here used a place-holder term to describe a cube with a variable number of dimensions (also known as an n -cube). A “2-dimensional hypercube” is a square, while a 3-dimensional hypercube is cube. Mathematically, the term hypercube is used to describe any cubic space with four or more dimensions.¹⁸⁴

^c In most full and fraction factorial experimental designs $L = 2$. Performing other response surface optimization designs are typically far more efficient than letting $L \geq 3$.

low number of experimental factors (≤ 4); however, as the number of factors increases, the number of required runs explodes exponentially and rapidly become impractical. A solution to this problem is the fractional factorial design, which reduces the overall number of experimental points by only including a fraction of the runs required by the full factorial design (Figure 18, C).

The fractional factorial approach sacrifices some of the resolution of the full factorial design; however, the amount and type of information obtained can be adjusted by carefully selecting which runs are performed across selected factors. These experimental matrices are generated by choosing an alias structure from a selection of pre-generated matrices.⁹⁴ The alias structure is chosen based on the number of factors, the desired number of runs, and the cost of lost information that is acceptable to the study at hand (Table 4). The alias structure determines which factors are confounded (where the effect of a variable is “mixed in” with the effect of another) and which interactions can be resolved. There are a wide variety of aliasing structures to choose from so that the information loss can be minimized in the context of the process under investigation.

Table 4: A) Fractional factorial designs provide an increasing amount and quality of information with increased resolution at the cost of more experimental effort. The legend explaining the properties of RES III-V(+) designs can be found below. (The number in parenthesis is a multiple of the full factorial design). Adapted from “Statistics for Experimenters” by Box, Hunter, and Hunter (2nd edition, p 272)⁹⁴ and “Process Improvement Using Data” by Kevin Dunn (Creative Commons Attribution-ShareAlike 4.0 Unported (CC BY-SA 4.0)).⁹⁵

Number of Runs N	Increasing Aliasing and Greater Loss of Information More Factors Investigated									
	3	4	5	6	7	8	9	10	11	
4	2_{III}^{3-1} (1/2)									
8	2^3 (Full)	2_{IV}^{4-1} (1/2)	2_{III}^{5-2} (1/4)	2_{III}^{6-3} (1/8)	2_{III}^{7-4} (1/16)					
16	2^3 (Full*2)	2^4 (Full)	2_V^{5-1} (1/2)	2_{IV}^{6-2} (1/4)	2_{IV}^{7-3} (1/8)	2_{IV}^{8-4} (1/16)	2_{III}^{9-5} (1/32)	2_{III}^{10-6} (1/64)	2_{III}^{11-7} (1/128)	
32	2^3 (Full*4)	2^4 (Full*2)	2^5 (Full)	2_{VI}^{6-1} (1/2)	2_{IV}^{7-2} (1/4)	2_{IV}^{8-3} (1/8)	2_{IV}^{9-4} (1/16)	2_{IV}^{10-5} (1/32)	2_{IV}^{11-6} (1/64)	
64	2^3 (Full*8)	2^4 (Full*4)	2^5 (Full*2)	2^6 (Full)	2_{VII}^{7-1} (1/2)	2_V^{8-2} (1/4)	2_{IV}^{9-3} (1/8)	2_{IV}^{10-4} (1/16)	2_{IV}^{11-5} (1/32)	
128	2^3 (Full*16)	2^4 (Full*8)	2^5 (Full*4)	2^6 (Full*2)	2^7 (Full)	2_{VIII}^{8-1} (1/2)	2_{VI}^{9-2} (1/4)	2_V^{10-3} (1/8)	2_V^{11-4} (1/16)	
RES < III:	Main effects are confounded with each other. Resolution too low to be useful.				RES III:	Main effects are not confounded. Main effects confounded with 2-factor interactions. Useful for Initial factor screening				
RES IV:	Main effects are not confounded with each other or with 2-factor interactions. 2-factor interaction confounded with each other. Useful for detailed factor screening and low level optimization.				RES V (+)	Main effects are not confounded with each other or 2-factor interactions. 2-factor interactions not confounded with each other. Can perform optimization studies with large sets of factors. resolves complex effects for RSO studies				
Full	Full factorial design				Full	Full factorial with repetitions				

The number of runs in a fractional factorial design = L^{k-p} , where L is the number of settings for each factor, k is the total number of factors, and p is the number of generators used by the chosen alias structure.⁹⁴ Thus,

a fractional factorial design given by 2^{5-2} (5 factors, 2 generators)^a would require a total number of 8 runs + 3 centerpoints (CP) for a total of 11 runs, in contrast to the ($2^5 = 32 + 3 \text{ CP} =$) 35 runs required by the full factorial design. It can be said the 2^{5-2} design is a $\frac{1}{4}$ fraction of the full factorial 2^5 design. An increasing number of generators used to construct the experimental matrix thus results in a lower experimental effort with an increasing loss of information due to factor confounding. This results in designs of lower resolution (RES). The resolution number is a reference to the amount and quality of information a particular design can reveal (Table 4). Typically, lower resolution designs will consist of fewer runs, have more factor confounding, and a lower number of resolved factor interactions. The “design specifications” for a fractional factorial design are thus given as L_{RES}^{k-p} .

The primary advantage of fractional factorial designs is that they allow one to efficiently screen a large number of factors to determine which effects have a significant influence on the process and should be investigated further. Additionally, they can also reveal specific 2-factor interactions of interest depending on the design resolution and the chosen aliasing structure. While higher resolution fractional factorial designs can give detailed information for optimization, most fractional factorial designs are usually used to guide decision making early on during a process’s development, and aid in the selection of factors and factor ranges for more detailed response surface modeling (RSM/RSO) studies.

4.2.2 Experimental Designs for Response Surface Optimization (RSO)

Once the critical experimental factors have been identified, and trivial effects have been eliminated, more detailed experimental designs can be constructed to generate predictive models of how each essential factor affects the system. The object of these designs is to accurately quantify the main effects, factor interactions, and estimate curvature (quadratic terms) in the response surface model, while still maintaining experimental efficiency. RSO designs naturally require more experiments, so reducing the number of investigated factors through a factor screening study is vitally important if the experimental effort is to be kept low.

There are several classical RSO design types with various advantages and disadvantages in terms of their experimental efficiency and resolution, each with very different structures.⁹¹ Doehlert designs make use of symmetrical hexagonal (not cubic) reaction spaces. They are useful when not all factors can be varied by the same number of settings. Mixture designs are another type of RSO design particularly suited to mixtures, where the sum of mixture’s components must be constant.^{b,c} By far the most important “classical” RSO

^a The 5-factor 2^{5-2} design can be considered to be a 3-factor design featuring factors A, B, and C. The remaining factors, D and E, are then confounded with the interactions A*B and A*C, respectively. These expressions, termed generators (p), are applied to the experimental matrix. The implication is that the if one is to estimate the effect of D, the estimation is a combination of the effect D and the interaction between A and B. Carefully choosing which factors to confound when generating the matrix can maximize the usefulness of the information obtained.⁹⁵

^b If one adds more of one component, one needs to add less of the other components to keep the sum of total components equal. Mixture designs are constructed to allow for this constraint.

^c Doehlert designs and mixture designs (amongst others) are essential and powerful DoE tools that are mentioned here for completeness; however, their use is outside the scope of this thesis, and they will not be discussed further.

experimental matrices are the classical 3-setting full factorial design (Figure 19: A), (mathematically important but seldom used as it is not as experimentally efficient as other RSO designs), the central composite design (CCD) and the Box-Behnken design (BBD) (Figure 19).

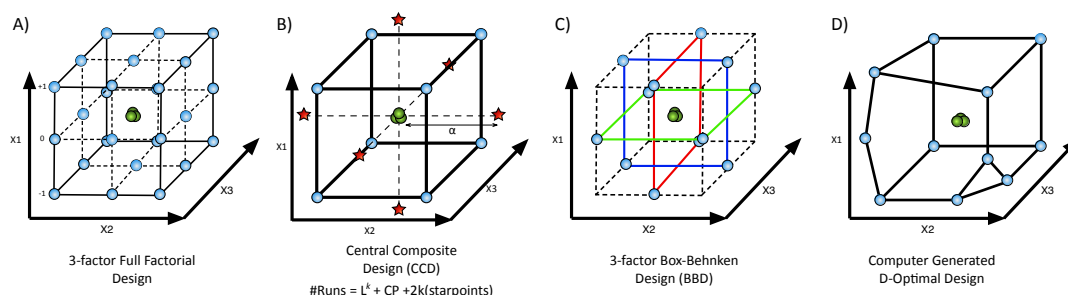


Figure 19: 3-Dimensional (3-factor) representations of: A) A 3-setting full factorial design (each factor held at settings: -1, 0, +1, in combination with all other factors), B) a central composite design (each factor held at settings: $-\alpha$, -1, 0, +1, $+\alpha$, in combination with all other factors), C) a Box-Behnken Design and D) an irregular and constrained D-optimal design.

The CCD features a 2-setting full factorial design with center points, as well as experimental points situated on the faces of the cube at a distance α from the center, termed “starpoints.” (Figure 19: B)^{88,91} The distance α determines the type of CCD and is adjusted based on the factor ranges being investigated and the structure of the desired study. A circumscribed central composite design (CCCD) has the starpoints set at α so as to circumscribe a (hyper)sphere around the factorial cube ($|\alpha| = (2^k)^{1/4}$). A face-centered central composite design (FCCD) has $\alpha = \pm 1$ so that the starpoints are situated on the faces of the factorial cube. The rotatable orthogonal central composite design (OCCD), which scales α according to the number and ranges of the factors of interest, ensures the mathematical properties of orthogonality^a and rotatability in the experimental matrix.^b Thus, the OCCD is often used as a general-purpose RSO design as it can be tailored to fit limited factor constraints. For a CCD, each factor is thus investigated at 5-settings ($-\alpha$, -1, 0, +1, $+\alpha$), providing enough data points to accurately estimate and model any quadratic (or even cubic) factor behaviors. This is beneficial when the study aims to generate a model of sufficient quality to provide an acceptable prediction of the optimum conditions for a given reaction.

The BBD is very experimentally efficient at low factor numbers and is still able to resolve quadratic terms.^{91,94} The experimental points are arranged on the edges of the reaction space cube and also circumscribe a sphere (Figure 19: C). One can interpret the BBD as several 2-dimensional full factorial designs performed in combination at 90° degrees to each other (Figure 19: C, 2D factorial designs represented by the blue, green and red lines). This structure is particularly useful for optimization if combinations of factor extremes should be avoided (i.e., the reaction does not work at the extremes of reaction space), as is the case with many chemical systems.

^a Orthogonality allows the effect of one factor to be estimated independently from the effect of another factor or factor interaction, simplifying the analysis.

^b In a rotatable design the variance of the predicted response ($Y_{\text{predicted}}$) at any location within the design space depends only on the distance of that location from the center of design (precision of the prediction will be greatest where the CP experiments are conducted and lowest at the extremes of design space), this is desirable when developing a predictive response surface model.

Modern D-optimal designs are increasingly taking over as the “go-to” experimental design method for both factor screening and RSO studies due to their flexibility and reliability (Figure 19, D).⁹¹ DoE software packages, like *JMP*, often build their semiautomated “all-purpose” DoE wizards around D-optimal designs. D-optimal designs must be constructed and analyzed using computer algorithms that select an optimal set of experiments from a “candidate set” of experiments. They are particularly useful for the analysis of multiple multi-level qualitative factors (such as different solvents or reagents) as well as for reaction spaces that are constrained or irregular and cannot be easily defined by a rotatable cube or a sphere. The high flexibility of D-optimal designs also allows one to build DoE studies around already performed experiments, saving time and cost, or easily add experiments to an existing D-optimal design to increase its size, resolution, and accuracy.

4.3 Model Construction and Data Interpretation

After the acquisition of experimental data according to the selected experimental matrix (design), the data is subjected to multiple linear regression (MLR).^a A requirement for a good MLR fit is that the acquired data is normally distributed; if need be, one approach to ensure this criterion is to perform an appropriate transformation on the data set (such as a logarithmic transformation: $10\log(Y)$). In general, the resulting regression model (response surface) can be described by the following polynomial for k factors:^{91,94}

$$Y = \beta_0 + \sum_{i=1}^k \beta_i x_i + \sum_{i \leq 1 < j}^k \beta_{ij} x_i x_j + \sum_{i=1}^k \beta_{ii} x_i^2$$

Y is the response, the different factors are represented by X_1, X_2, \dots, X_k , β_0 is the intercept, β_i are the main factor effect coefficients, β_{ij} are the 2-factor interaction effect coefficients, and β_{ii} are the quadratic effect coefficients.^b In modern DoE software, the scaled regression coefficients (effect magnitudes) are typically represented graphically by a bar chart, which is used to aid analysis. This allows one to visually gauge which factors are more or less influential (their relative magnitude) and whether their effects on the response is positive or negative. Error bar brackets are used to define the calculated confidence interval for each factor (usually 95%, $\alpha = 0.05$), and if the coefficient is less than the size of error bars, then the term is considered insignificant and can be excluded from the model to reduce noise and improve model fit. Statistics are then performed on the resulting regression model and the experimental data set to determine the quality of the data (outliers) and the validity of the model (goodness of fit, the goodness of the model’s predictive ability). Additionally, graphical methods, such as (residual) normal probability plots and observed versus predicted plots, can be used to identify outliers as well as other issues with the regression model (skewed distribution in the data set or missing terms in the model).

^a Other regression methods such as partial least squares are also often used, but they are outside of the scope of this thesis.

^b Higher-order interaction terms (3-factor interactions) and quadratic terms (cubic terms (X^3)) can also be included, but these higher-order effects are seldom significant and are excluded in the remainder of this work.

If a detailed RSO study has been conducted, the final RSM can then be evaluated graphically as either a series of 2D contour plots or as a 3D response surface, revealing the region of reaction space where the optimal settings may reside. For studies where more than one response is observed, the optimal setpoint (or sweet spot), which meets all the optimization specifications set at the beginning of the study (e.g., Y_1 = maximize yield, Y_2 = maximize specific activity and Y_3 = minimize byproduct formation) can be determined.

The final step of a DoE study is to validate the predicted optimal conditions through a stand-alone set of validation experiments. If a correct and predictive model has been obtained,^a the model can then be used to: guide further “fine-tuning” or “calibration” DoE studies, estimate the pilot study conditions for similar reactions, or be used “as is” for further repetitions of the desired reaction or synthesis.

4.4 DoE in Practice

Several practical elements need to be considered when planning any DoE study. Firstly, it is essential to have a basic idea of over which factor ranges the process still works (produce a non-zero result, $Y_i \neq 0$).⁸⁹ This information can be estimated through a combination of intuition, pilot experiments, and literature research. This is important as any failed results can be considered lost information.⁸⁹ Secondly, due to the number of experiments involved in a typical DoE study, it is necessary to have a reliable method to obtain the response data in a reasonable amount of time with minimal sources of error. For example, lengthy purifications of the final product do not provide any information about the actual reaction and are likely to introduce noise into the DoE data. Assessment of the crude reaction mixture through fast analytical methods such as high-performance liquid chromatography (HPLC), NMR, or, as in the case of radiochemistry, quantitative radio-TLC can provide accurate information about the response in a reasonable timeframe. Thirdly, the experimental protocols and workflows used in the DoE study should be standardized as much as possible to reduce experimental error.

As mentioned previously, the relatively sophisticated statistical methods required in DoE have been a significant barrier to entry for many research chemists outside of industrial process development.^{90,93} However, the advent of well-designed and user-friendly DoE specific software tools (such as *MODDE Go 12* (Umetrics, Umeå, Sweden) (used in chapter 7) or *JMP* (SAS institute)) has significantly lowered this barrier. *MODDE Go 12*, for example, features semi-automated wizards for design selection, regression model construction, and model analysis that allow for the ready application of the DoE approach to day-to-day synthesis problems. Work later in this thesis will investigate the use of DoE for improving radiochemical processes with a specific focus on the optimization of newly developed radiochemical methods.

^a George E.P. Box, the inventor of the Box-Behnken design, is famously quoted among statisticians for writing: “The most that can be expected from any model is that it can supply a useful approximation to reality: All models are wrong; some models are useful.” (p. 440, statistics for experimenters, 2nd ed.)⁹⁴

Chapter 5: Biomarkers and Probes for Beta Cell Imaging

5.1 Pharmacological Criteria for Probes and Biomarkers for BCI

The successful use of molecular imaging techniques for BCMI depends on the design and development of suitable radiotracers. Given the challenges to BCMI and the available modalities discussed above (*vide* chapter 2), any method developed to detect the BCM would have to be maximally sensitive and highly selective for a β cell-specific biomarker. In a review by Brom *et al.*,¹ the authors discussed a number of criteria that a probe/biomarker for the BCM would need to meet in order to be successful: i) The target of such a probe should be exclusively and stably expressed on the β cells of the endocrine pancreas so that an accurate estimation of the absolute BCM can be made across various healthy and diseased states. ii) The probe should show a high uptake in the target tissues and a low uptake in the surrounding exocrine pancreas.⁷ iii) The uptake of the tracer into the target tissue should directly correlate to the BCM as measured by histology. iv) The target-to-background ratio should be sufficiently high as to determine small changes in the BCM.¹ Additionally, v) the probe would need to display low chemo- and radiotoxicity to be safe enough for clinical use.^a

A radioligand must be constructed to fulfill these requirements with a high affinity for a β cell-specific target, a high specific activity (to maximize the sensitivity of the *in vivo* assay), and appropriate pharmacokinetic properties, in order to achieve the target-to-background ratio required for BCM quantification.⁸ Sweet *et al.* calculated that such a PET radioligand for BCMI would need to have a dissociation constant (K_d) in the picomolar to nanomolar range in order to achieve a sufficient contrast between specifically and non-specifically labeled regions.^{96,97} Laurent *et al.* went on to suggest that a greater sensitivity could be achieved (with more tolerance of probes with a lower target affinity) if the tracer was designed in such a way as to selectively accumulate in the target cells (targeted enrichment (*vide supra* 2.3.1.1)) and clear rapidly from the surrounding tissue and extracellular matrix.⁸

5.2 Biomarkers and Probes for β Cell Imaging

With these criteria in mind, several tracers and biomarkers for *in vivo* imaging have been investigated with varying degrees of success.⁸ As β cells are part of the neuroendocrine system, they exhibit high expression levels of somatostatin, serotonin and dopamine receptors as well as their associated metabolic and transport enzymes.^{1,7,17,98-104} Many of these systems have thus been investigated as potential BCM biomarkers using established neurological PET probes such as [¹¹C]DTBZ and 3-[¹²³I]IBZM, however, these targets were found to have widely varying levels of expression in different animal models with large interspecies variation.^{7,17,105-}

^a The β -cell mass in both diabetic and non-diabetic patients, as well as in many animal diabetes models, is sensitive to any loss in cell number or function. Probe chemotoxicity or radiotoxicity could, therefore, result in a further reduced capacity to mediate glucose homeostasis in already diseased or high-risk individuals. Special attention must be made to develop probes of low chemotoxicity that exhibit a safe dosimetric profile to both the islets themselves and other vital organs.

¹⁰⁹ Sulfonylurea receptors have also been extensively investigated as markers for BCM SPECT imaging with limited success,^{17,110,111} while calcium and potassium ion channel activities have been investigated as possible markers for BCF MRI (*vide supra* 2.3.1). Several antibodies that target β cell-specific cell surface antigens, such as TMEM27 and sphingomyelin, have also been investigated but have not seen widespread application due to slow *in vivo* pharmacokinetics and an excessively high background signal.¹⁷ The glucagonlike peptide-1 receptor (GLP-1R) is one of the more successful biomarkers for *in vivo* β cell quantification and has received significant attention as a biomarker for PET, SPECT and optical imaging of the BCM.

5.3 The Glucagon-Like Peptide-1 Receptor (GLP-1R)

GLP-1R is a key G-protein coupled receptor (GPCR) in the incretin system, which is responsible for sensing and responding to glucose intake through the digestive tract.^{17,112,113} GLP-1R, is highly expressed on the surface of pancreatic β cells, with limited expression elsewhere in endo- and exocrine pancreas, brain, duodenum, and lungs, making it a nearly ideal biomarker for specific β cell targeting.^{1,113-115} The structure of the receptor is also highly conserved across most species, thus making it a relevant biomarker for both preclinical and clinical research.¹¹³ GLP-1R is activated by glucagon-like peptide-1 (GLP-1), an endogenous peptide hormone that is secreted by the L-cells of the intestinal tract.¹¹⁶ Activation of GLP-1R, in combination with other incretin receptors, results in the synthesis and release of insulin,^a slows gastric emptying, and promotes a feeling of satiety in the brain and stomach.¹¹⁴ Additionally, activation of GLP-1R preserves β cell mass and function by reducing apoptosis and increasing β cell proliferation.¹¹⁶

Like all class-B GPCRs, GLP-1R consists of a 7-membered transmembrane domain (7TMD) and an extracellular domain (ECD) at the N-terminus, a fact confirmed by recently obtained (2017) crystal structures of the receptor.¹¹⁷⁻¹¹⁹ Crystal structures of both extracellular and TM domains in isolation also confirmed that GLP-1R exhibits a two-step, 2-domain binding mechanism for GLP-1 and other orthosteric ligands (Figure 20).¹¹⁷⁻¹²⁰ Initially, the ECD acts as an “affinity trap”, recognizing, the peptide ligand through a high-specificity, low-affinity hydrophobic interaction between the N-terminus ECD and the C-terminus of the ligand.^{118,120} The EDC then brings the N-terminus of the ligand into an optimized position for docking with the intra-helical cavity of the 7TMD. Here, the ligand undergoes a high-affinity interaction with the cavity which causes a conformational change in the receptor that results in receptor activation and agonist-mediated endocytosis.^{119,121} Signal transduction then occurs through a number of different pathways (intracellular Ca^{2+} mobilization, cAMP synthesis, extracellular signal-regulated kinase (ERK1/2) phosphorylation), depending on the activating ligand.^{117,122}

^a The incretin hormones GLP-1 and GIP are responsible for up to 70% of the glucose-dependent insulin release from healthy β -cells after the oral intake of nutrients and is the cause of a much higher insulin response when glucose is taken in orally vs. intravenously. This is known as the incretin effect.¹¹²

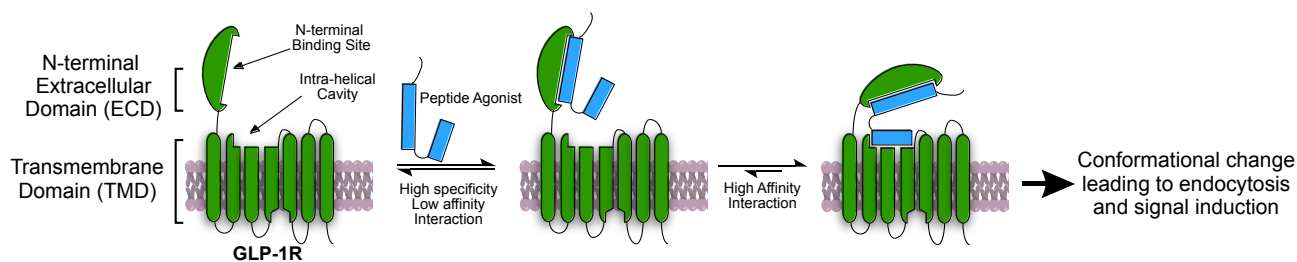


Figure 20: The “two-domain” binding mechanism for peptide ligands binding to GLP-1R.

5.3.1 Radiolabeled GLP-1R Ligands for BCMI

GLP-1(7-36)NH₂ is a potent, highly specific, and high-affinity agonist of GLP-1R; however, it is rapidly degraded to GLP-1(9-36)NH₂ (inactive) *in vivo* by dipeptidyl peptidase IV (DPPIV), resulting in a serum half-life of only 1-2 minutes. This makes its direct administration ineffective as either a therapy or imaging probe.¹²³ One strategy to overcome this limitation has been the development of stable GLP-1 analogs that resist degradation by DPPIV^a but are none-the-less highly potent agonists of GLP-1R. Exendin-3 (**Ex-3**) and exendin-4 (**Ex-4**), which were originally isolated from Gila monster venom (*Heloderma horridum* and *Heloderma suspectum* respectively), are stable (*in vivo* half-life > 1 hour) and selective exogenous GLP-1 mimetics that show picomolar (pM) affinity for GLP-1R (Figure 21).^{8,124,125} The two peptides share a 95% sequence homology, and they have both found use in various forms and formulations as long-acting treatments for T2DM. Another important exendin derivative is exendin (9-39); a truncated analog of exendin that is highly selective for GLP-1R but is unable to activate the receptor and hence acts as a GLP-1R antagonist.

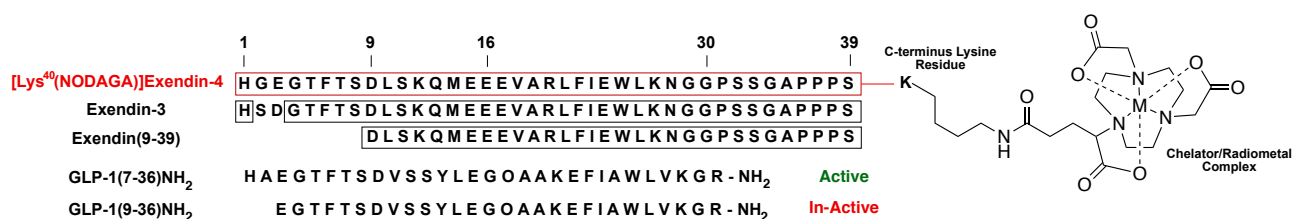


Figure 21: The primary structures of the exendin derivatives discussed in this thesis.^{119,124} Exendin-4 can be modified with a C-terminal lysine residue to facilitate the conjugation of a NODAGA chelator for radiolabeling.¹⁷

The selectivity and affinity of exendin derivatives for GLP-1R have made them prime imaging probe candidates for the *in vivo* targeting of β cells; thus, several radiolabeled exendin derivatives have been developed and evaluated. The exendin peptide can be conjugated to a prosthetic group or chelator at several sites along the peptide backbone.¹⁷ Modification and labeling of various auxiliary N- and C-terminal residues (such as Cys⁰, Cys⁴⁰, and Lys⁴⁰) with chelators and prosthetic groups has been successfully achieved with minimal losses of receptor binding affinity (Figure 21).^{126–128} Reiner *et al.* were able to demonstrate that the

^a Orally available DPPIV inhibitors are also used to increase the serum half-life of endogenous GLP-1 by slowing its degradation, thus resulting in a more sustained GLP-1R activation.

lysine residue at position 12 of **Ex-4** could be exchanged and modified with a non-natural alkyne bearing amino acid, which could be subsequently modified using a copper (I) catalyzed click reaction. Using this methodology the authors were able to generate fluorescently tagged, radiolabeled (^{18}F), as well as bimodal (optical and PET (^{64}Cu)) imaging probes.^{129–131}

Gotthardt *et al.* were able to use (Lys⁴⁰-DTPA)exendin-4 labeled with ^{111}In to successfully localize GLP-1R expressing tissues, namely the pituitary, pancreas, lungs, and adrenal glands, in rats using SPECT.¹²⁶ Wild *et al.* further developed and clinically evaluated the use of (Lys⁴⁰[^{111}In]In-Ahx-DTPA-NH₂)exendin-4 as both a SPECT probe and possible radiotherapy for the *in vivo* targeting of GLP-1R expressing tissues, including β cells and insulinoma, a β cell-derived tumor type.^{132–134} Wild *et al.* further developed a series of **Ex-4** derivatives that could be labeled with ^{68}Ga for PET imaging and $^{99\text{m}}\text{Tc}$, a commonly available SPECT isotope. These compounds were then used to successfully localize GLP-1R bearing insulinoma tissue in Rip1Tag2 transgenic mice.¹²⁸ Brom *et al.* were able to show, as possible alternatives to Ex-4, that radiolabeled **Ex-3** was similarly effective at labeling GLP-1R expressing cells *in vitro* and *in vivo*.^{135,136} Rylova *et al.* investigated radiolabeled exendin(9-39) (**Ex(9-39)**), a GLP-1R antagonist, for improved tracer pharmacokinetics; however, ^{68}Ga labeled derivatives of **Ex(9-39)** showed a reduced affinity and uptake in target tissues compared to **Ex-4** and **Ex-3**.¹³⁷

Kirsi *et al.* further developed ^{68}Ga and ^{64}Cu labeled (Nle¹⁴, Lys⁴⁰-Ahx-NODAGA-NH₂)exendin-4 tracers for pancreatic PET imaging in rats.¹³⁸ The authors claimed that exchanging the methionine at position-14 with norleucine (NLE) resulted in a compound that was more stable to oxidation and radiolysis with no apparent loss in receptor binding affinity. They were able to show that both the ^{68}Ga and ^{64}Cu labeled (Nle¹⁴, Lys⁴⁰-Ahx-NODAGA-NH₂)exendin-4 were able to selectively target the pancreatic islets (autoradiography); however, they were unable to visualize the BCM directly *in vivo* using PET, citing low tracer specific activity and an insufficient target-to-background ratio. These results highlight the substantial challenges of sensitivity and resolution to BCMI, as discussed above (*vide 2.2*); nevertheless, these studies demonstrated exendin's remarkable affinity and specificity for GLP-1R expressing cells.

Almost all radiolabeled exendin derivatives exhibit a high non-specific kidney uptake and slow renal clearance, which results in a high background signal due to spillover effects from the kidneys, as well as a heavy radiation burden to renal tissue in patients, especially when long-lived radioisotopes are used.¹³⁸ This has hindered the translation of exendin based tracers to routine clinical application. For this reason, the majority of more recent efforts to develop exendin as an imaging or theranostic agent have been focused on improving its imaging characteristics (i.e., positron range, molar activity through ^{18}F labeling)^{127,130,139} and pharmacological behavior (reduction of the renal uptake and enhancement of renal clearance).^{137,140,141} While significant progress has been made to address these issues, more work must be done before exendin based tracers for GLP-1R can meet the stringent requirements for longitudinal native BCM quantification.¹⁷

5.3.2 Allosteric Modulation of GLP-1R Activity and Ligand Binding

While exendin based tracers show excellent affinity and specificity for GLP-1R, the pharmacokinetic drawbacks of using peptide-based tracers (*vide supra*) warrants the investigation of alternative small molecule-based probes. Up until now, all efforts to image GLP-1R expressing tissues have been centered around peptide ligands which target the orthosteric binding site of the receptor; however, high throughput drug discovery programs and recent crystallographic studies have identified several small molecule modulators that can bind to allosteric sites on the receptor.^{142–145} Allosteric sites have not faced the same evolutionary pressure to maintain a strong interaction with an endogenous ligand and, thus, the internal structures of analogous allosteric pockets can vary considerably between different closely related receptor subtypes.¹⁴⁶ Allosteric sites on receptors and enzymes are thus important targets for drug discovery, as small molecules can be designed that are highly specific for an allosteric pocket on a particular receptor subtype. This is of particular interest when developing low molecular weight radiotracers for GPCRs like GLP-1R.

An allosteric interaction is defined as any interaction with an enzyme or receptor that is topographically removed from the main orthosteric binding site.¹⁴⁷ The binding of an allosteric ligand can affect the behavior of the receptor in several ways (Figure 22). Upon binding, many allosteric ligands can directly activate their target receptors to induce a response, usually through a conformational change brought about through the interaction at the allosteric site (allosteric agonists). Allosteric modulators may also be able to modulate the strength of the interaction between the orthosteric ligand and the orthosteric site, which can be observed as a change in specific receptor binding (affinity modulators). Additionally, allosteric ligands may affect the strength of the response that the orthosteric ligand can induce (efficacy modulators), which is observed as a change in the cellular response (cAMP production, Ca²⁺ influx, etc.) Allosteric modulators may also be able to induce a combination of these effects in addition to their potency, in which case they are termed *ago*-allosteric modulators.

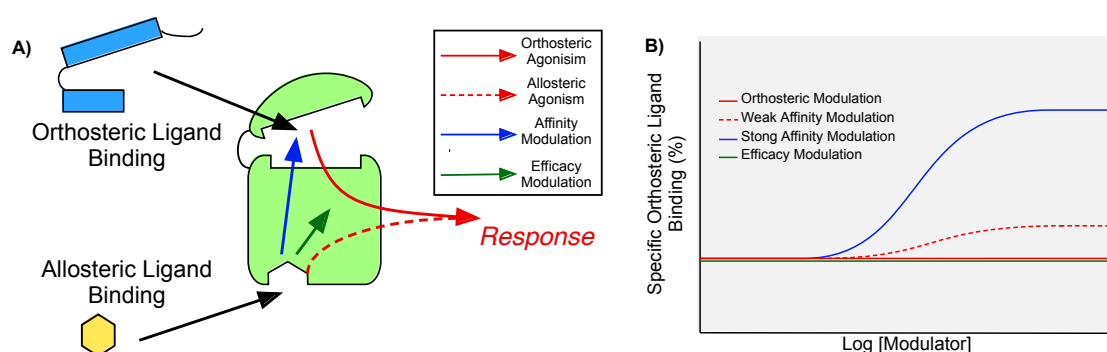


Figure 22: A) The different modes of action of allosteric modulators. B) The effect each mode of allosteric modulation has on the specific binding of the orthosteric ligand. This figure has been modified from the review by Conn et al.¹⁴⁷

The interplay between a GPCR (such as GLP-1R) and its orthosteric ligands and allosteric modulators can be described by a ternary complex model (Figure 23).¹⁴⁷ The strength of the interaction between a GPCR and an orthosteric ligand (OL) (arrow 1) is given by the dissociation equilibrium constant K_{OL} . Likewise, the binding

affinity of an allosteric modulator (AM) is given by K_{AM} (arrow 2). When an orthosteric ligand and an allosteric modulator are present at the receptor together, their binding affinities (and/or potencies) are both modified by a binding cooperativity factor (α). An allosteric modulator that increases the binding of the orthosteric ligand ($\alpha > 1$) is a positive allosteric modulator (PAM), a compound that has the inverse effect ($\alpha < 1$) is a negative allosteric modulator (NAM).

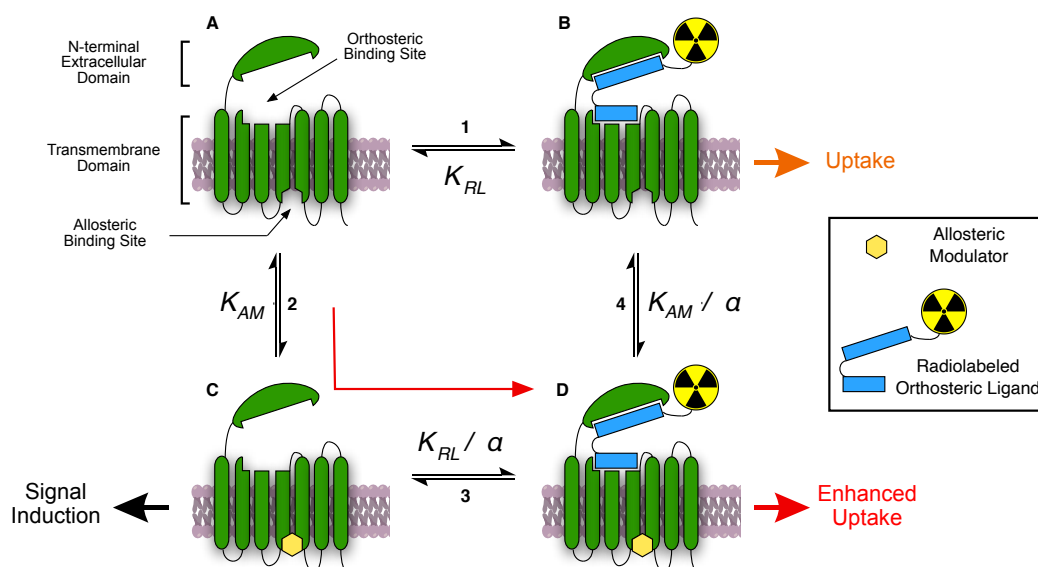


Figure 23: The ternary complex model as it pertains to GLP-1. K_{OL} is the equilibrium constant of orthosteric ligand (OL) binding, K_{AM} is the equilibrium constant of allosteric modulator (AM) binding, and α is the cooperativity factor that exists between the OL and the AM.

It has been suggested that, in the case of GLP-1R, the affinity modulating effect of certain compounds stems from their ability to stabilize the receptor/ligand complex in the active position.¹⁴⁸ Two of the most well-characterized allosteric modulators of GLP-1R that may be exploited for β cell imaging, both as orthosteric radioligand uptake enhancers and as small molecule radiotracers, are discussed in detail below.

5.3.2.1 “Compound 2” (C2): an Ago-Allosteric Affinity Modulator of GLP-1R

6,7-dichloro-2-methylsulfonyl-3- *N*-*tert*-butylaminoquinoxaline (often referred to as “compound 2” or **C2**) is an ago-allosteric modulator of GLP-1R that was first disclosed by Knudsen *et al.* and Teng *et al.* in 2007.^{149,150} **C2** was found to be an ago-allosteric agonist of GLP-1R and was able to potentiate the release of insulin in both *in vitro* and *in vivo* models, despite being considerably less potent than GLP-1 or Ex-4.¹⁵¹ More interestingly, **C2** was found to be an allosteric affinity modulator of GLP-1, the endogenous peptide ligands of GLP-1R; the presence **C2** (100 nM) was able to significantly enhance the binding affinity of [¹²⁵I]-GLP-1 and oxyntomodulin (OXM) to GLP-1R.^{149,152} Moreover, **C2** was able to significantly enhance the activity of GLP-1’s inactive metabolite GLP-1(9-36)NH₂.¹⁵³ This makes **C2** a potentially interesting model compound to assess in the uptake of orthosteric radiolabeled GLP-1R ligands that can be enhanced for β cell imaging using **C2**’s affinity modulating properties. However, it remains to be seen if these properties can be effectively leveraged *in vivo* using exendin based tracers, given **C2**’s low molecular weight (348 g/mol) and high lipophilicity.

One of the biggest challenges faced in the application of **C2** for *in vivo* experimentation is its unusual bell-shaped activity curve. Unlike typical allosteric modulators that reach an activity plateau at higher concentrations, the activity of **C2** peaks before dropping off steeply.¹⁴⁹ The exact mechanism of this behavior is not entirely understood; however, it may be associated with cytotoxic effects at high concentrations. Another proposed mechanism is the tendency of the highly lipophilic compound to form insoluble and inactive colloidal aggregates at higher concentrations in aqueous buffers.¹⁵⁴ This highlights the importance of correctly formulating **C2** for *in vitro* and *in vivo* experiments.

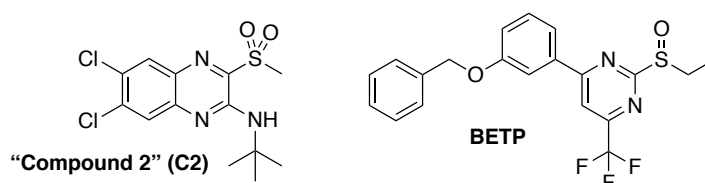


Figure 24: The chemical structures of both 6,7-dichloro-2-methylsulfonyl-3- N-tert-butylaminoquinoxaline "Compound 2" (**C2**) and 4-(3-benzyloxyphenyl)-2-ethylsulfinyl-6-(trifluoromethyl)pyrimidine (**BETP**)

5.3.2.2 BETP: A Covalent Modifier of GLP-1R

4-(3-Benzyloxyphenyl)-2-ethylsulfinyl-6-(trifluoromethyl)pyrimidine (Figure 24, **BETP**) was initially described as an agonist of GLP-1R capable of stimulating glucose-dependent insulin secretion from both human and rat pancreatic islets.¹⁵⁵ Additionally, **BETP**, like **C2**, has also been described as a positive allosteric modulator of GLP-1R that can potentiate the activity of GLP-1(9-36)NH₂ (the inactive metabolite of GLP-1) and OXM and has thus garnered interest as a lead compound for potential orally available incretin therapies for T2DM.^{156,157}

BETP possesses an electrophilic pyrimidinyl sulfoxide moiety and has been shown to irreversibly bind to GLP-1R at an allosteric site on the receptor's transmembrane domain through the formation of a covalent bond with cysteine residues (specifically C-347) in the allosteric pocket (Figure 25, A).¹⁵⁸ This property was further exploited by Broichhagen *et al.*, who were able to develop a photo-activated derivative of **BETP** (photoETP) that would "switch" its conformation while covalently bound inside GLP-1R's allosteric pocket when exposed to blue light (Figure 25, B). In conjunction with GLP-1(9-36)NH₂, the photoactivation of photoETP could be used to precisely control the activation of the receptor and insulin secretion in β cell models.¹⁵⁹ This approach demonstrated the viability of using covalently bound **BETP** derivatives to target GLP-1R, making **BETP** a potentially interesting tracer candidate. The irreversible binding of a **BETP** based tracer to GLP-1R would allow for the non-specifically bound tracer to wash out of the surrounding tissue, resulting in a superior signal-to-background ratio.

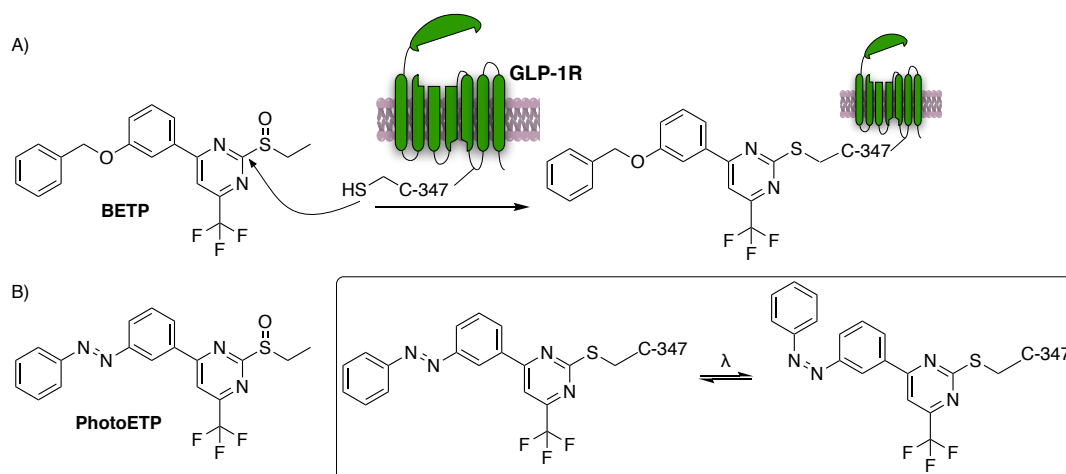


Figure 25: A) **BETP** covalently modifies cysteine residue C-347 on the transmembrane domain of GLP-1R.¹⁵⁸ B) **photoETP**, while similarly bonded to C-347, can switch its conformation upon exposure to blue light (inset).¹⁵⁹

The use of allosteric affinity modulators like **C2** or irreversible allosteric ligands such as **BETP** provides potential new avenues to improve on our abilities to target GLP-1R expressing tissues. The preliminary investigations of these compounds as potential new tools for β cell targeting are discussed further in the work below, along with an exploration and optimization of the radiochemical tools required to achieve these goals.

Results and Discussion

Chapter 6: Allosteric Affinity Modulators as GLP-1R Tracer Uptake Enhancers

6.1 Aims and Objective

As discussed above, highly selective orthosteric ligands for GLP-1R, such as exendin, have come to the forefront of BCMI research as highly specific probes for GLP-1R. Several radiolabeled exendin derivatives have been used to target and image GLP-1R, which has been established as a promising biomarker for pancreatic β cells and malignant β cell-derived insulinomas. However, exendin-based radiotracers suffer from several significant drawbacks that have prevented them from entering routine use. They show a high non-specific uptake in renal tissue, resulting in a high kidney radiation dose to the patients being studied. Additionally, the low *in vivo* binding capacity of GLP-1R and the high potency of exendin means that specific activity of any potential radiolabeled exendin derivative must be maximized. This is to ensure that the introduction of the tracer produces only a minimum insulinotropic effect, and that the tracer principle is not violated.

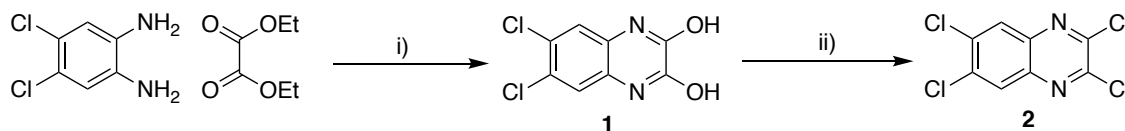
Compound 2 (**C2**) is a known positive *ago*-allosteric affinity modulator (PAM) of the GLP-1 receptor, which has been reported to enhance the affinity and efficacy of several endogenous orthosteric GLP-1R ligands.^{149–152} We hypothesized that **C2** could enhance the binding affinity of existing orthosteric GLP-1R radioligands, specifically radiolabeled exendin derivatives. A method to increase the specific uptake of an exendin-based tracer would be of great advantage to the β cell imaging community as it would potentially allow for the injection of lower tracer doses, a higher specific uptake of the tracer into the tissues of interest, and a reduced uptake in off-target tissues. This would lower the radiological dose to sensitive organs such as the kidney and improve the signal-to-background ratio of PET/SPECT images.

The development of a method to enhance the specific uptake of a radiotherapeutic or theranostic agent into specific tissues would also be beneficial for radiotherapeutic strategies designed to treat β cell-derived pathologies. Diseases that result in hyperinsulinism, such as insulinoma in adults or congenital hyperinsulinism in infants (CHI), are mainly treated surgically by pancreatectomy which results in a partial or complete loss of the patient's natural ability to regulate glucose homeostasis.^{10,12} Radiotherapeutic strategies present a potentially milder and more personalized approach to treating these illnesses that could result in improved treatment outcomes for the patients involved.

The goal of the research presented below was to assess the feasibility of using **C2** as an allosteric affinity modulator of GLP-1R to enhance the uptake of exendin derived radiotracers in both *in vitro* and *in vivo* β cell models.

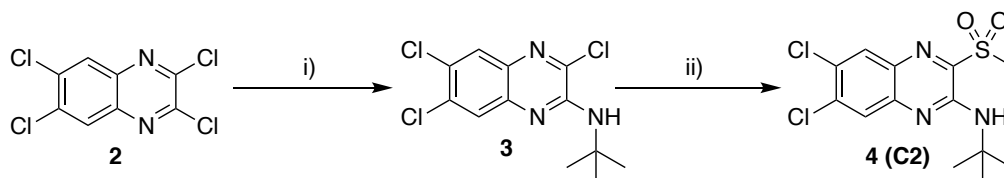
6.2 Synthesis of the Quinoxaline Derivative “Compound 2”

The synthesis of **C2** was adapted from the published routes by Teng *et al.* and Li *et al.*^{150,160} The synthesis involved the initial construction of symmetrical quinoxaline scaffold, which could then be further derivatized to achieve the asymmetric quinoxaline **C2** (Scheme 1).



Scheme 1: Preparation of a tetrachloroquinoxaline scaffold. Reagents and conditions: i) Reflux, 75%; ii) POCl₃, reflux, 87%.

To synthesize the quinoxaline core scaffold, 4,5-dichlorobenzene-1,2-diamine was condensed with diethyl oxalate by refluxing the two reactants overnight under solvent-free conditions. This resulted in the formation of **1** as a dark grey insoluble powder, which could be easily filtered from the reaction mixture, washed with ethanol, and dried under a high vacuum. The quinoxaline scaffold **2** could be achieved by refluxing **1** in phosphoryl chloride (POCl₃) under a stream of argon. The reaction was subsequently quenched by carefully pouring the reaction mixture into a rapidly stirring slurry of ice, saturated sodium bicarbonate solution, and ethyl acetate (EtOAc) (1:1:1 by volume). After extraction into EtOAc, the product residue could then be purified by flash chromatography to afford **2** as an off-white powder in moderate to good yields. ¹H and ¹³C NMR spectroscopy revealed the aromatic resonances expected of the symmetrical intermediate **2**.



Scheme 2: Preparation of **C2** from tetrachloroquinoxaline **2**. Reagents and conditions: i) *t*-Butylamine, Cs₂CO₃, DMF, 90 °C, 72%; ii) NaSO₂CH₃, DMF, room temperature, 94%.

With the reactive scaffold **2** in hand, **C2** could be easily synthesized in two steps (Scheme 2). 2,3,6,7-tetrachloroquinoxaline was heated to 90 °C in DMF with 0.5 equivalents of Cs₂CO₃ and one equivalent of *t*-butylamine. Thin-layer chromatography (TLC) revealed the reaction to slow and stop over time. Ninhydrin TLC dipping showed that over the course of two or more hours, the *t*-butylamine would evaporate from the reaction mixture (despite the presence of a reflux condenser) and the addition of an extra equivalent of the volatile amine after the first 2 hours would allow the reaction to proceed to completion (near-total consumption of the tetrachloroquinoxaline educt). The resulting reaction mixture could be quenched, extracted, dried, evaporated, and used directly in the next step without the need for a difficult chromatographic purification of the highly non-polar product. Nevertheless, a sample was isolated by flash chromatography and analyzed to confirm the formation of **3**. ¹H and ¹³C NMR spectroscopy confirmed the

formation of the asymmetric quinoxaline **3** through the presence of a larger number of distinct resonances (indicating a loss of symmetry) and the presence of the characteristic *t*-butyl singlet at δ_{H} 1.58 (s, 9H, C(CH₃)).

The treatment of **3** with 1.1 equivalents of sodium methanesulfinate (NaSO₂CH₃) in DMF overnight at room temperature afforded **C2 (4)** as an intensely yellow powder which could be easily separated from impurities carried over from the previous step with flash chromatography. ¹H and ¹³C NMR spectroscopy confirmed the formation of **C2** through the presence of the new diagnostic ¹H resonances at δ_{H} 3.41 (s, 3H, SO₂CH₃) and δ_{H} 1.54 (s, 9H, C(CH₃)₃) and the ¹³C resonances δ_{C} 40.6 (SO₂CH₃) and δ_{C} 28.6 (C(CH₃)₃). The acquired spectral data were identical to the data published by Knudsen et al.¹⁴⁹

The resulting compounds proved to be highly lipophilic and insoluble in water, which made formulating the compound for *in vivo* and *in vitro* experiments challenging. Two stock **C2** formulations were developed to help solubilize the compound during biological experiments. In formulation 1 (F1), **C2** was first dissolved in DMSO and then diluted with phosphate-buffered saline (PBS) to a final concentration of 2 mM and DMSO concentration of 5%. In formulation 2 (F2), **C2** was again dissolved in DMSO (5% total volume) and the surfactant binder Cremophor EL (15% total volume) with PBS to a concentration of 2 mM. Cremophor EL was used to ensure the prevention of **C2** colloid formation at higher **C2** concentrations. Both formulations were investigated as separate factors during *in vitro* testing.

6.3 *In vitro* Uptake Enhancement Experiments

(Lys⁴⁰-DTPA)exendin-3 and (Lys⁴⁰-DTPA)exendin(9-39) were labeled with [¹¹¹In]InCl₃ to produce (Lys⁴⁰-[¹¹¹In]In-DTPA)exendin-3 ([¹¹¹In]Ex-3) and (Lys⁴⁰-[¹¹¹In]In-DTPA)exendin(9-39) ([¹¹¹In]Ex(9-39)) for *in vitro* experiments. ¹¹¹In was chosen as a convenient isotope for the following *in vitro* studies due its 2.8-day half-life and relatively simple radiolabeling chemistry. Chinese hamster lung carcinoma cells overexpressing GLP-1R (CHL/GLP-1R cells) were used as an *in vitro* β cell model for all *in vitro* experiments.

6.3.1 Establishment of Dose-Response Curve of Tracer Uptake Enhancement

As a preliminary evaluation of the tracer uptake enhancing abilities of each of the **C2** formulations (F1 and F2) and to determine the optimal **C2** dose, CHL/GLP-1R cells were simultaneously administered with [¹¹¹In]Ex-3 (20000 cpm) and an increasing concentration of each **C2** formulation after which they were incubated for 4 hours at 37 °C (Figure 26). These results were compared to a tracer-only control (n = 6) where the cells were treated with the F2 buffer free of **C2** (Figure 26, blue line). Both **C2** formulations were able to increase the uptake of [¹¹¹In]Ex-3 into the GLP-1R cells at a concentration of 10 μ M; however, **C2** in F2 showed marginally better performance over **C2** in F1. **C2** concentrations higher than 10 μ M in both formulations resulted in a substantial reduction of tracer binding, producing the characteristic bell-shaped activity curve for **C2** that has been previously discussed in the literature.^{149,154} In this case, we believe that it may be as a result of toxic effects from higher **C2** concentrations or the tendency of the highly lipophilic **C2** to form

inactive aggregates above a critical concentration in aqueous solutions. An additional experiment was carried out in the same way using a more focused range of **C2** concentrations (1, 5, 10, 50 μM) and again a bell-shaped curve with a maximum binding enhancement effect at a **C2** concentration (F2) of 10 μM was observed (data not shown).

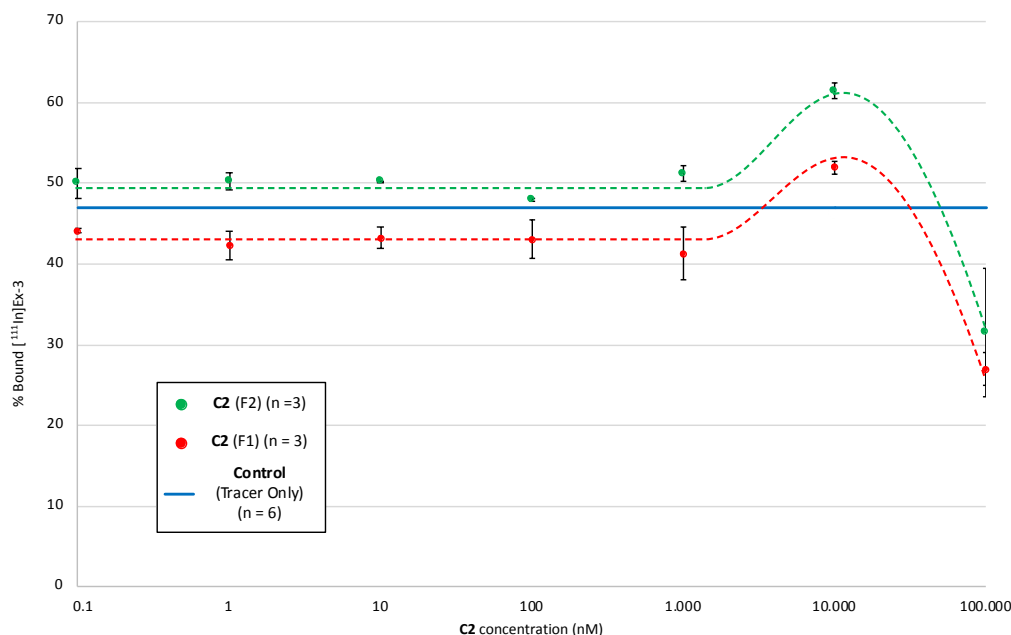


Figure 26: Dose-response curves for the tracer uptake enhancing effect of each **C2** formulation (F1: Red ($n = 3$), F2: Green ($n = 3$)) on $[^{111}\text{In}]\text{Ex-3}$ in CHL/GLP-1R cells. Uptake curves were measured against a tracer-only (with F2 buffer) control (blue line ($n = 6$)).

Given the ternary model of allosteric modulation (Figure 23), we hypothesized that the interaction of **C2** with the receptor before the introduction of the orthosteric tracer was an important factor to be maximized to achieve the best possible uptake enhancement. To evaluate this hypothesis, **C2** (10 μM) was pre-incubated with CHL/GLP-1R cells for 5, 10, and 20 minutes before the introduction of $[^{111}\text{In}]\text{Ex-3}$ (data not shown). No statistically significant difference in uptake enhancements at these time points was observed, relative to a control experiment where **C2** and $[^{111}\text{In}]\text{Ex-3}$ were introduced to the cells simultaneously. However, a trend favoring a pre-incubation time of 20 minutes was detected. It was thus decided that 10 μM **C2** would be incubated with the cells for 20 minutes before the introduction of the tracer in all further receptor binding experiments.

6.3.2 Receptor Binding Experiments

Further receptor binding assays were carried out to validate the above results and to confirm the specificity of the tracer in the presence of both **C2** formulations. Three groups of cells were incubated with vehicle, **C2** (10 μM) in F1, and **C2** (10 μM) in F2 for 20 minutes before the introduction of the tracer, after which they were incubated for 4 hours at 37 $^{\circ}\text{C}$ (Figure 27, A). An additional three groups were incubated under identical conditions but with the inclusion of non-radiolabeled Ex-3 (1000-fold excess introduced 1 minute before tracer administration). The presence of the non-radiolabeled peptide was able to eliminate the majority of $[^{111}\text{In}]\text{Ex-3}$ receptor binding in all blocking studies, confirming the specificity of the tracer under the control

and experimental conditions. The presence of **C2** in both formulations could significantly enhance the uptake of [¹¹¹In]Ex-3 into the CHL/GLP-1R cells with a 14% uptake enhancement noted for F2 (Figure 27: F1: $p = 0.017$; F2: $p = 0.0017$). No significant difference between the two **C2** formulations was detected under these conditions.

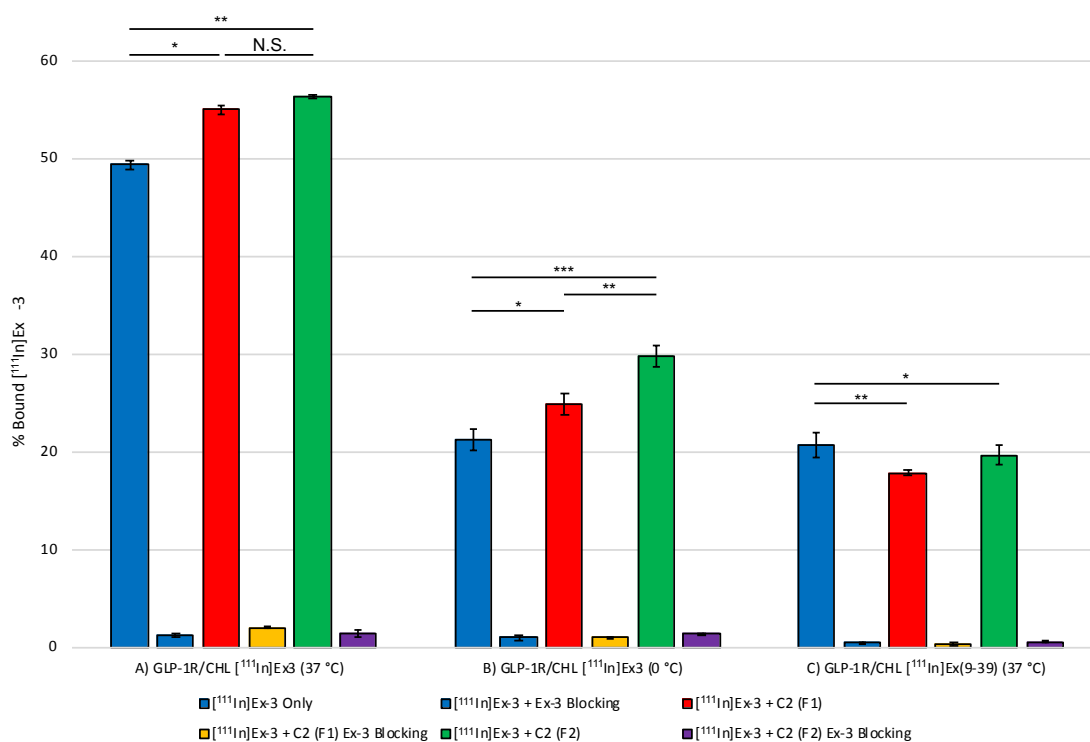


Figure 27: [¹¹¹In]Ex-3 and [¹¹¹In]Ex(9-39) receptor binding assays carried out in the presence of vehicle (blue), **C2** in F1 (10 μ M, red), and **C2** in F2 (10 μ M, green). Blocking studies were carried out by introducing non-radiolabeled Ex-3 (1000-fold excess) 1 minute before the introduction of [¹¹¹In]Ex-3. A) Cells were incubated with [¹¹¹In]Ex-3 for 4 hours at 37 °C. B) Cells were incubated with [¹¹¹In]Ex-3 for 4 hours at 0 °C. C) Cells were incubated with [¹¹¹In]Ex(9-39) for 4 hours at 37 °C. All experiments were conducted in triplicate. Differences were confirmed by two-sample t-test: * $p < 0.05$, ** $p < 0.01$, *** $p < 0.001$.

To further probe the mechanism of the uptake-enhancing effect, the identical experiment was carried out at 0 °C to inhibit the internalization of the receptor/allosteric modulator/tracer complex through endocytosis. In this case, the observed binding of the tracer to GLP-1R would be limited to interactions at the cell surface. **C2** in F2 was able to significantly ($p = 0.0007$) improve the binding of [¹¹¹In]Ex-3 to the receptor by 40%. **C2** in F1 was also able to significantly enhance receptor binding ($p = 0.017$), albeit to a lesser extent. **C2** in F2 was found to invoke a significantly stronger affinity-modulating effect than **C2** in F1 ($p = 0.005$), and this was thought to be attributed to the reduced solubility of **C2** in F1 at the lower experimental temperature. This experiment indicates that the mechanisms governing **C2** affinity modulation and uptake enhancement take place at the cell surface and not during receptor internalization.

Within the context of the ternary model of allosteric affinity modulation, the two possible routes by which the tracer binds to the receptor and triggers internalization compete with each other. Exendin can activate and internalize GLP-1R with pM affinity without the presence of an allosteric affinity modulator (Figure 28, 1). When **C2** is present, the affinity of this interaction is indeed significantly enhanced (Figure 28, 3); however,

binding enhancement relies on the secondary interaction of the affinity modulator with the allosteric pocket of the receptor (Figure 28, 2). While it leads to a stronger (lower energy) and more favorable interaction between the receptor and the tracer, this route proceeds by a two-step process and is therefore kinetically slower than direct tracer binding. In order to achieve a maximum uptake enhancement effect, the interaction between the allosteric modulator, the orthosteric tracer ligand, and the receptor must therefore be maximized at the surface of the cell before the receptor internalization can occur.

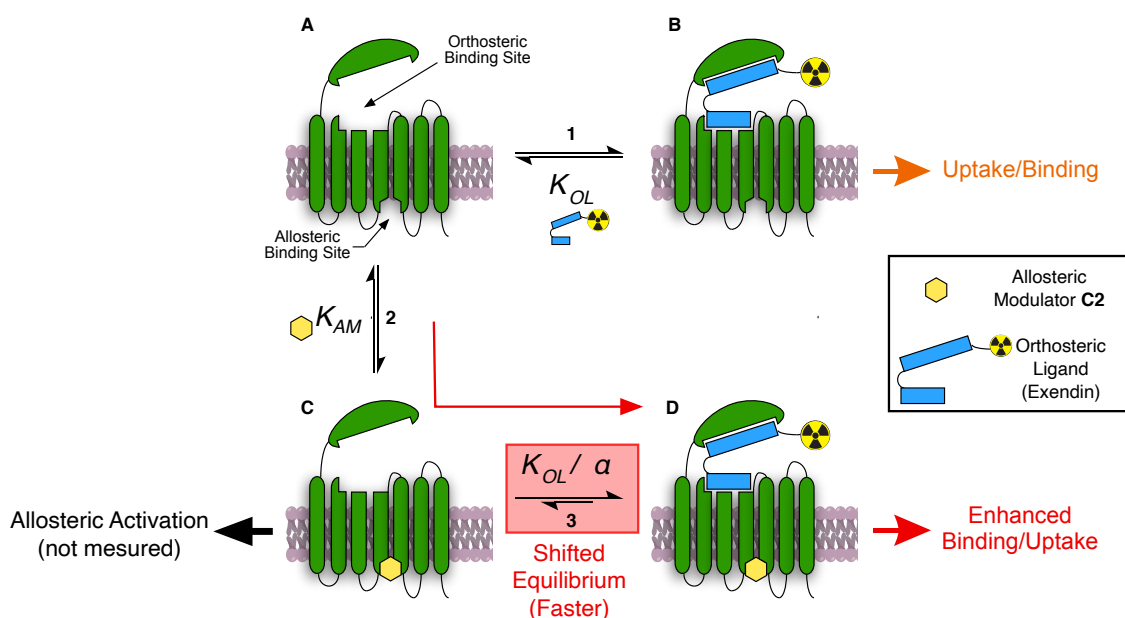


Figure 28: A proposed mechanism of C2 uptake enhancement based on the ternary complex model of allosteric modulation. α is the cooperativity factor that exists between the allosteric modulator and the orthosteric ligand.

A control experiment was carried out at 37 °C using the GLP-1R antagonist [^{111}In]Ex(9-39), a truncated derivative of exendin that can bind to GLP-1R without activating or internalizing the receptor. The specificity of [^{111}In]Ex(9-39) was again confirmed through blocking studies. Unexpectedly, no improvement in [^{111}In]Ex(9-39) binding was observed in the presence of either of the C2 formulations (a small but significant decrease in tracer binding was observed). While the mechanisms of C2 induced allosteric affinity modulation are not well understood, these results suggest that the affinity modulating properties of C2 are indeed probe dependent and rely on the nuanced conformational changes that occur within the receptor upon activation by an appropriate ligand.

6.4 *In vivo* Uptake Enhancement Experiments

For all *in vivo* PET imaging experiments, (Lys⁴⁰-NODAGA)exendin-4 was radiolabeled with ⁶⁴Cu via established literature-known protocols to produce (Lys⁴⁰-[⁶⁴Cu]Cu-NODAGA)exendin-4 ([⁶⁴Cu]Ex-4). ⁶⁴Cu is a positron-emitting isotope that is able to form highly stable complexes with the NODAGA chelator. Its half-life of 12.7 hours would allow for *in vivo* imaging and biodistribution experiments to be carried out up to 48 hours post tracer injection.

6.4.1 [⁶⁴Cu]Ex-4 *in vivo* GLP-1R Specificity and Binding

To evaluate the uptake and specificity of the [⁶⁴Cu]Ex-4 *in vivo*, blocking studies were carried out using BALB/c nude mice bearing subcutaneous INS-1 xenografts on their right shoulders. The INS-1 cell line is a β cell tumor model derived from rat insulinoma.¹⁶¹ Two groups of mice were injected with [⁶⁴Cu]Ex-4 (ca. 0.12 MBq/g body weight) and were allowed one hour of tracer uptake time under narcosis before being imaged with a 10-minute static PET protocol. The first group of mice showed a significant uptake of the injected radioactivity into the GLP-1R expressing INS-1 tumor relative to reference tissues (muscle). The second of the two groups of animals, which received non-radiolabeled Ex-4 (30 mg/kg) 3 min before tracer injection, showed a significantly lower uptake of the tracer into the tumor ($p < 0.01$), suggesting that the tracer was able to bind specifically to the β cell model.

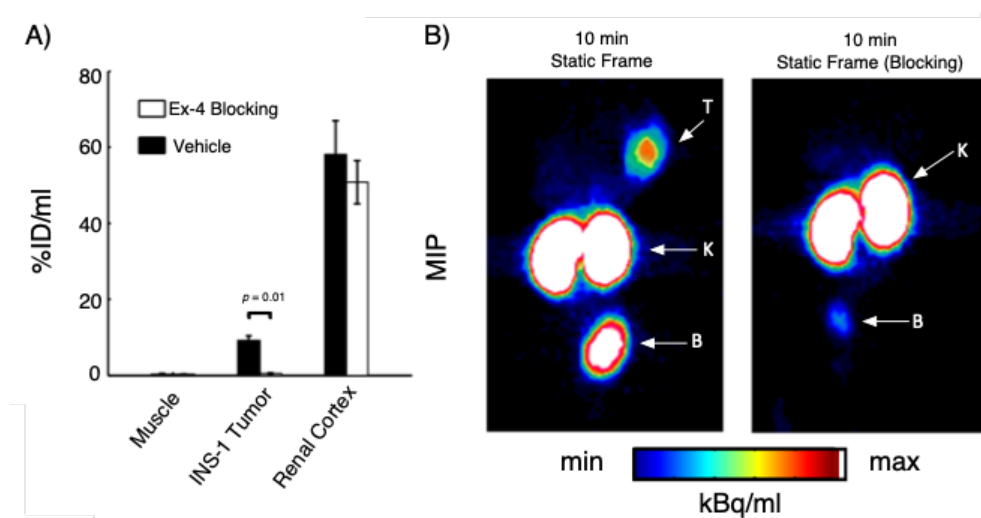


Figure 29: A) The bar chart shows the mean uptake (%ID/ml \pm StDev) of [⁶⁴Cu]Ex-4 into the muscle, renal cortex, and INS-1 tumors of BALB/c nude mice that were injected with either non-radiolabeled Ex-4 (30 mg/kg) or saline vehicle 3 minutes prior to tracer injection. The significance of the difference in tumor uptake between the two groups was verified by way of a two-sample Student's t-test. B) Representative maximal intensity projections (MIP) of 10-minute PET frames from each group. MIP labels: T, tumor; K, kidney; B, bladder. The data in this figure was obtained, analyzed, and provided by Filippo Michelotti.

6.4.2 The Effect of C2 on the Uptake of [⁶⁴Cu]Ex-4 into INS-1 Xenografts

To test the tracer uptake-enhancing effects of **C2** (F2) *in vivo*, the compound (0, 15, 25, 35 mg/kg) was injected into eight groups ($n = 4$) of INS-1 xenograft bearing BALB/c nude mice 30, 15, or 0 minutes before tracer injection. The maximum administered amount of **C2** was set to 35 mg/kg (ca 2 μ mol **C2** per injection) as doses exceeding 35 mg/kg causes a rapid (often fatal) decline in the condition of some animals. Mice injected with 25 mg/kg **C2** 15 min before tracer injection were scanned with dynamic PET frames for 1 hour ($n = 2$). The resulting time-activity curves (TAC) were compared to those from a control group ($n = 2$) injected with vehicle buffer. In both groups, a similar maximum tumor uptake was observed after 1 hour; however, mice treated with **C2** tended to display a slower uptake of the tracer into the xenograft tissue at earlier time points (Figure 30, A). Imaging with 10 min static scans at 1- and 24-hour time points post tracer injection showed no enhanced uptake in mice treated with **C2**.

After 48 hours, which allowed sufficient time for the wash-out of non-specific tracer uptake, the mice were sacrificed and subjected to *ex vivo* biodistribution analysis. [⁶⁴Cu]Ex-4 uptake into the INS-1 tumors ($\log_{10}(\%ID/ml)$) was slightly elevated in most groups treated with **C2**; however, statistical analysis on the \log_{10} transformed data set found this difference to be non-significant (Figure 30, B).

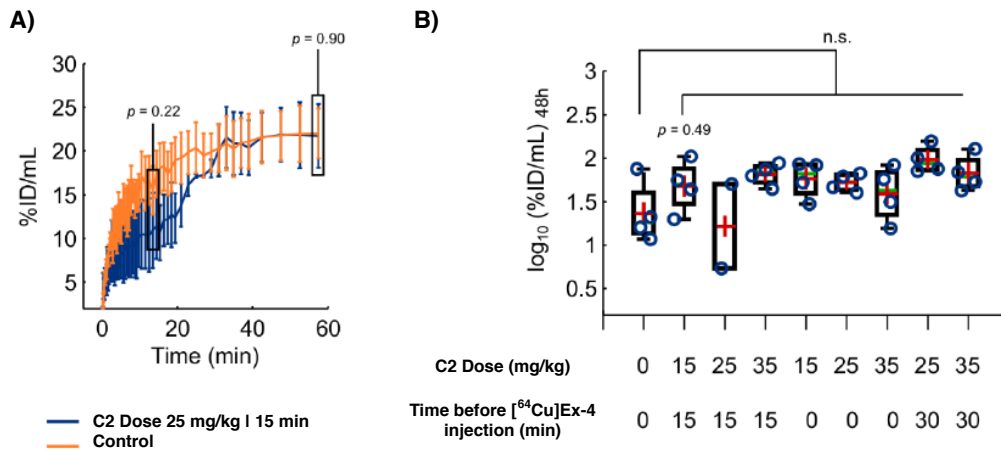


Figure 30: A) Dynamic PET scans of INS-1 xenograft BALB/c nude mice treated with 25 mg/kg of **C2** 15 min before tracer injection showed a slightly reduced uptake rate (non-significant; $p = 0.22$) when compared to mice treated with a saline control solution. B) Box-whisker plots (means marked in red) of the $\log_{10}(\%ID/ml)$ uptake values of the INS-1 tumors as measured by *ex vivo* γ -counter qualification. No significant difference in tracer uptake was observed between **C2** treated groups and a non-treated control group. Images and data were acquired and provided by Filippo Michelotti.

6.4.3 Dynamic PET Imaging of Native and Transplanted Pancreatic Islets

In a further attempt to increase [⁶⁴Cu]Ex-4 uptake into target β cell models, CH3 mice bearing transplanted islet grafts on their right legs were imaged with dynamic PET frames over the course of 1 hour. [⁶⁴Cu]Ex-4 was administered via a constant infusion (0-50 min, 120 μ l/hr, 0.24 MBq/g) of the tracer through a tail vein catheter. The uptake of the tracer was found to increase in the target islet grafts over the duration of the experiment. Two groups of mice ($n = 2$) were challenged with a bolus injection of **C2** (2 or 5 mg/kg) after 20 minutes, in an attempt to observe a change in the tracer uptake curve invoked by the presence of the affinity modulator (Figure 31, A and B). Lower **C2** doses of 5 and 2 mg/kg were chosen for reasons of animal safety based on literature precedent.¹⁵¹ No significant change in the islet- to-muscle ratio was observed over the course of the experiment (Figure 31).

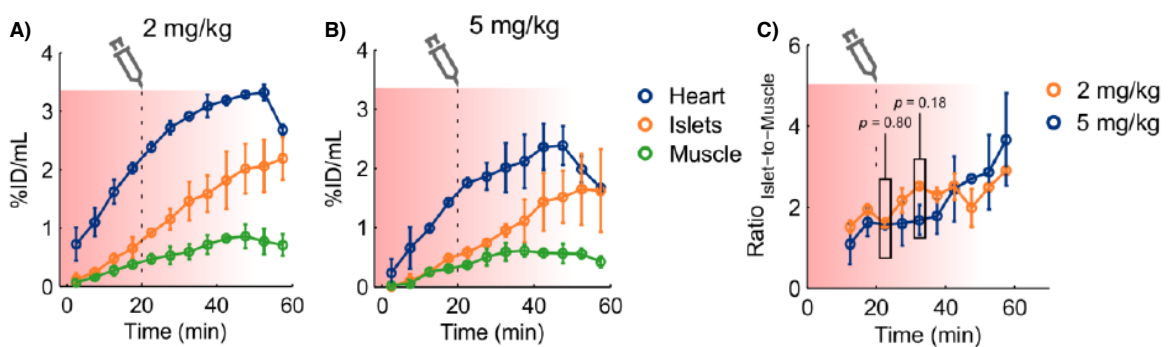


Figure 31: Two groups of mice ($n = 2$) were infused with [⁶⁴Cu]Ex-4 over the course of 50 min. Each group received a bolus injection of either A) 2 mg/kg **C2** or B) 5 mg/kg **C2** after 20 min tracer infusion. C) No significant difference between the islet-to-muscle ratios of the two groups was detected. Images and data were acquired and analyzed by Filippo Michelotti.

In a final attempt to increase tracer uptake, **C2** (5 mg/kg) and [⁶⁴Cu]Ex-4 (0.24 MBq/g) were infused into a cohort of three healthy CH3 mice using a bolus-infusion protocol (over 50 min) in order to maximize the interaction of the allosteric modulator and the tracer at the receptor. 60 min dynamic PET frames showed the tracer uptake to rapidly increase in the pancreas after the initial bolus injection of the **C2**/[⁶⁴Cu]Ex-4 mixture, followed by a steady increase in specific tracer uptake during the infusion phase of the protocol. The dynamic PET scans of the native pancreata were compared to those from a control group (n = 3) that was infused with [⁶⁴Cu]Ex-4 and saline vehicle via the same bolus-infusion injection protocol. No significant difference in tracer uptake was observed between the two groups at 20 min ($p = 0.78$) or at 60 min ($p = 0.32$).

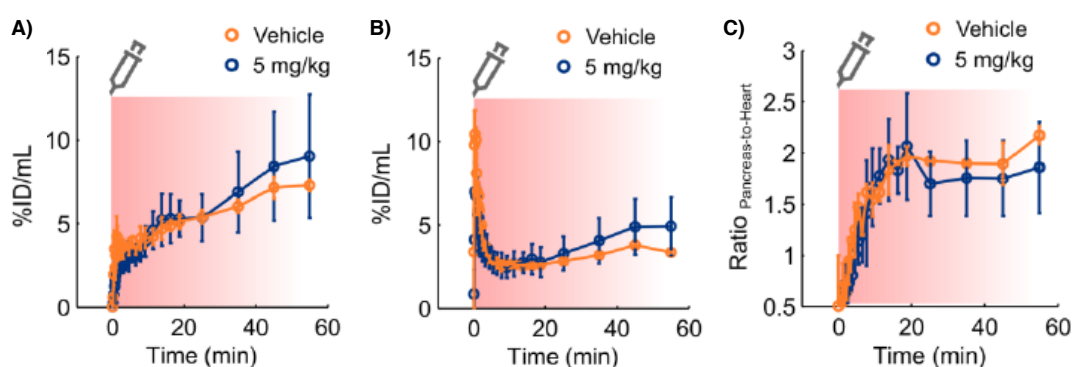


Figure 32: The uptake of [⁶⁴Cu]Ex-4 (%ID/ml \pm SD) into A) the native pancreata and B) the renal cortex of healthy CH3 mice over the course of 60 min. C) The ratio of pancreas-to-heart uptake over 60 min. Images and data were provided by Filippo Michelotti.

6.5 Summary and Discussion

Thus far, our attempts to increase the uptake of established exendin based tracers into GLP-1R expressing cell models using the allosteric affinity modulator **C2** have highlighted several significant challenges to the development of this imaging approach. The bell-shaped activity curve that describes the maximum tracer uptake enhancing effect with respect to **C2** concentration has made the translation of our *in vitro* protocols to *in vivo* imaging experiments difficult. Our *in vivo* pilot studies investigated a wide range of **C2** doses ranging from 35 – 2 mg/kg (1.25 mM – 71 μ M *in vivo* concentration, calculated assuming a mouse blood volume of 1.6 ml). None of these doses were able to invoke any significant change in tracer uptake and may have been excessively high. The uptake enhancing effect of **C2** relies heavily on the correct concentration of the compound at the receptor; doses below 10 μ M were not able to increase tracer uptake, while higher doses resulted in an overall reduction of tracer uptake. This, unfortunately, leaves a narrow **C2** dose window where the uptake enhancing effect can be invoked, and it is currently unclear how this window changes in response to the use of different *in vivo* β cell models, animal models, or disease states. It is also currently unclear how the clearance, metabolism, and biodistribution of **C2** affects the final *in vivo* concentration and potency of the allosteric affinity modulating effect.

The formulation of **C2** has also been of significant concern throughout the *in vitro* and *in vivo* investigations described above. While we were able to stably solubilize **C2** in a sufficiently concentrated formulation for *in*

in vitro studies, it has been difficult to gauge to what effect the presence of relatively high DMSO and Cremophor EL concentrations (5 and 15% of the injected volume respectively) have had on the affinity modulating efficacy of **C2** *in vivo*. This would also have to be further investigated as a critical factor when aiming to develop the correct **C2** dose formulation and injection/infusion protocol for future *in vivo* tracer uptake enhancement studies.

The allosteric affinity modulation effect is well known to be probe-dependent; the effect can only be observed using certain combinations of allosteric modulators and orthosteric probes.^{157,162} We were able to demonstrate this phenomenon *in vitro*: The presence of **C2** was able to enhance the receptor binding of [¹¹¹In]**Ex-3** to GLP-1R; however, **C2** was unable to produce a similar effect with the orthosteric GLP-1R antagonist [¹¹¹In]**Ex(9-39)**. This suggests that the affinity modulating effects of **C2** depend on the nuanced interactions and conformational changes that take place at both the orthosteric and allosteric binding sites on GLP-1R. Our *in vivo* experiments were designed and executed under the assumption the **Ex-3** and **Ex-4** would display a similar level of cooperativity with **C2**; however, this assumption may prove to be a significant limitation of the studies described above. The *in vitro* studies described above should be repeated using [⁶⁴Cu]**Ex-4** to conclusively prove that similar uptake enhancement can be achieved using the alternative exendin derivative.

A further limitation of our *in vivo* studies using [⁶⁴Cu]**Ex-4** was the use of ⁶⁴Cu in β cell tumor models. ⁶⁴Cu is well known to be a theranostic radionuclide as it decays by both β^- and β^+ decay pathways (*vide* 3.1.1). Although this effect was not directly investigated here, the prolonged use of [⁶⁴Cu]**Ex-4** in β cell tumor models in longitudinal studies may be radiotoxic to the model and thus decrease the uptake signal in the tumors at later imaging time points. This could potentially make repeated measurements on the same cohort of animals unreliable and carries negative implications for the clinical translation of ⁶⁴Cu-labeled radiotracers for β -cell localization.

Radiolabeled exendin derivatives were used for the above studies due to their position as established, effective, and available probes for GLP-1R targeting; however, **C2** has been shown to exhibit much stronger cooperativities with endogenous peptides GLP-1 and OXM.^{152,156} Moreover, **C2** has been shown to modulate both the efficacy and affinity of these peptides at GLP-1R with much higher potency and a more predictable dose-response window. Therefore, GLP-1 and OXM represent possible alternative candidate probes that could have their specific uptake in GLP-1R expressing tissues significantly enhanced by **C2**. However, as mentioned previously, GLP-1, as well as OXM, have short *in vivo* half-lives and are rapidly degraded and deactivated in the bloodstream. OXM is also able to bind to the glucagon receptor, and this raises concerns over the *in vivo* selectivity of OXM-based probes for β cell targeting.¹⁶³ Stable exendin radiotracers were specifically developed as GLP-1R tracers because of their increased *in vivo* stability. The option to obtain improved tracer enrichment in GLP-1R expressing tissues using allosteric affinity modulators like **C2** makes the development of novel stabilized derivatives of GLP-1 and OXM an attractive proposition.

6.6 Conclusion and Future Work

While we were able to demonstrate that the presence of **C2** can increase the specific uptake of [^{111}In]Ex-3 into GLP-1R expressing cells *in vitro*, we could not invoke this effect to a significant degree in several *in vivo* β cell models using [^{64}Cu]Ex-4. Finding the correct **C2** formulation and dose window to achieve a tracer uptake enhancement using exendin-based radiotracers remains a significant hurdle to the development of this approach.

For this approach to become a viable tool for *in vivo* BCMI, extensive work to find and develop alternative cooperative affinity modulators and orthosteric ligand combinations must be carried out. One possible avenue for achieving this goal would be the development of new GLP-1R binding tracers based on stabilized structures of the endogenous peptide hormones GLP-1 and OXM that are tailored to maximize the cooperative effect with **C2**.^{157,162,164} Alternately, the discovery of new, more potent allosteric affinity modulators with improved pharmacological properties over **C2** would greatly aid in this endeavor.

The idea of using allosteric modulators to increase the affinity of other tracers to other GPCR targets nonetheless remains an exciting and viable option for increasing specific binding and limiting off-target uptake. The potential benefit afforded by this approach extends not just to improved signal-to-noise ratios in *in vivo* PET images but also to the use of theranostic and radiotherapeutic agents. Enhancing the specific accumulation of a radiotherapeutic or theranostic agent would lead to a higher radiation dose specific to the diseased tissue.

The work described above was carried out in an attempt to improve the signal-to-noise ratios of exendin-based tracers by limiting the off-target accumulation of the tracer in the exocrine pancreas and renal cortex. While **C2**-induced uptake enhancement was not able to achieve these goals in the presented studies, we nonetheless believe that the pharmacokinetics and pharmacodynamics of small-molecule radiotracers for GLP-1R warrant further investigation. **BETP** (*vide* Chapter 8) is a potentially attractive candidate for development as a radiotracer for GLP-1R due to its ability to bind irreversibly to the allosteric pocket on the receptor through covalent modification (*vide* 5.3.2.2). However, the radiosyntheses of ^{18}F labeled **BETP** derivatives possess several challenges and required the establishment and optimization of recently-disclosed copper-mediated radiofluorination chemistry (*vide infra*).

Chapter 7: The Use of DoE for the Optimization of Copper-Mediated Radiofluorinations (CMRFs)

Parts of this chapter have been published: Bowden, G. D. *et al. Sci. Rep.* **9**, 11370 (2019).⁸⁶

7.1 Aims and Objectives

The rapid development of novel small molecule tracers for β cell mass imaging or any other application is a complex and time-consuming process that relies on a well-established and well-understood radiochemical toolbox. The ^{18}F tracer development pipeline has long been bottlenecked by the ^{18}F radiochemical toolbox available to radiochemists (especially where aromatic compounds have been concerned). This has limited the chemical diversity of novel ^{18}F radiotracers (Figure 33).⁴⁶ The recent advent of new radiolabeling methodologies (*vide* 3.3) has begun to expand this bottleneck while presenting a new and complex set of optimization problems inherent with multicomponent (radio)chemistry.

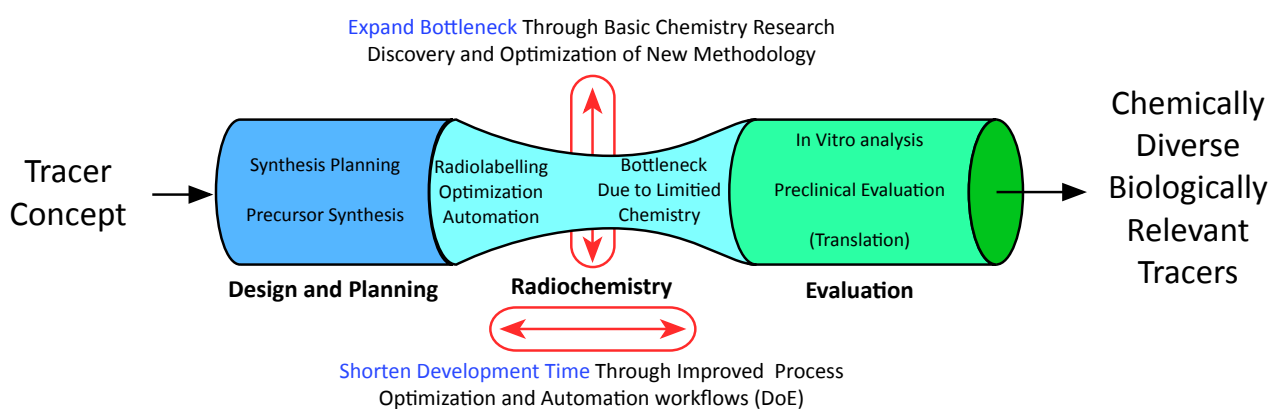


Figure 33: The tracer development pipeline. The development of new easy-to-apply methodologies, as well as improved optimization workflows, can help expedite the design and development of novel tracers.

The synthesis of novel tracer derivatives based on the compound **BETP** (*vide* chapter 8) requires the use of next-generation radiofluorination methodologies such as copper-mediated radiofluorinations (CMRFs) that can label electron-rich and neutral aromatic moieties. Our preliminary efforts to synthesize ^{18}F labeled **BETP** derivatives were hindered by a poor understanding of CMRF chemistry under various published CMRF conditions. This represented a significant challenge to the development of **BETP** and other novel tracers in our laboratory that were designed to be radiofluorinated using CMRF methodologies.

DoE is used routinely across a broad array of chemical industries to improve process robustness, yield, and product quality. In the context of radiochemistry, Mathiessen *et al.* have demonstrated the power and utility of the DoE approach as a potential tool to explore and develop new radiochemical methodologies across a broad range of factors.^{165,166} DoE can explicitly identify the most critical factor effects that should be considered when developing a radiosynthesis for automation. Additionally, response surface optimization (RSO) DoE designs may potentially accelerate the optimization of new tracer syntheses. Well-optimized

radiochemistry will ultimately lead to more robust synthesis protocols for tracer productions under current good manufacturing practice (cGMP) conditions, thus expediting the tracer's translation to (pre-)clinical use.

The studies presented below aimed to further highlight the use of the DoE approach for accelerating the optimization of radiochemical processes and as a research tool to glean new insights into the behavior of new radiochemical methodologies. By applying DoE to the CMRF of arylstannanes (as disclosed by Makaravage *et al.*⁷³) and arylboronates (as disclosed by Tredwell *et al.*⁶⁷ and Mossine *et al.*⁷⁰) we aimed to learn more about the important factors affecting this class of reaction and how best to apply that information to accelerate the development of ¹⁸F radiotracers for BCMI as well as for other applications.

7.2 DoE vs OVAT Efficiency Estimation

In their original paper, Makaravage *et al.* assessed the performance and behavior of their CMRF of arylstannane precursors by conducting an optimization study using the OVAT approach (Table 5). The authors investigated eight experimental factors with 3 to 6 settings each. To ensure reproducibility, the authors claimed to perform each experiment at least twice ($n=2$). Thus, the authors investigated the CMRF of a single model compound (4-tributyltinbiphenyl) over 74 individual experimental runs. Similarly, Zarrad *et al.* performed an OVAT study using a variation of this reaction with improved ¹⁸F processing conditions. The authors were successful in developing a scalable method for automated tracer syntheses using this methodology; however, this was also done with the limitations of the OVAT approach and at great experimental effort.

Table 5: The number of total experimental runs required for a selection of different experimental designs.

	Factor Screening Designs				Optimization	
	OVAT ^a	Fractional Factorial ^c			Full Factorial	Central Composite Design (CCD) ^g
		RES III ^d	RES IV ^e	RES V ^f		
Non-CP runs	NA	L^{k-p}	L^{k-p}	L^{k-p}	L^k	$L^k + 2k(\text{starpoints})$
Settings per Factor (L)	3 - 6	2	2	2	2	5
Factors investigated (k)	8	9	8	8	8	3
Formula	NA	2_{III}^{9-5}	2_{IV}^{8-4}	2_V^{8-2}	2^8	$2^3 + 6$
Repetitions/center-points	$n=2^b$	$Cp=3$	$Cp=3$	$Cp=3$	$Cp=3$	$Cp=3$
Total number of runs	74	19	19	67	259	17

a) The results of this column were tallied from the paper by Makaravage *et al.*⁷³ b) The authors stated that $n \geq 2$ runs were performed for each experimental point. For this tally, it was assumed that each run was performed twice. c) The number of runs for the corresponding fractional factorial RES III, RES IV, and RES V designs (with k factors and p generators) were taken from the table printed in Box, Hunter and Hunter 1979.⁹⁴ d)-f) Refer to Chapter 4: Table 4, for resolution definitions. g) A CCD is a response surface optimization design. This table was taken from the paper by Bowden *et al.*⁸⁶

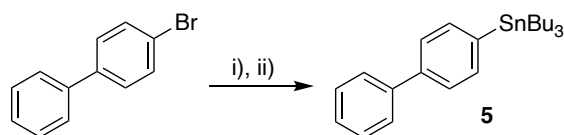
Using a fractional factorial factor screening design (RES IV), it was calculated that one could evaluate a similar number of factors and screen for the main effect contributions to the response in as few as 19 runs. Further RSO studies using either central composite, Box-Behnken or D-optimal designs could then be performed on

a reduced subset of significant factor effects on specific substrates to provide a more detailed optimization model in as few as 17 runs (for a 3 factor CCD). This would allow one to screen for and optimize important factors in as few 36 runs (vs. 74). These potentially substantial gains in experimental efficiency and the increased quality of the process information obtained by the application of DoE thus warranted further investigation.

7.3 DoE Optimization of the CMRF of Arylstannanes

7.3.1 Factor Screening DoE Study Using 4-Tributyltinbiphenyl

The first phase of the DoE investigation featured a preliminary factor screening study to determine which factors had a significant influence on the %RCC of a model CMRF of arylstannanes and which did not. The CMRF of 4-tributyltinbiphenyl (**5**) was chosen as a model compound for the DoE study as the product 4- ^{18}F fluorobiphenyl is non-volatile on silica TLC plates; hence, the %RCC of the reaction can be quickly and accurately assessed by radio-TLC. **5** was easily synthesized from 4-bromobiphenyl via a lithium-halogen exchange using *n*-butyllithium (*n*-BuLi) in diethyl ether (Et_2O), followed by the subsequent reaction of the aryl lithium intermediate with tributyltin chloride (Scheme 3). The non-radioactive standard compound **6** was procured commercially.



Scheme 3: Reagents and conditions: i) *n*-BuLi (2.5 M in hexanes), Et_2O , $-78\text{ }^\circ\text{C}$ - room temperature; ii) Bu_3SnCl (dropwise), $-78\text{ }^\circ\text{C}$ - room temperature, 84%.

For the formation of ^{18}F **6**, $\text{Cu}(\text{OTf})_2$ loading (1-4 equivalents relative to substrate), pyridine loading (4-30 eq), the total reaction volume (in DMA: 400-1000 μl), the reaction temperature (100-140 $^\circ\text{C}$), and the reaction atmosphere (argon or air) were identified as factors of interest from literature research as well as from a number of pilot experiments (Figure 34). Several other studies had suggested the atmosphere to affect the reaction's performance,^{67-69,71,74} however, in our hands, pilot experiments using arylstannane precursors and a variety of reaction conditions failed to reveal any obvious benefit afforded by using either argon or air as the reaction atmosphere. The reaction atmosphere was hence included here as a factor of interest. Reaction time was not included as a factor of interest as time is closely related to reaction temperature and, given the relatively short half-life of ^{18}F , it is more reasonable to limit the reaction time to a maximum of 30 min. The radiochemical conversion (%RCC) was chosen as the measured response as it could be quickly and easily evaluated by radio-TLC.

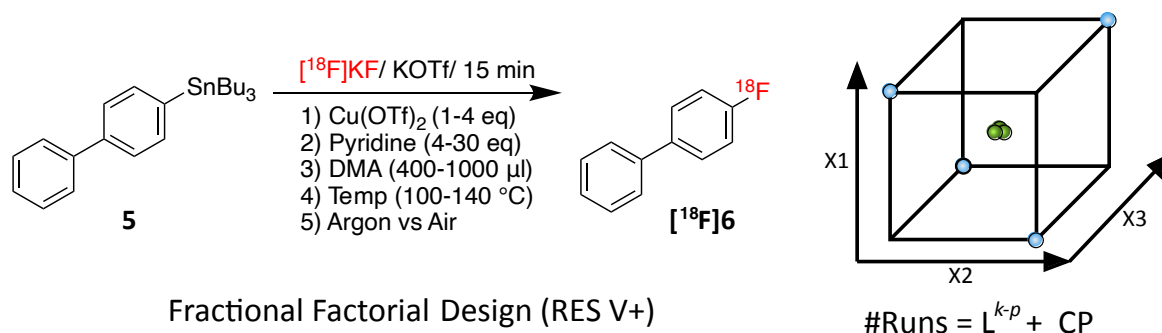


Figure 34: The CMRF of **5** to $[^{18}\text{F}]\mathbf{6}$ was chosen as a model reaction for a fractional factorial (RES V+) factor screening study (Inset, Vide 4.2.1). The above diagram has been taken and adapted from Bowden et al.⁸⁶

MODDE Go 12 was used to generate a fractional factorial design (RES V+) that was arranged into four experimental blocks, each consisting of six runs (4 experimental points, 2 centerpoints), bringing the total number of experiments to 24. The study was “blocked” in this way to account for day-to-day differences in uncontrollable factors such as QMA cartridge quality, QMA eluent composition, and ^{18}F fluoride quality. The centerpoints contained in each block would allow these variances to be measured between each block (each day of the study, 6 runs per day) and accounted for in the final regression model.

As previously mentioned, (*vide* 3.3.1) the final composition of the QMA eluent present in the reaction mixture can have a significant effect on the CMRF’s performance. To minimize any unwanted variability between each of the runs within a block, we elected to perform one QMA ^{18}F trapping and elution step per block. The resulting ^{18}F containing QMA eluent (Scott Eluent A: QMA- HCO_3^- , K_2CO_3 50 μg , KOTf 10 mg, Water 550 μl (*vide infra*)) could then be separately aliquoted into each reaction vessel in equal volumes (80 μl) prior to azeotropic drying, keeping the composition of the QMA eluent residue present within each run in the block as constant as possible. The limitations of using this so-called “aliquot” method have been noted repeatedly in the literature.^{68,69,71,74,75} The reduced amount of salts and strong bases present in small aliquots of QMA eluent have a less negative influence on the performance of the CMRF reaction than the much larger amounts present (6 fold more in this case) if a full batch of the QMA eluent is used (as in an automated synthesis). Nonetheless, we opted to use the aliquot strategy as the reduction of large sources of experimental error was seen to be of great importance.

Using the experimental worksheet table generated by the MODDE software (Table 6), the data were obtained and analyzed using the general procedures described in chapter 12. The construction of a valid regression model requires that the data be normally distributed; thus, the %RCC data set was transformed to $\log(10)$ to ensure a normal distribution, after which it was used to fit a model using multiple linear regression (MLR). The resulting model was then used to check the data set for outliers and assessed for model quality. The summary statistics ($R^2 = 0.91$ (goodness of fit) and $Q^2 = 0.57$ (goodness of prediction)) suggested the regression model to be valid and appropriate for factor screening.

Table 6: Worksheet table containing the required experimental conditions and %RCC data for each run in the fractional factorial factor screening study. Experimental points are displayed in blue, while centerpoints are shown in green. The table is taken from the paper by Bowden et al.⁸⁶

Exp No	Temp	DMA Volume (μ l)	Catalyst Loading (eq)	Catalyst mmol	Catalyst mass (mg)	Pyridine Loading (eq)	Pyridine mmol	Pyridine mass (mg)	Pyridine Volume (μ l)	Atmosphere	Block	RCC
1	100	400	1	0.0045	1.63	4	0.02	1.43	1.40	Air	B1	3
2	140	400	4	0.0180	6.50	4	0.02	1.43	1.40	Air	B1	10.9
3	140	1000	1	0.0045	1.63	30	0.14	10.69	10.50	Argon	B1	7
4	100	1000	4	0.0180	6.50	30	0.14	10.69	10.50	Argon	B1	31.2
5	120	700	2.5	0.0113	4.07	17	0.08	6.06	5.95	Argon	B1	22
6	120	700	2.5	0.0113	4.07	17	0.08	6.06	5.95	Argon	B1	33
7	100	1000	1	0.0045	1.63	4	0.02	1.43	1.40	Argon	B2	5.7
8	140	1000	4	0.0180	6.50	4	0.02	1.43	1.40	Argon	B2	6
9	140	400	1	0.0045	1.63	30	0.14	10.69	10.50	Air	B2	10.2
10	100	400	4	0.0180	6.50	30	0.14	10.69	10.50	Air	B2	23.2
11	120	700	2.5	0.0113	4.07	17	0.08	6.06	5.95	Argon	B2	35
12	120	700	2.5	0.0113	4.07	17	0.08	6.06	5.95	Argon	B2	23
13	140	1000	1	0.0045	1.63	4	0.02	1.43	1.40	Air	B3	5.9
14	100	1000	4	0.0180	6.50	4	0.02	1.43	1.40	Air	B3	13
15	100	400	1	0.0045	1.63	30	0.14	10.69	10.50	Argon	B3	8.3
16	140	400	4	0.0180	6.50	30	0.14	10.69	10.50	Argon	B3	33
17	120	700	2.5	0.0113	4.07	17	0.08	6.06	5.95	Argon	B3	31.2
18	120	700	2.5	0.0113	4.07	17	0.08	6.06	5.95	Argon	B3	36.7
19	140	400	1	0.0045	1.63	4	0.02	1.43	1.40	Argon	B4	2.1
20	100	400	4	0.0180	6.50	4	0.02	1.43	1.40	Argon	B4	19.6
21	100	1000	1	0.0045	1.63	30	0.14	10.69	10.50	Air	B4	12.3
22	140	1000	4	0.0180	6.50	30	0.14	10.69	10.50	Air	B4	15.9
23	120	700	2.5	0.0113	4.07	17	0.08	6.06	5.95	Argon	B4	29
24	120	700	2.5	0.0113	4.07	17	0.08	6.06	5.95	Argon	B4	29

The normalized (scaled and centered) regression coefficients for each term in the model were used to assess the significance ($\alpha = 0.05$) of the contribution of each factor to the %RCC of the reaction (Figure 35). Analysis of each of the 4 experimental blocks (Block 1-4) showed that there were no significant day-to-day experimental variances that need to be accounted for in the final model; i.e., the experimental protocol was stable to uncontrollable experimental factors introduced by running the DoE study over multiple days. Both the temperature (Temp) and the total reaction volume (DMA vol) were not significant contributors to the reaction's performance over the investigated ranges and can thus be excluded from future optimization studies. The $\text{Cu}(\text{OTf})_2$ (catalyst) and pyridine loading were, however, found to have significant effects on the response. Moreover, the model also suggested the presence of curvature (a quadratic term) in the response surface; however, these terms could not be fully resolved due to the lower resolution (confounding) of the fractional factorial design. Thus, a higher resolution study (e.g., using a full factorial or central composite design) would need to be conducted to generate a fully descriptive model of the system. The presence of the unmodelled curvature in this study may explain the lower than expected Q^2 term present in the model fit statistics.

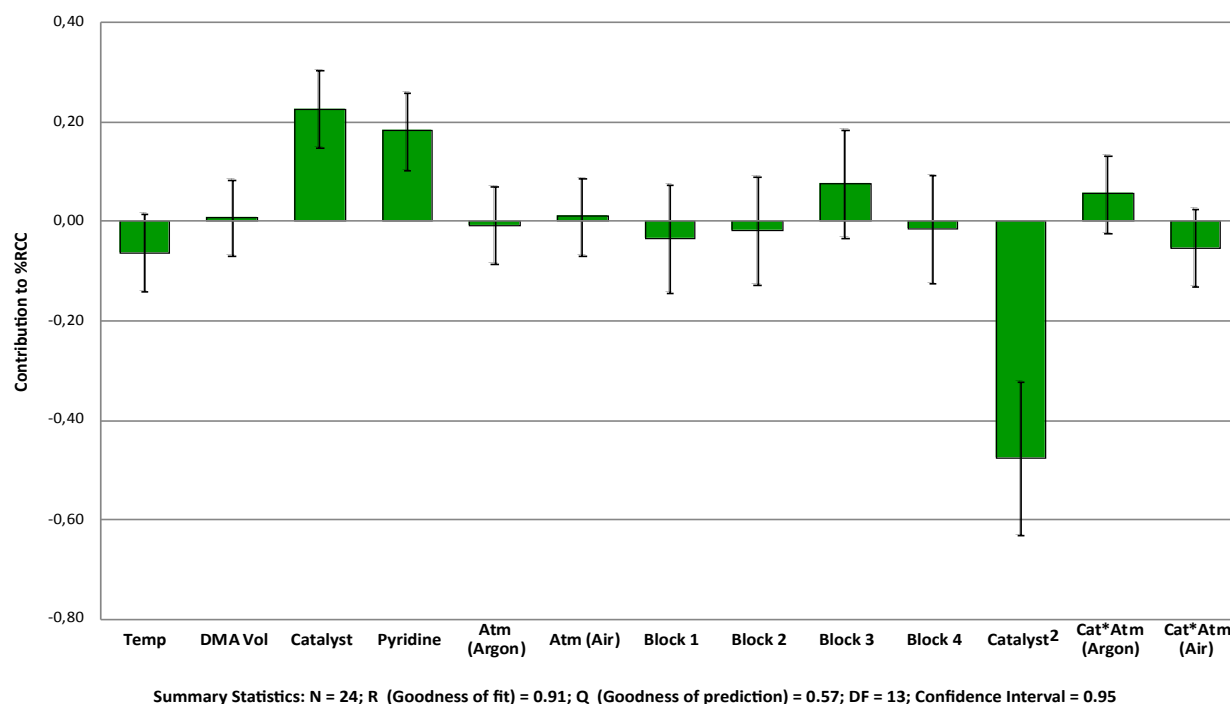


Figure 35: The normalized regression coefficients calculated from the results of the fractional factorial factor screening (RES V+) DoE study. The magnitude of the bar represents the magnitude of the contribution a factor has to the response (%RCC). If a factor's regression coefficient is smaller than the associated error bars it is unlikely that that factor is a significant contributor to the response (at the 95% confidence interval, $\alpha = 0.05$). This figure was adapted from the paper by Bowden *et al.*⁸⁶

Notably, the factor screening study found that, within the investigated factor ranges, the use of either argon or air as the reaction atmosphere did not have a significant effect on reaction performance. Performing this reaction under an oxidizing atmosphere (air) is not a requirement when using the stoichiometric quantities of $\text{Cu}(\text{OTf})_2$, as had been previously suggested by Zarrad *et al.*⁷⁴ This important conclusion means that this reaction can be performed in automated synthesis modules that are set up to operate using an inert carrier gas such as argon, nitrogen, or helium and that the often inconvenient modification of the synthesis module to operate using air is not necessary.

7.3.2 Response Surface Optimization of [¹⁸F]pFBC ([¹⁸F]8)

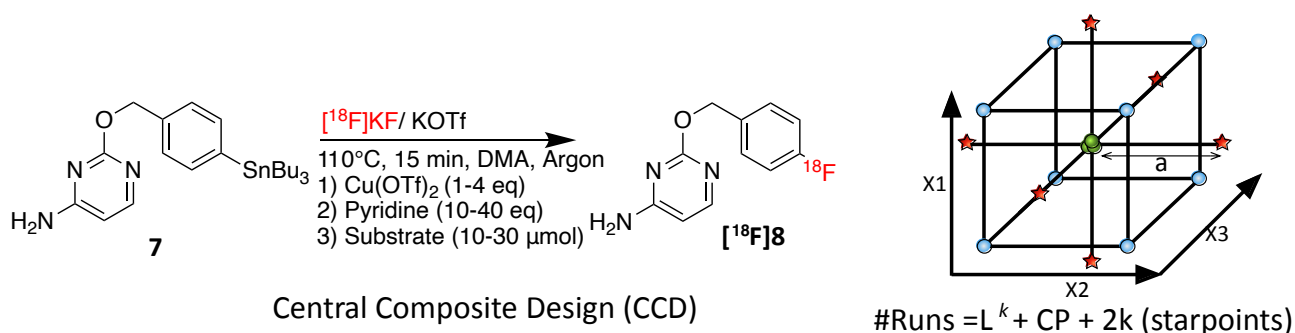
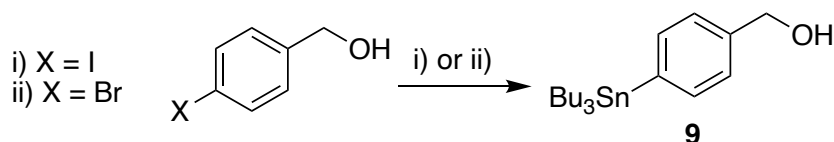


Figure 36: The late stage CMRF of [¹⁸F]8 ([¹⁸F]pFBC) was optimized using an orthogonal central composite (CCO) design with "a" scaled so as to ensure orthogonality throughout the design (Inset, Vide 4.2.2). This diagram has been adapted from Bowden *et al.*⁸⁶

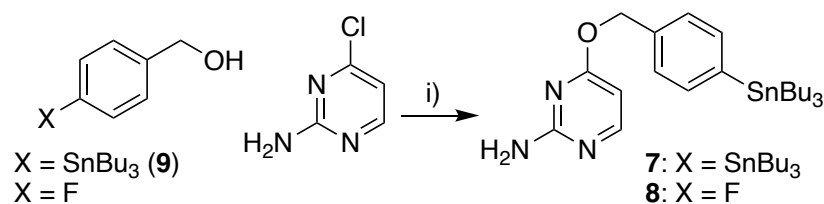
Having determined $\text{Cu}(\text{OTf})_2$ and pyridine loading to be significant factors affecting arylstannane CMRF reaction performance, a more detailed response surface optimization study was constructed to optimize the

radiofluorination of 2-((4-[^{18}F]fluorophenyl)methoxy)pyrimidine-4-amine ([^{18}F]pFBC, [^{18}F]**8**), a novel tracer that had suffered from poor synthesis performance when using published CMRF conditions (Figure 36).^{73,74} An orthogonal central composite (CCO) RSO study was constructed featuring 18 runs with 8 factorial point (Figure 36, inset: blue), 3 centerpoints (green), and 6 starpoints (red) to determine the optimal amounts of $\text{Cu}(\text{OTf})_2$ (1-4 eq), pyridine (10-40 eq), and the precursor 2-((4-(tributylstannyl)phenyl)methoxy)pyrimidine-4-amine (**7**) (10-30 μmol). $\text{Cu}(\text{OTf})_2$ and pyridine loads were calculated relative to the precursor amount used, and thus higher amounts of precursor would also equate to more concentrated reaction mixtures.



Scheme 4: Reagents and conditions: i) $\text{Pd}(\text{PPh}_3)_4$, Bis(tributyltin), LiCl , toluene, **9**: 57%; ii) 1) $n\text{-BuLi}$ (2.5 M in hexane), Tetrahydrofuran (THF), $-78\text{ }^\circ\text{C}$; 2) Bu_3SnCl , THF, $-78\text{ }^\circ\text{C}$ - room temperature, **9**: 56%.

The synthesis of the precursor **7** began with the production of (4-(tributylstannyl)phenyl)methanol **9** (Scheme 4). The synthon could not be sourced commercially and was thus synthesized from (4-(iodo)phenyl)methanol and bis(tributyltin) in the presence of $\text{Pd}(\text{PPh}_3)_4$ and lithium chloride (LiCl) in toluene via a reaction analogous to the Miyaura borylation (*vide* **8.2**).⁷³ This reaction was convenient and afforded the desired product in 57% yield; however, the cost of the reagents and the toxicity of bis(tributyltin) prompted an investigation into a more scalable synthetic route. **9** could thus be alternatively synthesized from (4-(bromo)phenyl)methanol through a two-step one-pot process that involved 1) a lithium-halogen exchange using $n\text{-BuLi}$ in THF at $-78\text{ }^\circ\text{C}$, followed by 2) the dropwise addition tributyltin chloride at $-78\text{ }^\circ\text{C}$.¹⁶⁷ After allowing the reaction to warm to room temperature over several hours, **9** could be isolated with a comparable and acceptable yield of 56%.



Scheme 5: Reagents and conditions: i) NaH , DMF or DMSO, room temperature- $100\text{ }^\circ\text{C}$, **7**: 63%, **8**: 93%.

7 was synthesized by adding the benzyl alcohol **9** dropwise to a suspension of NaH (60% in mineral oil) in DMSO (Scheme 5). Commercially available 2-chloro-4-aminopyridine was then reacted with the deprotonated **9** at $110\text{ }^\circ\text{C}$ for 2 hours to afford **7** with a moderate yield (63%), which after flash-chromatography, was isolated as thick oil which later crystallized. $^1\text{H NMR}$ and HPLC-MS ($[\text{M}]^+$ calculated for $\text{C}_{23}\text{H}_{37}\text{N}_3\text{OSn} = 491.20$; found $[\text{M}+\text{H}]^+$, 492.1) confirmed the formation and isolation of the desired product with sufficient purity for further radiochemical experiments. The non-radioactive standard compound **8** was synthesized through a similar procedure from 4-fluorobenzyl alcohol in a 93% yield and was later used to confirm compound identity in radiochemical experiments.

The 17 runs were performed according to the DoE worksheet (generated by *MODDE Go 12*) (Table 7), again using 80 μl aliquots of ^{18}F , which had been eluted from a QMA cartridge and dried by the same method described above. Each run was carried out at 110 $^{\circ}\text{C}$ for 15 minutes in a total reaction volume of 700 μl in DMA. After the formation of the regression model with MLR and the exclusion of non-significant model terms, the regression output summary statistics showed the model to have both a good fit ($R^2 = 0.97$) and predictive ability ($Q^2 = 0.91$), indicating a valid and useful model of the behavior of the reaction over the investigated factor ranges.

Table 7: Worksheet table containing the required experimental conditions and %RCC data for each run in the CCO RSO optimization study of [^{18}F]8. Experimental points are displayed in blue, starpoints are in red, and centerpoints are shown in green. All runs were performed in randomized order but, for clarity, are shown here according to the structure of the design. The table is taken from the paper by Bowden et al.⁸⁶

Exp No	Catalyst Load (eq)	Catalyst mmol	Catalyst Mass (mg)	Pyridine Load (eq)	Pyridine mmol	Pyridine Mass (mg)	Pyridine Vol (μl)	Substrate Load (μmol)	Substrate Mass (mg)	DMA total	DMA Vol (μl)	RCC
1	1	0.010	3.6	10	0.10	7.9	8.1	10	4.9	700	607	2.1
2	4	0.040	14.4	10	0.10	7.9	8.1	10	4.9	700	499	18.5
3	1	0.010	3.6	40	0.40	31.6	32.2	10	4.9	700	583	4.2
4	4	0.040	14.4	40	0.40	31.6	32.2	10	4.9	700	474	14.2
5	1	0.030	10.8	10	0.30	23.7	24.2	30	14.7	700	421	6.6
6	4	0.120	43.3	10	0.30	23.7	24.2	30	14.7	700	96	17.8
7	1	0.030	10.8	40	1.20	94.9	96.7	30	14.7	700	348	0.4
8	4	0.120	43.3	40	1.20	94.9	96.7	30	14.7	700	23	1.1
9	0.47031	0.009	3.4	25	0.50	39.6	40.3	20	9.8	700	528	2.7
10	4.5297	0.091	32.7	25	0.50	39.6	40.3	20	9.8	700	235	17.3
11	2.5	0.050	18.1	4.70305	0.09	7.4	7.6	20	9.8	700	414	9.4
12	2.5	0.050	18.1	45.297	0.91	71.7	73.0	20	9.8	700	349	1.5
13	2.5	0.016	5.8	25	0.16	12.8	13.0	6.46890	3.2	700	597	30.5
14	2.5	0.084	30.3	25	0.84	66.3	67.5	33.5313	16.4	700	166	5.9
15	2.5	0.050	18.1	25	0.50	39.6	40.3	20	9.8	700	381	11.4
16	2.5	0.050	18.1	25	0.50	39.6	40.3	20	9.8	700	381	15.0
17	2.5	0.050	18.1	25	0.50	39.6	40.3	20	9.8	700	381	21.3

All of the main factors were shown to contribute significantly to the performance of the reaction and, as suggested by the factor screening study, significant quadratic terms for both $\text{Cu}(\text{OTf})_2$ (Cat^2) and pyridine (Py^2) loading were detected (Figure 37, A). Interestingly, a strong factor interaction between the amount of precursor and the equivalents of pyridine used in the reaction was also shown to exist, whereby the optimal amount of pyridine required would change depending on the amount of precursor used in the synthesis. These model terms were used to plot a response surface that described how the reaction performance would vary as each of the three factors were adjusted (Figure 37, B).

The response surface showed that higher amounts of $\text{Cu}(\text{OTf})_2$ (3.5-4 eq relative to the precursor) were generally favorable. The reaction also performed best when a low amount precursor ($< 10 \mu\text{mol}$) was used and this, along with the precursor/pyridine factor interaction described above, dictated that 25 equivalents of pyridine were optimal. Thus, the optimal $\text{Cu}(\text{OTf})_2$ /pyridine ratio, in this case, was calculated to be $\approx 1:7$ when 10 μmol of precursor was used. These optimized conditions were then validated by performing three replicate experiments using 180 μl (400-500 MBq) aliquots of ^{18}F solution (eluted from the QMA cartridge). The resulting %RCCs of these validation runs were 24.9%, 25.3%, and 29.8% (27.6 ± 2.7 %RCC ($n = 3$)), which

were the highest and most reproducible results obtained thus far in the development of this synthesis for $[^{18}\text{F}]\mathbf{8}$.

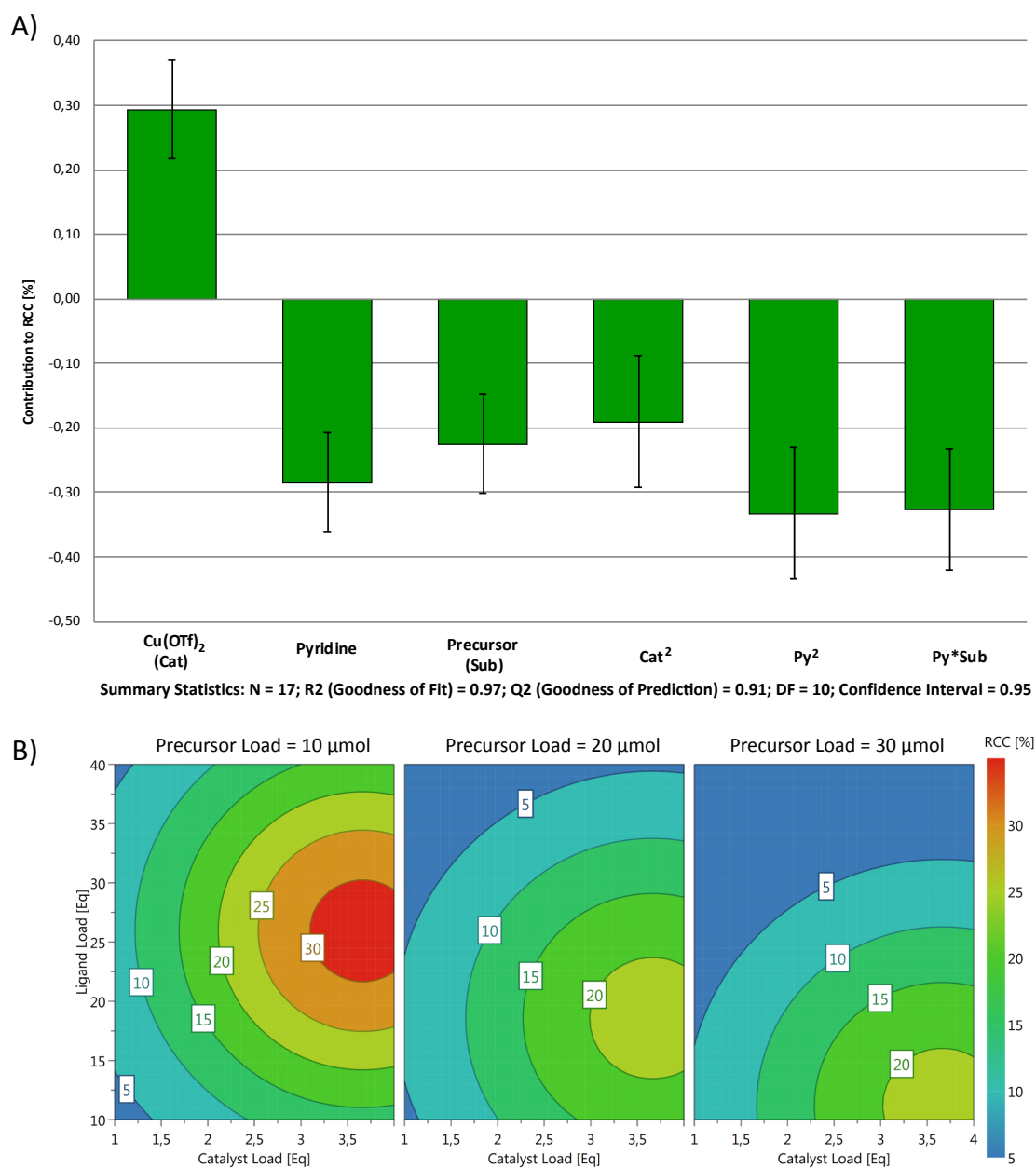


Figure 37: A) The normalized regression coefficients calculated from the results of the CCO RSO DoE study. The magnitude of the bar represents the magnitude of the contribution a factor has to the response (%RCC). If a factor's regression coefficient is smaller than the associated error bars, it is unlikely that that factor is a significant contributor to the response (at the 95% confidence interval). B) The response surface output (3D) from the CCO RSO of $[^{18}\text{F}]\mathbf{8}$ at three precursor (Sub) levels. This figure was adapted from the paper by Bowden et al.⁸⁶

7.3.3 Response Surface Optimization of [^{18}F]pFBnOH ([^{18}F]10)

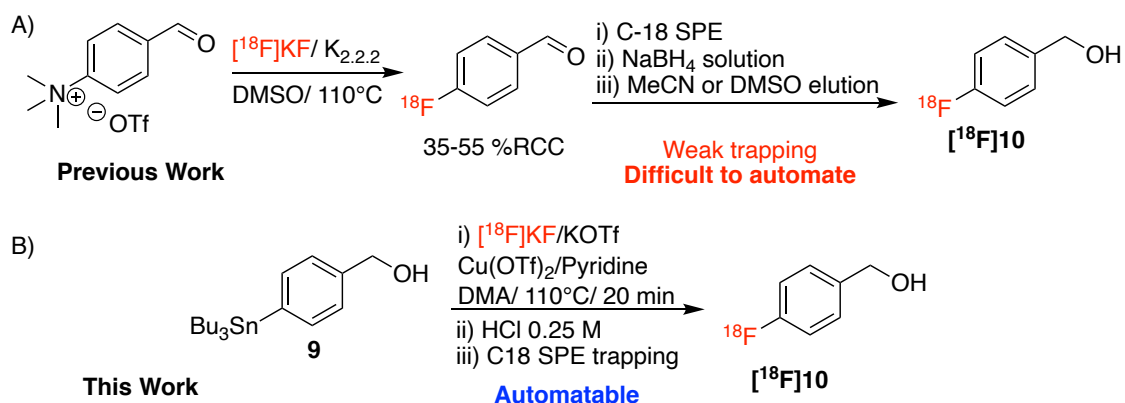


Figure 38: A) In our hands, the published synthesis of [^{18}F]10 failed to produce the desired synthon with a sufficient yield for use in a multistep radiosynthesis.^{168,169} B) A new single step approach was thus developed using CMRF chemistry.

4- ^{18}F fluorobenzyl alcohol ([^{18}F]pFBnOH, [^{18}F]10) is a synthon of interest for several ongoing multistep radiosynthesis projects in our laboratory as well as for the multistep synthesis of [^{18}F]F-BETP. Previously the synthesis of [^{18}F]10 has been accomplished via a 2-step procedure whereby [^{18}F]fluoride is reacted with 4-formyl-*N,N,N*-trimethylanilinium triflate via a nucleophilic aromatic substitution under standard radiochemical conditions (Figure 38, A).^{168,169} The resulting 4- ^{18}F fluorobenzaldehyde is then trapped on a C18 solid-phase extraction (SPE) cartridge, washed with water, then reduced on the cartridge with an aqueous solution of NaBH_4 . In our hands, the reduction step resulted in the loss of significant quantities of the trapped activity (>85%) in all likelihood due to the weak binding of the resulting [^{18}F]10 to the C18 SPE cartridge, which is prematurely eluted as the reducing solution is passed through the cartridge. Not only are the production of [^{18}F]10 ultimately unacceptably low for a multistep synthesis, this procedure is time-consuming and challenging to automate. We thus envisioned that a single-step and easily automatable production of [^{18}F]10 could be achieved via a CMRF of **9** with sufficient yield for use in extended multistep syntheses (Figure 38, B). Pilot experiments quickly demonstrated that such a route was possible and easily automatable and that the product [^{18}F]10 could be isolated with sufficient purity for use in subsequent synthetic steps using a series of SPE cartridges, barring the need for a complicated and time-consuming inter-step HPLC purification (*vide infra*).

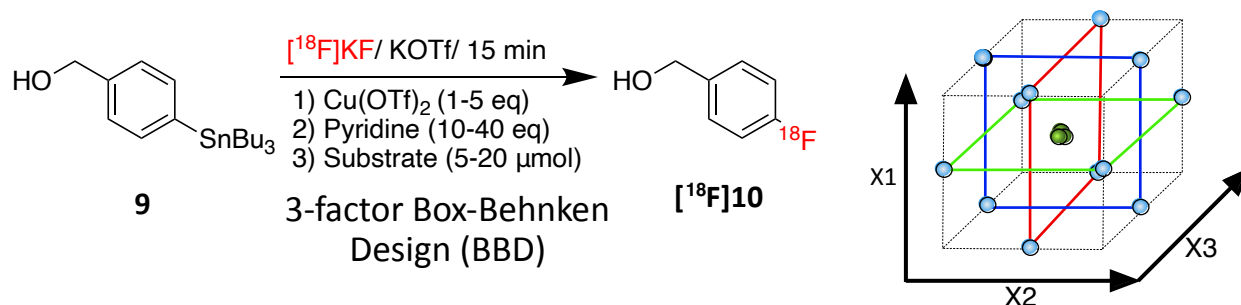


Figure 39: The CMRF of [^{18}F]10 was optimized using a Box-Behnken design (BBD) (Inset, *Vide 4.2.2*). This diagram has been adapted from Bowden et al.⁸⁶

A DoE study using a Box-Behnken design (BBD, *vide* 4.2.2) was thus constructed to again optimize the amounts of precursor **9** (5-20 μmol), $\text{Cu}(\text{OTf})_2$ (1-5 eq), and pyridine (10-40 eq) used in the synthesis of $[\text{}^{18}\text{F}]\text{10}$ (Figure 39). The 3-factor BBD required a total of 12 experimental points and 3 centerpoints (15 runs total). Each reaction was performed with a total reaction volume of 700 μl at 110 $^\circ\text{C}$ for 20 minutes. As before, 80 μl of ^{18}F (in the QMA eluent) was used and processed for each run separately. After the empirical data had been acquired and the DoE worksheet table (Table 8) completed, the data set was analyzed in *MODDE Go* 12. The resulting regression model summary statistics suggested the model to be both valid and useful ($R^2 = 0.96$; $Q^2 = 0.86$).

Table 8: Worksheet table containing the required experimental conditions and %RCC data for each run of the BBD RSO optimization study of $[\text{}^{18}\text{F}]\text{10}$. Experimental points are displayed in blue, and centerpoints are shown in green. All runs were performed in randomized order but, for clarity, are shown following the structure of the design. The table is taken from the paper by Bowden et al.⁸⁶

Exp No	Catalyst Load (eq)	Catalyst (mmol)	Catalyst Mass (mg)	Pyridine Load (eq)	Pyridine (mmol)	Pyridine Mass (mg)	Pyridine Vol (μl)	Substrate Load (μmol)	Substrate Mass (mg)	DMA total	DMA Vol (μl)	RCC
1	1	0.015	5.4	5	0.08	5.9	6.0	15	6.0	700	580	49.6
2	4	0.060	21.7	5	0.08	5.9	6.0	15	6.0	700	418	65.3
3	1	0.015	5.4	30	0.45	35.6	36.2	15	6.0	700	550	18.3
4	4	0.060	21.7	30	0.45	35.6	36.2	15	6.0	700	388	44.1
5	1	0.005	1.8	17.5	0.09	6.9	7.0	5	2.0	700	655	26.9
6	4	0.020	7.2	17.5	0.09	6.9	7.0	5	2.0	700	601	65.1
7	1	0.025	9.0	17.5	0.44	34.6	35.2	25	9.9	700	475	29.5
8	4	0.100	36.1	17.5	0.44	34.6	35.2	25	9.9	700	205	56.6
9	2.5	0.013	4.5	5	0.03	2.0	2.0	5	2.0	700	633	43.5
10	2.5	0.013	4.5	30	0.15	11.9	12.1	5	2.0	700	623	39
11	2.5	0.063	22.6	5	0.13	9.9	10.1	25	9.9	700	365	65.1
12	2.5	0.063	22.6	30	0.75	59.3	60.4	25	9.9	700	315	14.7
13	2.5	0.038	13.5	17.5	0.26	20.8	21.1	15	6.0	700	484	52.4
14	2.5	0.038	13.5	17.5	0.26	20.8	21.1	15	6.0	700	484	54.2
15	2.5	0.038	13.5	17.5	0.26	20.8	21.1	15	6.0	700	484	52.3

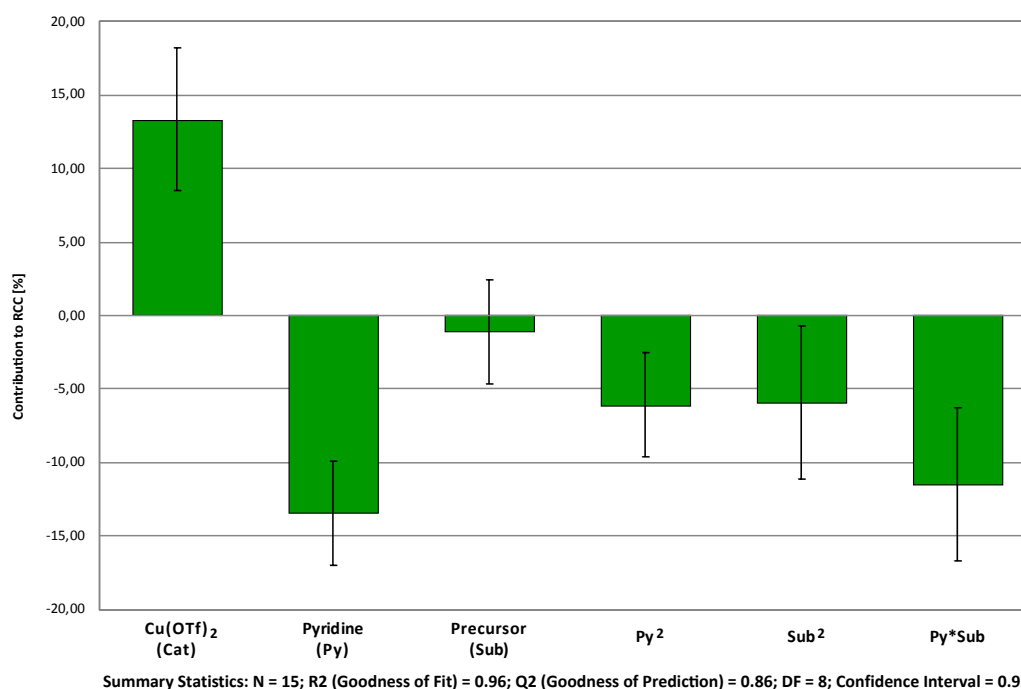


Figure 40: The normalized regression coefficients calculated from the results of the BBD RSO study. The magnitude of the bar represents the magnitude of the contribution that a factor has to the response (%RCC). If a factor's regression coefficient is smaller than the associated error bars, it is unlikely that that factor is a significant contributor to the response (at the 95% confidence interval). This figure was adapted from the paper by Bowden et al.⁸⁶

Analysis of the scaled and centered regression coefficients indicated that both the amount of $\text{Cu}(\text{OTf})_2$ (Cat) and pyridine (Py) had significant effects on the %RCC, while, unexpectedly, the amount of precursor (Sub) was not a significant contributor (Figure 40). The precursor term was nonetheless included in the final regression model for completeness as it was a main effect. The amount of pyridine displayed a significant quadratic term, as did the amount of precursor (the Sub^2 term could not be considered significant as the precursor's main effect term was non-significant but was included to provide a better fitting regression model). Additionally, an inverse factor interaction between the amount of pyridine and substrate was also detected.

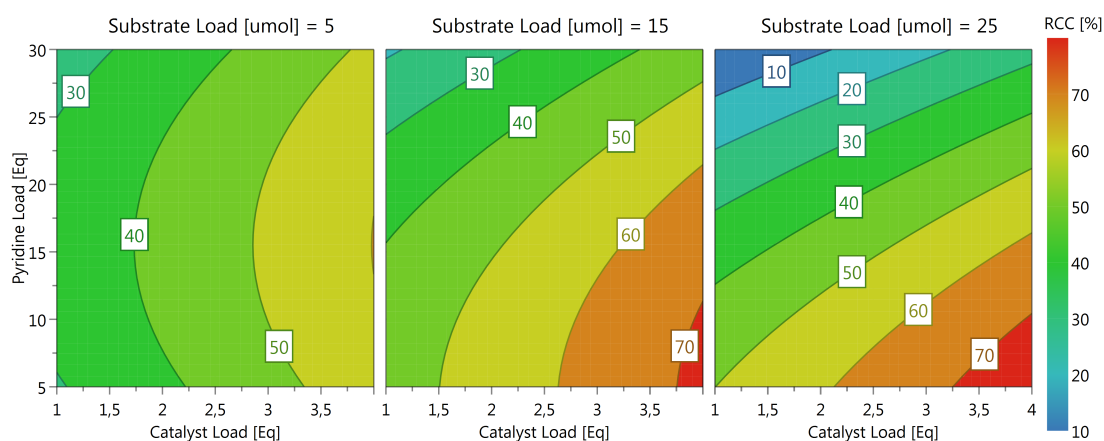


Figure 41: The response surface output (3D) from the BBD RSO of $[^{18}\text{F}]\mathbf{10}$ at three precursor (Sub) levels. This figure was adapted from the paper by Bowden et al.⁸⁶

The resulting response surface plot (Figure 41) showed that high amounts of $\text{Cu}(\text{OTf})_2$ were beneficial to maximizing %RCC (as was determined by the factor screening study and the RSO of $[^{18}\text{F}]\mathbf{8}$). The reaction was also (non-significantly) favored by higher amounts of precursor and minimal amounts of pyridine. Within the factor ranges investigated in this study, the optimal $\text{Cu}(\text{OTf})_2$ /pyridine ratio was calculated to be $\approx 1:1$, a substantial difference from the calculated 1:7 ratio optimal for the production of $[^{18}\text{F}]\mathbf{8}$. Using the optimal conditions predicted by the response surface, three validation experiments were again carried out using 180 μl aliquots of the ^{18}F solution eluted from the QMA. These experiments were able to reliably produce $[^{18}\text{F}]\mathbf{10}$ in a single step with an acceptable %RCC of $58 \pm 5.3\%$ ($n = 4$), avoiding the substantial losses of activity experienced when using the previously published synthesis. These results were, however, lower than the expected outcome predicted by the response surface model. This may be due to unmodeled effects from unidentified uncontrollable/controllable experimental factors or inaccuracies in the data or model brought about through either random or systematic experimental error.

7.4 The Development of Improved ^{18}F Processing Conditions for CMRF Reactions.

The results of both of the above RSO studies were used to guide decision making and aided the development of automated radiosynthesis of both $[^{18}\text{F}]\mathbf{8}$ and $[^{18}\text{F}]\mathbf{10}$, the latter used successfully in a multistep synthesis. However, as noted previously, the effect of the contents of the QMA eluent has also been shown to

contribute to the performance of CMRF chemistry, especially at large reaction scales. Indeed, when full batches (550 μl) of the Scott QMA eluent A were used during automated large-scales syntheses of both compounds, reaction performance was substantially reduced ($< 4\%$ RCC for [^{18}F]**8**). The deleterious effects associated with the higher amounts of basic CO_3^{2-} (typical in standard QMA Eluents) and HCO_3^- anions (introduced during preconditioning of the QMA cartridge) present in single batch QMA cartridge elutions, was a significant limitation of the aforementioned DoE studies. This led to the acquisition of relatively inflated %RCC results when only small (80 μl) aliquots of a full batch (550 μl) of QMA elution were used.

The DoE studies discussed above were conducted to address the specific experimental factors involved in the CMRF reactions themselves, and thus we saw the issues associated with the ^{18}F processing to be a separate problem that could be addressed independently. (i.e., we hypothesized that the effects modeled by the DoE studies were not influenced by the ^{18}F processing method via a significant factor interaction (reaction factors*QMA factors)). Comparing the above DoE studies to the existing OVAT optimization data published by Makaravage *et al.* and Zarrad *et al.* showed that, where directly comparable, the two optimization approaches yielded results with remarkably similar trends.^{73,74,86} While the absolute %RCC values differ significantly, in all likelihood due to the superior ^{18}F processing method used by Zarrad *et al.* (*vide 7.2*), the influence of the $\text{Cu}(\text{OTf})_2$ and precursor loading factors showed comparable quadratic behaviors and optima locations in both their OVAT and our DoE studies. The comparability of these optimization results, obtained using two very different ^{18}F processing methods, lends further weight to our hypothesis that the issues of ^{18}F processing and reaction condition optimization can be addressed separately.

Table 9: A selection of published ^{18}F processing conditions that have been applied for CMRF tracer synthesis.

Method Name	Cartridge	Preconditioning Anion	Loading Direction	Salt/PTC	Base	QMA Wash	Elution Solvent	Vol (μl)	Reference
"Standard"	QMA	HCO_3^-	Forward	K_{222} (15 mg)	K_2CO_3 (3 mg)	NA	$\text{MeCN}:\text{H}_2\text{O}$ (4:1)	1000	Tredwell <i>et al.</i> ⁶⁷
"Low Base"	QMA	HCO_3^-	Forward	K_{222} (270 μg)	K_2CO_3 (60 μg)	NA	$\text{MeCN}:\text{H}_2\text{O}$ (4:1)	1000	Zaltopolskiy <i>et al.</i> ⁶⁸
Scott A	QMA	HCO_3^-	Forward	KOTf (10 mg)	K_2CO_3 (50 μg)	NA	H_2O	550	Mossine <i>et al.</i> ⁷⁰
Scott B	QMA	OTf	Forward	KOTf (10 mg)	K_2CO_3 (50 μg)	NA	H_2O	550	Makaravage <i>et al.</i> ⁷³
Scott C	QMA	OTf	Forward	TBAOTf (10 mg)	Cs_2CO_3 (50 μg)	NA	H_2O	550	Mossine <i>et al.</i> ¹⁷⁰
"Minimalist" (Alcohol enhanced)	QMA	HCO_3^-	Reverse	Et_4NHCO_3 (2.7 mg)	NA	MeOH (1 ml)	<i>n</i> -BuOH	400	Zischler <i>et al.</i> ^{71,74}
Zhang	PS- CO_3	HCO_3^-	Forward	DMAPOTf (10 mg)	NA	MeCN (6 ml)	DMA or DMF	1000	Zhang <i>et al.</i> ¹⁷¹

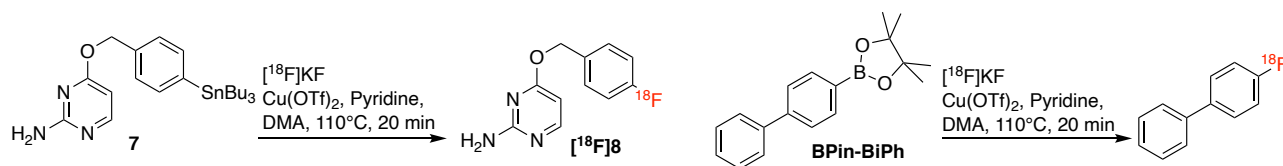
An ideal set of ^{18}F processing conditions would have to: i) have a minimal impact on the performance of the CMRF reaction, ii) allow for a reasonable %recovery of the ^{18}F from the QMA cartridge, and iii) be operationally simple (easily automatable) and time efficient. In order to address these issues, we began a literature review of established QMA and ^{18}F processing conditions (Table 9): The "Standard" and "low base"

^{18}F processing QMA conditions were not viable for large-scale CMRF reactions due to their adverse effects on reaction performance, the latter also yielding an inadequate release of the ^{18}F from the QMA cartridge (< 50% ^{18}F recovery). The Scott A QMA cartridge conditions were successfully used in small aliquots during our preliminary DoE studies but, as discussed above, resulted in poor reaction performance at large scales (Table 10, entry 1). Modified versions of this protocol (Table 9: Scott B, C; Table 10: entry 2) were also able to release the ^{18}F from the QMA resin with excellent efficiency (> 95% ^{18}F recovery); however, they afforded only marginal improvements in %RCC when used with a CMRF of a model compound.

The “minimalist” approach (alcohol-enhanced CMRF) by Zischler *et al.*⁷¹ (later refined for CMRFs of arylstannanes by Zarrad *et al.*)⁷⁴ has become a popular ^{18}F processing approach as it allows for good “single batch” CMRF reaction performance. However, the method is operationally complex, as the ^{18}F must be loaded onto the QMA cartridge in the reverse direction and then washed and eluted in the forward direction. Any automated synthesis module performing this procedure must be modified to switch the direction of the fluid path through the QMA cartridge. Additionally, the method reduces the QMA cartridge’s capacity to remove impurities from the cyclotron target water. The method by Zhang *et al.* mitigates the need for such inconvenient modifications by using a DMA stable PS-CO₃ QMA resin, which can be loaded and eluted in the forward direction using the reaction solvent. However, the factory-conditioned PS-CO₃ cartridges also introduce HCO₃⁻ ions into the reaction mixture and thus negatively affect reaction performance.¹⁷¹

Inspired by these latter two approaches, we tested several “single batch” ^{18}F processing conditions with the aim of developing a protocol that satisfied the three constraints of ^{18}F recovery, CMRF reaction performance, and operational simplicity (Table 10). To reduce the amount of carbonate and bicarbonate ions present in the reaction mixture, we preconditioned the QMA cartridge with KOTf (90 mg/ml, 10 ml) to produce QMA-OTf form cartridges (as performed by Makaravage *et al.*) These cartridges were able to efficiently trap [^{18}F]fluoride from a cyclotron target wash (> 95% trapping). The Scott A conditions were able to efficiently elute ^{18}F from the cartridge; however, when applied to the DoE optimized synthesis of [^{18}F]8 after a lengthy azeotropic drying step, the %RCC was, as expected, much lower than predicted (Table 10, entry 1). Using Scott eluent C (Table 9), it was confirmed that tetrabutylammonium triflate (TBAOTf) in combination with Cs₂CO₃ was able to elute the ^{18}F and was compatible with the CMRF reaction conditions (Table 10, entry 2). Unexpectedly, it was later found that a carbonate base was not required at all to elute the ^{18}F from the QMA cartridge, with lower amounts of the TBAOTf elution salt being beneficial to the performance of the reaction (Table 10, entries 3,4).

Table 10: A selection of test reactions carried out to test improved full-batch ^{18}F processing conditions and measure their effects on CMRF reaction performance.



Entry	Cartridge	^{18}F Loading Direction	Eluent Salt	Base	Solvent	Vol (μl)	% ^{18}F recovery	Azeotropic drying	%RCC (Precursor)
1	QMA-OTf	Forward	KOTf (10 mg)	K_2CO_3 (50 μg)	water	550	95%	Yes (3 x MeCN)	4-7% (7)
2	QMA-OTf	Forward	TBAOTf (10 mg)	Cs_2CO_3 (50 μg)	water	550	93%	Yes (3 x MeCN)	37% (Bpin-BiPh)
3	QMA-OTf	Forward	TBAOTf (10 mg)	None	water	550	92%	Yes (3 x MeCN)	29% (Bpin-BiPh)
4	QMA-OTf	Forward	TBAOTf (5 mg)	None	water	550	91%	Yes (3 x MeCN)	36% (Bpin-BiPh)
5	QMA-OTf	Forward	TBAOTf (10 mg)	None	MeOH	1000	83%	Evaporation	39% (Bpin-BiPh)
6	QMA-OTf	Forward	TBAOTf (10 mg)	None	MeOH	1000	85%	Evaporation	29% (7)

We next attempted to utilize a protocol for ^{18}F elution that was similar to the alcohol enhanced conditions published by Zischler *et al.* After loading the ^{18}F onto the QMA-OTf cartridge via the usual method (forward, female end) and washing with 1 ml of MeOH to remove any residual water from the QMA resin, we were delighted to find that TBAOTf (10 mg) in MeOH (1ml) possessed enough eluting power to recover $\approx 85\%$ of the ^{18}F from the QMA cartridge (when calculated from the initial amount of ^{18}F trapped on the QMA) (Table 10, entry 5,6). Moreover, this protocol removed the need for a lengthy azeotropic drying procedure as the methanol eluent solvent could be rapidly evaporated from the reaction vessel to afford dry ^{18}F TBAF, saving a significant amount of overall synthesis time (> 20 min). This not only reduced the activity losses often experienced during azeotropic drying (due to the volatility of ^{18}F HF) but also reduced the amount of activity lost due to radioactive decay, offsetting the slightly lower ^{18}F %recovery obtained using this method. When this protocol was applied to the batch synthesis of ^{18}F pFBC using the reaction conditions predicted by the RSO study (*vide supra*, **8.3.2**), the reaction was able to produce the radiofluorinated product with 29 %RCC, a result closely aligned with the maximized %RCC predicted by the regression model (Table 10, entry 6).

These preliminary results suggest that our hypothesis may be true; that the optimal reaction parameters for a CMRF reaction are not heavily influenced by the ^{18}F processing method and that the results of our previous DoE optimization studies are valid despite our use of the “aliquot” method. This is an important conclusion as it means that the large numbers of experimental runs required to optimize the synthesis of a new radiotracer do not have to be conducted on a “batch scale” in order to be valid (contrary to the current opinion in the radiochemical community). As discussed above, when multiple experiments need to be performed, the use of a number of small aliquots of ^{18}F solution from a single homogenous batch QMA elution is far more practical in terms of time, cost, and the minimization of random experimental error, than processing a whole batch of ^{18}F for each individual run.

7.5 DoE Optimization of the CMRF of Arylboronic Acid Pinacol Esters.

Since the CMRF of arylboronic acids and their pinacol esters were disclosed in the seminal papers by Mossine *et al.* and Tredwell *et al.* respectively, they have become popular substrates for CMRF based tracer syntheses due to the wide variety of stable and easy-to-handle commercially available synthons for precursor synthesis. With an improved set of ^{18}F processing conditions, we chose to investigate the optimal parameters required for the synthesis of $[^{18}\text{F}]\mathbf{10}$ from an arylboronic acid pinacol ester precursor. Working from our previous experiences with CMRF chemistry and the information obtained through our previous DoE studies, were selected to optimize the CMRF of $[^{18}\text{F}]\mathbf{10}$ from 4-(hydroxymethyl)phenylboronic acid pinacol ester (4-BPin-BnOH) with respect to substrate (5-30 μmol), pyridine (25-550 μmol) and $\text{Cu}(\text{OTf})_2$ (4-40 μmol) loading. Given reports on the reaction performance-enhancing properties of alcoholic co-solvents when using arylboronate precursors, the addition of *n*-butanol (*n*-BuOH) was also investigated as a 4th factor (0-75% of the total reaction volume).^{71,74} The choice of this factor range meant that the investigated reaction space was constrained and irregular and was thus inappropriate for the use of CCD or BBD RSO designs (the %*n*-BuOH cannot be set < 0% when starpoints are used). For this reason, a computer-generated D-optimal design was constructed using the algorithm available with *MODDE Go 12* (Figure 42). Pilot experiments had also demonstrated that in this case, the CMRF reaction performed better under air at 110 °C for 15 minutes with a total reaction volume of 700 μl .

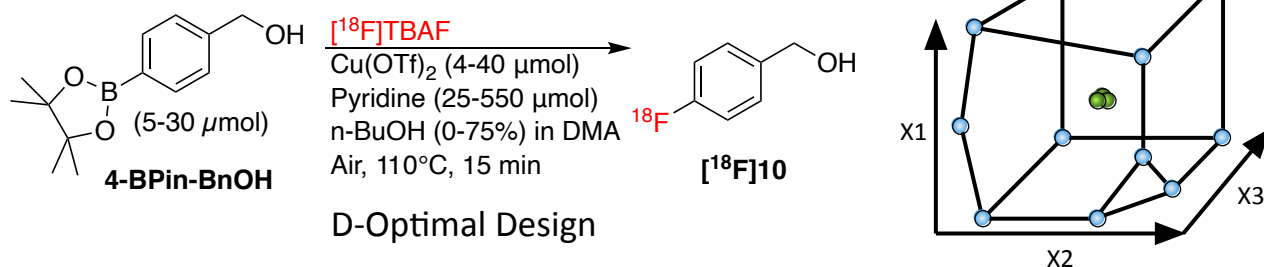
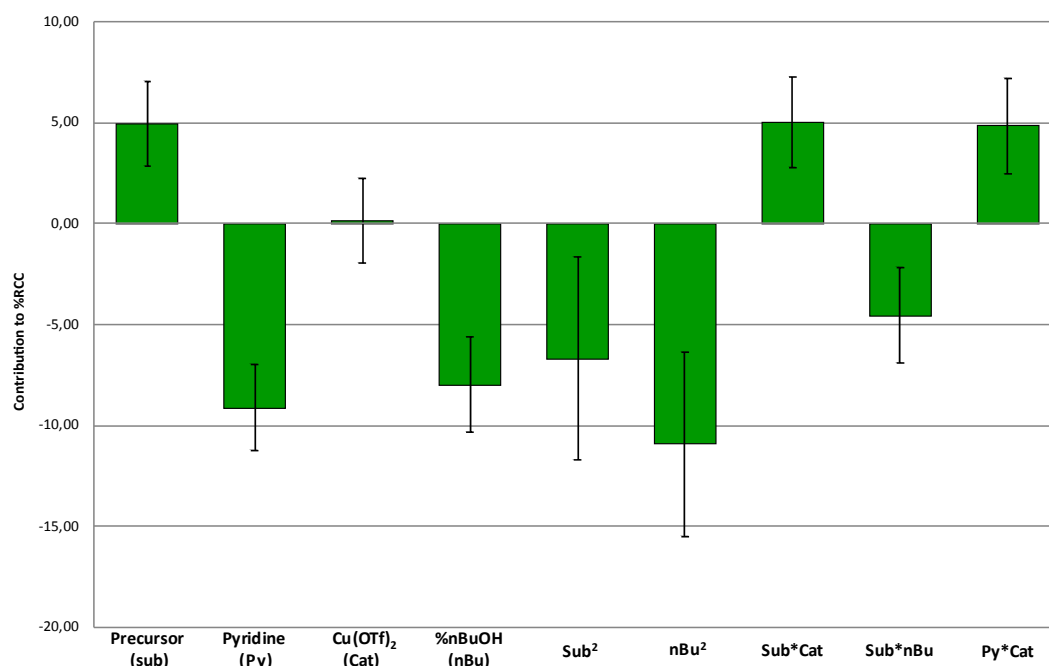


Figure 42: The CMRF of $[^{18}\text{F}]\mathbf{10}$ from (4-BPin-BnOH) was optimized using a D-optimal design (Inset, Vide 4.2.2).

The D-optimal DoE study was conducted over 4 days (6 runs per day) using the newly developed ^{18}F processing method discussed above: $[^{18}\text{F}]\text{Fluoride}$ from a cyclotron target wash was trapped, washed with MeOH (1 ml), and eluted from a QMA-OTf cartridge and each DoE run was performed using 150 μl aliquots of the eluted $[^{18}\text{F}]\text{TBAF}$ MeOH solution. The MeOH was then removed by evaporation under a stream of argon at 85 °C for 3 min without further azeotropic drying, and the reaction mixture required by the DoE worksheet table was then added to the $[^{18}\text{F}]\text{TBAF}$ residue. After each run in the DoE worksheet table had been performed (Table 11), MODDE Go 12 was used to analyze the data and fit a regression model. Analysis of the normal probability plot of residuals of the complete data set (not shown) revealed one run (Table 11, 17) to be a possible outlier. The exclusion of this data point resulted in improved model statistics ($R^2 = 0.96$; $Q^2 = 0.89$), suggesting a valid and predictive model.

Table 11: Worksheet table containing the required experimental conditions and %RCC data for each run of the D-optimal RSO optimization study of [18F]10. Experiment 17 was found to be a possible outlier and was excluded from the dataset. Replicate experiments are highlighted in green. The data were acquired by Nantanat Chailanggar.

Exp No	Cu(OTf) ₂ (μ mol)	Cu(OTf) ₂ (mg)	Pyridine Load (μ mol)	Pyridine (mg)	Pyridine (μ l)	Precursor Load (μ mol)	Precursor (mg)	n-BuOH (%)	n-BuOH (μ l)	RXN Vol (μ l)	%RCC
1	5.0	1.8	550.0	43.5	44.2	5.0	1.2	0.0	0	700	13.1
2	40.0	14.4	25.0	2.0	2.0	5.0	1.2	0.0	0	700	12.8
3	40.0	14.4	550.0	43.5	44.2	5.0	1.2	0.0	0	700	11.3
4	40.0	14.4	550.0	43.5	44.2	30.0	7.0	0.0	0	700	37.3
5	5.0	1.8	550.0	43.5	44.2	5.0	1.2	75.0	525	700	0.1
6	40.0	14.4	25.0	2.0	2.0	5.0	1.2	75.0	525	700	14.2
7	40.0	14.4	550.0	43.5	44.2	5.0	1.2	75.0	525	700	1.7
8	40.0	14.4	550.0	43.5	44.2	30.0	7.0	75.0	525	700	12.7
9	5.0	1.8	25.0	2.0	2.0	5.0	1.2	25.0	175	700	43.1
10	5.0	1.8	25.0	2.0	2.0	30.0	7.0	50.0	350	700	41.7
11	40.0	14.4	25.0	2.0	2.0	30.0	7.0	25.0	175	700	49
12	16.7	6.0	25.0	2.0	2.0	30.0	7.0	0.0	0	700	46.6
13	28.3	10.2	25.0	2.0	2.0	30.0	7.0	75.0	525	700	18.8
14	5.0	1.8	550.0	43.5	44.2	30.0	7.0	25.0	175	700	20.5
15	5.0	1.8	200.0	15.8	16.1	30.0	7.0	0.0	0	700	32.9
16	5.0	1.8	375.0	29.6	30.2	30.0	7.0	75.0	525	700	0.7
17	5.0	1.8	25.0	2.0	2.0	21.7	5.1	0.0	0	700	31.9
18	5.0	1.8	25.0	2.0	2.0	13.3	3.1	75.0	525	700	32.9
19	22.5	8.1	287.5	22.7	23.1	5.0	1.2	37.5	262.5	700	21
20	22.5	8.1	550.0	43.5	44.2	17.5	4.1	37.5	262.5	700	22.4
21	40.0	14.4	287.5	22.7	23.1	17.5	4.1	37.5	262.5	700	36.6
22	22.5	8.1	287.5	22.7	23.1	17.5	4.1	37.5	262.5	700	33.4
23	22.5	8.1	287.5	22.7	23.1	17.5	4.1	37.5	262.5	700	41.1
24	22.5	8.1	287.5	22.7	23.1	17.5	4.1	37.5	262.5	700	41.7



Summary Statistics: N = 23; R² (Goodness of Fit) = 0.96; Q² (Goodness of Prediction) = 0.89; DF = 8; Confidence Interval = 0.95

Figure 43: The normalized regression coefficients calculated from the results of the D-optimal RSO DoE study. The magnitude of the bar represents the magnitude of the contribution a factor has to the response (%RCC). If a factor's regression coefficient is smaller than the associated error bars, it is unlikely that that factor is a significant contributor to the %RCC (at the 95% confidence interval).

Unexpectedly, analysis of the regression coefficients showed that, over the investigated range, the amount of Cu(OTf)₂ (Cat) present in the reaction mixture had no significant contribution to the reaction performance; however, both the quantities of the substrate and pyridine were found to be significant factors. The presence

of *n*-BuOH was found to have a significant and quadratic effect on reaction performance. The amount of substrate also showed a quadratic behavior, as well as a factor interaction with the Cu(OTf)₂ loading and the amount of *n*-BuOH co-solvent. Pyridine was found to have a negative contribution to reaction performance as well as a factor interaction with the Cu(OTf)₂.

Plotting the 4D response surface suggested a precursor load of $\approx 19 \mu\text{mol}$, a pyridine load of $25 \mu\text{mol}$, and a Cu(OTf)₂ load of $5 \mu\text{mol}$. The presence of *n*-BuOH as a percentage of the total reaction volume (in DMA) was found to be optimal at 23%. The optimal Cu(OTf)₂:pyridine ratio was calculated to be 1:4, which is the ratio of the commercially available catalyst ([Cu(II)(OTf)₂Py₄]) used by Tredwell *et al.*, Zaltopolskiy and Zischler *et al.* and others^{67–69,71} However, it is important to note that both the pyridine and Cu(OTf)₂ loading factors are optimum at the extreme minima of their investigated ranges, and thus the true optimal Cu(OTf)₂:pyridine ratio may lie outside of the reaction space investigated here.

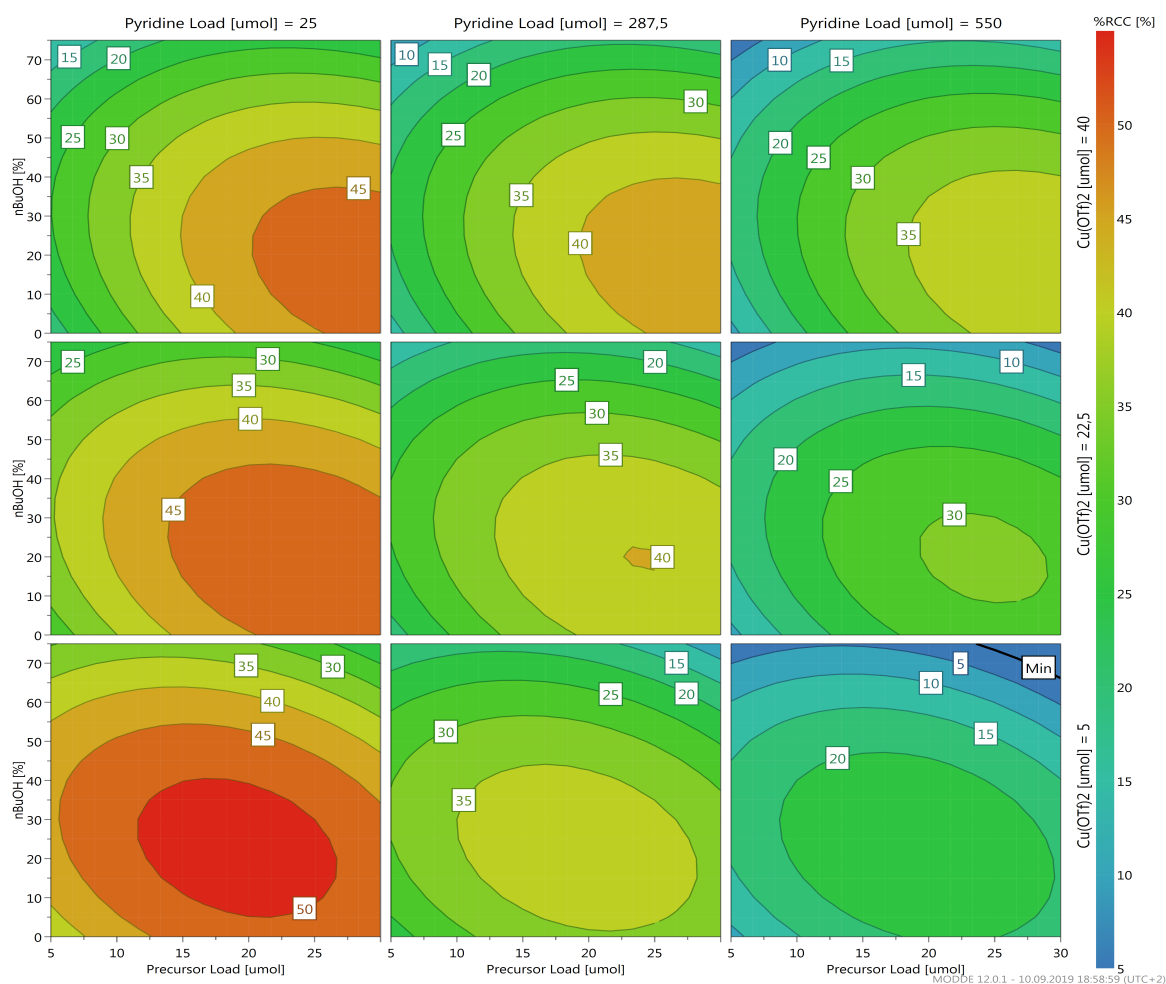
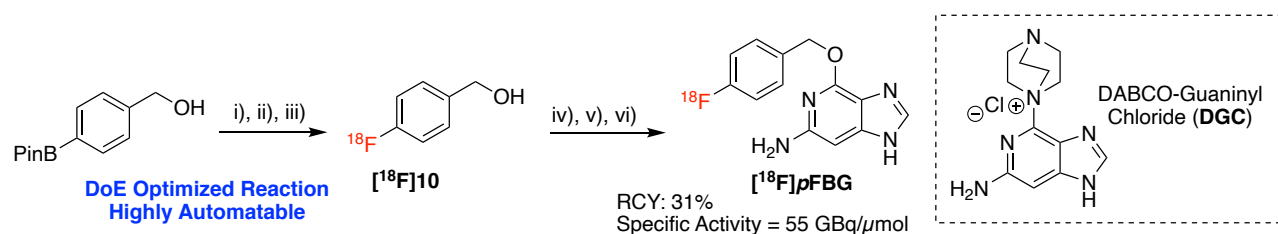


Figure 44: The response surface output (4D) from the D-optimal RSO of [¹⁸F]10 from an arylboronic acid pinacol ester precursor with respect to %*n*-BuOH and precursor load at three pyridine (horizontal) and three Cu(OTf)₂ levels (vertical).

The optimal reaction composition parameters derived from the RSO study were validated by performing the radiosynthesis in triplicate; however, instead of using aliquots of ¹⁸F solution from a single QMA cartridge elution, a separate QMA cartridge and a full batch of QMA eluent were used for each run. Validation runs

performed under an inert atmosphere produced the expected product in 7.7 ± 3 %RCC ($n = 3$), while the same experiments carried out under air afforded the product in excellent radiochemical conversions (65 ± 8 %RCC ($n = 3$)). These results demonstrate the importance of air to the performance of the CMRF when using arylboronic acid ester precursors. These results were slightly higher than the results predicted by the response surface model, and this may be due to several uncontrolled experiment factors in the experimental setup or through other model inaccuracies. Nonetheless, these conditions allowed for the reliable production of [^{18}F]10 in improved radiochemical yields for use in both the manual and automated syntheses of a variety of novel PET tracers under development in our laboratory (Scheme 6, this synthesis falls outside of the scope of this thesis and will not be discussed further, it is included here to exemplify the use of [^{18}F]10 as an important radiochemical synthon). Comparable %RCCs were obtained when using an arylboronic acid precursor with the same reaction conditions (data not shown).



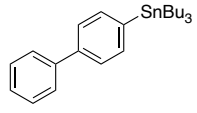
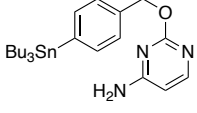
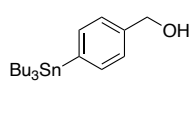
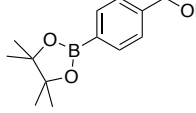
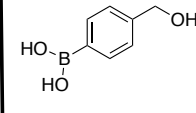
Scheme 6: An improved two-pot synthesis of [^{18}F]pFBG, a novel reporter gene tracer under development in our laboratory, relies on the efficient production of [^{18}F]10 through a CMRF reaction. Reagents and conditions: i) [^{18}F]TBAF, $\text{Cu}(\text{OTf})_2$, pyridine, DMA, 110 °C, 20 min; ii) HCl (0.25 M); iii) C18 SPE trapping and elution with Et_2O ; iv) SEP-PAK Dry cartridge (Na_2SO_4); v) DGC, NaH, DMSO, 70 °C, 20 min; vi) Semiprep-HPLC purification. This synthesis has been fully automated using an Elixys FLEX/CHEM synthesizer and PURE/FORM purification module.

7.6 Summary and Discussion

Comparing the two response surfaces obtained for [^{18}F]8 and [^{18}F]10 showed that the two syntheses have differing requirements concerning the optimal loadings of precursor and pyridine, while higher concentrations of $\text{Cu}(\text{OTf})_2$ were beneficial in both cases. [^{18}F]8 can be more effectively produced if lower amounts of precursor are used while the opposite is true for [^{18}F]10. The synthesis of [^{18}F]8 also has an optimal $\text{Cu}(\text{OTf})_2$:pyridine ratio of $\approx 1:7$ at low precursor concentrations. The formation of [^{18}F]10, however, is favored by minimizing the amount of pyridine resulting in a $\text{Cu}(\text{OTf})_2$:pyridine ratio of $\approx 1:1$ (over the ranges investigated). These differences between the two response surface models suggest that the nature of the precursor has a marked influence on the factor requirements for the reaction, particularly with respect to the pyridine load. Thus, each new precursor developed for use with this methodology must be optimized separately as no unified set of truly optimal reaction conditions is likely to exist. Several published reaction scope studies have previously identified that Lewis-basic amine and heterocyclic moieties (as present in 7, the precursor to [^{18}F]8) can have varying deleterious effects on CMRF reaction performance, possibly due to the formation of unreactive $\text{Cu}(\text{OTf})_2$ /precursor complexes. As the $\text{Cu}(\text{OTf})_2$ mediator is in a reversible equilibrium with its ligands, higher pyridine (or other ligand) concentrations may help to reduce the formation of unreactive $\text{Cu}(\text{OTf})_2$ /precursor complexes.

Taylor *et al.* studied the effect of a large number of drug-like moieties on the CMRF of arylboronic acid esters by performing reactions with a model compound under a unified set of reactions conditions while doping each reaction mixture with the moiety of interest.¹⁷² The authors were thus able to generate an extensive database of moieties and functional groups common in drug-like structures that were tolerated (or not-tolerated) by their CMRF chemistry. They were then able to use their database to plan and carry out the synthesis of complex radiotracers using CMRF chemistry by avoiding problematic moieties, introducing them after the radiolabeling, or by mitigating their influence through protecting group strategies. Using a DoE approach when studying the effects of specific reaction substrates when using new radiochemical methodologies may provide valuable mechanistic and practical information. This information, in combination with a database such as the one developed by Taylor *et al.*, would allow radiochemists to quickly identify the most feasible direct and productive radiosynthetic strategy early-on in a tracer's development, saving both time and resources.

Table 12: A summary of the results obtained by the DoE based optimization studies discussed above.

Investigated Factors	Substrate Type				
	Aryl Stannanes (Ar-SnR ₃)			Aryl Boronates (Ar-B(OR) ₂)	
					
Temperature (110-140°C)	NS	NS ^b	NS ^b	NS ^b	NS ^b
DMA Vol (400-1500 µl)	NS	NS ^b	NS ^b	NS ^b	NS ^b
Atmosphere (Air/Argon)	NS	NS	NS	Sig. Air	Sig. Air
Precursor Load	Unknown ^c	Sig. Minimize	NS Maximize	Sig. 19 µmol	Sig. 19 µmol
Pyridine	Sig. Minimize	Sig. 25 eq	Sig. Minimize	Sig. Minimize	Sig. Minimize
Cu(OTf) ₂	Sig. Maximize	Sig. Maximize	Sig. Maximize	NS	NS
% n-BuOH	NS ^d	NS ^d	NS ^d	Sig. 22%	Sig. 22%

NS = Not significant Sig. = Significant

a: Optimal conditions inferred from the analogous CMRF of BPin-BnOH. b: Inferred from the initial factor screening study. c: Not measured in the initial factor screening study. d: observed and discussed by Zarrad *et al.*⁷⁴

When comparing the experimental factors significant to the performance of the CMRF of either arylstannanes or arylboronates, several characteristic differences can be observed (Table 12). In all instances investigated here, the CMRF of arylstannanes benefits from higher loads of Cu(OTf)₂, while this factor is non-significant when using arylboronates. Additionally, the reaction atmosphere is a non-significant factor when

using arylstannane precursors, while the presence of air is vital to reaction performance when using arylboronates. The reaction, therefore, behaves differently, with respect to the oxidation cycle of the $\text{Cu}(\text{OTf})_2$ mediator, depending on which of the two precursor types are used. The use of *n*-BuOH as co-solvent was also found to be of significant benefit to only the CMRF of arylboronate precursors (Zarrad *et al.* showed that presence of *n*-BuOH did not have a significant positive influence on radiolabeling performance when using arylstannanes.)

When this information is viewed in light of the mechanistic studies on the analogous Chan-Lam cross-coupling published by King *et al.*, we were able to infer several important mechanistic conclusions that affect how CMRF chemistry can be practically applied to automated tracer synthesis. The need for higher $\text{Cu}(\text{OTf})_2$ loadings when using arylstannane precursors arises from the inability of the byproduct stannyl triflate (formed as a result of the transmetalation step) to facilitate the oxidative regeneration of the copper mediator back to a Cu(II) species (Figure 45: F to A). Higher stoichiometric loads of $\text{Cu}(\text{OTf})_2$ are thus needed to drive the activation of the catalytic complex through a single electron transfer (Figure 45: C to D). When arylboronate precursors are used, the boronate triflate generated during transmetalation can mediate the rapid regeneration of Cu(II) (Figure 45, F to A, dashed red box) in the presence of atmospheric oxygen thus allowing $\text{Cu}(\text{OTf})_2$ to be used as a true catalyst.

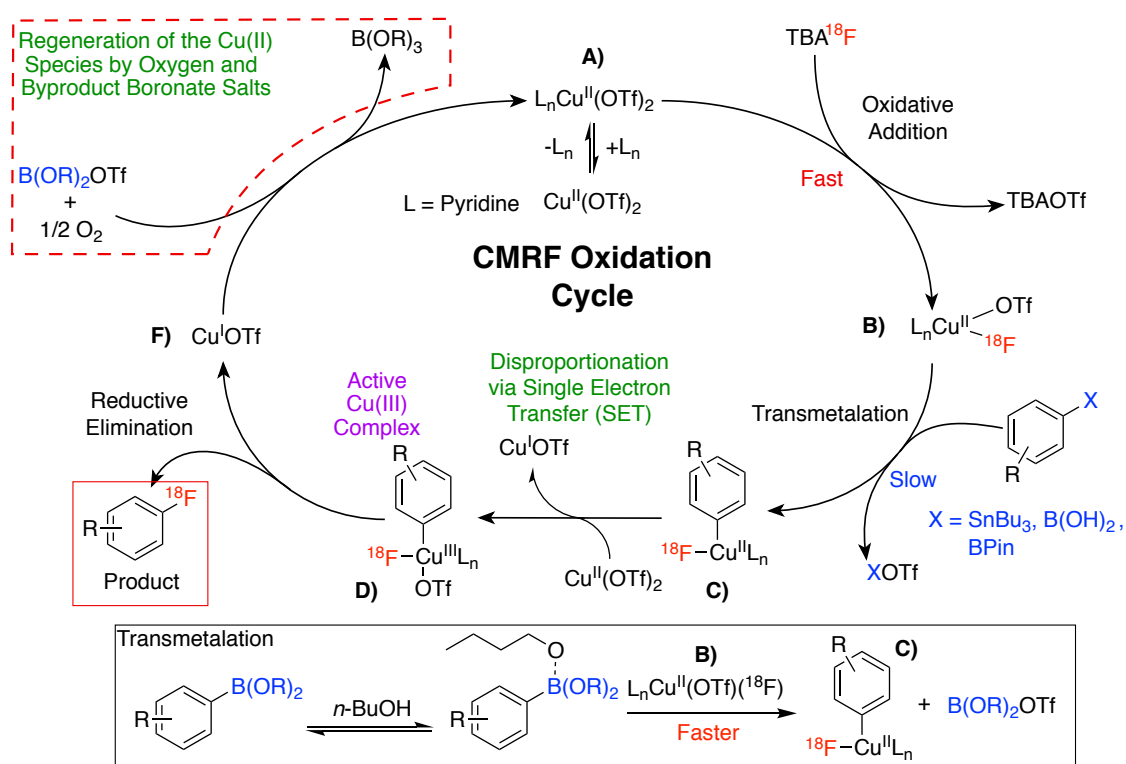


Figure 45: A possible mechanism of the CMRF reactions of both arylstannanes and arylboronates (blue) based on the mechanism of the Chan-Lam coupling published by King *et al.*⁶⁶ Byproduct boronate salts in the presence of atmospheric oxygen are able to oxidatively regenerate the Cu(II) mediator (highlighted by the dashed red box). *n*-BuOH can enhance the rate of the transmetalation step (inset below).⁷⁴

In all cases, the transmetalation step is the slowest step of the catalytic cycle.⁶⁶ When using an arylboronate precursor, the rate of this step can be enhanced by the inclusion of *n*-BuOH as an alcoholic co-solvent (Figure 45, Inset).⁷¹ The *n*-BuOH can donate electron density in the empty p-orbital present on the boron center, which stabilizes the transition state of the transmetalation step, increasing the rate of the reaction. As tin has no such empty p-orbital, this effect is lost when performing the CMRF reaction with arylstannane precursors in the presence of alcoholic co-solvents, as observed by Zarrad *et al.*⁷⁴

These conclusions have exposed several critical practical considerations that must be made while designing tracer syntheses with these methodologies. A large number of diverse and inexpensive arylboronic acid and boronic acid ester synthons are readily available from several commercial sources. They are also typically shelf-stable and easy to handle, making them convenient for precursor synthesis. CMRF reactions using these precursors can be carried out using catalytic quantities of a copper mediator, which lowers the risk of introducing harmful heavy metal contaminants into the final tracer formulation. The radiolabeling reaction can also be enhanced by using *n*-BuOH as a co-solvent; however, these reactions must be performed under an oxidative atmosphere to maximize reaction performance.

Arylstannanes are also easy to synthesize and fairly shelf-stable; however, due to their toxicity and their presence as thick oils, they are less easy to handle. As CMRFs using these precursors must be performed using Cu(OTf)₂ as a reagent in high stoichiometric loads (> 3 eq), the purification of the product tracer must be stringently controlled to minimize the presence of toxic copper and tin contaminants in the final tracer formulation. Notably, the labeling reaction can be performed under inert atmospheres without any substantial loss in reaction performance. This is particularly important when designing syntheses that must be performed on automated synthesis modules that run exclusively using inert carrier gases such as helium, argon, or nitrogen or if the precursor is sensitive to atmospheric oxygen.

7.7 Conclusions and Future Work

The DoE studies presented here have not only allowed us to optimize the radiosyntheses of the novel tracer [¹⁸F]pFBC ([¹⁸F]**8**) and the radiochemical synthon [¹⁸F]pFBnOH ([¹⁸F]**10**), but have also enabled us to draw valuable mechanistic insights in the chemistry governing the performance of different variations of the CMRF reaction. An improved understanding of this chemistry has highlighted several important practical considerations that must be considered when planning and designing automated radiosyntheses using this methodology. This information can be used to save time and resources when developing and optimizing the radiosyntheses of new radiotracers. The next chapter will discuss the application of this information to guide the rapid development of a novel small molecule tracer for β cell imaging. We have highlighted the utility of a DoE based approach to help clarify and accelerate the tracer development process; however, it must be noted that the DoE approach can also be applied to other essential tasks in the radiochemical laboratory,

such as the optimization of tracer purification protocols (HPLC and SPE) and the improvement of difficult precursor syntheses.

Despite the large quantity of detailed information that was obtained from experiments with a relatively limited library of precursors, more work must be done to truly understand the behavior of CMRF chemistry across a broader scope of precursor compounds. We are thus currently applying the DoE approach to several biologically relevant tracer development projects to accelerate the delivery of novel ^{18}F labeled radiotracers to our collaborating imaging scientists while building on the chemical knowledgebase established here. We also plan to use the DoE approach to study other advanced radiochemical methodologies so that we may more readily apply them to (pre-)clinically relevant tracer development projects and expedite the adoption of these methods into routine use.

Chapter 8: The Synthesis of ^{18}F labeled BETP Derivatives

8.1 Aims and Objectives

In addition to **C2**, **BETP** was also found to be a promising modulator of GLP-1R activity. Its confirmed ability to irreversibly modify the cysteine residue C-347 of GLP-1R makes it a particularly interesting candidate for β cell imaging. Once bound, **BETP** cannot be removed from the receptor while it may be more readily cleared from the surrounding off-target tissue, potentially increasing the signal-to-background ratio of the image at later imaging time points. However, the specificity and stability of the compound in both *in vitro* and *in vivo* environments remain significant concerns; nonetheless, **BETP** warrants further investigation as a potential tracer candidate for probing GLP-1R expressing tissues.

To facilitate our investigation of **BETP** as a candidate tracer for BCMI, the radiosynthesis of $[^{18}\text{F}]\text{BETP}$ and **4- $[^{18}\text{F}]\text{F-BETP}$** (Figure 46) requires the application of recent copper-mediated radiofluorination methodologies. The synthesis of the novel ^{18}F labeled **BETP** derivatives described below would thus also serve as a testbed to evaluate how the reaction data and optimization workflows discussed in chapter 7 could be applied directly to novel tracer development. This would provide further general information on how detailed reaction optimization using DoE can best fit into the radiotracer development pipeline.

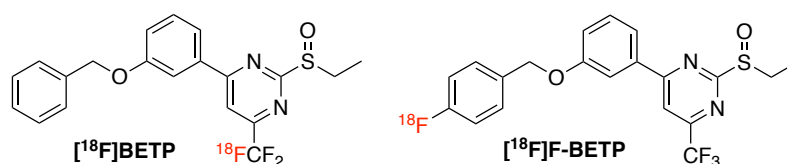


Figure 46: Two envisioned ^{18}F tracers based on **BETP**. $[^{18}\text{F}]\text{BETP}$ is isotopically labeled and is chemically indistinguishable from **BETP**. $[^{18}\text{F}]\text{F-BETP}$ is labeled at the para-position of the benzyl group.

8.2 Synthesis of **BETP** and **FBETP** Standards by Literature Published Routes

In order to study the radiosyntheses of $[^{18}\text{F}]\text{BETP}$ and $[^{18}\text{F}]\text{F-BETP}$, non-radioactive standards of each compound were synthesized from 4-chloro-2-(methanesulfanyl)-6-(trifluoromethyl)pyrimidine (**13**) via the convergent synthetic route disclosed by Eng *et al*, the key step of which is the palladium-catalyzed cross-coupling between the pyrimidine core and the (3-(benzyloxy)phenyl)borate.¹⁷³ The (3-(benzyloxy)phenyl)borate can be synthesized from either benzyl bromide (for **BETP**) or 4-fluorobenzyl bromide (for **F-BETP**) (Figure 47). **13** could be easily prepared in 3 steps from ethyl 2,2,2-trifluoroacetate (Scheme 7).

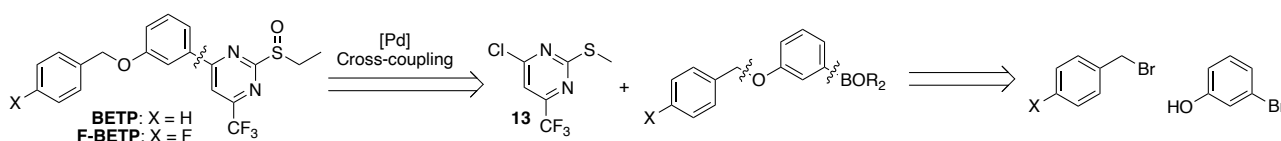
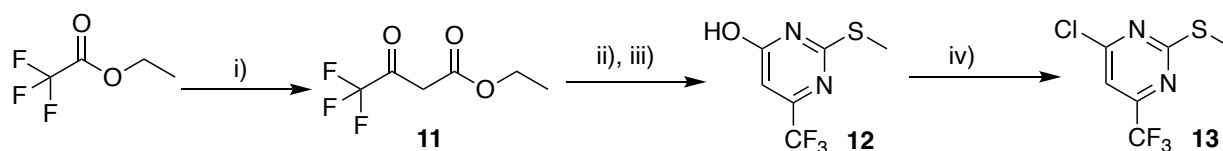


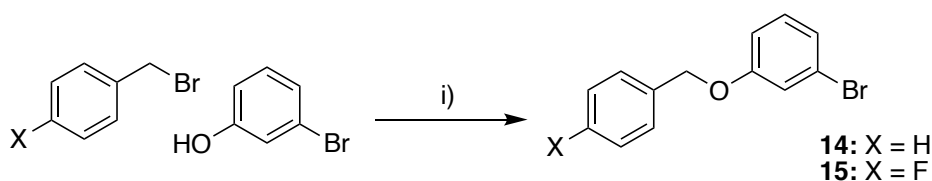
Figure 47: A retrosynthetic analysis of **BETP** ($X=\text{H}$) and the non-radioactive standard **F-BETP** ($X=\text{F}$) following a convergent synthetic strategy.



Scheme 7: Reagents and conditions: i) EtOAc, NaOEt, EtOH, reflux, **11**: 32%; ii) thiourea, NaOMe, MeOH, reflux; iii) MeO₂SO₂, water, room temperature, **12**: 43%; iv) POCl₃, NEt₃, reflux, **13**: 88%.

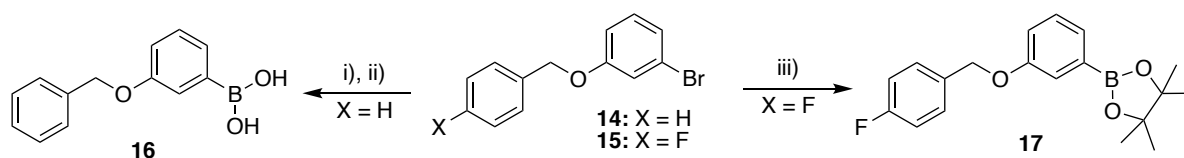
The first step of this synthesis featured a Claisen condensation with ethyl 2,2,2-trifluoroacetate and EtOAc in the presence of sodium ethoxide (NaOEt) in ethanol. The product β -diketone **11** was purified via distillation and was declared pure enough for use in the next reaction based on its boiling point. **11** was then condensed with thiourea by refluxing the two reactants in the presence of freshly prepared sodium methoxide in methanol. The solvents were removed, and the resulting thiophenol product residue was dissolved in the water, after which it was methylated using dimethyl sulfate. After acidification of the reaction mixture, the product **12** precipitated from the solution and could be isolated by filtration. ¹H NMR confirmed the successful formation of the aromatic pyrimidine ring through the presence of the resonance at δ_{H} 6.57 (s, 1H) and subsequent methylation, resulting in the methyl thioether with the resonance at δ_{H} 2.64 (s, 3H).

The 4-hydroxy pyrimidine **12** was then refluxed in POCl₃ and triethylamine (NEt₃) to afford the pyrimidine chloride **13** in good yield through a deoxygenative halogenation. ¹³C NMR analysis confirmed the presence of the trifluoromethyl group with a strong quartet at δ_{C} 120.34 (q, ¹J_{CF} = 274.9 Hz) representing the trifluoromethyl carbon. The aromatic carbon centers C-6 and C-5 also show C-F coupling at their respective resonances at δ_{C} 153.69 (q, ²J_{CF} = 35.7 Hz) and δ_{C} 108.42 (q, ³J_{CF} = 3.2), with the coupling constant decreasing quickly as they become topographically more removed (increasing number of bonds (*J* number)) from the CF₃ moiety.



Scheme 8: Reagents and conditions: i) K₂CO₃, acetone, reflux; **14**: 99%; **15**: 99%.

The synthesis of the phenylboronate synthons **16** and **17** commenced with the benzylation of 3-bromophenol with either benzyl bromide or 4-fluorobenzyl bromide. The corresponding benzyl bromide was refluxed with 3-bromophenol with solid K₂CO₃. After each reaction reached completion, the acetone was removed under reduced pressure and residue was taken up with water and subsequently extracted with either EtOAc or dichloromethane (DCM). In both cases, flash chromatography was used to isolate the desired products **14** or **15** in near quantitative yields.



Scheme 9: Reagents and conditions: i) Mg, THF, reflux; ii) B(OMe)₃, THF, -78 °C - room temperature, **16**: 40%; iii) B₂Pin₂, KOAc, Pd(II)(dppf)Cl₂, dioxane, 80 °C, **17**: 85%.

The benzylated 3-bromophenyl derivatives **14** and **15** were then respectively transformed into the boronic acid (**16**) and the boronic acid pinacol ester (**17**) (Scheme 9). **16** was synthesized by refluxing the aryl bromide **14** with small shavings of freshly sand-papered magnesium ribbon to form the corresponding aryl Grignard reagent. The Grignard reagent was subsequently reacted with trimethyl borate and quenched with 6 M HCl to afford the boronic acid **16** in 40% yield. The yield was lower than expected and may have been due to the use of damp solvent. Attempts to produce a similar boronic acid from **15** using the same method were unsuccessful, and thus, it was decided to produce the analogous boronic acid pinacol ester **17** through a Miyaura borylation reaction. Reacting the aryl bromide **15** with bis(pinacolato)diboron (B₂Pin₂) and potassium acetate (KOAc), in the presence of [1,1'-bis(diphenylphosphino)ferrocene]dichloropalladium(II) (Pd(dppf)Cl₂), in dioxane at 80 °C was able to afford **17** with a yield of 85%.

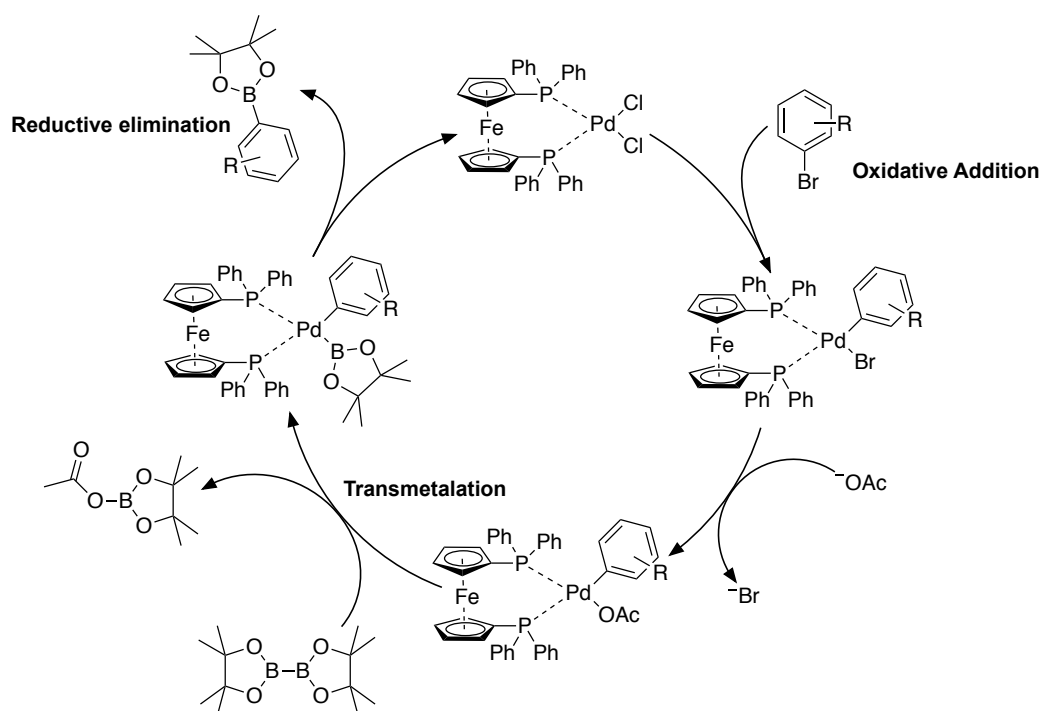
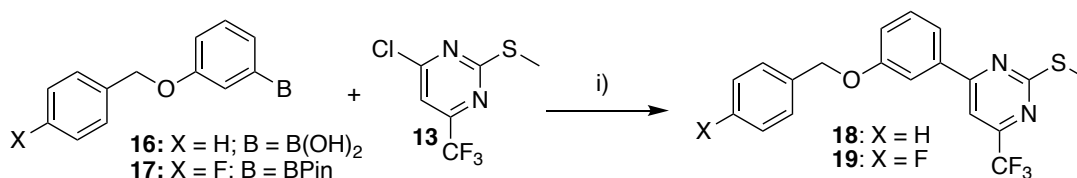


Figure 48: The catalytic cycle of the Miyaura Borylation reaction using Pd(dppf)Cl₂ as the catalyst. The use of KOAc as the base is essential to disfavor the competing Suzuki cross-coupling.

The Miyaura borylation is an important methodology of the synthesis of arylboronates. While the use of palladium catalysts and B₂Pin₂ make it a more expensive and less scalable approach than the boronic acid synthesis described above, it is nonetheless useful for rapid access to diverse arylboronates for use with Suzuki cross-coupling conditions (for precursor synthesis (*vide infra*)) or for copper-mediated radiofluorination reactions (*vide 3.3.1 and 7.5*). It proceeds via the oxidative addition of the aryl halide to the

palladium catalyst complex. An exchange of the halide anion with OAc^- results in the formation of a reactive Pd-O species, which allows for transmetalation to take place; the formation of a stable B-O bond is also a thermodynamic promoter of transmetalation. The use of a base stronger than OAc^- would result in the activation of the product arylboronic ester and would thus favor the competing Suzuki reaction (*vide infra*); hence, the use of an appropriate base (usually KOAc) is essential. After transmetalation, the product is then formed through a reductive elimination at the palladium center regenerating the catalytic species.



Scheme 10: Reagents and conditions: i) Pd(PPh₃)₄, Cs₂CO₃, DME/H₂O (4:1), 85 °C, **18**: 88%, **19**: 72%.

With the boronates **16** and **17** in hand, they could both be coupled with the 4-chloropyrimidine **13** through the related Suzuki-Miyaura cross-coupling. Heating either the boronic acid **16** or the boronic pinacol ester **17**, with the chloropyrimidine **13**, cesium carbonate (Cs₂CO₃), and tetrakis(triphenylphosphine)palladium(0) (Pd(0)(PPh₃)₄) in a mixture of dimethoxyethane (DME) and water (4:1) was able to afford both products **18** and **19** in good yields. The Suzuki-Miyaura cross-coupling reaction is closely related to the Miyaura borylation and makes use of both arylboronic acid or acid esters and aryl halide substrates. The key difference is in the base driven activation of the arylboronic acid (ester) in the transmetalation step.

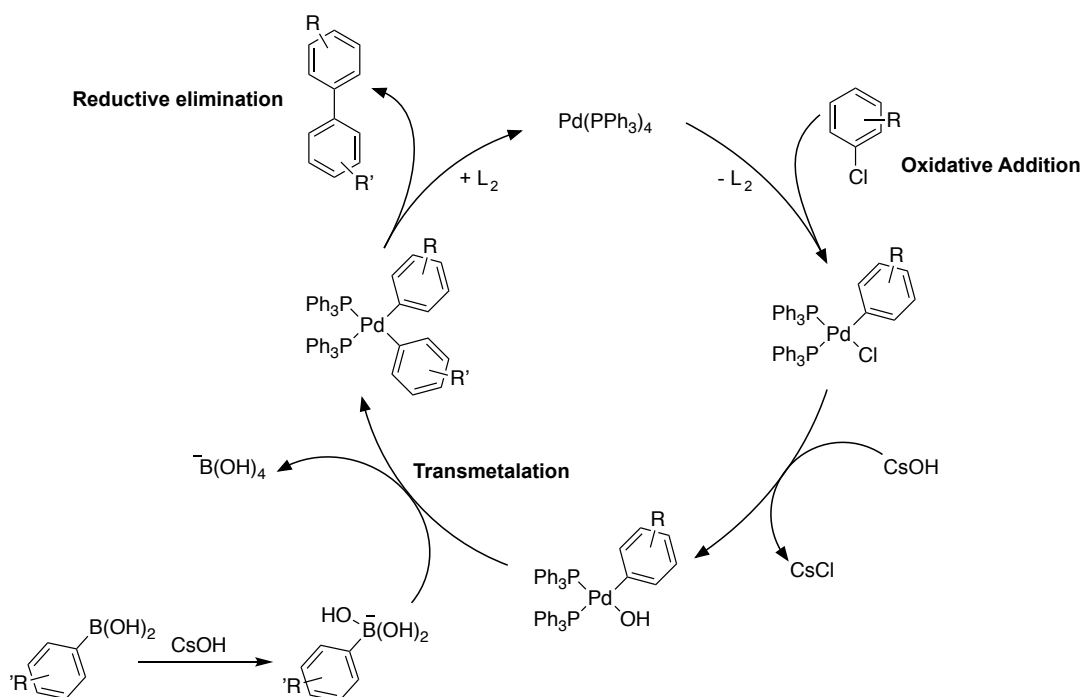
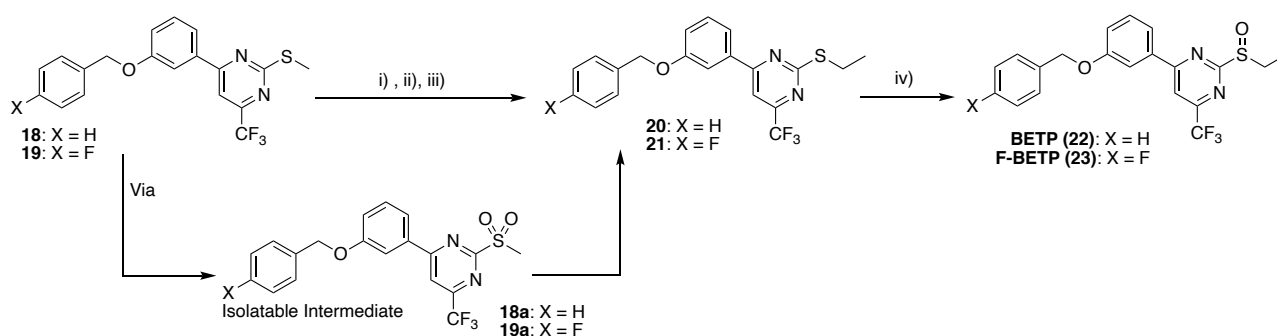


Figure 49: The catalytic cycle of the Suzuki-Miyaura cross-coupling reaction. The activation of the arylboronic acid substrate by a strong base can facilitate C-Pd bond formation in the transmetalation step of the cycle.



Scheme 11: Reagents and conditions: i) *m*-CPBA (2.2 eq), DCM, 0 °C - room temperature; ii) NaHCO₃, DCM extraction and work-up; iii) NaSEt, EtSH, THF, reflux, **20**: 91%, **21**: 64%; iv) *m*-CPBA (1 eq), DCM, 0 °C - room temperature, **22**: 64%, **23**: 95%.

The final step in the synthesis of **BETP** (**22**) and **F-BETP** (**23**) was the transformation of the aryl methylthioether group into the ethyl sulfoxide present in **BETP** (Scheme 11). This was achieved by first converting the methyl thioether into a good leaving group, an aryl sulfone, by oxidizing it with 2.2 equivalents of *meta*-chloroperoxybenzoic acid (*m*-CPBA) in DCM at 0 °C. TLC monitoring of the reaction clearly showed the conversion of the starting material to the more polar sulfone. The reaction was then quenched with saturated aqueous NaHCO₃ (to remove any remaining *m*-CPBA and byproduct benzoic acid) and extracted with DCM. The intermediate sulfone could either be isolated from the product residue for analysis or re-dissolved in THF for use directly in the next step. ¹H NMR of the isolatable sulfones **18a** and **19a** showed similarly pronounced downfield shifts of the methylsulfone resonance from δ_{H} 2.66 (s, 3H) in **19** to δ_{H} 3.46 in **19a** due to the formation of the strongly electron-withdrawing sulfone group.

The reactive sulfones **18a** and **19a** could then be substituted (S_NAr) with sodium ethylthiolate (NaSEt) to achieve the ethanethioethers **20** and **21** in good yields. ¹H NMR of both compounds shows the substitution of the methyl sulfone singlet with the diagnostic ethyl resonances at δ_{H} 3.25 (q, *J* = 7.4 Hz, 2H, SCH₂CH₃) and δ_{H} 1.46 (t, *J* = 7.4 Hz, 3H, SCH₂CH₃). In addition to their use as substrates for the synthesis of **BETP** and **F-BETP** standard compounds, both **20** and **21** were also used as non-radioactive standards for several radiochemical experiments.

20 and **21** were then oxidized to the more polar sulfoxides **BETP** and **F-BETP** using 1.1 equivalents of *m*-CPBA in DCM. The oxidizer was added dropwise to each substrate at 0 °C over the course of 30 minutes to favor the single oxidation to the more polar ethyl sulfoxide and reduce the probability of over-oxidation to the undesirable ethyl sulfone. TLC showed the sulfoxide to be fluorescent at 366 nm. The oxidation results in the formation of a racemic mixture of the two enantiomers of **BETP** and **F-BETP**. The presence of the chiral sulfoxide group was confirmed by ¹H NMR analysis of **BETP** through the presence of the two resonances at δ_{H} 3.31 (dq, *J*²_{Gem} = 13.4, *J*³_{Vic} = 7.4 Hz, 1H, H-a) and 3.19 (dq, *J*²_{Gem} = 13.4, *J*³_{Vic} = 7.4 Hz, 1H, H-a') for each of the diastereotopic S(O)CH₂CH₃ protons (Figure 50). The presence of the chiral moiety makes the two methylene protons of the ethyl sulfoxide group diastereotopic, and hence visible in the NMR spectrum as two distinct resonances with a geminal coupling constant of *J*²_{Gem} = 13.4 Hz and a vicinal coupling constant

to the neighboring methyl resonance of $J^3_{HH} = 7.4$ Hz. The presence of this coupling pattern was also used to confirm the formation of the sulfoxide moiety in **F-BETP** and all other ethyl sulfoxide bearing BETP derivatives (described below).

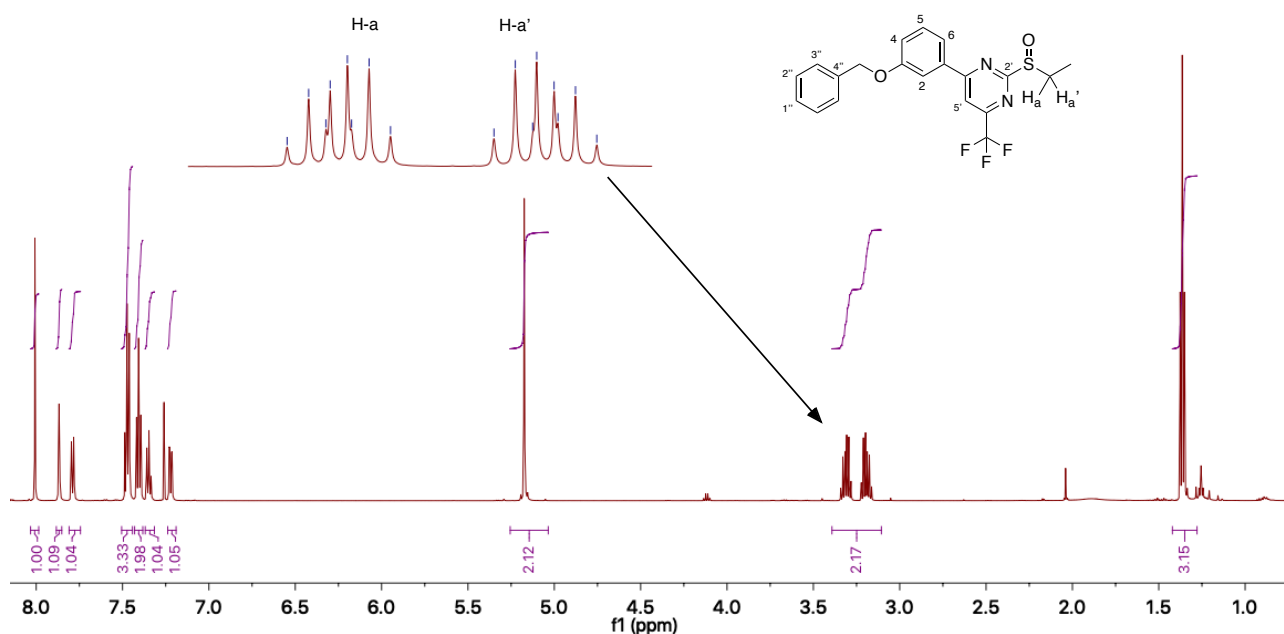


Figure 50: The ^1H NMR spectrum of **BETP**. The doublets of quartets representing the diastereotopic ethyl sulfoxide protons at δ_{H} 3.31 and δ_{H} 3.19 have been expanded (inset).

8.3 The Synthesis of Isotopically Labeled [^{18}F]BETP

8.3.1 Precursor Synthesis

The trifluoromethyl group present on the **BETP** pyrimidine core presented an opportunity for isotopic radiolabeling. Isotopic radiolabeling involves the substitution of a non-radioactive isotope for the radioisotope at the same position; thus, [^{18}F]BETP would be chemically indistinguishable from **BETP** and would possess identical pharmacological properties. The radio-trifluoromethylation disclosed by Huiban *et al.* provided a possible route to achieve this (*vide supra* 3.3.2); however, this methodology requires an aryl halide precursor. Ideally we aimed to produce [^{18}F]BETP from a single step late-stage radio-trifluoromethylation to form an ethyl sulfoxide bearing precursor (Figure 51, A); however, given the possible sensitivity of the sulfoxide to the harsh reaction conditions required for radio-trifluoromethylation, we also planned to investigate a two-step radiosynthetic route (Figure 51, B). The alternative route would begin with the radio-trifluoromethylation of the less reactive ethylthioether bearing substrate, which would subsequently be oxidized to the sulfoxide in a second step.

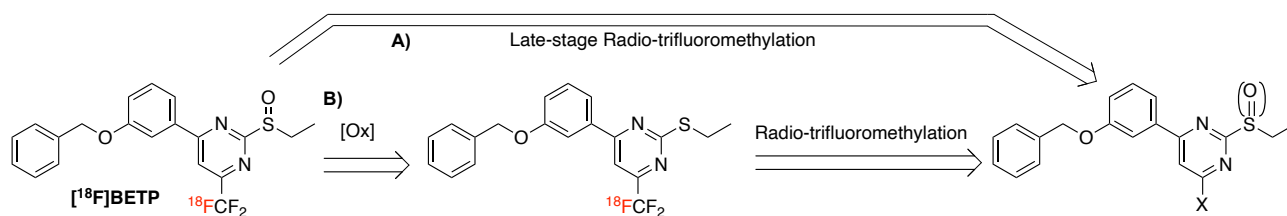
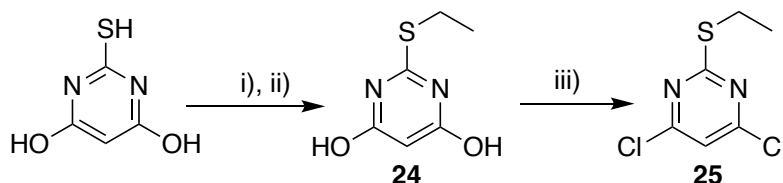


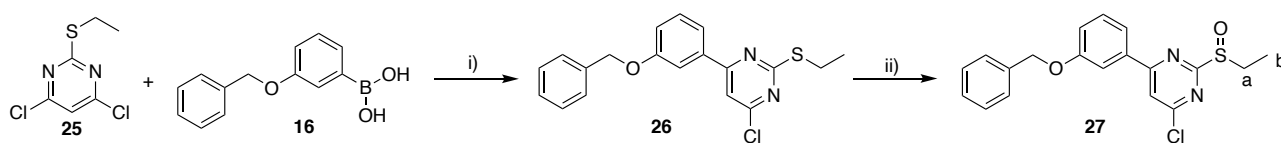
Figure 51: Retrosynthetic analysis revealed two possible routes towards $[^{18}\text{F}]\text{BETP}$. A) The ideal case would involve the single-step late-stage radiotrifluoromethylation of an ethyl sulfoxide ($\text{O}=\text{S}$) bearing aryl halide precursor. B) However, given the general sensitivity of the ethyl sulfoxide group, a 2-step strategy featuring an oxidation step after the radio-trifluoromethylation was also identified for investigation.

To this end, 4,6-dichloro-2-(ethylthio)pyrimidine (**25**) was synthesized as the pyrimidine scaffold over two steps (Scheme 12). Thiobarbituric acid was treated with ethyl bromide and potassium hydroxide (KOH) and refluxed in a water/ethanol solution to afford the 2-(ethylthio)pyrimidine-4,6-diol (**24**) which could be isolated by precipitation from an acidic aqueous solution. 4,6-Dichloro-2-(ethylthio)pyrimidine **25** was then obtained in good yields by treating **24** with POCl_3 . ^{13}C NMR confirmed the formation of the product with the five expected resonances accruing at δ_{c} 174.4 (C-2), 161.5 (C-4, C-6), 115.9 (C-5), 26.0 (SEt), and 14.1 (SEt). This was later confirmed by HPLC-MS ((ESI) (m/z): $[\text{M}]$ calcd. for $\text{C}_6\text{H}_6\text{Cl}_2\text{N}_2\text{S}$, 207.9; found $[\text{M}+\text{H}]^+$, 208.9).



Scheme 12: Reagents and conditions: i) KOH, H_2O ; ii) EtBr, EtOH, reflux, **24**: 64%; ii) POCl_3 , NEt_3 , Reflux, **25**: 89%.

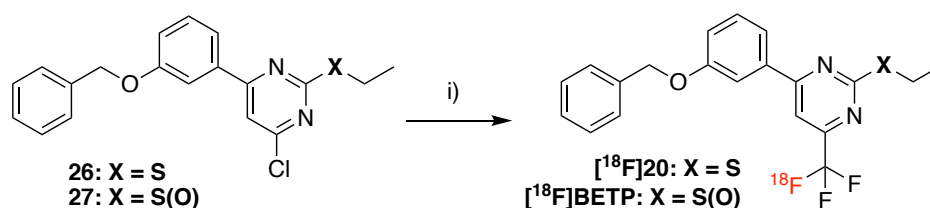
25 and (3-(benzyloxy)phenyl)boronic acid **16** were then subjected to the Suzuki-Miyaura cross-coupling conditions described above to afford the precursor compound **26** in a 60% yield (Scheme 13). ^1H and ^{13}C NMR spectroscopy confirmed this result through the presence of all the expected aromatic resonances as well as the up-field ^1H resonances corresponding to the benzyl methylene at δ_{H} 5.15 (s, 2H, PhCH_2O) and the ethylthioether at δ_{H} 3.22 (q, $J = 7.4$ Hz, 2H, SCH_2CH_3) and 1.45 (t, $J = 7.4$ Hz, 3H, SCH_2CH_3). ^1H NMR confirmed **26** to be sufficiently pure for use as a precursor for radiosynthesis. **26** was finally converted to **27** via oxidation to the sulfoxide through the same general procedure described above for the synthesis of **BETP** and **F-BETP**. The presence of the newly diastereotopic ethylsulfoxide protons (Scheme 13, **27**, H-a) was again confirmed by ^1H NMR by the two doublets of quartets at δ_{H} 3.27 (dq, $J^2_{\text{Gem}} = 13.4$, $J^3_{\text{HH}} = 7.4$ Hz, 1H, H-a) and δ_{H} 3.15 (dq, $J^2_{\text{Gem}} = 13.4$, $J^3_{\text{HH}} = 7.4$ Hz, 1H, H-b) respectively.



Scheme 13: Reagents and conditions: i) $\text{Pd}(\text{PPh}_3)_4$, Cs_2CO_3 , DME/ H_2O (4:1), 85 °C, **26**: 60% ii) *m*-CPBA (1 eq), DCM, 0 °C - room temperature, **27**: 78%.

8.3.2 Radiosynthesis of [^{18}F]BETP via Radiotrifluoromethylation

With the precursors **26** and **27** in hand, a radiolabeling study was conducted to assess the feasibility of an isotopic radiolabeling through the ^{18}F trifluoromethylation reaction published by Huiban *et al.* [^{18}F]Fluoride from a cyclotron target wash was processed by trapping and subsequently eluting it from a QMA cartridge with K_2CO_3 and K_{222} as a PTC. The eluted ^{18}F was azeotropically dried and then transferred into reaction vials containing $\text{Cu}(\text{I})$. After the MeCN was removed by evaporation, a solution of the substrate (**26** or **27**), methyl chlorodifluoroacetate ($\text{ClF}_2\text{CCO}_2\text{Me}$), and N,N,N',N' -tetramethylethylenediamine (TMEDA, a ligand to increase the solubility of $\text{Cu}(\text{I})$) in DMF was added to the vial and left to stir for 20 minutes at $150\text{ }^\circ\text{C}$ (Scheme 1).



Scheme 14: Reagent and conditions: i) [^{18}F]KF/ K_{222} , $\text{ClF}_2\text{CO}_2\text{Me}$, CuI , TMEDA, DMF , $150\text{ }^\circ\text{C}$, 20 min.

Radio-TLC and radio-HPLC analysis showed a limited conversion of each substrate to the corresponding product ($[^{18}\text{F}]14$: 4.0 %RCC; $[^{18}\text{F}]BETP$: 4.6 %RCC), while incorporation of the [^{18}F]trifluoromethyl moiety was confirmed by comparing the radio-HPLC retention times against those of the non-radioactive standard compounds **20** and **BETP**. While the unoptimized %RCCs obtained in these pilot experiments were too low to be useful and would have to be improved, a more pressing concern was the molar activity of the trifluoromethylated product, which in the case of $[^{18}\text{F}]BETP$ was calculated to be as low as $4.85\text{ MBq}/\mu\text{mol}$, as much as 1000 – 10000 fold lower than other more standard radiofluorination methods. As $[^{18}\text{F}]BETP$ is intended as a tracer for GLP-1 receptor targeting, a high tracer specific activity is required so as not to saturate the receptor binding sites and induce a “self-blocking” effect.

The reaction mechanism may explain the low specific activity of this reaction (Figure 52).⁷⁹ Methyl chlorodifluoroacetate decomposes thermally to afford difluorocarbene, which can receive a [^{18}F]fluoride anion to form a trifluoromethyl carbanion. The carbanion is then stabilized by a $\text{Cu}(\text{I})$ cation, which also acts as a catalyst to transfer the trifluoromethyl group to the aryl halide precursor. However, the trifluoromethyl carbanion is in equilibrium with the copper salt and is highly unstable, decomposing back to the carbene via the loss of a fluoride ion (^{19}F or ^{18}F).⁸⁰ This process releases ^{19}F into the reaction system and rapidly leads to the substantial reductions in specific activities observed in practice. Several publications have discussed and attempted to address this problem; however, most newer methods require the use of specialist equipment to produce high specific activity [^{18}F]fluoroform ($[^{18}\text{F}]\text{CHF}_3$).^{80,81,174} Therefore, given the unacceptably low specific activity afforded by this method, it was decided not to pursue the isotopic radiolabeling of $[^{18}\text{F}]BETP$ any further.

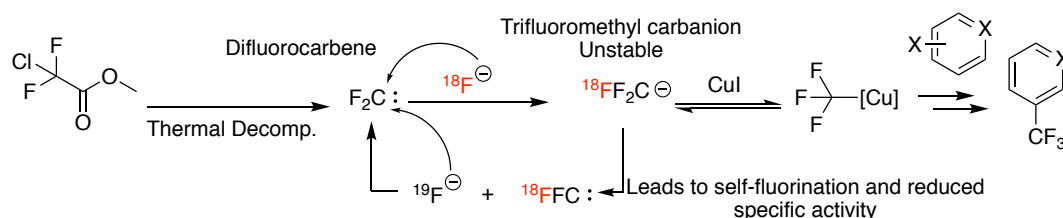


Figure 52: A proposed mechanism for the formation of the trifluoromethylating agent formed in situ during the reaction. The instability of the intermediate trifluoromethyl carbanion may be the cause of the poor specific activity of the final tracer.

8.4 The Synthesis of [¹⁸F]F-BETP

8.4.1 The Synthesis of Diverse Precursors of [¹⁸F]F-BETP

The radiotrifluoromethylation method described by Huiban *et al.* was unable to provide [¹⁸F]BETP in a %RCY or specific activity high enough for GLP-1R receptor imaging. Thus, a new synthesis route was developed to make use of the CMRF methodologies discussed above (*vide Chapter 7*). Moreover, the information afforded by the DoE optimization studies discussed above would allow us to quickly compare and evaluate a CMRF based synthesis of [¹⁸F]F-BETP from a selection of arylstannane, arylboronic acid, and arylboronic acid ester precursors. In order to rapidly generate a small library of precursor compounds, a divergent synthesis approach via an advanced intermediate was envisioned (Figure 53). The exposed phenol present on the advanced intermediate scaffold could be rapidly derivatized with a number of boron or tin bearing benzyl groups to quickly generate a small library of precursors, which could be used to subsequently evaluate and compare the various CMRF methodologies available for use towards the synthesis of [¹⁸F]F-BETP.

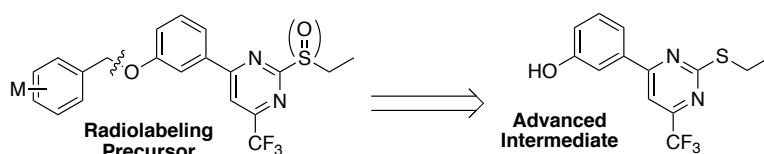
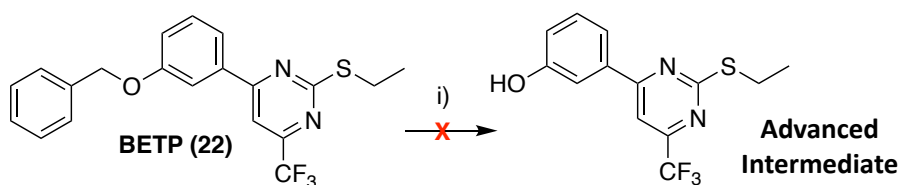


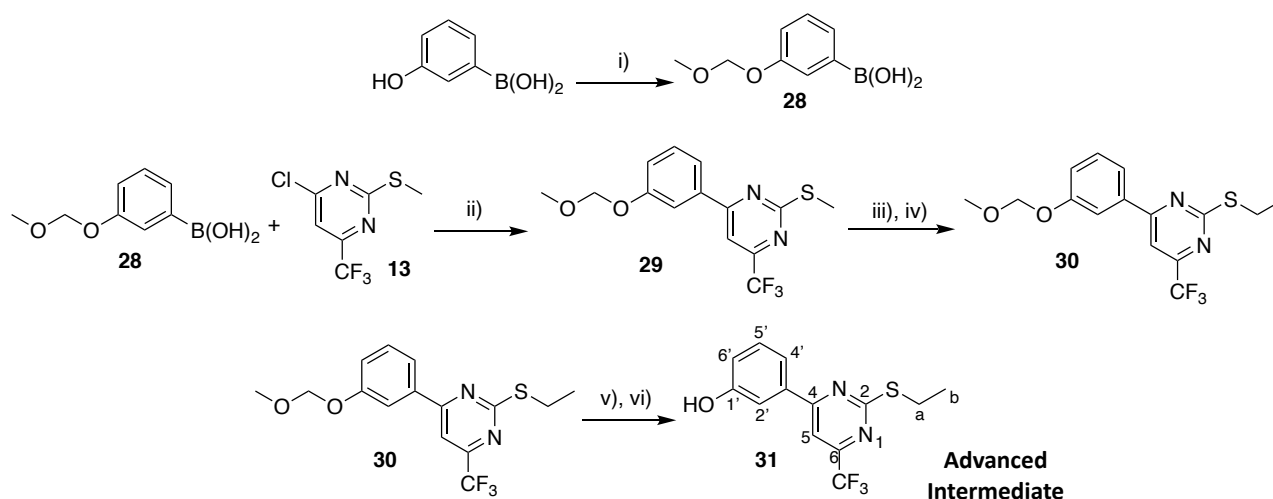
Figure 53: A variety of precursors can be divergently synthesized from a nucleophilic phenolic advanced intermediate.

It was hoped that the advanced intermediate could be generated quickly via the palladium-mediated hydrogenation of the existing BETP standard compound; however, this reaction proved to be unsuccessful (Scheme 15). Even after multiple days under a positive pressure of hydrogen gas and the addition of near stoichiometric quantities of palladium on carbon (10%) (Pd/C), the reaction showed little to no conversion to a more polar product. It was thought that either the BETP substrate or ethanethiol impurities inhibited the reaction as it is known that sulfur-containing hydrocarbons can poison the noble metal catalysts used in many hydrogenation reactions.¹⁷⁵ Thiols (and some thioethers) can also be reduced under common hydrogenation conditions to yield foul-smelling hydrogen sulfide gas (H₂S, itself a poison of noble metal catalysts), which was evidently present as a byproduct of the reaction, thus lending further weight to this hypothesis.



Scheme 15: Reagents and conditions: i) Pd(0)/C, H₂ (1 atm), THF/MeOH (1:1).

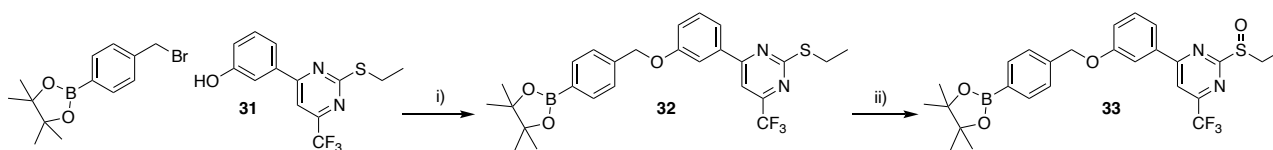
The synthesis of the advanced intermediate was thus redesigned and began with the methoxymethyl protection of 3-hydroxyphenyl boronic acid with chloromethyl methyl ether in DMF in the presence of NaH to afford **28** (Scheme 16). **28** was coupled to **13** under Suzuki-Miyaura cross-coupling conditions to afford **29**, which was subsequently oxidized to the sulfone and then reacted with sodium ethane thiolate to afford **30** in an overall yield of 44% from 3-hydroxyphenyl boronic acid. The resonances corresponding to the methoxymethyl ether (MOM) protecting group were identified in the ¹H NMR spectrum as two singlets at δ_{H} 5.25 and δ_{H} 3.51, integrating for 2H and 3H respectively. Finally, **30** could be quantitatively deprotected with 2 M HCl in methanol (1:10) to afford the advanced intermediate **31**. ¹H NMR spectroscopy confirmed the formation of **31** with the presence of the ethyl thioether confirmed by the aliphatic resonances at δ_{H} 3.26 (q, $J = 7.3$ Hz, 2H, H-a) and 1.46 (t, $J = 7.3$ Hz, 3H, H-b). The integrals of the corresponding aromatic signals added up to 5H, as expected, and a total elimination of the two singlets corresponding to the MOM protecting group was observed, indicating a successful deprotection. The presence of the quartet resonances at δ_{C} 120.64 (q, $J_{\text{CF}} = 275.4$ Hz, CF₃), 156.58 (q, $J_{\text{CF}} = 36.0$ Hz, C-6), and 107.64 (q, $J_{\text{CF}} = 3.0$ Hz, C-5) in the ¹³C NMR spectrum confirmed the integrity of the aromatic trifluoromethyl moiety.



Scheme 16: Reagents and conditions: i) NaH (60% in mineral oil), DMF, MOMCl, 0 °C - room temperature, **28**: 84%. ii) Pd(PPh₃)₄, Cs₂CO₃, DME/H₂O (4:1), **29**: 85 °C, 78%; iii) *m*-CPBA (2.2 eq), DCM, 0 °C - room temperature, **29a**: 72%; iv) NaSEt, EtSH, THF, reflux, **30**: 94%. v) HCl (1 M)/ MeOH (1:10), room temperature; vi) NaHCO₃, **31**: 95%.

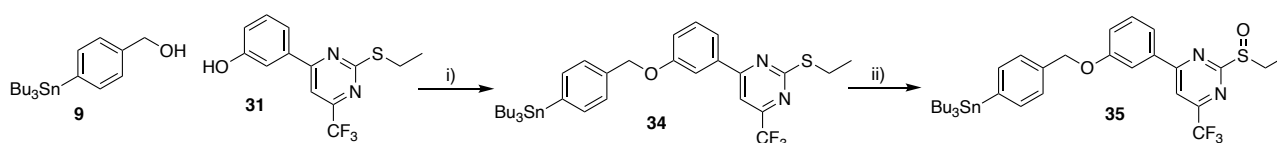
31 was then first reacted with the commercially available 4-bromomethylphenyl boronic acid pinacol ester, with K₂CO₃ in acetonitrile to afford the first **F-BETP** labeling precursor **32** with 83% yield (Scheme 17). ¹H NMR showed the diagnostic singlet corresponding to the pinacol methyl group at δ_{H} 1.35 (s, 12H) as well as the distinctive A-B coupling system, at δ_{H} 7.85 (d, $J = 7.8$ Hz, 2H) and δ_{H} 7.46 (d, $J = 7.8$ Hz, 2H), corresponding to the protons in the boronate ester-bearing phenyl ring. **32** was then oxidized under the same conditions

discussed previously to afford the sulfoxide **33** which could be identified by the characteristic diastereotopic resonances at δ_{H} 3.31 (dq, $J^2_{\text{Gem}} = 13.1$ Hz, $J^3_{\text{Vic}} = 7.4$ Hz, 1H, H-a) and 3.18 (dq, $J^2_{\text{Gem}} = 13.1$ Hz, $J^3_{\text{Vic}} = 7.4$ Hz, 1H, H-a').



Scheme 17: Reagents and conditions: i) K_2CO_3 , MeCN, reflux, **32**: 83%; ii) *m*-CPBA (1.1 eq), DCM, 0 °C - room temperature, **33**: 55%.

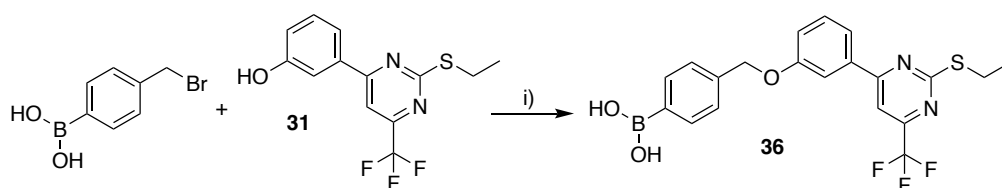
9 and **31** could be conveniently coupled together without further modification though a Mitsunobu reaction using diisopropyl azodicarboxylate (DIAD) and triphenylphosphine to produce the arylstannane precursor **34** (Scheme 18). All reaction components were dissolved together in MeCN and cooled to 0 °C, after which the DIAD is added dropwise to the reaction mixture. The initial reaction between DIAD and triphenylphosphine proceeds rapidly and must be kept cool to avoid unwanted side reactions; however, the formation of the oxyphosphonium intermediate proceeds slowly, and thus, the reaction to form **34** was left to stir overnight. The addition of an extra quarter equivalent of DIAD was also sometimes required to drive the reaction to completion and to react out any residual triphenylphosphine, which shared a very similar retardation factor (R_f) to that of the desired product and would make the isolation of the product challenging. The addition of the stannyl bearing benzyl group in **34** was confirmed by ^1H NMR spectroscopy through the presence of the aromatic A-B coupling system with two strong doublets at δ_{H} 7.69 (d, $J = 7.7$ Hz, 1H) and 7.54 (d, $J = 7.7$ Hz, 1H). Additionally, the tributyltin moiety was confirmed to be intact by the presence of the series of resonances corresponding to the three *n*-butyl groups at δ_{H} 1.66 - 1.50 (m, 6H), 1.36 (q, $J = 7.4$ Hz, 6H), 1.16 - 1.01 (m, 6H), and 0.91 (t, $J = 7.4$ Hz, 9H). As with the thioether **32**, **34** was similarly oxidized to the sulfoxide **35**, the formation of which was again verified by the presence of the diastereotopic proton resonances at δ_{H} 3.32 (dq, $J^2_{\text{Gem}} = 13.3$ Hz, $J^3_{\text{Vic}} = 7.4$ Hz, 1H, H-a) 3.20 (dq, $J^2_{\text{Gem}} = 13.3$ Hz, $J^3_{\text{Vic}} = 7.4$ Hz, 1H, H-a').



Scheme 18: Reagents and conditions: iii) DIAD, PPh_3 , MeCN, 0 °C - room temperature -45 °C, **34**: 79%; iv) *m*-CPBA (1.1 eq), DCM, 0 °C - room temperature, **35**: 68%.

A fifth labeling substrate was produced from phenol **31** and 4-bromomethylphenyl boronic acid by refluxing the two reactants together in acetone in the presence of K_2CO_3 and a catalytic quantity of KI (Scheme 19). After quenching with water, the reaction mixture was acidified with HCl (1 M) to ensure that the product could be efficiently extracted from the aqueous phase with EtOAc. The crude product residue could then be isolated by column chromatography using a more polar mobile phase (5 -15% MeOH in DCM) than required by the analogous compounds **32** and **34**. The unexpectedly high affinity of **36** to silica gel columns may have been due to an acid-base interaction between the boronic acid and the weakly basic pyrimidine nitrogen

atoms that resulted in the formation of a highly polar zwitterion. ^1H NMR in CD_3OD revealed the presence of the expected A-B coupling system associated with benzyl boronic acid moiety δ_{H} 7.76 (d, $J = 7.2$ Hz, 2H) and 7.43 (d, $J = 7.2$ Hz, 2H).



Scheme 19: Reagents and conditions: i) K_2CO_3 , KI, acetone, reflux, **36**: 84%.

As with compounds **33** and **35**, we attempted to oxidize **36** to the corresponding sulfoxide using the standard conditions of *m*-CPBA (1.1 equivalents) in DCM at 0°C . By TLC, this reaction showed a total consumption of starting material, but the product spot did not possess the TLC fluorescence characteristic of all the previously synthesized sulfoxide-bearing BETP derivatives. Additionally, the main product spot was significantly less polar than expected, and upon further investigation proved to be the undesired phenol formed through an oxidative hydroxylation (Figure 54). It was found that Chen *et al.* had previously investigated the use of *m*-CPBA to convert boronic acid into phenols, through a mechanism similar to the Baeyer-Villiger ketone oxidation.¹⁷⁶

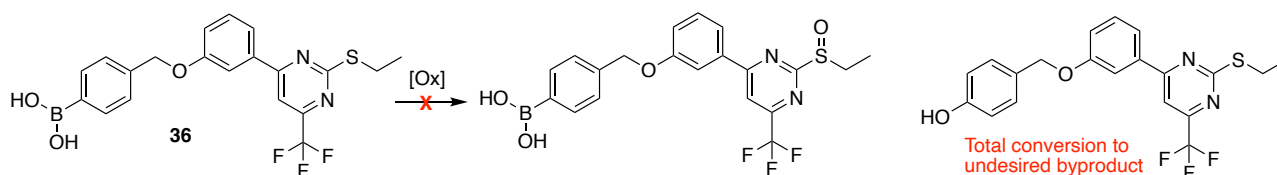


Figure 54: Attempts to oxidize **36** to the corresponding sulfoxide using *m*-CPBA were unsuccessful.

8.4.2 Radiosynthesis of 4- ^{18}F -BETP from Arylstannane and Arylboronate Precursors.

With a library of precursors in hand, we began to investigate possible radiosynthetic strategies that would afford ^{18}F -BETP with an adequate %RCC for preliminary preclinical evaluation (Figure 55). An important goal of these radiolabeling studies was to investigate and compare the functional group tolerance of the ethyl thioether (**32**, **34**, **36**) and sulfoxide precursors (**33**, **35**) to the CMRF conditions studied in chapter 7. This would determine if a true late-stage (single step) radiolabeling of ^{18}F -BETP was feasible or if a multi-step synthesis approach would be required.

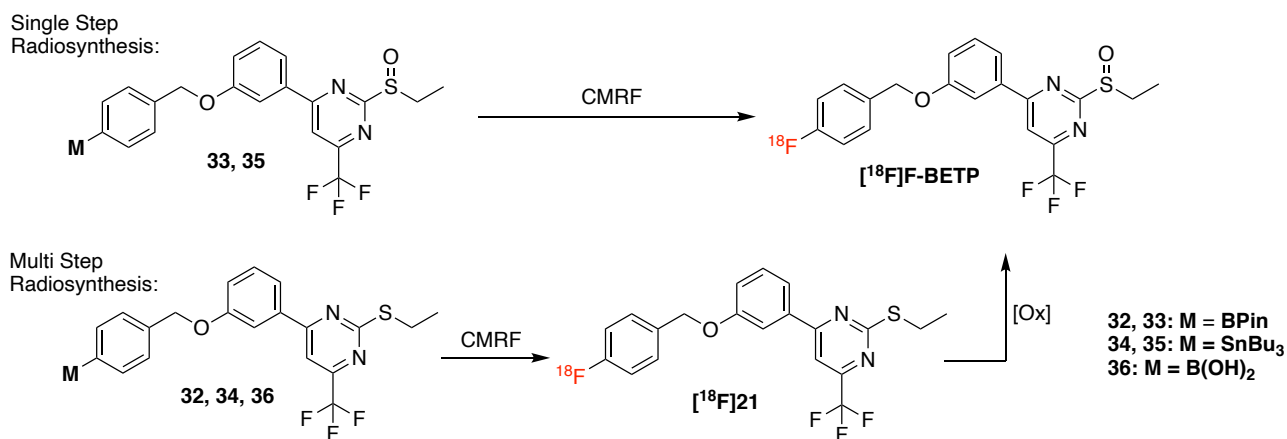
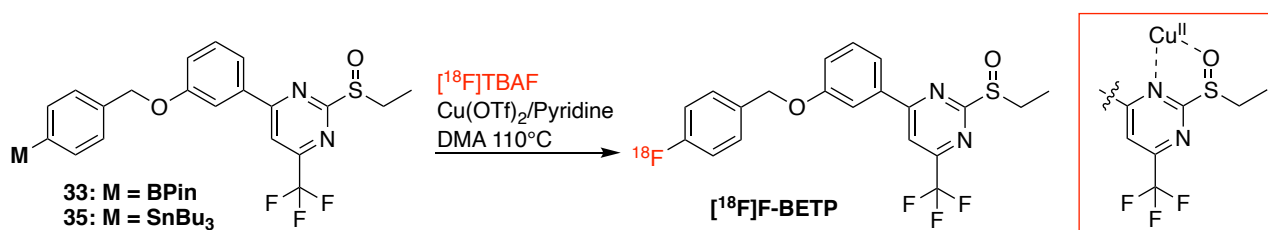


Figure 55: The single and multistep radiosynthetic strategies envisioned for the synthesis of [¹⁸F]-BETP.

The sulfoxides **33** and **35** were thus subjected to the CMRF conditions developed above. ¹⁸F from a cyclotron target wash processed using the improved processing conditions developed in chapter 7 (*vide* 7.3.4). After ¹⁸F processing, the reaction mixture was added, and each reaction was allowed to proceed at 110 °C for 20 min (Table 13).

Table 13: A selection of CMRF test syntheses using precursors **33** and **35**. The reaction conditions were derived from the DoE optimization studies in chapter 7.



Entry	Precursor	Precursor Load (μmol)	Cu(OTf) ₂ (μmol)	Pyridine (μmol)	Solvent	Atmosphere	%RCC (n = 1)
1	33	15	15	25	DMA:nBuOH (25%)	Air	ND*
2	33	15	15	60	DMA:nBuOH (25%)	Air	ND*
3	35	15	60	300	DMA	Argon	26%
4	35	15	60	150	DMA	Argon	6%

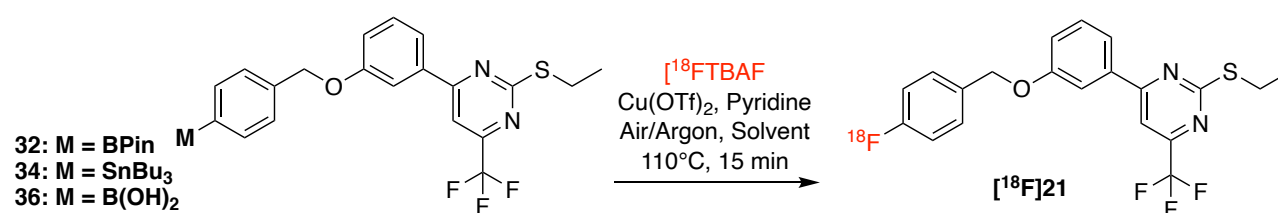
*: A non-polar radioactive byproduct was observed that was similar in HPLC retention time to [¹⁸F]**21**. It is hypothesized that this product is a result of the *n*-BuOH displacing the ethyl sulfoxide group through a nucleophilic aromatic substitution.

Under these conditions, the CMRF of precursor **33** failed to produce detectable quantities of [¹⁸F]-BETP (Table 13, entries 1 and 2). A possible explanation for this may be that the precursor complexes the copper between the pyrimidine nitrogen and the sulfoxide oxygen to form a non-reactive species, thus inhibiting the reaction (Table 13, Inset). When higher Cu(OTf)₂ and pyridine amounts are used (entries 3 and 4), the pyridine can inhibit this complexation, resulting in more available Cu(OTf)₂, which allows the reaction to proceed. Despite the low but acceptable reaction performances obtained when using precursor **35** (entry 3), radio-HPLC revealed the reaction to generate a large number of radioactive and non-radioactive byproducts, which would be difficult to separate from the final product. These syntheses also showed a high degree of variability

when repeated (data not shown), making any possible tracer production by this approach unreliable. For these reasons, we elected to abandon a late-stage radiosynthetic strategy in favor of a multistep approach.

Precursors **32**, **34**, and **36** were subjected to a similar set of reaction conditions, which were again chosen based on the information obtained by our DoE optimization studies, to investigate an alternative multistep radiosynthetic strategy (Table 14). As pyridine was revealed to be the main factor influenced by the nature of the substrate, we performed each test using both low (Table 14: entries 1a, 2a, 3a) and high (entries 1b, 2b, 3b) pyridine loadings to estimate the effect of pyridine on the synthesis. Each of the three precursors could be labeled in excellent %RCC, with the boronate precursors **32** and **36** showing a marginally better labeling performance with higher pyridine loads under these unoptimized (with respect to the substrate) conditions. In contrast, the CMRF of substrates **32** and **34** showed only moderate %RCC when reacted under the labeling conditions adapted directly from the literature (Table 14: entries 4 and 5). The performance of the CMRF of the boronic acid **36** (Table 14: entry 3b) was deemed to be acceptable for further development without the need for an additional optimization study.

Table 14: A selection of CMRF test syntheses using precursors **32**, **34**, and **36**. The reaction conditions were derived from the DoE optimization studies in chapter 7.

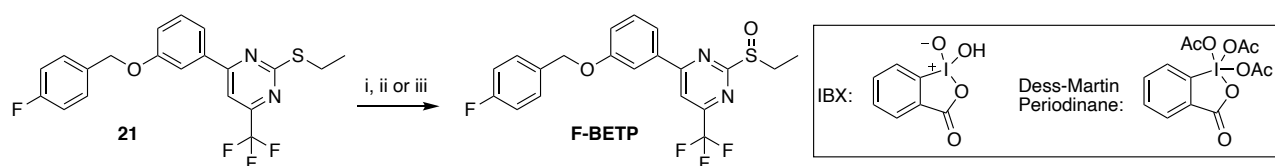


Entry	Precursor	Precursor Load (μmol)	Cu(OTf) ₂ (μmol)	Pyridine (μmol)	Solvent	Atmosphere	%RCC*
1a	32	15	15	25	DMA: <i>n</i> -BuOH (25%)	Air	72%
1b	32	15	15	60	DMA: <i>n</i> -BuOH (25%)	Air	76%
2a	34	15	60	150	DMA	Argon	71%
2b	34	15	60	300	DMA	Argon	71%
3a	36	15	15	25	DMA: <i>n</i> -BuOH (25%)	Air	81%
3b	36	15	15	60	DMA: <i>n</i> -BuOH (25%)	Air	86%
4 ⁷⁰	32	5	7.5	625	DMA	Air	28 ± 5% (n = 2)
5 ⁷³	34	14	20	150	DMA	Air	49 ± 6% (n = 2)

*%RCC data (n = 1) was collected by radio-TLC. Compound identities were confirmed by radio-HPLC against a non-radioactive standard.

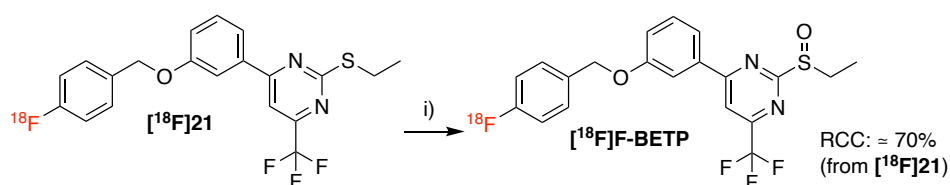
With a set of reliable and high-performing reaction conditions for the synthesis of [¹⁸F]**21** in hand, the next step in the synthesis of [¹⁸F]**F-BETP** would require the oxidation of the ethyl thioether to the corresponding ethyl sulfoxide. The standard oxidation conditions using *m*-CPBA in DCM at 0 °C were found to be too aggressive for the reliable production of [¹⁸F]**F-BETP**. These reaction conditions require that the stoichiometry of the *m*-CPBA is carefully controlled. As the educt [¹⁸F]**21** is formed in sub-nmol quantities at typical reaction scales, the small quantities of *m*-CPBA required to limit the formation of the undesired

sulfone are thus impossible to handle accurately. An alternative mild oxidation strategy that would favor the formation of the sulfoxide over the sulfone was therefore required.



Scheme 20: Synthetic studies conducted to investigate mild oxidation conditions for the multi-step synthesis of [^{18}F]F-BETP. Reagents and conditions: i) IBX, TEAB, DMSO: acetone (8:2), room temperature – 60 °C; 0% conversion ii) Dess-Martin periodinane, TEAB, DMA:H₂O (9:1), room temperature – 60 °C; 0% conversion iii) H₂O₂, AcOH: DMA (1:1), room temperature – 80 °C, ca. 50-75% conversion.¹⁷⁷ Reaction conversions were estimated by TLC.

Several mild oxidizing reagents were tested using the non-radioactive standard compound **21** to evaluate the reaction kinetics (Scheme 20). IBX (freshly synthesized from 3-iodobenzoic acid and oxone) with tetraethylammonium bromide (TEAB) as a PTC in DMSO: acetone (8:2) was unable to oxidize **21** its sulfoxide (**F-BETP**), even at elevated temperatures (> 60 °C). Dess-Martin periodinane with TEAB in DMA at 80 °C was able to oxidize **21** in a reasonable time; however, it was discovered that the TEAB PTC would react with the product sulfoxide to form the pyrimidine bromide, resulting in a complete loss of the desired product within two hours. The exclusion of the PTC would not allow the reaction to proceed at a rate fast enough for use in a radiosynthesis. Ultimately, hydrogen peroxide (H₂O₂ (30% in water), 5 eq) in a DMA:AcOH (1:1) solution was found to be able to oxidize **21** to **F-BETP** at room temperature, with little over oxidation to the sulfone.¹⁷⁷ It was also found that this reaction could be accelerated to near completion within 20 minutes when using high temperatures (80 °C), while still maintaining an acceptably low rate of over oxidation. Moreover, doping the DMA solution with pyridine, Cu(OTf)₂, and Cu(I) salts did not inhibit the oxidation reaction, showing that these conditions could be applied immediately after a CMRF step, allowing for a one-pot synthesis of [^{18}F]F-BETP.



Scheme 21: Reagents and conditions: i) H₂O₂, AcOH, one-pot, 80 °C, 15 min.

These conditions were easily translated to the radiosynthesis of [^{18}F]F-BETP (Scheme 21). After the synthesis of [^{18}F]21 via a CMRF reaction, a mixture of H₂O₂ (30% in water, 50 μl) and glacial AcOH (450 μl) was added directly to the preceding reaction mixture. The reaction was allowed to proceed at 80 °C for 15 min, after which it was quenched by the addition of 0.5 M NaCl. Radio-TLC and radio-HPLC showed that these conditions were able to efficiently convert [^{18}F]21 to [^{18}F]F-BETP (\approx 70% conversion) with a small quantity of the undesired sulfone (\approx 8%) as a result of over oxidation (conversions calculated from radio-TLC relative to the amount of [^{18}F]21). Both the sulfone and unreacted [^{18}F]21 could be separated from the product by

semipreparative HPLC. The two-step one-pot synthesis was then automated on an Elixys FLEX/CHEM synthesis module (*vide infra*) coupled to a PURE/FORM purification and formulation module.

8.4.3 Automated Radiosynthesis

The Elixys FLEX/CHEM synthesizer is a cassette-based automated synthesis module that features three reactor/cassette sub-assemblies that can be linked together to perform one-, two-, or three-pot radiosyntheses (Figure 56, A). Each cassette houses the necessary fluid/gas paths, QMA/SPE cartridges, and reagent vials (up to 12 x 3 ml rubber septum sealed sample vials) required to perform most standard radiosynthetic operations (QMA cartridge elution, reagent additions, solvent evaporation, and reaction steps)(Figure 56, B). The operations are carried out by a robotic arm fitted with a gripper to manipulate the reagent vials, a nozzle to pressurize the cassette fluid paths with argon gas, and a nozzle to apply a vacuum to the reactor during evaporation steps. The underside of each cassette features a teflon-coated septum, which seals the reactor vial during the different operations (Figure 56, C). The reactor vial (5 ml v-vial) is placed in a movable heating/cooling block and is situated below the cassette. The reactor block can move laterally to different positions where it is pneumatically lifted to access the different functional positions on the cassette septum. Additionally, the reactor can be lifted onto a plastic dip tube, which extends below each cassette, to transfer the contents of the reactor vial either to the adjacent cassette/reactor block, an external semi-preparative HPLC purification system, a product vial, or SPE purification cartridges (for purification via solid-phase extraction). The module is programmed and controlled from an external computer through a series of user-defined unit operations.

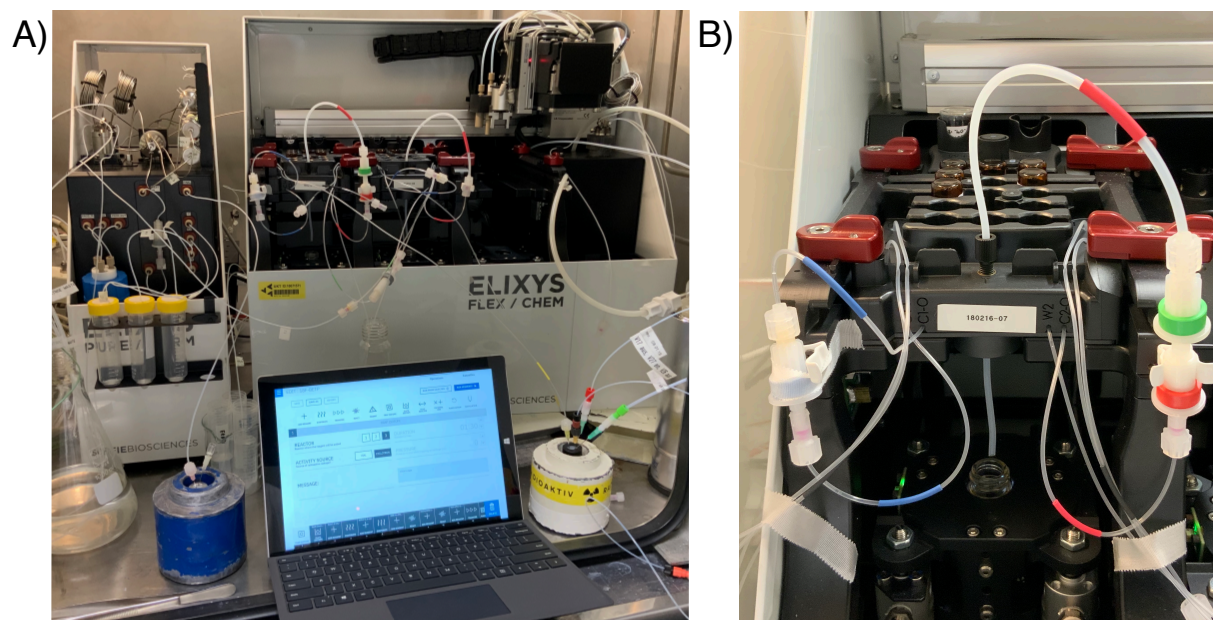
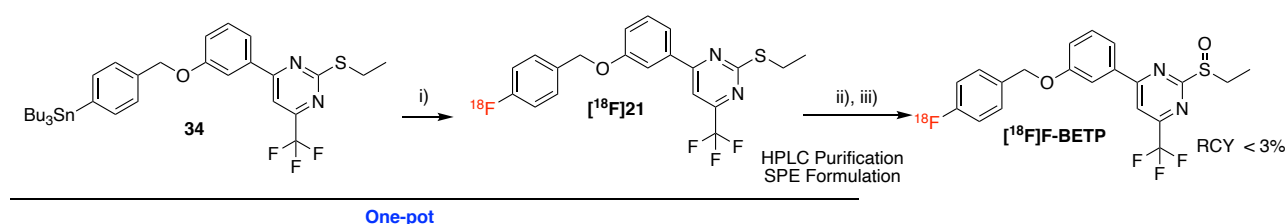


Figure 56: A) The Elixys FLEX/CHEM synthesizer with cassettes and cartridges loaded. The PURE/FORM purification and formulation module is situated on the left. B) The Elixys cassette mounted into the machine (front view).

The FLEX/CHEM synthesizer can be coupled to an external Pure/Form purification and formulation module, which houses a Rheodyne HPLC injector with two 5 ml injection loops, up to 4 HPLC columns, UV and NaI

(radiation) HPLC detectors, a HPLC fraction collection system, a dilution reservoir (to dilute the HPLC solvent for better SPE cartridge trapping), and syringe pump for SPE formulation. Once the content of a reactor vial has been transferred to an HPLC injection loop, the loop is switched to inject the reaction mixture on an HPLC column, which is used to isolate the desired radioactive product peak. A valve is then switched to divert the output flow of the HPLC column into the dilution reservoir, which is used to reduce the percentage of the organic HPLC solvent. The content of the reservoir is then pushed over an SPE cartridge, which traps the lipophilic product from the diluted HPLC eluent mixture. Finally, the syringe pump, which is connected to water, organic solvent (EtOH), and formulation buffer reservoirs, is then used to rinse, elute, and reconstitute the product tracer from the SPE cartridge into a product vial for quality control and delivery.



Scheme 22: The one-pot automated synthesis of $[^{18}\text{F}]\text{F-BETP}$. Reagents and conditions: i) **34**, $[^{18}\text{F}]\text{KF}$, $\text{Cu}(\text{OTf})_2$, pyridine, DMA, 15 min, 110 °C; ii) $\text{AcOH}/\text{H}_2\text{O}_2$, 80 °C, 15 min, iii) H_2O dilution resulted in precipitation.

Our initial attempts to automate a one-pot synthesis of $[^{18}\text{F}]\text{F-BETP}$ were carried out using the ^{18}F processing and reaction conditions disclosed by Makaravage *et al.* (Scheme 22).⁷³ The arylstannane precursor **34** and its associated reaction conditions were chosen due to their tolerance of an argon reaction atmosphere. ^{18}F from a cyclotron (≈ 45 GBq calc) was trapped directly on a QMA-OTf cartridge and was eluted (K_2CO_3 , 50 μg ; KOTf, 10 mg; H_2O , 600 μl) directly into the reactor, where it was azeotropically dried with MeCN (3 X 1 ml). The reaction mixture containing the arylstannane precursor **34** (7 mg, 10 μmol), $\text{Cu}(\text{OTf})_2$ (10 mg, 30 μmol), pyridine (20 μl , 250 μmol) in DMA (700 μl) was added to the dry $[^{18}\text{F}]\text{KF}$ and reacted under an argon atmosphere for 15 min at 110 °C. After the reaction was complete, a mixture of AcOH (585 μl) and H_2O_2 (65 μl) was added directly to the reaction vial, and the resulting solution was allowed to stir for a further 15 min at 80 °C. This reaction was finally quenched with water (3 ml) and transferred onto the HPLC loop for purification. Using this procedure resulted in the precipitation of solid materials in the reactor vessel, which often blocked the transfer line to the HPLC loop. This caused the HPLC purification step to perform poorly, resulting in the isolation and formulation of $[^{18}\text{F}]\text{F-BETP}$ in very low %RCY (< 3%) with a high content of unreacted $[^{18}\text{F}]\text{fluoride}$ (> 25%). Concerns over the precipitation of the crude product mixture, difficulties with purification, as well as the development of improved ^{18}F processing and CMRF conditions (chapter 7), prompted us to reevaluate the use of a one-pot synthesis approach.

An automated two-pot radiosynthetic strategy utilizing the improved ^{18}F processing and reaction conditions developed during our DoE studies was thus devised. A key feature of this approach was the inclusion of an SPE purification step between the two reaction steps, which would allow for the removal of many reaction byproducts and a reduction of the final reaction mixture concentration (reducing the risk of precipitation) for

better purification. The boronic acid precursor **36** was chosen due to its superior performance over the other [^{18}F]F-BETP precursors during manual test syntheses (Table 14). Furthermore, the polar boronic acid precursor was expected to be easier to remove from the reaction mixture (during SPE and HPLC purification) over the other precursor variants, simplifying the purification of the final product. The requirement for CMRF reactions of arylboronates to be performed under an oxygen atmosphere was fulfilled as the Elixys synthesizer features an open reactor to which air can be easily introduced inbetween synthetic operations.

The QMA processing conditions developed in chapter 7 excluded the possibility of delivering the cyclotron-produced ^{18}F directly into the Elixys cassette. The activity was delivered into a separate “delivery” v-vial, which was fitted with a filtered vent and placed in line before the cassette. The Elixys module was then used to pressurize this vial to push the ^{18}F over the QMA-OTf cartridge, trapping the activity and recovering the [^{18}O]H $_2$ O in a collection vial (Figure 57). MeOH (1 ml) was then injected into the delivery vial and passed over the QMA cartridge, again using gas pressure from the synthesizer, to wash off any residual water from the cartridge. A solution of TBAOTf (10 mg) in MeOH (1 ml) (from a reagent vial placed in the Elixys cassette) was then used to elute the ^{18}F into the reactor, after which the MeOH was removed by evaporation under reduced pressure at 85 °C.

A solution of **36** (6.5 mg, 15 μmol), Cu(OTf) $_2$ (5.4 mg, 15 μmol), and pyridine (4.8 μl , 60 μmol) in 700 μl DMA/*n*-BuOH (25%) was added to the [^{18}F]TBAF residue, after which 10 ml of air was blown into the reactor vessel (Figure 57). The reactor was then sealed, and the mixture left to stir at 110 °C for 20 min before it was quenched with HCl (4 ml, 0.25 M). The resulting solution was passed over an Alox N cartridge (neutral aluminum oxide, Waters) stacked on top of a C18 SPE cartridge. The Alox N cartridge successfully removed any remaining [^{18}F]fluoride and other byproduct salts present in the reaction mixture, while the C18 cartridge was able to efficiently trap the product [^{18}F]**21**. Two separate 1.5 ml portions of Et $_2$ O were then used to elute the lipophilic product from the Alox N/SPE stack over a Na $_2$ SO $_4$ cartridge (SEP-PAK Dry) to remove any residual water. The dry Et $_2$ O solution was collected in the second reactor, where the Et $_2$ O was evaporated, and [^{18}F]**21** was dissolved with DMA (400 μl). A mixture of AcOH (400 μl) and H $_2$ O $_2$ (60 μl) was then added to the reactor and allowed to stir at 80 °C, for 15 min. The final reaction solution was quenched and diluted with ammonium formate buffer and transferred to the PURE/FORM HPLC system. Semipreparative HPLC was able to separate the product [^{18}F]F-BETP from residual [^{18}F]**21** and the minor sulfone byproduct. The HPLC peak containing the product was then isolated, diluted, and passed over a second C18 SPE cartridge for trapping, concentration and formulation (10% EtOH in PBS, 5 ml), affording [^{18}F]F-BETP with $40 \pm 21\%$ RCY ($n = 2$, 3.2 GBq and 5.7 GBq from ≈ 22 GBq). QC HPLC against a non-radioactive standard compound confirmed the formation of [^{18}F]F-BETP, while radio-TLC showed the final formulation to be free of [^{18}F]fluoride (< 1%).

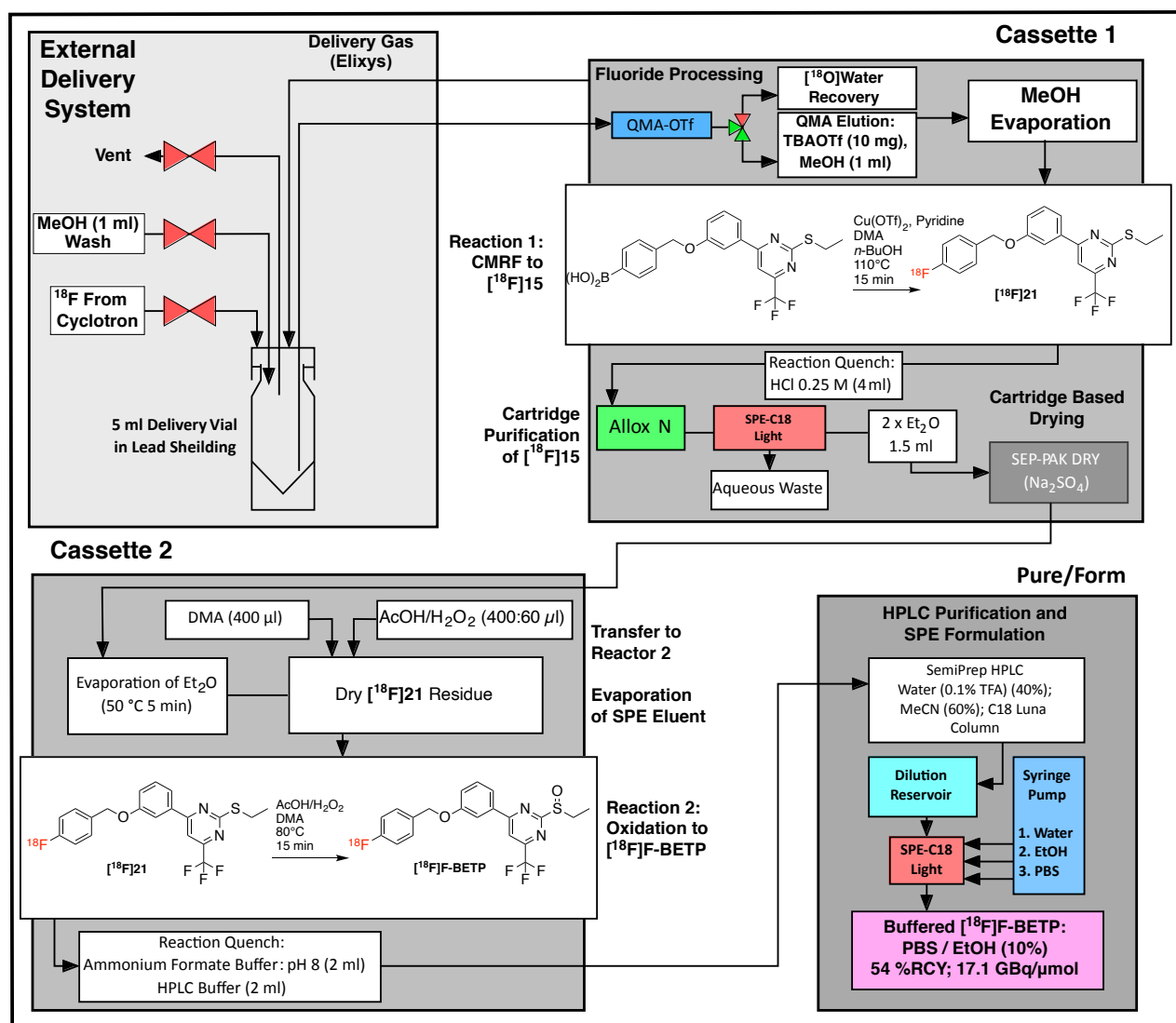


Figure 57: Schematic diagram of the fluid paths and synthesis operations for the automated synthesis of $[^{18}\text{F}]\text{F-BETP}$ using an external manually-operated ^{18}F delivery system, Elixys FLEX/CHEM synthesizer, and Elixys PURE/FORM purification and formulation module (results are from the best representative synthesis).

The molar activity of the final product was calculated to be $15.9 \pm 1.7\%$ GBq/ μmol ($n = 2$) from a calibration curve made from the UV HPLC signal of the non-radioactive standard. The specific activity obtained was lower than expected for CMRF reactions (> 50 GBq/ μmol), despite a number of precautions taken to limit ^{19}F fluoride contamination, such as the use of non-fluorinated plastic tubing and glass-encapsulated stirrer bars over the use of standard teflon-coated stirrer bars. The reduced specific activity may have been as a result of a spontaneous defluorination of the strongly electron-withdrawing trifluoromethyl group present in the precursor under the copper-mediated reaction conditions (Figure 58). While this is currently speculation, we are working to establish the specific activity tolerance of CMRF chemistry to other per-fluorinated reaction precursors and additives.

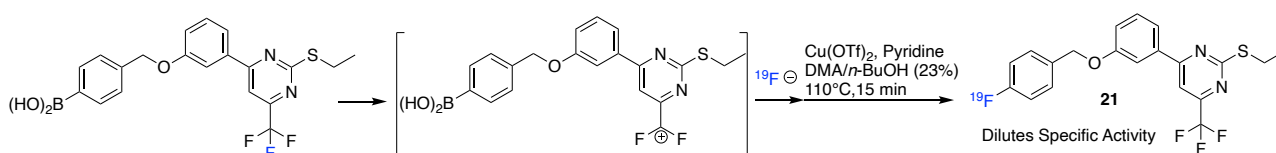


Figure 58: A possible route for ^{19}F fluorine contamination from the trifluoromethylated precursor.

Nonetheless, this automated two-pot synthesis protocol could provide [^{18}F]F-BETP in 1 hour 52 minutes in a sufficiently high yield and activity concentration for *in vitro* biological testing.

8.5 [^{18}F]F-BETP *In vitro* Experiments

[^{18}F]F-BETP was administered to CHL/GLP-1R cells *in vitro* to evaluate its specific cellular uptake. Tracer uptake into the GLP-1R expressing cell line was observed. This uptake could be blocked by simultaneously incubating the cells with 25 μM of the non-radioactive standard compound. When the same experiment was carried out using control HEK293 cells, uptake was also observed, which could also be blocked by the addition of the non-radioactive standard; however, this non-specific uptake was significantly lower ($p < 0.01$) than the specific uptake into CHL/GLP-1R cells. Although statistically significant, this difference is in all likelihood too small to suggest that [^{18}F]F-BETP could be a useful β cell-specific probe given the high chemical resolution required for *in vivo* β cell mass imaging. As a positive control, the CHL/GLP-1R cells were able to show specific [^{64}Cu]Ex-4 uptake, while the HEK293 cells showed no specific uptake of the tracer, confirming the integrity of the β cell model (no antibody for GLP-1R Western blot was available. Data not shown).

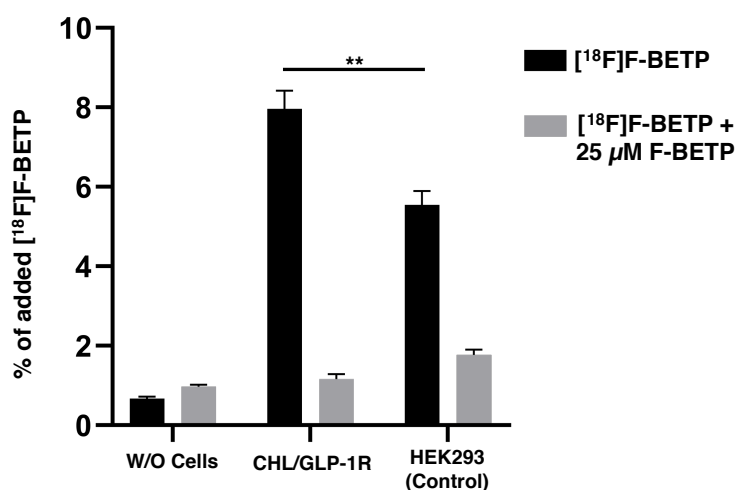


Figure 59: Cell uptake experiments confirmed that [^{18}F]F-BETP can bind to GLP-1R expressing CHL cells (** $p < 0.01$). This figure was kindly provided by Sophie Stotz who carried out the experiments and analyzed the data.

Sodium dodecyl sulfate-polyacrylamide gel electrophoresis (SDS-PAGE) was performed on the same cells to determine if the tracer was indeed able to modify GLP-1R irreversibly (Figure 60, B). Several strong bands were detected by autoradiography between 40-70 kDa, which is in the expected mass range for GLP-1R, which has a molecular mass of 53 kDa. However, common serum proteins, such as bovine serum albumin

(BSA) also reside in this molecular mass range, and it is thus difficult to evaluate the selectivity of [^{18}F]F-BETP by this assay. The presence of this band was almost eliminated when the cells were treated with 25 μM of non-radioactive F-BETP, suggesting [^{18}F]F-BETP uptake could be selectively blocked, possibly by saturating nucleophilic protein moieties with the non-radioactive standard molecule.

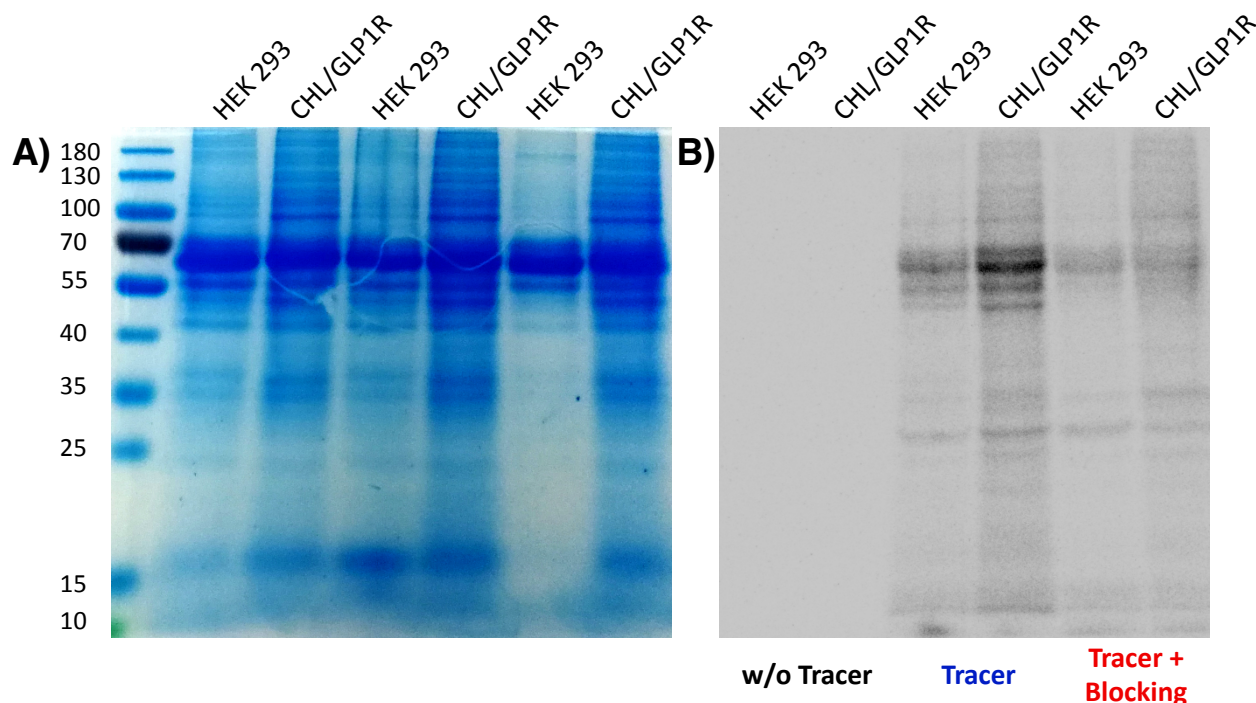


Figure 60: SDS-PAGE gel of treated CHL/GLP-1R cells alongside HEK293 cells as a control. A) Coomassie protein staining with the molecular mass ladder on the left of the image. B) Autoradiography of the cell lysate treated with binding buffer (PBS, w/o tracer), with the tracer, or with the tracer + 25 μM of the non-radioactive standard.

While the gamma-counting experiment indicated some specific GLP-1R uptake, it is likely that the target to background ratio of the [^{18}F]F-BETP signal is too low to be useful as a probe for β cell mass. Autoradiography shows [^{18}F]F-BETP to bind to several distinct proteins, but it is not possible to determine which of these is GLP-1R. Furthermore, studies by Eng *et al.* and Bueno *et al.* have demonstrated the strong electrophilicity and hence, poor stability of BETP to weak endogenous nucleophilic peptides like glutathione.^{148,173}

An additional potential issue with [^{18}F]F-BETP, as synthesized by CMRF chemistry, is its relatively low specific activity. The low specific activity means that the high quantity of carrier molecules present in the tracer formulation may induce a “self-blocking” effect, reducing the number of radiolabeled molecules that ultimately bind to the GLP-1R target. This effect is further exacerbated by the low binding capacity of GLP-1R (and many GPCRs in general). The poor stability, specificity, and specific activity of [^{18}F]F-BETP means that it is unlikely to afford the high chemical resolution necessary to find application as a specific probe for β cell imaging.

8.6 Summary and Conclusion

Unfortunately, our preliminary *in vitro* investigations revealed that it is unlikely that [^{18}F]F-BETP will find any application for the targeting of GLP-1R expressing tissues *in vivo* due to its low specificity, poor

pharmacological properties, instability to serum protein nucleophiles, and relatively low specific activity. As BETP is an affinity modulator (like **C2**) of certain orthosteric GLP-1R ligands, it would, however, also be interesting to investigate if **BETP** could find application as allosteric affinity modulator for increasing tracer uptake in GLP-1R expressing tissues.

Nonetheless, the radiosynthesis of [^{18}F]**F-BETP** from a diverse selection of precursors proved to be a good testbed for the knowledge obtained from our DoE studies on CMRF chemistry. The practically applicable information obtained from our improved understanding of CMRF reactions, brought about through the DoE studies described in chapter 7, was applied directly to the synthesis of [^{18}F]**F-BETP**. Having a good understanding of CMRF chemistry allowed us to make informed decisions about which synthetic strategies that would give us the fastest access to [^{18}F]**F-BETP** for *in vitro* evaluation. We were thus able to quickly develop an efficient automated radiosynthesis of [^{18}F]**F-BETP** in good radiochemical yields without the need for a detailed synthesis optimization of [^{18}F]**F-BETP** itself. This establishes and strongly justifies the use of the DoE approach to reaction study and optimization in the tracer development pipeline.

Chapter 9: General Conclusion

The work discussed above has explored several novel approaches for the *in vivo* visualization and quantification of pancreatic β cells using PET imaging. It has specifically explored the role that small molecule allosteric modulators of GLP-1R could play in achieving this goal, both as tracer uptake enhancers and as stand-alone GLP-1R probes.

Chapter 6 describes our first attempts to use an allosteric affinity modulator of GLP-1R, "Compound 2," to enhance the uptake of orthosteric radioligands into GLP-1R expressing tissues for improved BCMI and theranostic strategies. While we were unable to induce this effect in *in vivo* β cell models, we nonetheless believe that this approach is still of great interest. Further investigations of this approach would require the discovery and development of new allosteric modulator/probe combinations. Moreover, this approach could also potentially be applied to the imaging of a wide range of GPCRs associated with other pathologies outside of diabetes research.

Chapters 7 and 8 focused on the optimization and utilization of CMRF chemistry to accelerate the development of new radiotracers. Specifically, we aimed to develop the role of the DoE approach in the tracer development pipeline. The detailed information afforded by our DoE studies allowed us to not only optimize the production of several novel tracers, tracer synthons, and radiosyntheses ($[^{18}\text{F}]\text{pFBC}$, $[^{18}\text{F}]\text{pFBG}$, and $[^{18}\text{F}]\text{FBnOH}$), but also gave us an improved understanding of CMRF chemistry with a number of practically important insights. DoE has thus proved to be a valuable tool for both reaction and tracer synthesis development efforts.

Despite being unsuccessful as a potential tracer candidate, the radiosynthesis of $[^{18}\text{F}]\text{F-BETP}$ served as a test-bed to show how an improved understanding of CMRF chemistry can be directly applied to a tracer development problem. The knowledge base developed in chapter 7 was successfully applied to the synthesis of $[^{18}\text{F}]\text{F-BETP}$, a potential tracer of GLP-1R expressing tissues, accelerating and simplifying our efforts to develop an effective automated radiosynthesis protocol.

We are now applying the DoE approach to several preclinically relevant radiosynthesis projects. It is helping us optimize problematic radiosyntheses quickly, thus accelerating our delivery of novel PET tracers to our collaborating preclinical imaging scientists. We will continue to use the DoE approach to broaden our understanding of CMRF chemistry as well as other cutting-edge radiosynthesis methodologies. We hope that DoE will be more widely used as a powerful tool that will help expand the radiochemical toolbox and play a more significant role in defining a better tracer development pipeline for bringing novel tracer ideas from bench to bedside.

Experimental

Chapter 10: General Information Pertaining to Materials and Methods

10.1 General Organic Chemistry Information

All chemicals, reagents, catalysts, and solvents were purchased either from *Sigma Aldrich* (St. Louis, Missouri, USA), *Merck* (Darmstadt, Germany), *abcr GmbH* (Karlsruhe, Germany), *Karl Roth* (Karlsruhe, Germany), or *TCI GmbH* (Eschborn, Germany) and were used without any additional purification unless otherwise stated. SPE and SEP-PAK cartridges were obtained from *Waters* (Milford, Massachusetts, USA) unless otherwise stated.

The glassware used for organic synthesis was cleaned after use by soaking in a KOH/isopropanol bath for, followed by soaking in an HCl bath (6M). The glassware was then rinsed with deionized water and dried overnight at 100 °C in a drying oven.

Reactions were monitored using thin-layer chromatography (TLC) on 0.20 mm Polygram SIL G/UV₂₅₄ (silica gel 60) TLC plates and were developed with an appropriate running buffer/solvent mixture. Spots were visualized with UV light (254 or 366 nm). Alternatively, TLCs were stained by gentle heating with either iodine vapor; ninhydrin/n-butanol spray (amines); a solution of potassium permanganate (3 g), potassium carbonate (20 g), and sodium hydroxide (5%, 5 ml) in water (300 ml); a 2.5% solution of anisaldehyde in ethanol with concentrated sulfuric acid (1:1) (freshly prepared before use); or a 5% solution of phosphomolybdic acid in ethanol.

Preparative flash chromatography was performed using pre-packed silica gel columns (SNAP KP-Sil or SNAP Ultra (25 µm HP-Sphere), 10 g, 25 g, 50 g, or 100 g, *Biotage*, Uppsala, Sweden) on an automated chromatography system, (*Isolera 4*, *Biotage*) which featured a UV detector and fraction collector. Unless otherwise stated, all columns were dry loaded by absorption onto either silica gel or diatomaceous earth packing material (*Isolute*, *Biotage*).

¹H and ¹³C NMR spectra were obtained at 300 K using an Avance III AV 600 (¹H: 600.13 MHz and ¹³C: 150.61 MHz) spectrometer (*Bruker*, Billerica, Massachusetts, USA). All chemical shifts (δ) are reported in ppm and all *J* values are reported in Hz. The following abbreviations are used to describe multiplicities: s (singlet), d (doublet), t (triplet), q (quartet), m (multiplet) brs (broad singlet). All compounds were dissolved in chloroform (CDCl₃) unless otherwise stated. All chemical shifts were referenced to residual chloroform (δ_H = 7.26 and δ_C = 77.00), methanol (δ_H = 3.31 and δ_C = 49.00), or DMSO (δ_H = 2.50 and δ_C = 39.52).

Analytical HPLC-MS data was collected using a 1200 series HPLC machine coupled to quadrupole 6120 series MS detector in ESI mode (*Agilent*, Santa Clara, California, USA) under the following conditions: Column: Luna 5 µm C18 (2) 100 Å, 50 x 2 mm; Solvent A: H₂O + Formic acid (0.1%); Solvent B: acetonitrile; Gradient: 0 - 7.60 min (0% - 100% B), 7.60 - 7.80 min (100% B), 7.80 - 8.30 min (100% - 0% B), 8.30 - 12.0 min (0% B). Analytical

GC-MS data was collected using a 7890 GC system coupled to a 5975C inert MSD with a triple axis detector (*Agilent*).

The compounds listed below are grouped according to the general procedures used to produce them and are numbered as they appear in the results and discussion section of this thesis.

10.2 General Radiochemistry Information

Unless otherwise stated, all radioisotopes were produced using a PETtrace 890 (16 MeV protons) cyclotron (*GE Healthcare*, Uppsala, Sweden). ^{18}F was produced from ^{18}O via the $^{18}\text{O}(\text{p},\text{n})^{18}\text{F}$ nuclear reaction and was delivered either as a target wash in H_2O (1.5-2.5 ml, 1-3 GBq/ml) for manual radiochemical experiments or in ^{18}O (1.5-2.5 ml) through direct delivery from the cyclotron for automated synthesis (activity concentration dependent on bombardment time (10 min \approx 21 GBq)). ^{64}Cu was produced using the $^{64}\text{Ni}(\text{p},\text{n})^{64}\text{Cu}$ nuclear reaction, processed through ion exchange, and was delivered in a 0.1 M HCl solution. All ^{64}Cu radiolabeling experiments were carried out manually. Automated ^{18}F tracer syntheses were either performed on a customized synthesis module running with *TRACERlab* (*GE Healthcare*, Münster, Germany) control and user-interface software or with an Elixys FLEX/CHEM radiosynthesizer coupled to an Elixys PURE/FORM purification and formulation module (*Sofie Biosciences*, Los Angeles, California, USA) using proprietary Elixys FLEX/CHEM control software.

Manual radiochemical experiments were performed using Wheaton v-vial reactor vessels (5 ml, *VWR*, Radnor, Pennsylvania, USA) fitted with disposable silicon septa under screw-top caps. All reaction vials were reused multiple times and were cleaned after use by soaking in a KOH/isopropanol bath for 24 hours, after which they were rinsed with deionized water and dried overnight at 100 °C in a drying oven. The reactions were stirred using either teflon or glass coated micro stirrer bars.

Radiochemical reaction performance was monitored using radio-TLC on 0.20 mm Polygram SIL G/UV₂₅₄ (silica gel 60) TLC plates. Radio-TLC plates were developed with an appropriate running buffer/solvent mixture. All radio-TLCs were run behind appropriate shielding. Radio-TLC data was acquired using a Cyclone Plus storage phosphor imaging system (*PerkinElmer*, Waltham, Massachusetts, USA).

Analytical radio-HPLC data was collected using an Agilent HPLC (1260 Infinity series with an automated sample injector) coupled to an inline radiation detector (NaI(Tl)). In all cases, analytical radio-HPLC data was obtained under the following general conditions unless otherwise stated: Column: Luna 5 μm C18 (2) 100 Å column (250 x 4.6 mm). The following gradient was run in all instances: Solvent A: H_2O + 0.1% TFA; Solvent B: MeCN; 0 - 2 min: (5% B); 0-17 min: (5 - 100% B); 17 - 23 min: (100% B); 23-28 min: (100-5% B).

For all radiochemical experiments, reagents, solvents, QMA eluents, reaction mixtures, and buffers were freshly prepared and dispensed directly before use unless otherwise stated.

A Note on Terminologies Describing the Outcome of a Radiochemical Process:

There are several ways to report the results of a radiochemical experiment and each provides different information depending on what is being measured.

Radiochemical Conversion (%RCC): The performance of a radiochemical reaction is best described by the incorporation of the starting radioactivity into the radioactive product as a percentage. The %RCC is measured directly after the reaction and before purification.

Radiochemical Yield (%RCY): Describes the decay corrected % yield of an entire synthesis including purification and formulation.

Activity yield (%AY): Describes efficiency of the process with respect to time. It is given by the activity at start of synthesis over the activity at end of synthesis as a percentage. %AY is not decay corrected and is thus time dependent.

10.3 General *In vivo* Information

All animals were purchased from *Charles River Laboratories, GmbH* (Sulzfeld, Germany). *In vivo* PET imaging experiments were carried out using Inveon small animal PET scanners (*Siemens Healthineers*, Knoxville, Tennessee, USA). Anatomical MRI data was obtained using a Clinscan 7 T small animal MRI scanner (*Bruker Biospin GmbH*, Entlingen, Germany) All animals were anesthetized with Isoflurane in a warmed anesthesia box. The animals were placed into self-regulating heating beds, which maintained a body temperature of 37 °C. The narcosis was sustained during imaging experiments with a mixture of Isoflurane (1.5%) and oxygen.

PET imaging data were reconstructed and analyzed using Inveon Acquisition Workplace software (*Siemens Healthineers*) with user defined time framing. Image reconstructions were performed using an ordered subset expectation maximization (OSEM) 3D algorithm.

Cell tracer uptake experiments and ex vivo biodistribution analysis results were obtained using a 2480 WIZARD2 automatic gamma counter (*PerkinElmer*).

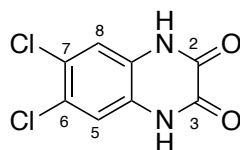
10.4 Ethics Disclaimer

All experiments involving animals were conducted in accordance with the German Animal Welfare Act after authorization from the local authorities (Regierungspräsidium Tübingen).

Chapter 11: Allosteric Affinity Modulators as GLP-1R Tracer Uptake Enhancers

11.1 Organic Synthesis

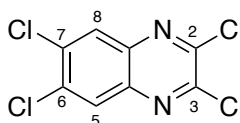
6,7-Dichloroquinoxaline-2,3-diol (**1**)¹⁶⁰



4,5-dichlorobenzene-1,2-diamine (5.0 g, 28.25 mmol) was refluxed in diethyl oxalate (15 ml, 113 mmol) for 12 hours. The grey reaction mixture was allowed to cool to room temperature, after which the product was filtered off and washed with three portions of ethanol. The resulting diol (**1**) (4.9 g, 75%), obtained as a fine dark grey powder, was dried under high vacuum and used directly in the next step. The acquired spectral data corresponded with the previously published data.¹⁶⁰

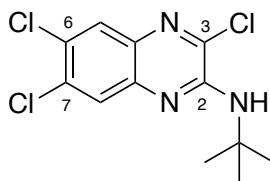
¹H NMR (600 MHz, DMSO): δ = 12.03 (s, 2H, NH), 7.24 (s, 2H, Ar); ¹³C NMR (151 MHz, DMSO): δ = 154.8 (C-2, C-3), 126.1 (C-6, C-7), 124.4 (C-5a, C-8a), 116.1 (C-5, C-8).

2,3,6,7-Tetrachloroquinoxaline (**2**)¹⁷⁸



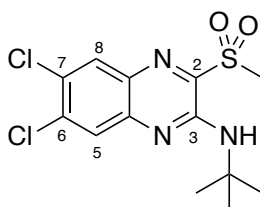
1 (500 mg, 2,164 mmol) was refluxed in POCl₃ under a gentle stream of argon in a 25 ml reaction flask fitted with a condenser and a T-joint take-off. The outlet of the T-joint led to a NaOH (2 M) filled bubble trap to trap any evolved HCl gas. The reaction was monitored by TLC from aliquots of the reaction mixture that were quenched with NaHCO₃ (sat.) and extracted with EtOAc in a 2 ml sample vial. After 20 hours, the cooled reaction mixture was carefully poured into a rapidly stirring slurry consisting of saturated Na₂CO₃ solution (50 ml) and equal volumes of crushed ice and EtOAc. Na₂CO₃ solution (sat.) was slowly added to this mixture, and until the evolution of CO₂ gas abated, and the pH of the aqueous phase was found to be neutral. The mixture was then poured into a separating funnel and extracted with EtOAc (3 x 100 ml), after which the organic fractions were washed with brine, dried with magnesium sulfate, and evaporated to afford the crude product. The residue was then flushed through a thick pad of silica (5% EtOAc in hexanes), which yielded the product **2** as an off-white powder with sufficient purity for use in the next step (505 mg, 87%).

¹H NMR (600 MHz, CDCl₃): δ = 8.15 (s, 2H, Ar); ¹³C NMR (151 MHz, CDCl₃): δ = 146.9 (C-2, C-3), 139.3 (C-6, C-7), 136.4 (C-5a, C-8a), 128.9 (C-5, C-8).

3,6,7-Trichloro-2-*N*-*tert*-butylaminoquinoxaline (3)

To a suspension of **2** (100 mg, 0.376 mmol) and cesium carbonate (61 mg, 0.188 mmol) in DMF 3 ml was added *t*-butyl amine (79 μ l, 0.752 mmol) after which the mixture was warmed to 90 °C and left to stir for 4 hours. Due to the volatility of the amine, an extra equivalent was added, and the mixture was allowed to stir for a further 2 hours. The reaction was then cooled and poured into a separating funnel containing water (30 ml) whereupon it was extracted with EtOAc (3 x 30 ml). The pooled organic fractions were subsequently washed with brine, dried with magnesium sulfate, and evaporated. The crude product could be used directly in the next step, eliminating the need for intermittent purification; however, purification of the crude material via column chromatography yielded **3** as yellow solid (82.4 mg, 72%).

^1H NMR (600 MHz, CDCl_3): δ = 7.87 (s, 1H, Ar), 7.84 (s, 1H, Ar), 5.64 (s, 1H, NH), 1.58 (s, 9H, CH_3); ^{13}C NMR (151 MHz, CDCl_3): δ = 147.8 (C-2), 140.3 (C-3), 139.6 (C-6), 134.6 (C-7), 134.2 (Ar), 128.5 (Ar), 128.4 (Ar), 127.1 (Ar), 53.0 ($\text{C}(\text{CH}_3)_3$), 28.5 ($\text{C}(\text{CH}_3)_3$).

6,7-Dichloro-2-methylsulfonyl-3-*N*-*tert*-butylaminoquinoxaline (4 or C2)^{149,150}

To a solution of **3** (100 mg, 0.329 mmol) in DMF (2 ml) was added sodium methanesulfinate (40.0 mg, 0.395 mmol) in a single portion. The reaction was left to stir at room temperature overnight. The intensely yellow reaction mixture was then poured into a separating funnel containing water (25 ml) and was then extracted using EtOAc (3 x 30 ml). The pooled organic fractions were washed with brine, dried with magnesium sulfate, and evaporated. The crude residue was purified via column chromatography (20% EtOAc in hexanes) to afford **4** as a bright yellow solid (108 mg, 94%). The obtained spectroscopic data for **4/C2** corresponded with those published in the literature.¹⁵⁰

^1H NMR (600 MHz, CDCl_3): δ = 7.93 (s, 1H, Ar), 7.82 (s, 1H, Ar), 6.98 (s, 1H, NH), 3.41 (s, 3H, $-\text{SO}_2\text{CH}_3$), 1.54 (s, 9H, *t*-Bu(CH_3)₃); ^{13}C NMR (151 MHz, CDCl_3): δ = 147.8 (C-2), 142.7 (C-3), 142.5 (Ar), 137.4 (Ar), 132.8 (Ar), 129.8 (Ar), 129.2 (Ar), 127.3 (Ar), 53.1 (CCH_3), 40.6 (SO_2CH_3), 28.6 (CCH_3).

11.2 C2 Formulation

The highly lipophilic **C2** was formulated for biological studies to a stock concentration of 1 mM in one of two preparations:

Formulation 1 (F1): DMSO (5%) in phosphate-buffered saline (PBS). The required amount of **C2** was dissolved in DMSO (this required sequential sonication and vigorous stirring to achieve a concentrated homogenous mixture.) PBS was slowly added to this solution in small measured portions for *in vivo* experiments or binding buffer for *in vitro* receptor binding experiments to bring the final concentration of the solution to 1 mM.

Formulation 2 (F2): DMSO (5%) and Cremophor EL (15%) in PBS: **C2** was likewise dissolved in DMSO to a concentration of 2 mM. The required amount of this solution was then added to an aliquot of warm Cremophor EL, which was dispensed by weight due to the surfactant's high viscosity. The resulting mixture was sequentially and repeatedly vortexed, sonicated, and centrifuged until a homogeneous mixture was obtained. PBS was then added to this mixture in 250-500 µl aliquots to bring the concentration of the solution to 1 mM (5% DMSO and 15% Cremophor EL in PBS). Between each PBS addition, the solution was vortexed, sonicated, and checked visually for **C2** precipitation to ensure homogeneity.

Both formulations were then diluted to the required concentrations for *in vitro* and *in vivo* experiments with a stock solution of the corresponding formulation buffer (5% DMSO in PBS or 5% DMSO and 15% Cremophor EL in PBS). Both formulations were prepared directly before use and held at room temperature throughout all experiments. Each mixture was checked periodically for signs of **C2** precipitation.

11.3 Radiolabeling of Exendin Derivatives for BCMI

(Lys⁴⁰-NODAGA)exendin-4 (**Ex-4**), (Lys⁴⁰-DTPA)exendin-3 (**Ex-3**), and (Lys⁴⁰-DTPA)Exendin(9-39) (**Ex(9-39)**) were obtained from Prof. Martin Gotthardt at Radboud University Medical Center (RUMC, Nijmegen, Netherlands). The peptide precursors were originally purchased from Peptide Specialty Laboratories (Heidelberg, Germany). All exendin radiolabeling protocols were carried out using the relevant published procedures.

11.3.1 (Lys⁴⁰-[¹¹¹In]In-DTPA)Exendin-3 and (Lys⁴⁰-[¹¹¹In]In-DTPA)exendin(9-39) for *In vitro* Studies¹³⁶

(Lys⁴⁰-[¹¹¹In]In-DTPA)exendin-3 ([¹¹¹In]Ex-3) and (Lys⁴⁰-[¹¹¹In]In-DTPA)exendin(9-39) ([¹¹¹In]Ex(9-39)) were both produced using [¹¹¹In]InCl₃ via the same the literature published procedure.¹³⁶ 150 MBq of [¹¹¹In]InCl₃ solution was buffered with 5 volumes of 2-(*N*-morpholino)ethanesulfonic acid (MES) buffer (0.1 M, pH 5.5) and to this solution was added 1 µg of either (Lys⁴⁰-DTPA)exendin-3 or (Lys⁴⁰-DTPA)exendin(9-39). The reaction mixture was incubated for 30 min at room temperature. A solution of ethylenediaminetetraacetic

acid (EDTA) was added to a concentration of 5 mM and the mixture was incubated for a further 5 min at room temperature. Finally, Tween 80 was added to the solution to a concentration of 0.1%. Instant thin-layer chromatography (ITLC) run on silica ITLC strips was used to assess radiolabeling efficiency (> 98%) and for quality control analysis. A running buffer of EDTA (0.1 M) in NH₄OAc (0.1 M, pH 5.5) was used to separate the radiolabeled peptide ($R_f = 0$) from unreacted [¹¹¹In]InCl₃ ($R_f = 1$). A second running buffer consisting NH₄OAc (0.25 M, pH 5.5) in methanol (1:1) was used to separate the radiolabeled peptide ($R_f = 0.2-0.8$) from insoluble colloidal residues ($R_f = 0$). The tracers were used for *in vitro* studies without further purification.

11.3.2 (Lys⁴⁰-[⁶⁴Cu]Cu-NODAGA)Exendin-4 ([⁶⁴Cu]Ex-4)¹³⁸

(Lys⁴⁰-NODAGA)exendin-4 was radiolabeled with ⁶⁴Cu via a modified procedure obtained from the literature.¹³⁸ 100 MBq [⁶⁴Cu]CuCl₂ in a 0.1 M HCl solution was dispensed (10-20 µl) into a 1.5 ml Eppendorf tube. This solution was neutralized with 1.5 volumes of ammonium acetate buffer (0.5 M, pH 6), which had been treated with Chelex 100 resin (4.6 g/200 ml). 1 µl of the resulting solution was used to confirm the pH being between 5.5 and 6.5. 4 µg of (Lys⁴⁰-NODAGA)exendin-4 (from a 1 µg/µl stock solution) was then added to the buffered [⁶⁴Cu]CuCl₂ solution and the mixture was incubated at 42 °C for 20 minutes with gentle agitation. For reaction monitoring, 0.5 µl of the reaction solution was transferred to a TLC plate, which was subsequently developed in a citrate TLC running buffer (0.1 M, pH 5). Typically, the reaction yielded the desired [⁶⁴Cu]Ex-4 in 93-99% RCY with a molar radioactivity of 104 ± 6,1 GBq/µmol and a free ⁶⁴Cu content of < 2%. The reaction solution was then diluted to a final volume of 400 µl (PBS, 0.1% Tween 20) and used for *in vivo* studies without further purification.

11.4 In Vitro Studies

All *in vitro* experiments were carried out in triplicate using Chinese hamster lung carcinoma (CHL) cells stably transfected with the GLP-1R gene (GLP-1R/CHL). The cells which were kindly provided by Prof. Martin Gotthardt from the Department of Nuclear Medicine at RUMC. The *in vitro* experiments described here (11.4) were carried out at the Department of Nuclear Medicine at RUMC.

11.4.1 Cell Culture

GLP-1R/CHL cells were cultured in Dulbecco's Modified Eagle's Medium (DMEM) with 4.5g/l D-glucose and GlutaMax-I in accordance with the procedure from Jodal *et al.*¹⁷⁹ The cell culture medium also contained 10% fetal calf serum (FCS), penicillin G (100 IU/ml), streptomycin (10 mg/ml), geneticin sulfate (500 µg/ml), sodium pyruvate (1 mM), and non-essential amino acids (0.1 mM). The cells were cultured in a humidified 5% CO₂ atmosphere at 37 °C and passaged 1:15 every 2-3 days when 90% confluent. They were then counted (C-Chip disposable counting chamber, NanoEnTek, Seoul, South Korea) and subsequently transferred to 24-well plates for *in vitro* experiments.

11.4.2 C2 Dose Calibration Experiments

To measure the **C2** dose-response curve, GLP-1R/CHL cells in a 24-well plate (0.5×10^6 cells/well in 300 μ l medium) were simultaneously treated with [^{111}In]Ex-3 (20000 cpm/well) and each formulation of **C2** (100 μ l) in an increasing concentration (0 (tracer only control), 0.1, 1, 10, 100, 1000, 10000, and 100000 nM). The cells were then incubated at 37 °C for 4 hours, after which the medium was removed, and the cells were washed with two portions of fresh medium (500 μ l). After the cells had been washed, they were lysed with 1 M NaOH (500 μ l), agitated, and transferred to gamma counter tubes. Each well was then again washed with 1 M NaOH (500 μ l), which was also transferred to the corresponding gamma counter tube. The tracer uptake was then recorded against a standard sample of [^{111}In]Ex-3 (20000 cpm) using a gamma counter. The resulting data was analyzed using Microsoft Excel. Additionally, a second dose calibration experiment was similarly carried out using a narrower range of **C2** concentrations (both formulations, 1, 5, 10 50 μ M).

11.4.3 Receptor Binding Experiments

GLP-1R/CHL cells in medium (300 μ l/well) were prepared in three 24-well plates for receptor binding experiments under different conditions (Table 15). Each experimental point was performed in triplicate. Additionally, each set of experiments was repeated as a blocking study featuring the addition of the non-radiolabeled tracer compound (1000 x excess). In each experiment, **C2** in either formulation 1 or 2 (100 μ l) was administered to the cells 20 min before the introduction of the tracer compound. In control experiments, formulation buffer 1 that was prepared free of **C2** was administered at the same time point. The cells were then incubated for 20 min after which the relevant tracer compound was introduced (20000 cpm). In blocking experiments, the non-radiolabeled tracer compound was introduced 2 minutes before the introduction of the radiolabeled tracer.

Table 15: Conditions for receptor binding experiments using different combinations of tracer and affinity modulator formulations at different temperatures. Each set of experimental conditions was repeated in triplicate. Each set of experiments was repeated as a blocking study that included the corresponding non-radioactive standard compound (1000 x excess).

Expt	Tracer	Temp(°C)	Modulator	Rationale
A	[^{111}In]Ex-3	37	None (Control)	Optimized uptake experiment and control
			C2 (Formulation 1)	
			C2 (Formulation 2)	
B	[^{111}In]Ex-3	0	None (Control)	Internalization arrested experiment. Surface binding only.
			C2 (Formulation 1)	
			C2 (Formulation 2)	
C	[^{111}In]Ex(9-39)	37	None (Control)	Non-internalizing truncated exendin derivative. (antagonist)
			C2 (Formulation 1)	
			C2 (Formulation 2)	

The cells in experimental sets A) and C) were then incubated at 37 °C for 4 hours after the introduction of the tracer. In experimental set B), the cells were incubated at 0 °C by sealing the 24-well plate and covering it in ice. After 4 hours, the binding buffer was removed, and the cells were washed with two portions of the

binding buffer. After washing, the cells were lysed with 1 M NaOH (500 μ l), and the resulting cell lysate was transferred to gamma counter tubes. The wells were washed with an additional portion of 1 M NaOH (500 μ l), after which the washing solution was again transferred to the corresponding gamma counter tubes. The amount of activity was then quantified in the gamma counter against a reference standard solution of the corresponding tracer (20000 cpm). The resulting data was analyzed using Microsoft Excel. The statistical significance of the differences between the experimental groups were calculated using a two-sample two-tailed Student's t-test assuming unequal variances.

11.5 *In Vivo* Studies

The experimental design, preparation, data acquisition, and data analysis described below for the *in vivo* imaging studies towards the investigation of **C2** induced tracer uptake enhancement were carried out by Filippo Michelotti.

11.5.1 *In vivo* Experiments to Validate Tracer Specificity

INS-1 cells were kindly provided by Prof. Martin Gotthardt from the Department of Nuclear Medicine at RUMC. $0.5-1 \times 10^6$ cells were cultured in a 175 cm² cell culture flask with 15 ml of Roswell Park Memorial Institute (RPMI) 1640 cell culture medium, 10% FCS, 4-(2-Hydroxyethyl)piperazine-1-ethanesulfonic acid (HEPES, 10 mM), sodium pyruvate (1 mM), β -mercaptoethanol (50 μ M), penicillin (100 UI/ml), and streptomycin (100 μ g/ml). The cells were incubated at 37 °C in a humidified 5% CO₂ atmosphere and were passaged every 5-7 days when 90% confluent (less than 20 passages). The cells were prepared for inoculation by resuspending them in PBS, after which a sample of the suspended cells was counted using a Neubauer cell counting chamber. 1×10^6 cells (in 200 μ l) were then subcutaneously inoculated at the right shoulders of 6–8-week-old female BALB/c nude mice (*Charles River*). The tumors were allowed to grow for 2-4 weeks until they reached a diameter of 2-5 mm. Blood glucose levels were regularly monitored using a blood glucose analyzer (HemoCue Hb 201+, HCE, Staines, UK) to ensure that the blood glucose levels remained above 30 mg/dl.

To evaluate and establish the specificity of [⁶⁴Cu]Ex-4 uptake into the GLP-1R expressing INS-1 cell line, a group (n = 2) of anesthetized (isoflurane, O₂) BALB/c nude mice bearing INS-1 xenograft tumors on their right shoulders were injected with [⁶⁴Cu]Ex-4 (± 0.12 MBq/g bodyweight) as a single bolus through a tail vein catheter. A second group (n = 2) received non-radiolabeled Ex-4 (40 mg/kg) two minutes prior to tracer injection. The mice were imaged with a 20-minute static PET frame after 1 hour of uptake time, and a Student's t-test was used to confirm the difference between the 2 groups.

11.5.2 C2 Enhanced Tumor Uptake

A cohort of INS-1 xenograft bearing BALB/c nude mice was split into 8 groups of 4 animals and each group was pretreated with varying doses of **C2** (15, 25, 35 mg/kg) at varying time points (0, 15, 30 min) prior to

tracer injection (Table 16, Figure 61). All injections were made through a tail vein catheter. A control group (Table 16, group 1) was treated with the **C2** free formulation buffer simultaneously with the injection of the tracer (0 minutes). All mice were given a single bolus injection of [⁶⁴Cu]Ex-4 (\pm 0.12 MBq/g bodyweight) through the same catheter. Representative mice (n =2) from groups 1 and 3 were imaged using dynamic PET frames to quantify differences in the time-activity curves (TAC). All other mice were imaged using 15-minute static PET frames after 1 hour of uptake time. The mice were again imaged after 24 hours. After 48 hours, the mice were sacrificed and subjected to *ex vivo* biodistribution studies using a gamma counter.

Table 16: The nine groups of INS-1 xenograft bearing mice were injected at different time points prior to tracer injection with varying doses of the GLP-1R affinity modulator **C2**. This table corresponds to the data presented above in Figure 30, B.

Group	1	2	3	4	5	6	7	8	9
C2 dose (mg/kg)	0	15	25	35	15	25	35	25	35
C2 injection time point (min prior to [⁶⁴ Cu]Ex-4 injection)	0	15	15	15	0	0	0	30	30

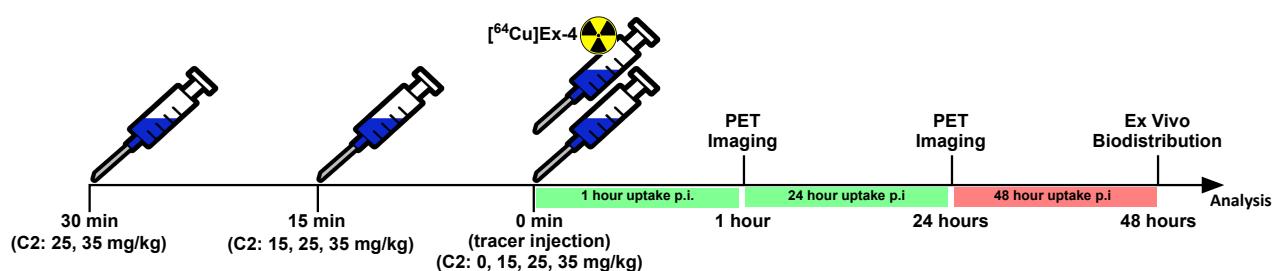


Figure 61: The experimental time plan to investigate the tracer uptake enhancing properties of **C2**. **C2** (0, 15, 25, or 35 mg/kg) was injected 30, 15, and 0 min prior to the injection of the [⁶⁴Cu]Ex-4 tracer. The mice were imaged 1 and 24 hours post-injection and were subjected to *ex vivo* biodistribution analysis after 48 hours.

11.5.3 Tracer Infusion with a **C2** Bolus Challenge in Transplanted Islets

For the preparation of a transplanted islet β cell model, a cohort of 40 CH3 mice was prepared and maintained for one week before the isolation and transplantation of the pancreatic islets. Thirty mice were sacrificed and used as islet donors, while ten mice were used as recipients. The pancreatic islets from the donor mice were isolated and transplanted into the rear calf muscles of the recipient CH3 mice using the protocol developed by Eter *et al.*^{180,181} From the resulting cohort of ten CH3 mice bearing transplanted islet grafts, four mice (2 groups, n = 2) were used for the study described below.

The mice were imaged six weeks after islet transplantation using dynamic PET imaging. Each mouse was fitted with two tail vein catheters under narcosis. Through the first catheter, the mice received a constant infusion of [⁶⁴Cu]Ex-4 over 50 minutes (120 μ l/hour, 0.24 MBq/g bodyweight total injected dose). Dynamic PET data were acquired from the start of the infusion protocol until 10 minutes after its completion (60 min total). After 20 minutes of [⁶⁴Cu]Ex-4 infusion, the first group of mice received 2 mg/kg **C2** in formulation 2, while the second group received 5 mg/kg **C2** through the second tail vein catheter. From the acquired data,

tracer uptake curves from the islet grafts, heart, and muscle were quantified. The resulting TAC curves are displayed in Figure 31 (*vide* 6.4.3).

11.5.4 Tracer Infusion with C2 Infusion in Native Pancreatic Islets

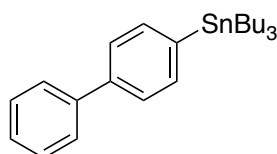
A bolus-infusion injection protocol to induce **C2** mediated tracer uptake enhancement into healthy native pancreatic islets in CH3 mice was developed. Healthy littermate CH3 mice were fitted with a single tail vein catheter, and a solution of **C2** (5 mg/kg in formulation 2) and [⁶⁴Cu]Ex-4 (0.24 MBq/g) was infused into each mouse (n = 3) via bolus-infusion protocol. The mice received an initial bolus injection of the **C2**/[⁶⁴Cu]Ex-4 mixture over 5 minutes (120 μmol/min; **C2**: 2 mg/kg; [⁶⁴Cu]Ex-4: 0.1 MBq/g) followed by a constant infusion of the mixture (80 μmol/min; **C2**: 3 mg/kg; [⁶⁴Cu]Ex-4: 0.14 MBq/g) for a further 45 minutes. As a control experiment, an additional group of mice (n =3) received [⁶⁴Cu]Ex-4 (0.24 MBq/g) and **C2** free vehicle buffer via the same injection protocol. The mice were imaged for 60 minutes using dynamic PET imaging, starting at the beginning of the bolus injection program. After the acquisition of the imaging data, ROIs were drawn to quantify the tracer uptake in the heart, renal cortex, and native pancreas. The resulting TAC curves are displayed in Figure 32 (*vide* 6.4.3).

Chapter 12: The Use of DoE for the Optimization of Copper-Mediated Radiofluorinations (CMRFs)

Parts of the work featured in this section have been published.⁸⁶

12.1 Organic Synthesis

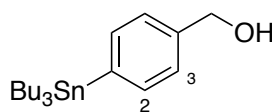
4-(Tributylstanyl)biphenyl (**5**)^{73,86}



A reaction flask fitted with a rubber septum was purged with argon and charged with 4-bromobiphenyl (500 mg, 2.15 mmol) in dry Et₂O (20 ml). The reaction vessel was cooled to -78 °C using an acetone/dry ice bath under a stream of argon, after which *n*-BuLi in hexane (2.5 M, 950 μl, 2.36 mmol) was added through the septum to the stirring solution. The reaction mixture was allowed to warm to room temperature and left to stir for 1 hour. The vessel was again cooled to -78 °C, after which tributyltin chloride (780 μl, 2.36 mmol) was added to the organolithium derivative in dropwise fashion. The reaction was warmed to room temperature and left to stir overnight. After the reaction deemed complete, it was quenched with sat. ammonium chloride (10 ml), diluted with Et₂O (10 ml), and poured into a separating funnel containing water (30 ml) and Et₂O (30 ml). The product was then extracted from the aqueous phase with Et₂O (3 x 30 ml), and the organic fractions were collected and dried with magnesium sulfate. The solvent was then removed under reduced pressure, and the remaining residue was purified by silica chromatography (1% - 10% EtOAc in hexanes) to afford **5** as a colorless oil (798 mg, 84%). The acquired analytical data were found to be in agreement with the previously published data.⁷³

¹H NMR (600 MHz, CDCl₃): δ = 7.64 – 7.59 (m, 2H, Ar), 7.59 – 7.50 (m, 4H, Ar), 7.48 – 7.40 (m, 2H, Ar), 7.37 – 7.32 (m, 1H, Ar), 1.67 – 1.48 (m, 6H, SnBu₃-CH₂), 1.36 (m, 6H, SnBu₃-CH₂), 1.16 – 1.02 (m, 6H, SnBu₃-CH₂), 0.91 (t, *J* = 7.3 Hz, 9H, SnBu₃-CH₃); ¹³C NMR (151 MHz, CDCl₃): δ = 141.5 (Ar), 141.0 (Ar), 140.9 (Ar), 137.0 (Ar), 128.9 (Ar), 127.3 (Ar), 127.3 (Ar), 126.8 (Ar), 29.3 (SnBu₃), 27.6 (SnBu₃), 13.8 (SnBu₃), 9.8 (SnBu₃).

4-(Tributylstannyl)benzyl alcohol (**9**)^{73,86,167}



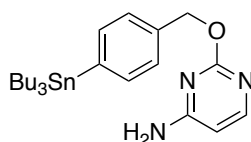
4-Iodobenzyl alcohol (2.0 g, 8.53 mmol), bis(tributyltin) (6.5 ml, 12.80 mmol) and lithium chloride (1.81 g, 42.66 mmol) were added to an argon-purged reaction flask fitted with a reflux condenser. The mixture was

dissolved in freshly distilled toluene (30 ml), and tetrakis(triphenylphosphine)palladium(0) (492 mg, 0.853 mmol, 5 mol%) was added. The reaction mixture was then warmed to reflux temperature for 1.5-3 hours with vigorous stirring. After TLC confirmed the formation of a product, the reaction was quenched with a 20% aqueous solution of potassium fluoride, and the grey/black precipitate was filtered through a pad of Celite. The biphasic filtrate was poured into a separating funnel containing brine (200 ml), and the product was extracted using EtOAc (3 x 100 ml). The organic fractions were pooled, dried with magnesium sulfate, and evaporated under reduced pressure. The crude product residue was then purified via column chromatography (1 - 10% EtOAc in hexanes) to afford **9** as a clear liquid (1.93 g, 57%).

Alternatively, a larger-scale synthesis of **9** was adapted from the published procedure.¹⁶⁷ 4-Bromobenzyl alcohol (2.00 g, 15.80 mmol) was dissolved in anhydrous THF (80 ml) under a stream of argon in a two-neck Schlenk flask fitted with two equalizing dropping funnels. The reaction vessel was cooled to -78 °C using an acetone/dry ice bath under a positive pressure of argon, after which *n*-BuLi in hexanes (2.5 M, 12.72 ml, 31.80 mmol) was added dropwise via the first dropping funnel. The reaction was stirred at -78 °C for 1.5 hours, after which tributyltin chloride was added dropwise through the second dropping funnel over a period of 45 min. The reaction was left to stir at -78 °C under positive pressure of argon for 2 hours. It was then allowed to warm to room temperature and left to stir over night, after which it was quenched with saturated ammonium chloride solution (10 ml), diluted with Et₂O (20 ml), and transferred to a separating funnel containing saturated ammonium chloride (90 ml). The product was extracted with Et₂O (3 x 100 ml), the organic fractions were washed with brine (50 ml), dried with magnesium sulfate, and evaporated under reduced pressure. The resulting residue was finally purified by silica chromatography (5 - 20% EtOAc in hexanes) to afford **9** as a clear oil (3.52 g, 56%). NMR data were found to be identical to previously published and obtained spectra.¹⁶⁷

¹H NMR (600 MHz, CDCl₃): δ = 7.53 – 7.41 (m, 2H, Ar), 7.37 – 7.30 (m, 2H, Ar), 4.68 (s, 2H, CH₂OH), 1.54 (m, 6H, SnBu₃-CH₂), 1.33 (m, 6H, SnBu₃-CH₂), 1.13 – 0.98 (m, 6H, SnBu₃-CH₂), 0.89 (t, *J* = 7.4, Hz, 9H, SnBu₃-CH₃);
¹³C NMR (151 MHz, CDCl₃): δ = 141.5 (Ar), 140.6 (Ar), 136.9 (Ar), 126.8 (Ar), 65.6 (CH₂OH), 29.2 (SnBu₃), 27.5 (SnBu₃), 13.8 (SnBu₃), 9.7 (SnBu₃).

4-((4-(Tributylstannyl)phenyl)methoxy)pyrimidin-4-amine (**7**)⁸⁶

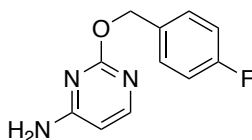


A solution of **9** (1.68 mg, 4.24 mmol) in DMSO (2 ml) was added in dropwise fashion to a vigorously stirring suspension of sodium hydride (60% in mineral oil, 308 mg, 7.70 mmol) in DMSO (5 ml) over a period of 2 minutes. The resulting solution was left to stir for 1 hour at room temperature, after which 2-chloro-4-

aminopyrimidine (500 mg, 3.85 mmol) was added in small portions under a gentle flow of argon. The resulting reaction mixture was warmed to 110 °C for 2 hours. When the reaction was deemed to be complete, it was diluted with EtOAc (10 ml) and poured into a separating funnel containing aqueous saturated ammonium chloride (250 ml). The product was then extracted with EtOAc (3 x 80 ml), dried with magnesium sulfate, evaporated under reduced pressure, purified via column chromatography (10 - 80% EtOAc in hexane) to afford **7** as a thick oil (1.12 g, 63%).

^1H NMR (600 MHz, CDCl_3): δ = 8.01 (d, J = 5.8 Hz, 1H, ArCH), 7.51 – 7.34 (m, 4H, Ar-SnBu₃), 6.14 (d, J = 5.8 Hz, 1H, ArCH), 5.35 (s, 2H, CH₂O), 5.15 (s, 2H, NH₂), 1.53 (m, 6H, SnBu₃-CH₂), 1.38 – 1.27 (m, 6H, SnBu₃-CH₂), 1.15 – 0.95 (m, 6H, SnBu₃-CH₂), 0.88 (t, J = 7.3 Hz, 9H, SnBu₃-CH₃); ^{13}C NMR (151 MHz, CDCl_3): δ = 165.0 (NCON), 164.8 (Ar), 156.8 (Ar), 141.7 (Ar), 136.6 (Ar), 136.4 (Ar), 127.5 (Ar), 99.7 (Ar), 68.9 (CH₂), 29.2 (SnBu₃), 27.5 (SnBu₃), 13.8 (SnBu₃), 9.7 (SnBu₃); HPLC: (retention time = 10.2 min); HPLC-MS (ESI) (m/z): [M] calcd. for C₂₃H₃₇N₃OSn, 491.20; found [M+H]⁺, 492.1.

4-((4-Fluorophenyl)methoxy)pyrimidin-4-amine ([¹⁸F]pFBC, **8**)⁸⁶



In an argon-purged reaction vessel, a solution 4-fluorobenzyl alcohol (175 mg, 1.385 mmol) in DMF (1 ml) was added in dropwise fashion to a cooled (0 °C) suspension of sodium hydride (60% in mineral oil, 70 mg, 1.731 mmol) in DMF (2 ml). The resulting solution was allowed to warm to room temperature and stir for 1 hour. The reaction mixture was then again cooled to 0 °C in an ice/water bath, after which 2-chloro-4-aminopyrimidine (150 mg, 1.154 mmol) was added to the solution in small portions under a gentle stream of argon. The reaction mixture was then heated at 100 °C for 6 hours, after which it was cooled to room temperature and left to stir overnight. A saturated solution of NH₄Cl (10 ml) was added to the reaction mixture, and the resulting solution was poured into a separation funnel containing NH₄Cl (sat.) and EtOAc (50 ml). The compound was then extracted from the aqueous phase with EtOAc (3 x 50 ml), the organic fractions were pooled and dried with magnesium sulfate. After concentrating the residue onto silica gel, the product was purified via column chromatography (15 - 80% EtOAc in hexane) to afford **8** as a white crystalline solid (235 mg, 93%).

^1H NMR (600 MHz, DMSO-*d*₆): δ = 7.9 (d, J = 5.7 Hz, 1H, HC=CH), 7.5 – 7.4 (m, 2H, Ar), 7.2 – 7.1 (m, 2H, Ar), 6.9 (s, 2H, NH₂), 6.1 (d, J = 5.7 Hz, 1H, HC=CH), 5.2 (s, 2H, OCH₂Ph); ^{13}C NMR (151 MHz, DMSO-*d*₆): δ = 165.4 (NCN), 164.5 (CNH₂), 161.6 (d, J_{CF} = 243.5 Hz, (CH)₂CF), 156.2 (HC=CH), 133.7 (Ar), 129.9 (d, J_{CF} = 8.3 Hz, (CH)₂(CH)₂CF), 115.0 (d, J_{CF} = 21.2 Hz, (CH)₂(CH)₂CF), 99.6 (HC=CH), 66.4 (CH₂); HPLC: (retention time = 4.34 min); HPLC-MS (ESI) (m/z): [M] calcd. for C₁₁H₁₀FNO, 219.08; found [M+H]⁺, 220.1.

12.2 General Procedure for DoE Design and Data Analysis

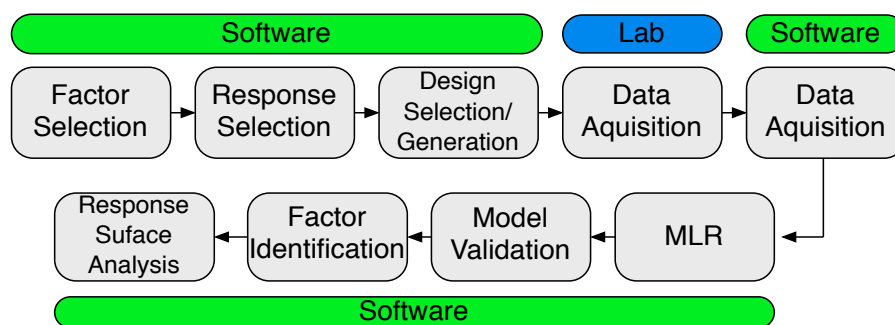


Figure 62: The general DoE workflow from factor selection to factor identification and response surface plotting.

All experimental designs were constructed and analyzed using *MODDE Go 12* software (Umetrics, Umeå, Sweden). In general (Figure 62), the factors of interest (quantitative and qualitative) were chosen, and their ranges were defined. Radiochemical conversion (%RCC) via radio-TLC was chosen as the response variable (Y_i) in all cases. This information was used to generate a DoE worksheet table, which was used to calculate the required reagent amounts for each experimental run. The experiments were then carried out in a randomized order. In DoE studies where temperature was a factor, runs were performed in the order of increasing temperature for practical reasons. The temperatures of the hotplates were allowed sufficient time to reach thermal equilibrium inbetween each run at a new temperature. The data were checked for normality and transformed appropriately to ensure a normal distribution, after which a regression model was generated using multiple linear regression (MLR). Non-significant effect terms were then removed to refine the model, after which the summary statistics were evaluated to identify outliers, check the goodness of model fit, and to ensure a valid and predictive regression model. In the case of factor screening studies, significant and non-significant factors could then be identified, and this information could be used to plan further RSO experiments or guide general decision-making. In the case of the RSO studies, a response surface could be plotted and analyzed to determine the optimal reaction conditions or estimate the response surface vector (steepest slope) that would predict the direction/location of where the optimal conditions could reside.

12.3 Development of Base-Free ^{18}F Processing Conditions

QMA cartridges were preconditioned by passing a 10 ml solution of KOTf (90 mg/ml) through each cartridge from the female end. This was followed with 10 ml of air, then 10 ml water, and finally 10 ml air. Depending on the experiment, an aliquot of [^{18}F]fluoride from a cyclotron target wash was measured in a dose calibrator (300-600 MBq) and then passed over the QMA cartridge from either the female end or through the male end using a female-female Luer adapter. The amount of ^{18}F trapped on the cartridge was again measured to calculate the QMA trapping efficiency (in all cases > 95%). Residual water on the QMA resin was washed away by passing 1 ml MeOH through the cartridge from the female end, followed by a stream of argon for 1 minute.

The cartridge was then measured in a dose calibrator to determine the amount of activity lost to the washing step. The ^{18}F was eluted from the QMA cartridge by passing a solution of TBAOTf (10 mg) in MeOH (1 ml) over the cartridge from the female end. The ^{18}F bearing eluent was then collected in a reaction vial, which was subsequently sealed with a rubber septum, and the radioactivity was again measured. The methanol was removed by evaporation at 80 °C under a stream of argon gas for 2 min. The resulting ^{18}F residue was then reconstituted in reaction solvent and used for subsequent radiochemical experiments.

The % ^{18}F recovery (not decay corrected) was calculated by the following formula:

$$\% \text{ }^{18}\text{F Recovery} = \frac{\text{Activity Trapped on QMA (MBq)}}{\text{Activity Eluted from QMA (MBq)}} \times 100$$

12.4 General Radiochemistry Procedures for DoE Studies

12.4.1 General CMRF Procedure 1⁸⁶

Aqueous [^{18}F]fluoride delivered from a cyclotron target wash was passed over a QMA cartridge which had been previously conditioned by sequentially passing NaHCO_3 (1 M, 10 ml), air (10 ml), water (10 ml) and air (10 ml) through it. The trapped [^{18}F]fluoride was eluted using the published QMA eluent (KOTf (10 mg), K_2CO_3 (50 μg) in water (550 μl)).⁷³ The eluted ^{18}F was dispensed in 80 μl aliquots (200-300 MBq) into the required number of 5 ml Wheaton v-vials (typically 6 per day (block)). 1 ml MeCN was added to each vial, the vials were capped and sealed using a silicon septum and were then subjected to azeotropic drying under a stream of argon gas. An additional two aliquots of MeCN (1 ml) were added to ensure the complete azeotropic removal of water. Each reaction mixture was prepared in DMA as required by the DoE worksheet table. The reaction mixtures were then injected into the reaction vials containing dry [^{18}F]fluoride and allowed to stir under the time, atmosphere, and temperature conditions required by the experimental design. When complete, each reaction was quenched with HCl (0.25 M) (or HPLC eluent for basic compounds) and sampled for radio-TLC (for %RCC quantification) and radio-HPLC analysis (on representative samples for validation of compound identity).

12.4.2 General CMRF Procedure 2

Aqueous [^{18}F]fluoride delivered from a cyclotron target wash was passed over a QMA cartridge that had been previously conditioned by sequentially passing KOTf (90 mg/ml, 10 ml), air (10 ml), water (10 ml) and air (10 ml) through it. The cartridge was then washed with MeOH (1 ml) to remove any residual water bound to the resin, after which the cartridge was purged with a stream of dry argon for ca. 30 seconds. The [^{18}F]fluoride was then eluted from the cartridge using a solution of TBAOTf (10 mg) in MeOH (1 ml). This procedure was able to recover 85-90% of the trapped ^{18}F . The eluted ^{18}F solution could then either be aliquoted into separate reaction v-vials for optimization studies or used as a full batch elution for a single radiosynthesis. Once the ^{18}F solution had been collected in a reaction vial containing a magnetic stirrer bar, the vial was sealed, and

the MeOH solvent was removed by evaporation at 85 °C for 2-4 min under a stream of argon gas. After the removal of the solvent was complete, the resulting [¹⁸F]TBAF residue could be subjected to the desired radiochemical reaction conditions. Each reaction mixture was prepared fresh from reagent stock solutions in DMA (1 mg/10 µl). The reaction mixtures were then injected into the reaction vials containing [¹⁸F]TBAF and were allowed to stir under the required experimental conditions. When complete, each reaction was quenched with HCl (0.25 M) (or HPLC eluent for basic compounds) and sampled for radio-TLC (for %RCC quantification, reported in the DoE worksheet tables in the results section) and radio-HPLC analysis (on representative samples for validation of compound identity).

12.5 DoE Optimization of the CMRF of Arylstannanes

12.5.1 DoE Factor Screening Study Using Precursor 5⁸⁶

A factor screening DoE study was designed and carried out according to the **general procedure for DoE design and data analysis**. A fractional factorial (RES V+) DoE design was selected to evaluate the influence of 5 experimental factors on a model copper-mediated radiofluorination of **5** (4.5 µmol). The 2_{V}^{5-1} design was performed in 4 blocks consisting of four experimental points and two centerpoints each (six runs per block) with a total of 24 runs. The factors selected were temperature (Temp: 100-140 °C), reaction solvent volume (DMA: 400-1000 µl), atmosphere (Atm: argon vs air(qualitative)), Cu(OTf)₂ loading (Cat: 1-4 eq), and pyridine loading (Lig: 4-30 eq). After the worksheet tables were generated using *Modde Go 12*, the experiments were carried out in accordance with **general CMRF procedure 1**. Radio-TLCs were performed from each run using a mixture of 10% EtOAc in hexanes as the mobile phase. To ensure the correct compound identity, radio-HPLC was performed on representative samples using the general radio-HPLC conditions described above. The data were transformed to ensure normality, after which the experimental effects were evaluated for significance. These data were used to guide future response surface optimization studies.

12.5.2 DoE Factor Response Surface Optimization of [¹⁸F]pFBC ([¹⁸F]8)⁸⁶

To optimize the reaction parameters of the copper-mediated radiofluorination **7** to **8** ([¹⁸F]pFBC), an orthogonal central composite design (OCCD) response surface optimization (RSO) study was carried out according to the **general procedure for DoE design and data analysis**. The OCCD design was constructed to investigate the effects of copper triflate loading (1-4 eq), pyridine loading (10-40 eq), and substrate loading (10-30 µmol). The study consisted of eight vertex points (blue, on the vertices of the reaction space cube), six starpoints (positioned in the center of the faces of the cube at a distance $\alpha = 1.353$ from the center of the investigated reaction space) and three replicate centerpoints with a total of 17 runs. The experiments were performed using **general CMRF procedure 1**. Radio-TLCs were performed from each run using a mixture of 10% MeOH in DCM as the mobile phase. To ensure the correct compound identity, radio-HPLC was performed on representative samples using the general radio-HPLC conditions described above. The resulting %RCC data was transformed and subjected to MLR, after which the resulting model was refined by

removing non-significant non-main effects. The refined model was then used to plot a response surface that was analyzed to reveal the behavior of the process over the investigated factor ranges and predict optimal reaction conditions.

12.5.3 DoE Factor Response Surface Optimization of [^{18}F]pFBnOH ([^{18}F]10)⁸⁶

A Box-Behnken design (BBD) was used to optimize the synthesis of [^{18}F]4-fluorobenzyl alcohol ([^{18}F]pFBnOH) from 4-(tributyltin)benzyl alcohol. The BBD was constructed and carried out according to the **general procedure for DoE design and data analysis**. The study investigated the effects of copper triflate loading (1-5 eq), pyridine loading (10-40 eq), and substrate loading (5-20 μmol). The study consisted of 12 experimental points (positioned at the centers of the edges of the cube defined the investigated factor ranges) and 3 replicate centerpoints with a total of 15 runs. The data was acquired in accordance with **general CMRF procedure 1**. Radio-TLCs were performed from each run using a mixture of 80% EtOAc in hexanes as the mobile phase. To ensure the correct compound identity, radio-HPLC was performed on representative samples using the general radio-HPLC conditions described above. The acquired %RCC data was modeled, corrected, and analyzed per the **general procedure for DoE design and data analysis**. The resulting regression model was used to construct a response surface that was analyzed to reveal process behavior and predict optimal reaction conditions.

12.6 D-Optimal Response Surface Optimization of [^{18}F]10 from Arylboronic Acid Pinacol Esters

To study the synthesis of [^{18}F]10 from 4-(hydroxymethyl)phenylboronic acid pinacol ester (**4-BPin-BnOH**) a D-optimal DoE study was constructed to examine the effects of precursor amount (5-30 μmol), $\text{Cu}(\text{OTf})_2$ amount (4-40 μmol), pyridine amount (25-550 μmol), and *n*-BuOH (0-75% total reaction volume in DMA). The design worksheet table was generated by the D-optimal design algorithm featured in *MODDE Go 12*. The study was planned and analyzed using the **general procedure for DoE design and data analysis**, and radiochemical experiments were carried out in accordance with **general CMRF procedure 2**. Radio-TLCs were performed from each run using a mixture of 80% EtOAc in hexanes as the mobile phase. To ensure the correct compound identity, radio-HPLC was performed on representative samples using the general radio-HPLC conditions described above. After the analysis of the resulting regression model and response surface plot, the “sweet-spot” optimizer tool in *MODDE Go 12* was used to locate the optimal reaction conditions. Validation runs were carried out using the optimal reaction conditions following **general CMRF procedure 2** under both air ($n = 3$) and argon ($n = 3$) atmospheres. For each validation experiment, a single full batch of [^{18}F]fluoride was processed using **general CMRF procedure 2**.

12.7 Automated Radiosynthesis

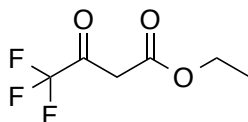
Both [^{18}F]pFBC ([^{18}F]8) and [^{18}F]pFBnOH ([^{18}F]10) were automated using an Elixys FLEX/CHEM synthesizer coupled to a PURE/FORM purification and formulation module; however, these procedures are outside the

scope of this thesis and will not be discussed further. The use of the Elixys synthesizer for the production of [¹⁸F]F-BETP for β cell imaging is described in sections **8.4.3** (*vide supra*) and **13.3** (*vide infra*).

Chapter 13: The Synthesis of ^{18}F Labeled BETP Derivatives

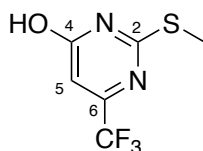
13.1 Organic Synthesis

Ethyl 4,4,4-trifluoro-3-oxobutanoate (**11**)



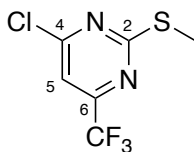
Under a blanket of argon, small, clean slices of sodium metal (3.9 g, 0.14 mmol) were dissolved in dry absolute ethanol (40 ml), and this solution was then added to a stirring solution of ethyl 2,2,2-trifluoroacetate (16.75 ml, 140.85 mmol) and EtOAc (18.81 ml; 140.85 mmol). The reaction flask was fitted with a reflux condenser, flushed with argon, and refluxed overnight. The reaction was monitored by NMR, and when found to be complete, it was quenched by the addition of H_2SO_4 (2 M 10 ml). Water (100 ml) was then added to the reaction mixture, which was subsequently poured into a separating funnel, and extracted with Et_2O (3 x 50 ml). The organic fractions were dried with magnesium sulfate and carefully evaporated to remove the bulk of the volatile solvents. The concentrated product mixture was then distilled to yield the pure product (bp: 126-129 °C at 759 mmHg. Lit bp: 129-130 °C at 760 mmHg (from commercial supplier)) as a clear liquid (8.2 g, 32%). The product **11** was used directly in the next step without further analysis.

2-(Methylthio)-6-(trifluoromethyl)pyrimidin-4-ol (**12**)¹⁸²



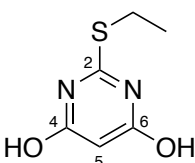
Sodium methoxide (4.8 g, 89.7 mmol) was dissolved in dry methanol (90 ml) under a stream of argon, and to this solution was added thiourea (3.10 g, 40.76 mmol) and **11** (7.5 g, 40.76 mmol). The resulting mixture was then refluxed for 6 hours, at which point TLC showed the formation of a new UV-active spot and the consumption of the starting materials. The reaction solvents were removed under reduced pressure and the residue was taken up with water (100 ml). Dimethyl sulfate (3.9 ml, 40.76 mmol) was then added dropwise to the vigorously stirring solution, after which the reaction was left to stir for a further 24 hours. Finally, the reaction was neutralized with concentrated HCl, which resulted in the formation of **12** as a white precipitate. Once dried under high vacuum, it was found to be pure enough for use in subsequent reactions (3.66 g, 43%).

^1H NMR (600 MHz, CDCl_3): δ = 6.57 (s, 1H, H-5), 2.64 (s, 3H, CH_3); ^{13}C NMR (151 MHz, CDCl_3): δ = 164.87 (C-2), 164.36 (C-4), 153.70 (q, $J_{\text{CF}} = 35.7$ Hz, C-6), 120.34 (q, $J_{\text{CF}} = 275.1$ Hz, CF_3), 108.40 (q, $J_{\text{CF}} = 3.2$ Hz, C-5), 13.63 (SCH_3).

4-Chloro-2-(methylthio)-6-(trifluoromethyl)pyrimidine (13)

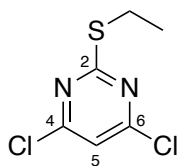
POCl₃ (12.5 ml) was added to a mixture of **12** (3.0 g, 14.30 mmol) and trimethylamine (2.19 ml, 15.71 mmol) under a stream of argon. The mixture was then heated to 100 °C for 3 hours. The reaction mixture was slowly poured into a vigorously stirring slurry of crushed ice (ca. 100 g), saturated sodium bicarbonate (100 ml) and EtOAc (100 ml). Portions of solid sodium bicarbonate were added until carbon dioxide gas ceased to evolve, and the pH was found to be neutral. The slurry was then poured into a separating funnel, where it was extracted with EtOAc (2 x 100 ml). The organic fractions were washed with brine, dried with magnesium sulfate, and evaporated to yield **13** as a clear liquid (2.9 g, 88%) that required no further purification.

¹H NMR (600 MHz, CDCl₃): δ = 6.58 (s, 1H, H-5), 2.64 (s, 3H, CH₃); ¹³C NMR (151 MHz, CDCl₃): δ = 164.85 (C-2), 164.29 (C-4), 153.69 (q, *J*_{CF} = 35.7 Hz, C-6), 120.34 (q, *J*_{CF} = 274.9 Hz, CF₃), 108.42 (q, *J*_{CF} = 3.2 Hz, C-5), 13.63 (SCH₃).

2-(Ethylthio)pyrimidine-4,6-diol (24)

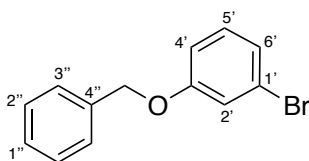
Thiobarbituric acid (1.0 g, 6.9 mmol) was added portion-wise to a rapidly stirring aqueous solution (10 ml) of potassium hydroxide (1.17 g, 20.9 mmol). A solution of ethyl bromide (515 μl, 6.9 mmol) in ethanol (10 ml) was then added to the reaction mixture, after which the solution was brought to reflux for 3 hours. After cooling to room temperature, the reaction was transferred to a conical flask for precipitation. Acidification (pH 3-4) of the solution resulted in the slow formation of white crystals, and the resulting suspension was allowed to sit in a refrigerator overnight. The product **24** was collected via vacuum filtration, washed with cold water, and allowed to air-dry overnight (766 mg, 64%).

¹H NMR (600 MHz, CDCl₃): δ = 11.71 (Brs, 2H, OH), 5.11 (s, 1H, H-5), 3.07 (q, *J* = 7.3 Hz, 2H, SEt), 1.27 (t, *J* = 7.3 Hz, 3H, SEt); ¹³C NMR (151 MHz, CDCl₃): δ = 167.3 (C-2), 162.81 (C-4, C-6), 86.0 (C-5), 24.5 (SCH₂CH₃), 15.1 (SCH₂CH₃).

4,6-Dichloro-2-(ethylthio)pyrimidine (25)

POCl_3 (8 ml, 85.75 mmol) was added to a two-neck round bottom flask containing **24** (1.0 g, 5.8 mmol) at 0 °C. To this mixture was added triethylamine (2.4 ml, 19.1 mmol) with vigorous stirring. The flask was fitted with a condenser and a two-way gas line adapter. The input line on the gas adapter was fitted with an argon line, and the output line was connected to a Drechsel bottle trap containing a solution of NaHCO_3 (sat.) to trap any resulting fumes. The reaction flask and condenser were purged with argon, and the reaction was heated to reflux for 1 hour. The reaction mixture was then allowed to cool to room temperature, after which it was slowly poured into a slurry of ice (ca. 50 g), Na_2CO_3 (sat., 50 ml), and EtOAc (100 ml). Saturated Na_2CO_3 solution was added to the slurry until the evolution of CO_2 gas abated, and the pH of the aqueous phase was found to be above 7. The mixture was poured into a separating funnel, and the product was extracted with EtOAc (3 x 100 ml). The organic fractions were collected, washed with brine, dried with magnesium sulfate, and concentrated under reduced pressure. The resulting residue was diluted with EtOAc and filtered through a 4 (diameter) X 6 cm pad of silica gel. The solvent was then again removed under reduced pressure to afford **25** (1.08 g, 89%), which was found to be sufficiently pure for use in the next step.

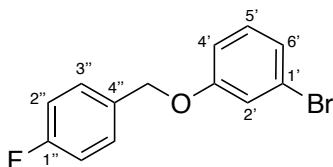
^1H NMR (600 MHz, CDCl_3): δ = 7.02 (s, 1H, H-5), 3.15 (q, J = 7.4 Hz, 2H, SET), 1.40 (t, J = 7.4 Hz, 3H, SET); ^{13}C NMR (151 MHz, CDCl_3): δ = 174.4 (C-2), 161.5 (C-4, C-6), 115.9 (C-5), 26.0 (SCH_2CH_3), 14.1 (SCH_2CH_3); HPLC: (retention time = 8.75 min); HPLC-MS (ESI) (m/z): [M] calcd. for $\text{C}_6\text{H}_6\text{Cl}_2\text{N}_2\text{S}$, 207.9; found [M+H] $^+$, 208.9.

3-(Benzyloxy)phenyl bromide (14)

Potassium carbonate (9.6 g, 69 mmol) was added to a solution of 3-bromophenol (6.0 g, 34 mmol) and benzyl bromide (4.9 ml, 41 mmol) in acetone (40 ml), after which the mixture was heated to reflux for 2 hours. The solvent was then evaporated, and the residue was taken up in water (30 ml) and DCM (30 ml) and poured into a separating funnel where the product was further extracted with DCM (2 x 30 ml). The pooled organic fractions were washed with brine (30 ml), dried with magnesium sulfate, and evaporated under reduced pressure. The product residue was purified by flash chromatography (15% EtOAc in hexanes) to afford **14** as a crystalline solid (9.1 g, 99%).

^1H NMR (600 MHz, CDCl_3): δ = 7.45 – 7.37 (m, 4H, Ar), 7.37 – 7.32 (m, 1H, Ar), 7.17 – 7.13 (m, 2H, H-5', H-2'), 7.10 (ddd, J = 8.1, 2.5, 1.1 Hz, 1H, H-4'), 6.91 (ddd, J = 8.1, 2.5, 1.1 Hz, 1H, H-6'), 5.05 (s, 2H, $\underline{\text{CH}_2}$); ^{13}C NMR (151 MHz, CDCl_3): δ = 159.68 (C-1'), 136.54 (C-3'), 130.71 (C-2'), 128.80 (C-2''), 128.30 (C-4'), 127.64 (C-3''), 124.22 (C-4''), 122.96 (C-1''), 118.34 (C-5'), 113.98 (C-6'), 70.37 ($\underline{\text{CH}_2}$).

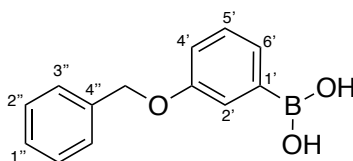
3-((4-Fluorophenyl)methoxy)phenyl bromide (**15**)



4-Fluorobenzyl bromide (2.0 g, 10.6 mmol), 3-bromophenol (2.0 g, 11.6 mmol), and potassium carbonate (2.9 g, 21.2 mmol) were dissolved in acetone and were refluxed together for 3 hours. The bulk of the reaction solvent was then removed under reduced pressure. The reaction residue was then taken up in water (20 ml) and EtOAc (20 ml). The product was further extracted from the aqueous phase with EtOAc (2 x 30 ml), and the pooled organic fractions were washed with brine, dried with magnesium sulfate, and evaporated under reduced pressure. The resulting mixture was purified by flash chromatography (10% EtOAc in hexanes) to afford **15** as a white crystalline solid (3.1 g, 99%).

^1H NMR (600 MHz, CDCl_3): δ = 7.43 – 7.36 (m, 2H, Ar), 7.18 – 7.05 (m, 5H, Ar), 6.89 (ddd, J =8.1, 2.5, 1.1 Hz, 1H, H-6'), 5.00 (s, 2H, $\underline{\text{CH}_2}$); ^{13}C NMR (151 MHz, CDCl_3): δ = 162.73 (d, J_{CF} = 246.5 Hz, C-1''), 159.49 (C-1'), 132.29 (d, J_{CF} = 3.3 Hz, C-4''), 130.74 (C-2'), 129.50 (d, J_{CF} = 8.3 Hz, C-3''), 124.37 (C-4'), 123.00 (C-3'), 118.32 (C-5'), 115.72 (d, J_{CF} = 22.0 Hz, C-2''), 113.96 (C-6'), 69.69 ($\underline{\text{CH}_2}$).

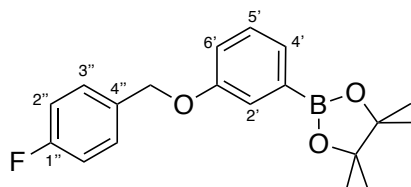
3-(Benzoyloxy)phenylboronic acid (**16**)



Freshly ground magnesium powder (90 mg, 3.75 mmol) and dry THF were added to an oven-dry flask under a blanket of argon. A solution of the bromide **14** (1.0 g, 3.8 mmol) in dry THF was added dropwise to the stirring magnesium powder. After the resulting mixture was left to reflux for 1.5 hours, the solution turned dark grey. Under a positive pressure of argon, the reaction was then cooled to $-78\text{ }^\circ\text{C}$, and a solution of trimethyl borate in dry THF was added in dropwise fashion. The reaction was slowly allowed to warm to room temperature and was left to stir overnight, after which HCl (6 M, 10 ml) was added. The reaction was allowed to stir for a further 1.5 hours at which point it was diluted with water (20 ml) and extracted with EtOAc (3 x 30 ml). The organic fractions were dried, evaporated, and the resulting residue was then stirred in hexane, causing **16** to crystallize as an off-white powder (350 mg, 40%).

^1H NMR (600 MHz, CDCl_3): δ = 7.87 – 7.77 (m, 2H, Ar), 7.55 – 7.49 (m, 2H, Ar), 7.47 – 7.38 (m, 3H, Ar), 7.38 – 7.31 (m, 1H, H-5'), 7.21 (ddd, J =8.2, 2.8, 1.1 Hz, 1H, H-6'), 5.17 (s, 2H, PhCH_2O); ^{13}C NMR (151 MHz, CDCl_3): δ = 158.62 (C-1'), 137.18 (C-3'), 129.36 (C-2'), 128.77 (C-2''), 128.42 (C-6'), 128.15 (C-4'), 127.73 (C-3''), 121.70 (C-5'), 119.36 (C-4''), 70.24 (CH_2).

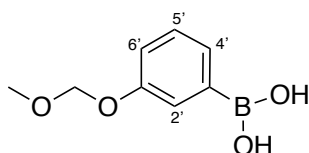
3-((4-Fluorophenyl)methoxy)phenylboronic acid pinacol ester (**17**)



To an argon-purged reaction flask containing a stirring mixture of the aryl bromide **15** (1.00 g, 3.56 mmol), bis(pinacolato)diboron (993 mg, 3.91 mmol), and potassium acetate (1.05 g, 10.68 mmol) in deoxygenated dioxane (20 ml) was added the catalyst [1,1'-bis(diphenylphosphino)ferrocene] dichloropalladium(II) (130 mg, 0.18 mmol). The reaction was warmed to 80 °C and was left to stir for 3 hours. The cooled reaction mixture was poured into a separating funnel containing saturated ammonium chloride (30 ml) and EtOAc (30 ml). The product was extracted with EtOAc (3 x 30 ml), and the pooled organic fractions were then washed with water (50 ml) and brine (50 ml). The organic layer was dried with magnesium sulfate and evaporated under reduced pressure to afford the crude product residue, which was purified by column chromatography (10 % EtOAc in hexanes). This yielded **17** as a crystalline white solid (1.0 g, 85%).

^1H NMR (600 MHz, CDCl_3): δ = 7.46 – 7.39 (m, 4H, Ar), 7.31 (t, J = 8.2 Hz, 1H, H-5'), 7.10 – 7.04 (m, 3H, Ar), 5.05 (s, 2H, CH_2), 1.35 (s, 12H, $\text{Pin}(\text{CH}_3)_4$); ^{13}C NMR (151 MHz, CDCl_3): δ = 162.61 (d, J_{CF} = 246.0 Hz, C-1''), 158.29 (C-1'), 134.88 (C-3'), 133.06 (d, J_{CF} = 3.1 Hz, C-4''), 129.48 (d, J_{CF} = 8.1 Hz, C-3''), 129.17 (C-2'), 127.73 (C-4'), 120.08 (C-5'), 118.65 (C-6'), 115.54 (d, J_{CF} = 21.5 Hz, C-2''), 84.02 (CH_2), 69.41 ($\text{Pin}(\text{C}(\text{CH}_3)_2)_2$), 25.02 ($\text{Pin}(\text{C}(\text{CH}_3)_2)_2$).

3-(Methoxymethoxy)phenylboronic acid (**28**)



A solution of 3-hydroxyphenylboronic acid (1.62 g, 11.72 mmol) in DMF (5 ml) was added dropwise to a stirring slurry of sodium hydride (60% in mineral oil, 1.88 g, 46.89 mmol) in DMF (15 ml) at 0 °C under a positive pressure of argon. The reaction was allowed to warm up to room temperature for 20 min, after which it was cooled back down to 0 °C. A solution of chloromethyl methyl ether (980 μl , 12.90 mmol) in DMF (5 ml) was then added dropwise over a period of 20 minutes, and the reaction was subsequently left to warm

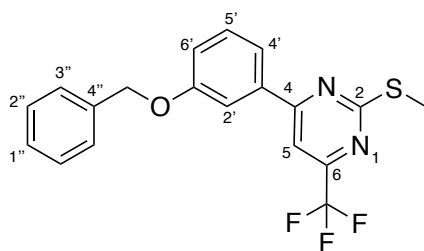
up to room temperature. After 2 hours, the reaction was quenched by the slow addition of saturated ammonium chloride solution (10 ml). The reaction mixture was poured into a separating funnel containing water (300 ml), and the product was extracted using EtOAc (3 x 100 ml). The pooled organic fractions were washed once with brine (200 ml), dried with magnesium sulfate, and evaporated under reduced pressure. The crude product residue was flushed through a short pad of silica to afford the protected phenylboronic acid **28** as a white crystalline solid pure enough for use in the next step (1.80 g, 84%).

^1H NMR (600 MHz, CDCl_3): δ = 7.88 (dt, J = 7.7, 1.1 Hz, 1H, H-4'), 7.86 (d, J = 2.6 Hz, 1H, H-2'), 7.45 (t, J = 7.7 Hz, 1H, H-5'), 7.29 (ddd, J = 7.8, 2.7, 1.1, 1H, H-6'), 5.28 (s, 2H, OCH_2O), 3.54 (s, 3H, OCH_3); ^{13}C NMR (151 MHz, CDCl_3): δ = 156.95 (C-4'), 129.32 (C-1'), 129.28 (C-3'), 129.24 (C-2'), 123.18 (C-5'), 120.62 (C-6'), 94.55 (OCH_2O), 56.08 (CH_3O).

General Procedure 1 (GP1) for the synthesis of 3-phenyl-2-(methylsulfinyl)-6-(trifluoromethyl) pyrimidines via Suzuki cross-coupling reactions between 3-chloro-2-(methylsulfinyl)-6-(trifluoromethyl) pyrimidine and various phenyl boronic acids/esters:¹⁷³

The required phenylboronic acid or acid ester **16**, **17**, or **28** (1.1 eq), cesium carbonate (4 eq), and either pyrimidine **13** or **25** were added together in an argon purged flask fitted with a reflux condenser. The mixture was dissolved with deoxygenated DME/water (4:1), after which $\text{Pd}(\text{PPh}_3)_4$ (10 mol%) was added to the resulting solution. The flask was again purged with argon and warmed to 85 °C for 5-6 hours. TLC was used to monitor the reaction, and after it was deemed to be complete, the cooled reaction mixture was poured in a separating funnel containing saturated brine (100 ml). The reaction was extracted with EtOAc (3 x 50 ml), and the pooled organic fractions were dried with magnesium sulfate. The organic solvent was removed under reduced pressure, and the resulting residue was purified by flash chromatography (10% EtOAc in hexanes).

4-(3-(benzyloxy)phenyl)-2-(methylthio)-6-(trifluoromethyl)pyrimidine (**18**)

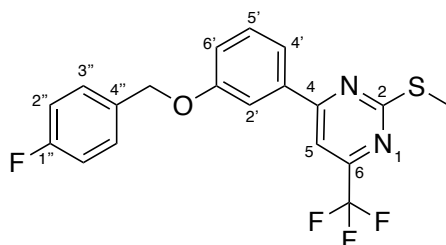


GP1 1 was followed using **16** (1.00 g, 4.39 mmol), **13** (1.50 g, 6.58 mmol), cesium carbonate (3.14 g, 9.65 mmol), and $\text{Pd}(\text{PPh}_3)_4$ (991 mg, 0.857 mmol, 10 mol%) in DME/water (4:1, 50 ml). Column chromatography (10% EtOAc in hexanes) yielded **18** as a crystalline white solid (1.45 g, 88%).

^1H NMR (600 MHz, CDCl_3): δ = 7.79 (t, J = 2.1 Hz, 1H, H-2'), 7.68 (d, J = 7.7 Hz, 1H, H-4'), 7.61 (s, 1H, H-5), 7.48 (d, J = 7.3 Hz, 2H, Ar), 7.46 – 7.39 (m, 3H, Ar), 7.38 – 7.33 (m, 1H, H-5'), 7.17 (dd, J = 8.2, 2.7 Hz, 1H, H-6'),

5.16 (s, 2H, $\underline{\text{CH}}_2$), 2.66 (s, 3H, $\underline{\text{SCH}}_3$); ^{13}C NMR (151 MHz, CDCl_3): δ = 174.43 (C-2), 166.08 (C-4), 159.51 (C-3'), 156.42 (q, J_{CF} = 35.9 Hz, C-6), 136.90 (C-1'), 136.66 (C-4''), 130.30 (C-1''), 128.80 (C-3''), 128.29 (C-5'), 127.65 (C-2''), 120.66 (q, J_{CF} = 275.3 Hz, $\underline{\text{CF}}_3$), 120.15 (C-4'), 118.72 (C-6'), 113.91 (C-2'), 107.56 (q, J_{CF} = 2.7 Hz, C-5), 70.39 ($\underline{\text{CH}}_2$), 14.46 ($\underline{\text{SCH}}_3$).

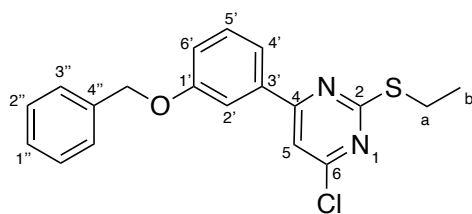
4-(3-((4-fluorobenzyl)oxy)phenyl)-2-(methylthio)-6-(trifluoromethyl)pyrimidine (**19**)



GP1 was followed using **17** (474 mg, 1.45 mmol), **13** (300 mg, 1.32 mmol), cesium carbonate (1.72 g, 5.26 mmol), and $\text{Pd}(\text{PPh}_3)_4$ (152 mg, 0.132 mmol, 10 mol%) in DME/water (4:1, 10 ml). Column chromatography (10 % EtOAc in hexanes) yielded **19** as a crystalline white solid (376 mg, 72%).

^1H NMR (600 MHz, CDCl_3): δ = 7.77 (dd, J = 2.6, 1.7 Hz, 1H, H-2'), 7.68 (ddd, J = 7.7, 1.7, 0.9 Hz, 1H, H-4'), 7.61 (s, 1H, H-5), 7.48 – 7.40 (m, 3H, Ar), 7.15 (ddd, J = 8.5, 2.6, 0.9 Hz, 1H, H-6'), 7.09 (t, J_{HH} = 8.5 Hz, J_{HF} = 8.5 Hz, 1H, H-2''), 5.12 (s, 2H, $\underline{\text{CH}}_2$), 2.66 (s, 3H, $\underline{\text{SCH}}_3$); ^{13}C NMR (151 MHz, CDCl_3): δ = 174.36 (C-2), 165.93 (C-4), 162.62 (d, J_{CF} = 246.6 Hz, C-1''), 159.25 (C-3'), 156.36 (q, J_{HF} = 35.8 Hz, C-6), 136.86 (C-1'), 132.30 (d, J_{CF} = 3.3 Hz, C-4''), 130.23 (C-5'), 129.43 (d, J_{CF} = 8.3 Hz, C-3''), 120.53 (q, J_{CF} = 275.4 Hz, $\underline{\text{CF}}_3$), 120.19 (C-4'), 118.58 (C-6'), 115.62 (d, J_{CF} = 21.7 Hz, C-2''), 113.74 (C-2'), 107.47 (q, J_{CF} = 2.8 Hz, C-5), 69.62 ($\underline{\text{CH}}_2$), 14.35 ($\underline{\text{SCH}}_3$).

4-(3-(benzyloxy)phenyl)-6-chloro-2-(ethylthio)pyrimidine (**26**)

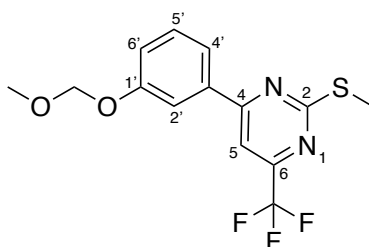


GP1 was followed using **16** (545 mg, 2.39 mmol), **25** (500 mg, 2.39 mmol), cesium carbonate (1.72 g, 5.26 mmol), and $\text{Pd}(\text{PPh}_3)_4$ (277 mg, 0.24 mmol, 10 mol%) in DME/water (4:1, 10 ml). Flash chromatography (10% EtOAc in hexanes) yielded **26** as a clear oil (515 mg, 60%).

^1H NMR (600 MHz, CDCl_3): δ = 7.71 (dd, J = 2.6, 1.6 Hz, 1H, H-2'), 7.61 (ddd, J = 7.7, 1.7, 0.9 Hz, 1H, H-4'), 7.49 – 7.44 (m, 2H, Ar), 7.44 – 7.37 (m, 3H, Ar), 7.37 – 7.32 (m, 2H, Ar), 7.14 (ddd, J = 8.2, 2.6, 0.9 Hz, 1H, H-6'), 5.15 (s, 2H, $\underline{\text{CH}}_2$), 3.22 (q, J = 7.4 Hz, 2H, H-a), 1.45 (t, J = 7.4 Hz, 3H, H-b); ^{13}C NMR (151 MHz, CDCl_3): δ = 173.4 (C-2), 165.3 (C-4), 161.7 (C-6), 159.5 (C-3'), 137.0 (C-1'), 136.7 (C-4''), 130.2 (C-1''), 128.8 (C-3''), 128.3 (C-5'),

127.7 (C-2''), 120.1 (C-4'), 118.4 (C-6'), 113.8 (C-5), 112.1 (C-2'), 70.4 (CH₂), 25.8 (C-a), 14.4 (C-b); HPLC: (retention time = 9.92 min); HPLC-MS (ESI) (m/z): [M] calcd. for C₂₀H₁₇F₃N₂OS, 356.1; found [M+H]⁺, 357.1.

4-(3-(methoxymethoxy)phenyl)-2-(methylthio)-6-(trifluoromethyl)pyrimidine (29)



GP1 was followed using the boronic acid **28** (1.80 g, 9.89 mmol), **13** (2.26 g, 9.89 mmol), Pd(PPh₃)₄ (572 mg, 0.495 mmol, 5 mol%), and potassium carbonate (4.1 g, 29.67 mmol) instead of the cesium carbonate in DME/water (4:1) (30 ml). Column chromatography (10 % EtOAc in hexanes) yielded **29** as a crystalline white solid (2.49 g, 76 %).

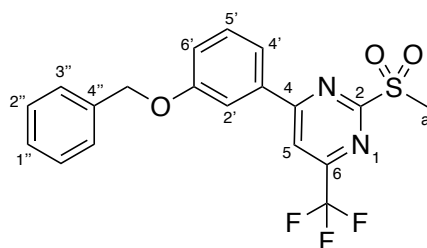
¹H NMR (600 MHz, CDCl₃): δ = 7.81 (dd, *J* = 2.4, 1.8 Hz, 1H, H-2'), 7.74 (ddd, *J* = 7.8, 1.7, 0.9 Hz, 1H, H-4'), 7.62 (s, 1H, H-5), 7.44 (t, *J* = 8.0 Hz, 1H, H-5'), 7.24 (ddd, *J* = 8.3, 2.5, 0.9 Hz, 1H, H-6'), 5.26 (s, 2H, OCH₂O), 3.51 (s, 3H, OCH₃), 2.67 (s, 3H, SCH₃); ¹³C NMR (151 MHz, CDCl₃): δ = 174.49 (C-2), 166.08 (C-4), 158.04 (C-3'), 156.51 (q, *J*_{CF} = 35.9 Hz, C-6), 137.02 (C-1'), 130.36 (C-5'), 121.08 (C-4'), 120.67 (q, *J*_{CF} = 275.5 Hz, CF₃), 119.93 (C-6'), 115.44 (C-2'), 107.60 (q, *J*_{CF} = 2.8 Hz, C-5), 94.65 (OCH₂O), 56.31 (CH₃O), 14.49 (SCH₃).

General Procedure 2 for the synthesis of 3-phenyl-2-(ethylsulfinyl)-6-(trifluoromethyl) pyrimidines via an oxidation (**GP2 (i)**) and subsequent ethane thiolation (**GP2 (ii)**) from 3-phenyl-2-(methylsulfinyl)-6-(trifluoromethyl) pyrimidines:¹⁷³

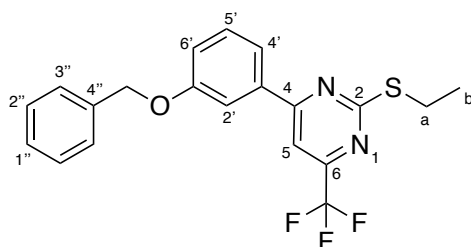
GP2 (i): A solution of the required 3-phenyl-2-(methylsulfinyl)-6-(trifluoromethyl) pyrimidine in DCM (3-5 ml) was cooled to 0 °C while the flask was flushed with argon. A solution of *m*-CPBA (77%, 2.2 eq) in DCM (3-5 ml) was then added to the reaction mixture in dropwise fashion over the course of 5-10 minutes. The reaction was then allowed to warm to room temperature for 30 min. After TLC showed the reaction to be complete, the reaction was quenched with saturated aqueous sodium hydrogen carbonate (20 ml) and the product was then extracted with DCM (3 x 20 ml). (If TLC analysis found the reaction progress to have halted before completion, an extra 0.5 eq of *m*-CPBA was added until total consumption of the starting material was observed.) The organic fractions were then dried with magnesium sulfate, and the solvent was removed under reduced pressure. The resulting sulfone could be isolated for analysis, but in most cases, it was immediately re-dissolved in dry THF (3-10 ml) and transferred to an argon-flushed three-neck reaction flask fitted with a reflux condenser and a rubber septum.

GP2 (ii): Solid sodium ethanthiolate (1.2 eq) was then added in one portion to the rapidly stirring reaction mixture through the third neck of the flask, which was subsequently sealed. Ethanethiol (1-3 ml) was then injected into the reaction flask through the rubber septum (caution: stench), after which the reaction was warmed to reflux for 1-2 hours. The volatiles were removed directly from the reaction under reduced pressure, and the resulting residue was taken up with ammonium chloride solution (20 ml) and extracted with EtOAc (3 x 30 ml). The pooled organic fractions were then washed with brine, dried with magnesium sulfate, and concentrated under reduced pressure, after which the product was isolated with column chromatography.

4-(3-(benzyloxy)phenyl)-2-(ethylthio)-6-(trifluoromethyl)pyrimidine (18a and 20)

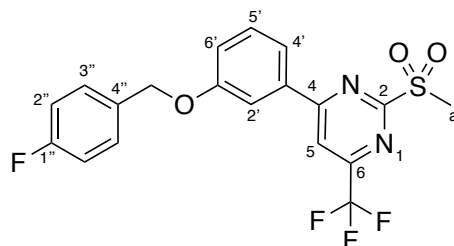


GP2 (i) was followed using the substrate **18** (654 mg, 1.74 mmol) and *m*-CPBA (660 mg, 3.83 mmol) in DCM (10 ml). The intermediate could be isolated by column chromatography (20% EtOAc in hexanes) to afford the sulfone **18a** as a white solid (560 mg, 79%) and was found to be pure enough for direct use in the next step.

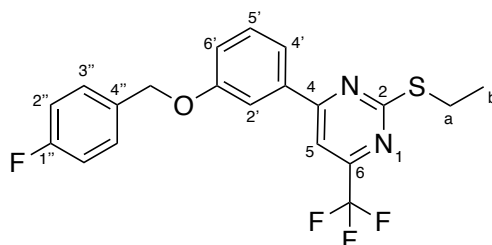


GP2 (ii) was followed using the sulfone obtained from GP2 (i) **18a** (510 mg, 1.25 mmol) and sodium ethanthiolate (126 mg, 1.5 mmol) in THF (4 ml). The intermediate could be isolated by column chromatography (1 - 10% EtOAc in hexanes) to afford the ethylthioether **20** as a white solid (445 mg, 91%).

^1H NMR (600 MHz, CDCl_3): δ = 7.77 (dd, J = 2.6, 1.6 Hz, 1H, H-2'), 7.68 (ddd, J = 7.7, 1.7, 0.9 Hz, 1H, H-4'), 7.60 (s, 1H, H-5), 7.51 – 7.39 (m, 5H, Ar), 7.39 – 7.32 (m, 1H, H-5'), 7.17 (ddd, J = 8.3, 2.6, 0.9 Hz, 1H, H-6'), 5.16 (s, 2H, CH_2), 3.25 (q, J = 7.4 Hz, 2H, H-a), 1.46 (t, J = 7.4 Hz, 3H, H-b); ^{13}C NMR (151 MHz, CDCl_3): δ = 174.17 (C-2), 166.18 (C-4), 159.51 (C-3'), 156.51 (q, J_{CF} = 35.8 Hz, C-6), 136.97 (C-1'), 136.64 (C-4''), 130.34 (C-1''), 128.83 (C-3''), 128.33 (C-5'), 127.69 (C-2''), 120.65 (q, J_{CF} = 275.3 Hz, CF_3), 120.16 (C-4'), 118.75 (C-6'), 113.81 (C-2'), 107.61 (q, J_{CF} = 2.9 Hz, C-5), 70.39 (CH_2), 25.79 (H-a), 14.38 (H-b); HPLC: (retention time = 9.97 min); HPLC-MS (ESI) (m/z): [M] calcd. for $\text{C}_{20}\text{H}_{17}\text{F}_3\text{N}_2\text{OS}$, 390.1; found [M+H] $^+$, 391.1.

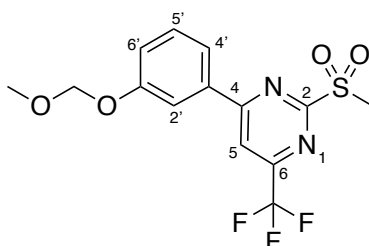
2-(ethylthio)-4-(3-((4-fluorobenzyl)oxy)phenyl)-6-(trifluoromethyl)pyrimidine (19a and 21)

GP2 (i) was followed using the substrate **19** (330 mg, 0.838 mmol) and *m*-CPBA (361 mg, 2.094 mmol) in DCM (6 ml). The intermediate could be isolated by column chromatography (20% EtOAc in hexanes) to afford the sulfone **19a** as a white solid (348 mg, 97%) and was found to be pure enough for direct use in the next step.

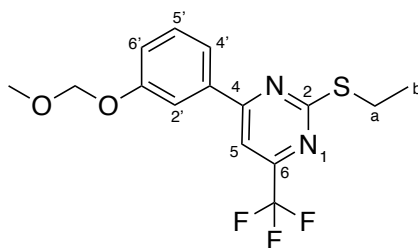


GP2 (ii) was followed using the sulfone obtained from GP2 (i) **19a** (295 mg, 0.69 mmol) and sodium ethanethiolate (70 mg, 0.83 mmol) in THF (4 ml). The intermediate could be isolated by column chromatography (1 - 10% EtOAc in hexanes) to afford the ethylthioether **21** as a white solid (181 mg, 64%).

^1H NMR (600 MHz, CDCl_3): δ = 7.76 (dd, J = 2.6, 1.6 Hz, 1H, C-2'), 7.68 (ddd, J = 7.7, 1.7, 0.9 Hz, 1H, H-4'), 7.60 (s, 1H, H-5), 7.47 – 7.41 (m, 3H, Ar), 7.15 (ddd, J = 8.2, 2.6, 0.9 Hz, 1H, H-6'), 7.10 (d, J_{HH} = 8.7 Hz, J_{HF} = 8.7 Hz, 2H, C-2''), 5.11 (s, 2H, CH_2), 3.25 (q, J = 7.4 Hz, 2H, H-a), 1.46 (t, J = 7.3 Hz, 3H, H-b); ^{13}C NMR (151 MHz, CDCl_3): δ = 174.24 (C-2), 166.12 (C-4), 162.74 (d, J_{CF} = 246.6 Hz, C-1''), 159.37 (C-3'), 156.54 (q, J_{CF} = 35.9 Hz, C-6), 137.03 (C-1'), 132.43 (d, J_{CF} = 3.3 Hz, C-4''), 130.36 (C-5'), 129.55 (d, J_{CF} = 8.3 Hz, C-3''), 120.66 (q, J_{CF} = 275.4 Hz, CF_3), 120.29 (C-4'), 118.73 (C-6'), 115.73 (d, J_{CF} = 21.6 Hz, C-2''), 113.78 (C-2'), 107.59 (q, J_{CF} = 2.8 Hz, C-5), 69.72 (CH_2), 25.78 (C-a), 14.35 (C-b); HPLC: (retention time = 9.90 min); HPLC-MS (ESI) (m/z): [M] calcd. for $\text{C}_{20}\text{H}_{16}\text{F}_4\text{N}_2\text{OS}$, 408.1; found $[\text{M}+\text{H}]^+$, 409.1.

2-(ethylthio)-4-(3-(methoxymethoxy)phenyl)-6-(trifluoromethyl)pyrimidine (29a and 30)

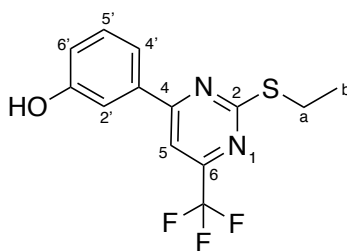
GP2 (i) was followed using the substrate **29** (122 mg, 0.370 mmol) and *m*-CPBA (191 mg, 1.1 mmol) in DCM (5 ml). The intermediate could be isolated by column chromatography (15% EtOAc in hexanes) to afford the sulfone **29a** (97 mg, 72%) and was found to be pure enough for direct use in the next step.



GP2 (ii) was followed using the sulfone **29a** obtained from GP2 (i) (190 mg, 0.525 mmol) and sodium ethanthiolate (75 mg, 0.89 mmol) in THF (5 ml). The intermediate could be isolated by column chromatography (1 - 10% EtOAc in hexanes) to afford the sulfone **30** as a colorless oil (169 mg, 94%).

^1H NMR (600 MHz, CDCl_3): δ = 7.81 (dd, J = 2.1, 1.7 Hz, 1H, H-2'), 7.73 (ddd, J = 7.9, 1.7, 0.9 Hz, 1H, H-4'), 7.61 (s, 1H, H-5), 7.43 (t, J = 8.0 Hz, 1H, H-5'), 7.24 (ddd, J = 8.0, 1.7, 0.9 Hz, 1H, H-6'), 2.5 (s, 2H, OCH_2O), 3.51 (s, 3H, OCH_3), 3.26 (q, J = 7.4 Hz, 2H, SET: H-a), 1.47 (t, J = 7.4 Hz, 3H, SET: H-b); ^{13}C NMR (151 MHz, CDCl_3): δ = 174.22 (C-2), 166.11 (C-4), 158.05 (C-3'), 156.56 (q, J_{CF} = 35.8 Hz, C-6), 137.05 (C-1'), 130.34 (C-5'), 121.03 (C-4'), 120.66 (q, J_{CF} = 275.5 Hz, CF_3), 119.95 (C-6'), 115.36 (C-2'), 107.55 (q, J_{CF} = 2.8 Hz, C-5), 94.66 (OCH_2O), 56.28 (OCH_3), 25.80 (SET: C-a), 14.39 (SET: C-b).

3-(2-(ethylthio)-6-(trifluoromethyl)pyrimidin-4-yl)phenol (**31**)

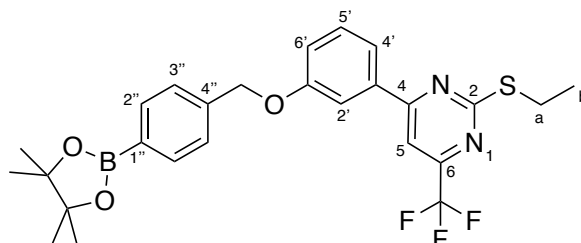


A stirring solution of **30** (159 mg, 0.462 mmol) in methanol (5 ml) was treated with HCl (12 M, 1 ml) at 0 °C. The reaction was then warmed to room temperature and left to stir for 2-5 hours. When TLC showed the reaction to be complete, it was quenched with saturated aqueous NaHCO_3 (10 ml) and extracted with EtOAc (3 x 20 ml). The pooled organic fractions were dried with magnesium sulfate, concentrated under reduced pressure, and passed through a short pad of silica (50% EtOAc in hexanes). Evaporation of the solvents afforded the phenol **31** as a yellow solid (132 mg, 95 %).

^1H NMR (600 MHz, CDCl_3): δ = 7.67 – 7.62 (m, 2H, H-2', H-4'), 7.60 (s, 1H, H-5), 7.39 (t, J = 7.7, 1H, H-5'), 7.04 (dd, J = 8.1, 2.5, 1H, H-6'), 3.26 (q, J = 7.3 Hz, 2H, H-a), 1.46 (t, J = 7.3 Hz, 3H, H-b); ^{13}C NMR (151 MHz, CDCl_3): δ = 174.22 (C-2), 166.04 (C-4), 156.58 (q, J_{CF} = 36.0 Hz, C-6), 156.53 (C-3'), 137.09 (C-1'), 130.56 (C-5'), 120.64

(q, $J_{CF} = 275.4$ Hz, \underline{CF}_3), 119.99 (C-4'), 119.34 (C-6'), 114.34 (C-2'), 107.64 (q, $J_{CF} = 3.0$ Hz, C-5), 25.82 (C-a), 14.36 (C-b); HPLC: (retention time = 8.37 min); HPLC-MS (ESI) (m/z): [M]⁺ calcd. for C₁₃H₁₁F₃N₂O₂S, 300.1; found [M+H]⁺, 301.1.

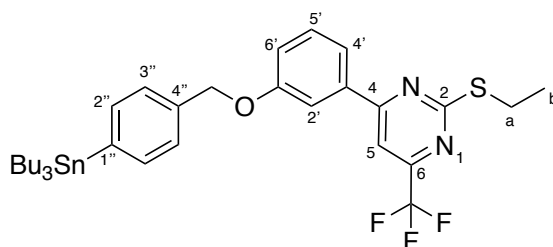
2-(ethylthio)-4-(3-((4-(4,4,5,5-tetramethyl-1,3,2-dioxaborolan-2-yl)benzyl)oxy)phenyl)-6-(trifluoromethyl)pyrimidine (32)



Phenol **31** (132 mg, 0.44 mmol), potassium carbonate (91 mg, 0.66mmol), and 4-bromomethylphenyl boronic acid pinacol ester (144 mg, 0.48 mmol) were dissolved in acetonitrile (8 ml), and the resulting solution was brought to reflux for 2 hours. After TLC analysis showed complete consumption of the starting material, the reaction mixture was concentrated under reduced pressure, diluted with saturated aqueous ammonium chloride (10 ml), washed with EtOAc (10 ml), and poured into a separating funnel containing water (100 ml). The product was extracted from the aqueous phase using EtOAc (3 x 50 ml), after which the pooled organic fractions were washed with brine (50 ml), dried with magnesium sulfate, and evaporated under reduced pressure. Column chromatography (10% EtOAc in hexanes) of the crude material afforded pure **32** as a thick clear oil (189.3 mg, 83%).

¹H NMR (600 MHz, CDCl₃): $\delta = 7.85$ (d, $J = 7.8$ Hz, 2H, H-2''), 7.75 (t, $J = 2.1$ Hz, 1H, H-2'), 7.66 (d, $J = 7.8$ Hz, 1H, H-4'), 7.59 (s, 1H, H-5), 7.46 (d, $J = 7.8$ Hz, 2H, H-3''), 7.42 (t, $J = 8.0$ Hz, 1H, H-5'), 7.15 (dd, $J = 8.2, 2.5$ Hz, 1H, H-6'), 5.19 (s, 2H, \underline{CH}_2), 3.24 (q, $J = 7.3$ Hz, 2H, H-a), 1.46 (t, $J = 7.4$ Hz, 3H, H-b), 1.35 (s, 12H, Pin); ¹³C NMR (151 MHz, CDCl₃): $\delta = 174.19$ (C-2), 166.18 (C-4), 159.47 (C-3'), 156.52 (q, $J_{CF} = 35.8$ Hz, C-6), 139.79 (C-1''), 136.99 (C-1'), 135.26 (C-2''), 130.32 (C-5'), 128.85 (Brs, C-4''), 126.68 (C-3''), 120.66 (q, $J_{CF} = 275.4$ Hz, \underline{CF}_3), 120.19 (C-4'), 118.81 (C-6'), 113.90 (C-2'), 107.60 (q, $J_{CF} = 2.8$ Hz, C-5), 84.01 (Pin- $\underline{C}(\text{CH}_3)_2$), 70.29 (\underline{CH}_2), 25.78 (C-a), 25.01 (Pin- \underline{CH}_3), 14.37 (C-b); HPLC: (retention time = 10.54 min); HPLC-MS (ESI) (m/z): [M] calcd. for C₂₆H₂₈BF₃N₂O₃S, 516.1; found [M+H]⁺, 517.0.

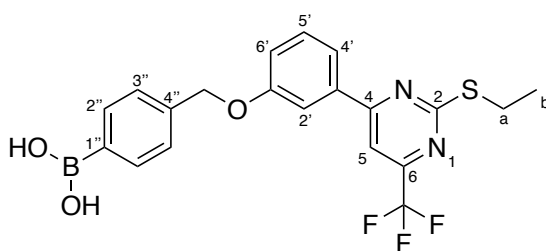
2-(ethylthio)-4-(3-((4-(tributylstannyl)benzyl)oxy)phenyl)-6-(trifluoromethyl)pyrimidine (34)



9 (132 mg, 0.333 mmol) and triphenylphosphine (173 mg, 0.666 mmol) were weighed out into a dry argon purged reaction flask fitted with a rubber septum and were then dissolved in dry acetonitrile (5 ml). **31** (100 mg, 0.333 mmol) was then added to the resulting solution. The reaction mixture was cooled down to 0 °C and left to stir for 10 minutes, after which a solution of diisopropyl azodicarboxylate (DIAD, 172 μ l, 0.726 mmol) in acetonitrile (2 ml) was added dropwise through the rubber septum over the course of 2 minutes. The reaction was then warmed to room temperature where it was left to stir overnight. TLC analysis showed the formation of a new product and triphenylphosphine oxide. After the reaction was deemed to be complete, the solvent was evaporated under reduced pressure, and the residue was transferred to a separating funnel using EtOAc (30 ml) and Water (50 ml). The products were extracted with further portions of EtOAc (2 x 30 ml), and the combined organic fractions were washed with brine, dried with magnesium sulfate, and evaporated under reduced pressure. The resulting residue was purified via column chromatography (5-10% Et₂O in hexanes) to afford **34** as a thick colorless oil (177 mg, 79%).

¹H NMR (600 MHz, CDCl₃): δ = 7.79 (t, J = 2.1 Hz, 1H, H-2'), 7.69 (d, J = 7.7 Hz, 1H, H-4'), 7.61 (s, 1H, H-5), 7.57 – 7.46 (m, 2H, H-3''), 7.47 – 7.39 (m, 3H, H-2'', H-5'), 7.19 (dd, J = 8.3, 2.6 Hz, 1H, H-6'), 5.15 (s, 2H, CH₂), 3.26 (q, J = 7.3 Hz, 2H, H-a), 1.66 – 1.50 (m, 6H, SnBu₃), 1.48 (t, J = 7.4 Hz, 3H, H-b), 1.36 (q, J = 7.4 Hz, 6H, SnBu₃), 1.16 – 1.01 (m, 6H, SnBu₃), 0.91 (t, J = 7.4 Hz, 9H, SnBu₃); ¹³C NMR (151 MHz, CDCl₃): δ = 174.20 (C-2), 166.20 (C-4), 159.64 (C-3'), 156.52 (q, J_{CF} = 35.8 Hz, C-6), 142.34 (C-4''), 137.02 (C-1''), 136.91 (C-2''), 136.21 (C-1'), 130.31 (C-5'), 127.26 (C-3''), 120.67 (q, J_{CF} = 276.6 Hz, CF₃), 120.09 (C-4'), 118.73 (C-6'), 113.82 (C-2'), 107.57 (q, J_{CF} = 2.2 Hz, C-5), 70.51 (CH₂), 29.22 (SnBu₃), 27.51 (SnBu₃), 25.77 (C-a), 14.36 (C-b), 13.80 (SnBu₃), 9.73 (SnBu₃); HPLC: (retention time = 9.94 min); HPLC-MS (ESI) (m/z): [M-SnBu₃] calcd. for C₂₀H₁₇F₃N₂OS, 390.1; found [M-SnBu₃+H]⁺, 391.0.

(4-((3-(2-(ethylthio)-6-(trifluoromethyl)pyrimidin-4-yl)phenoxy)methyl)phenyl)boronic acid (**36**))



Phenol **31** (210 mg, 0.70 mmol), potassium carbonate (388 mg, 2.80 mmol), potassium iodide (11.6 mg, 0.07 mmol, 10 mol%), and 4-bromomethylphenyl boronic acid (150 mg, 0.70 mmol) were dissolved in acetone (5 ml) and the resulting solution was brought to reflux for 3 hours. After the consumption of the starting material was observed, the reaction mixture was concentrated under reduced pressure. The reaction was then quenched with water, after which the pH was adjusted to pH 2-3 with HCl (1 M). The aqueous mixture was then poured into a separating funnel containing water (100 ml) and EtOAc (50 ml), where it was further extracted with EtOAc (2 x 50 ml). The pooled organic fractions were then washed with brine (50 ml), dried

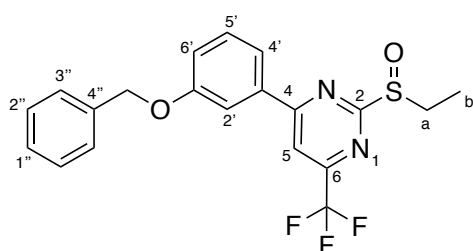
with magnesium sulfate, and evaporated under reduced pressure. The residue was finally purified by column chromatography (5 -15% MeOH in DCM) to afford the boronic acid **36** as an off-white solid (256 mg, 84%).

^1H NMR (600 MHz, MeOD): δ = 7.87 (s, 1H, H-5), 7.83 (t, J = 2.1 Hz, 1H, H-2'), 7.80 – 7.74 (m, 2H, H-2''), 7.63 (d, J = 7.6 Hz, 1H, H-4), 7.48 – 7.38 (m, 5H, H-3'', H-5'), 7.21 (dd, J = 8.2, 2.6 Hz, 1H, H-6), 5.19 (s, 2H, CH_2), 3.22 (q, J = 7.4 Hz, 2H, H-a), 1.43 (t, J = 7.3 Hz, 3H, H-b); ^{13}C NMR (151 MHz, MeOD): δ = 175.19 (C-2), 167.73 (C-4), 160.86 (C-3'), 157.51 (q, J_{CF} = 35.8 Hz, C-6), 138.01 (C-1''), 135.16 (C-1'), 134.80 (C-2''), 131.35 (C-5'), 127.66 (C-4''), 127.53 (C-3''), 122.06 (q, J_{CF} = 274.4 Hz, CF_3), 121.27 (C-4'), 120.16 (C-6'), 114.64 (C-2'), 108.77 (q, J_{CF} = 2.9 Hz, C-5), 71.11 (CH_2), 26.36 (C-a), 14.72 (C-b); HPLC: (retention time = 8.81 min); HPLC-MS (ESI) (m/z): [M] calcd. for $\text{C}_{20}\text{H}_{18}\text{BF}_3\text{N}_2\text{O}_3\text{S}$, 434.1; found $[\text{M}+\text{H}]^+$, 435.1.

General procedure 3 (GP3) for the oxidation of 2-(ethylthio)pyrimidines to 2-(ethylsulfinyl)pyrimidines:

A solution of the required 2-(ethylthio)-6-(trifluoromethyl) pyrimidine in DCM (3-5 ml) was cooled to 0 °C while the flask was flushed with argon. A solution of *m*-CPBA (77% pure, 1 eq) in DCM (3-5 ml) was then added to the reaction mixture in dropwise fashion over the course of 5-10 minutes. The reaction was then allowed to warm to room temperature for 30 min. After TLC showed the reaction to be complete, the reaction was quenched with saturated aqueous sodium hydrogen carbonate (20 ml) and the product was extracted with DCM (3 x 20 ml). The organic fractions were then dried with magnesium sulfate, and the solvent was removed under reduced pressure. The resulting residue was purified using flash chromatography, to afforded the desired product.

4-(3-(benzyloxy)phenyl)-2-(ethylsulfinyl)-6-(trifluoromethyl)pyrimidine (**22**, BETP)

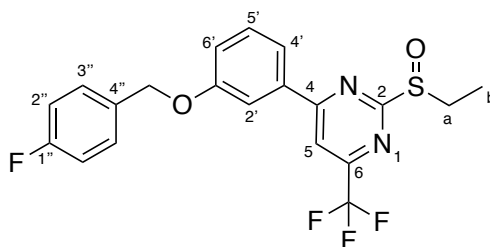


GP3 was followed using **14** (266 mg, 0.68 mmol) and *m*-CPBA (129.5 mg, 0.750 mmol). The product could be isolated by flash chromatography (10 – 50% EtOAc in hexanes) to afford **16** (**BETP**) as an off-white solid (176 mg, 64%).

^1H NMR (600 MHz, CDCl_3): δ = 8.01 (s, 1H, H-5), 7.87 (dd, J = 2.6, 1.7 Hz, 1H, H-2'), 7.79 (ddd, J = 7.8, 1.7, 0.9 Hz, 1H, H-4'), 7.51 – 7.44 (m, 3H, H-3'', H-1''), 7.43 – 7.38 (m, 2H, H-2''), 7.37 – 7.32 (m, 1H, H-5'), 7.22 (ddd, J = 8.2, 2.6, 0.9 Hz, 1H, H-6'), 5.17 (s, 2H, CH_2), 3.31 (dq, J^2_{Gem} = 13.4, J^3_{HH} = 7.4 Hz, 1H, H-a), 3.19 (dq, J^2_{Gem} = 13.4, J^3_{HH} = 7.4 Hz, 1H, H-a'), 1.36 (t, J = 7.4 Hz, 3H, C-b); ^{13}C NMR (151 MHz, CDCl_3): δ = 174.82 (C-2), 168.09 (C-4), 159.72 (C-3'), 157.51 (q, J_{CF} = 36.9 Hz, C-6), 136.45 (C-1'), 135.66 (C-4''), 130.68 (C-1''), 128.83 (C-2''), 128.37 (C-5'), 127.73 (C-3''), 120.60 (C-4'), 120.36 (q, J_{CF} = 275.7 Hz, CF_3), 119.74 (C-6'), 114.39 (C-2'), 112.84

(q, $J_{CF} = 2.8$ Hz, C-5), 70.53 ($\underline{\text{CH}_2}$), 47.80 (C-a), 6.61 (C-b); HPLC: (retention time = 8.23 min); HPLC-MS (ESI) (m/z): [M] calcd. for $\text{C}_{20}\text{H}_{17}\text{F}_3\text{N}_2\text{O}_2\text{S}$, 406.1; found [M+H]⁺, 407.1.

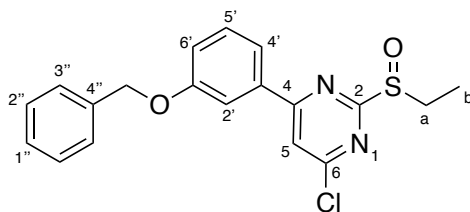
2-(ethylsulfinyl)-4-(3-((4-fluorobenzyl)oxy)phenyl)-6-(trifluoromethyl)pyrimidine (23, F-BETP)



GP3 was followed using **15** (142 mg, 0.348 mmol) and *m*-CPBA (60 mg, 0.348 mmol). Column chromatography (30% EtOAc in hexanes) afforded **17** (**F-BETP**) as a white solid (159.7 mg, 95%).

¹H NMR (600 MHz, CDCl₃): $\delta = 8.02$ (s, 1H, H-5), 7.88 (t, $J = 2.1$ Hz, 1H, H-2'), 7.79 (d, $J = 7.7$ Hz, 1H, H-4'), 7.51 – 7.41 (m, 3H, H-3'', H-5'), 7.21 (dd, $J = 8.1, 2.1$ Hz, 1H, H-6'), 7.09 (d, $J_{HH} = 8.6$ Hz, $J_{HF} = 8.6$ Hz, 2H, H-2''), 5.13 (s, 2H, $\underline{\text{CH}_2}$), 3.32 (dq, $J^2_{Gem} = 13.4$ Hz, $J^3_{HH} = 7.4$ Hz, 1H, H-a), 3.20 (dq, $J^2_{Gem} = 13.4$ Hz, $J^3_{HH} = 7.4$ Hz, 1H, H-a'), 1.37 (t, $J = 7.4$ Hz, 3H, H-b); ¹³C NMR (151 MHz, CDCl₃): $\delta = 174.89$ (C-2), 168.08 (C-4), 162.79 (d, $J_{CF} = 246.6$ Hz, C-1''), 159.59 (C-3'), 157.53 (q, $J_{CF} = 36.6$ Hz, C-6), 135.74 (C-1'), 132.23 (d, $J_{CF} = 3.3$ Hz, C-4''), 130.72 (C-5'), 129.67 (d, $J_{CF} = 8.3$ Hz, C-3''), 120.71 (C-4'), 120.36 (q, $J_{CF} = 275.8$ Hz, $\underline{\text{CF}_3}$), 119.77 (C-6'), 115.79 (d, $J_{CF} = 21.6$ Hz, C-2''), 114.33 (C-2'), 112.83 (d, $J_{CF} = 2.7$ Hz, C-5), 69.86 ($\underline{\text{CH}_2}$), 47.84 (C-a), 6.63 (C-b); HPLC: (retention time = 8.26 min); HPLC-MS (ESI) (m/z): [M] calcd. for $\text{C}_{20}\text{H}_{17}\text{F}_4\text{N}_2\text{O}_2\text{S}$, 424.1; found [M+H]⁺, 425.0.

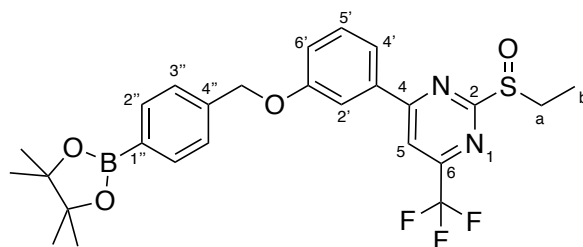
4-(3-(benzyloxy)phenyl)-6-chloro-2-(ethylsulfinyl)pyrimidine (27)



GP3 was followed using **20** (200 mg, 0.56 mmol) and *m*-CPBA (134.3 mg, 0.56 mmol). Column chromatography (20% EtOAc in hexanes) afforded the desired product as a white solid (162 mg, 78%).

¹H NMR (600 MHz, CDCl₃): $\delta = 7.77$ (dd, $J = 2.6, 1.7$ Hz, 1H, H-2'), 7.72 (s, 1H, H-5), 7.68 (ddd, $J = 7.8, 1.7, 0.9$ Hz, 1H, H-4'), 7.48 – 7.37 (m, 5H, Ar), 7.36 – 7.31 (m, 1H, Ar), 7.17 (ddd, $J = 8.3, 2.6, 0.9$ Hz, 1H, H-6'), 5.15 (s, 2H, $\underline{\text{CH}_2}$), 3.27 (dq, $J^2_{Gem} = 13.4$, $J^3_{HH} = 7.4$ Hz, 1H, H-a), 3.15 (dq, $J^2_{Gem} = 13.4$, $J^3_{HH} = 7.4$ Hz, 1H, H-a'), 1.35 (t, $J = 7.4$ Hz, 3H, H-b); ¹³C NMR (151 MHz, CDCl₃): $\delta = 174.0$ (C-2), 166.6 (C-4), 163.7 (C-6), 159.6 (C-3'), 136.5 (C-1'), 135.6 (C-4''), 130.5 (C-1''), 128.8 (C-3''), 128.3 (C-5'), 127.7 (C-2''), 120.3 (C-4'), 119.1 (C-6'), 117.3 (C-5), 114.2 (C-2'), 70.4 ($\underline{\text{CH}_2}$), 47.7 (C-a), 6.5 (C-b); HPLC: (retention time = 7.99 min); HPLC-MS (ESI) (m/z): [M] calcd. for $\text{C}_{19}\text{H}_{17}\text{ClN}_2\text{O}_2\text{S}$, 372.0; found [M+H]⁺, 373.0.

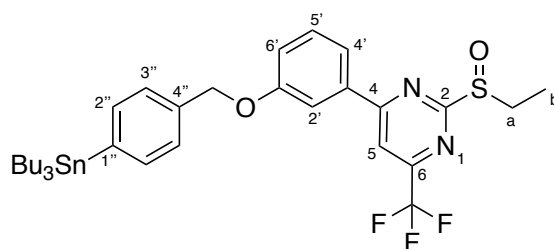
2-(ethylsulfinyl)-4-(3-((4-(4,4,5,5-tetramethyl-1,3,2-dioxaborolan-2-yl)benzyl)oxy)phenyl)-6-(trifluoromethyl)pyrimidine (33)



GP3 was followed using **26** (190 mg, 0.368 mmol) and *m*-CPBA (82 mg, 0.368 mmol). Column chromatography (20% EtOAc in hexanes) afforded **27** (122.2 mg, 55%) as amorphous solid.

^1H NMR (600 MHz, CDCl_3): δ = 8.00 (s, 1H, H-5), 7.86 – 7.81 (m, 3H, H-2'', H-2'), 7.78 (d, J = 7.8 Hz, 1H, H-4'), 7.48 – 7.42 (m, 3H, H-3'', H-5'), 7.20 (dd, J = 8.3, 2.6 Hz, 1H, H-6'), 5.20 (s, 2H, CH_2), 3.31 (dq, J^2_{Gem} = 13.1 Hz, J^3_{HH} = 7.4 Hz, 1H, H-a), 3.18 (dq, J^2_{Gem} = 13.1 Hz, J^3_{HH} = 7.4 Hz, 1H, H-a'), 1.36 (t, J = 7.4 Hz, 3H, H-b), 1.34 (s, 12H, Pin(CH_3)); ^{13}C NMR (151 MHz, CDCl_3): δ = 174.87 (C-2), 168.08 (C-4), 159.66 (C-3'), 157.56 (q, J_{CF} = 37.0 Hz, C-6), 139.57 (C-1''), 135.67 (C-1'), 135.29 (C-2''), 130.69 (C-5'), 128.85 (Brs, C-4''), 126.74 (C-3''), 120.64 (C-4'), 120.38 (q, J_{CF} = 275.2 Hz, CF_3), 119.83 (C-6'), 114.44 (C-2'), 112.86 (q, J_{CF} = 2.9 Hz, C-5), 84.04 (Pin- $\text{C}(\text{CH}_3)_2$), 70.42 (CH_2), 47.82 (C-a), 25.01 (Pin- CH_3), 6.61 (C-b); HPLC: (retention time = 9.03 min); HPLC-MS (ESI) (m/z): [M] calcd. for $\text{C}_{26}\text{H}_{28}\text{BF}_3\text{N}_2\text{O}_4\text{S}$, 532.2; found $[\text{M}+\text{H}]^+$, 533.2; $[\text{M}+\text{Na}]^+$, 555.2.

2-(ethylsulfinyl)-4-(3-((4-(tributylstannyl)benzyl)oxy)phenyl)-6-(trifluoromethyl)pyrimidine (35)



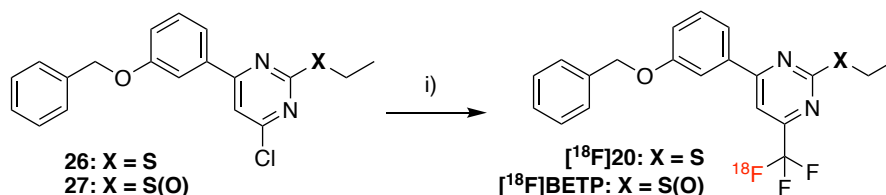
GP3 was followed using **29** (177 mg, 0.260 mmol) and *m*-CPBA (64.2 mg, 0.286 mmol). Column chromatography (20% EtOAc in hexanes) afforded the sulfoxide **30** as a thick oil (124 mg, 68%).

^1H NMR (600 MHz, CDCl_3): δ = 8.01 (s, 1H, H-5), 7.87 (t, J = 2.1 Hz, 1H, H-2'), 7.80 (d, J = 7.8 Hz, 1H, H-4'), 7.57 – 7.44 (m, 3H, H-3'', H-5'), 7.42 (d, J = 7.6 Hz, 2H, H-2''), 7.23 (dd, J = 8.1, 1.9 Hz, 1H, H-6'), 5.15 (s, 2H, CH_2), 3.32 (dq, J^2_{Gem} = 13.3 Hz, J^3_{HH} = 7.5 Hz, 1H, H-a), 3.20 (dq, J^2_{Gem} = 13.3, J^3_{HH} = 7.4 Hz, 1H, H-a'), 1.74 – 1.44 (m, 6H, SnBu_3), 1.40 – 1.26 (m, 9H, SnBu_3 , H-b), 1.13 – 0.99 (m, 6H, SnBu_3), 0.88 (t, J = 7.3 Hz, 9H, SnBu_3); ^{13}C NMR (151 MHz, CDCl_3): δ = 174.81 (C-2), 168.13 (C-4), 159.83 (C-3'), 157.52 (q, J_{CF} = 36.7 Hz, C-6), 142.48 (C-1''), 136.92 (C-2''), 135.98 (C-1'), 135.65 (C-4''), 130.67 (C-5'), 127.30 (C-3''), 120.55 (C-4'), 120.37 (q, J_{CF} = 275.1

Hz, CF_3), 119.67 (C-6'), 114.40 (C-2'), 112.84 (q, $J_{\text{CF}} = 2.8$ Hz, C-5), 70.65 (CH_2), 47.79 (C-a), 29.20 (SnBu₃), 27.48 (SnBu₃), 13.78 (SnBu₃), 9.73 (SnBu₃), 6.60 (C-b); HPLC: (retention time = 9.94 min); HPLC-MS (ESI) (m/z): [M-SnBu₃] calcd. for C₂₀H₁₇F₃N₂O₂S, 406.1; found [M-SnBu₃+H]⁺, 407.1.

13.2 Manual Radiosynthesis Experiments

13.2.1 Radiosynthetic Studies Towards [¹⁸F]BETP



The radiotrifluoromethylation of compounds **26** and **27** was carried out using the same general procedure adapted from the protocol published by Huiban *et al.*⁷⁹ Aqueous [¹⁸F]fluoride delivered from a cyclotron target wash was passed over a QMA cartridge that had been previously conditioned with NaHCO₃ (1 M, 10 ml), air (10 ml), water (10 ml) and air (10 ml). The [¹⁸F]fluoride was eluted using the standard QMA eluent (kryptofix (K₂₂₂) (9.5 mg), K₂CO₃ (1.7 mg) in water (80 μ l) and MeCN (1.92 ml)) into a 5 ml Wheaton v-vial. The eluted ¹⁸F was then subjected to 3 azeotropic drying cycles using additions of MeCN (1.5 ml) under a stream of argon. The dry [¹⁸F]KF/K₂₂₂ residue was then resolubilized with 600 μ l of DMF, which was then dispensed into two 5 ml reaction vials (ca. 800 MBq), each containing CuI (11 mg) and a magnetic stirrer bar (teflon coated). A solution containing **26** (13 mg, 37 μ mol) or **27** (14 mg, 37 μ mol), methyl chlorodifluoroacetate (F₂ClCCO₂Me, 6 μ l, 57 μ mol), and *N,N,N',N'*-tetramethylethylenediamine (TMEDA, 9 μ l, 60 μ mol) in DMF (150 μ l) was then injected into each reaction vial. Each reactor was stirred at 150 °C for 20 min after which it was quenched with water (200 μ l) and left to cool. The RCC performance of each reaction was monitored by radio-TLC (50% EtOAc in hexanes) and product identity was confirmed using radio HPLC.

13.2.2 Radiosynthetic Studies Towards [¹⁸F]F-BETP

Radiosynthetic studies towards the synthesis of [¹⁸F]F-BETP from precursors **32**, **33**, **34**, **35**, **36** were carried out using **general CMRF procedure 2** described above (*vide* **12.4.2**). Each reaction mixture was prepared fresh from reagent stock solutions in DMA (1 mg/10 μ l). The reaction mixtures were then injected into the reaction vials containing [¹⁸F]TBAF and were allowed to stir under the required experimental conditions (*vide* **8.4.2**, Table 13 and Table 14). When complete, each reaction was quenched with HCl (0.25 M, 1 ml) and sampled for radio-TLC (for %RCC quantification) and radio-HPLC analysis (for validation of compound identity against a non-radioactive standard compound).

13.3 Automated Radiosynthesis

13.3.1 General Information

Radiosyntheses were automated using an Elixys FLEX/CHEM automated synthesizer coupled to a PURE/FORM purification and formulation module. The general steps of ^{18}F processing, radiosynthesis, purification (HPLC/SPE), isolation, and formulation were all performed as part of a programmed sequence.

13.3.2 ^{18}F Processing on the Elixys FLEX/CHEM Synthesizer

To adapt the ^{18}F processing steps developed for CMRF chemistry (chapter 7), ^{18}F delivered from a cyclotron was transferred into a 5 ml delivery vial fitted with a filtered vent (Figure 63). Once the delivery was completed, the vent was closed, and an argon gas line (controlled by the Elixys module) was used to pressurize the delivery vial and push the ^{18}F (in ^{18}O]H $_2\text{O}$) over a QMA cartridge, collecting the ^{18}O]H $_2\text{O}$ waste into a sample vial for recovery. The vent was then opened and MeOH (1 ml) for QMA washing was injected into the delivery vial. The vent was again shut, and the gas line (from the Elixys module) was opened to push the MeOH over the QMA, removing any residual water trapped in the QMA resin. After the washing step was completed, the QMA eluent (TBAOTf (10 mg) in MeOH (1 ml)) contained in a reagent vial in the cassette (position 1) was passed over the QMA cartridge to elute the activity into the reactor vessel (reactor 1). Once in the reactor, the MeOH was removed by evaporation under vacuum to afford dry ^{18}F]TBAF (with residual TBAOTf).

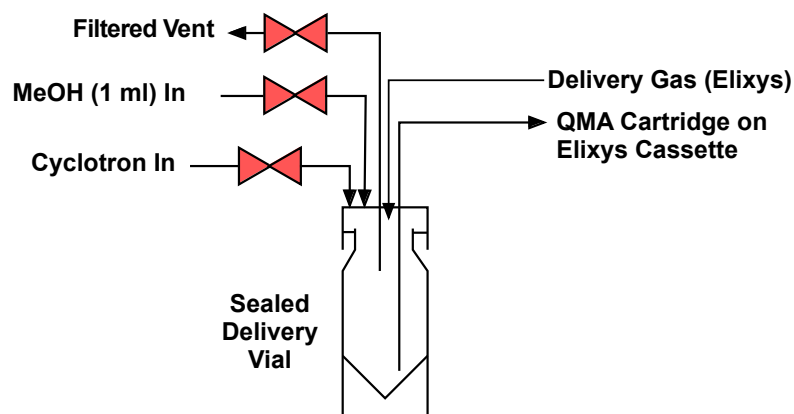


Figure 63: A schematic diagram of the external delivery vial used to collect ^{18}F from the cyclotron before ^{18}F processing.

13.3.3 Automated Synthesis of ^{18}F]F-BETP (Two-Pot)

The reaction mixture containing $\text{Cu}(\text{OTf})_2$ (5.4 mg, 15 μmol) and pyridine (4.8 μl , 60 μmol) in DMA (325 μl) and *n*-BuOH (175 μl) was prepared in an Elixys reagent vial. The boronic acid precursor **36** (6.5 mg, 15 μmol , dissolved in 200 μl DMA) was injected into the reagent vial just before the start of synthesis. The reaction mixture (700 μl total volume) was then added to the processed ^{18}F]TBAF present in the reactor vessel. The reactor was sealed and allowed to stir using a glass-coated stirrer bar at 110 $^\circ\text{C}$ for 15 minutes. HCl (0.25 M, 2 x 2 ml) was then used to quench the reaction mixture.

The contents of the reactor were then passed over an alox N cartridge, which was stacked on top of a C18 Plus Light SPE cartridge (preconditioned with EtOH (10 ml) and water (10 ml)), trapping the desired product ($[^{18}\text{F}]\mathbf{15}$). Et₂O (1.5 ml) was then added to the reactor and transferred over the cartridge stack through a SEP-PAK dry cartridge (Na₂SO₄) to elute the product into a second reactor vessel (reactor 2). This process was repeated to ensure maximum recovery of the synthesis intermediate into reactor 2. The Et₂O eluent solvent was then removed by evaporation at 50 °C with a stream of argon under reduced pressure. DMA (300 μl) was then added to the dry residue, and to this was added a mixture of AcOH (99%, 400 μl) and H₂O₂ (30% aq, 60 μl). The reactor was sealed and left to stir with a teflon coated stirrer bar at 80 °C for 15 min. Ammonium formate buffer (pH 8, 2 ml) was then added to quench the reaction, followed by the addition of aqueous HPLC eluent (H₂O with 0.1% TFA, 2 ml).

The contents of the second reaction were then transferred to the 5 ml HPLC injection loop and were subsequently injected onto a semi-prep HPLC column for purification (Luna 10 μm C18 (2) 100 Å (250 x 10 mm)). The mixture was separated using an isocratic mix of MeCN (60%) and water + 0.1% TFA (40%). The product peak (ca 9-11 min) was diverted into a dilution reservoir containing 70 ml H₂O. This solution was then passed over a C18 Plus Light SPE cartridge (preconditioned with EtOH (10 ml) and water (10 ml)), trapping the purified product. The SPE cartridge was then rinsed with water (5 ml), after which the product was eluted into a vented product vial with EtOH (500 μl) where it was reconstituted with PBS (4.5 ml).

The best synthesis yielded 5.7 GBq of product (54% RCY) in 5 ml (1.14 GBq/ml) with a molar radioactivity of 17.1 GBq/μmol. Radio-HPLC using the QC radio-HPLC gradient (*vide* **12.4.3**) was used to confirm product identity by comparison of the retention time (17.95 min) with that of an authentic non-radioactive standard compound (18.01 min). A minor difficult-to-separate chemical impurity was occasionally detected at 17.66 min. Radio-TLC (50% EtOAc in hexanes) revealed the final product to contain < 0.2% free [¹⁸F]fluoride.

13.4 *In Vitro* Studies

In vitro studies were performed with the assistance of Sophie Stotz at the Werner Siemens Imaging Center in Tübingen, Germany.

13.4.1 Cell Culture

GLP-1R/CHL cells were cultured using a modified procedure to the one described above (*vide* **11.4.1**). The GLP-1R/CHL cell were cultured in a 175 cm² cell culture flask in RPMI medium (*Sigma Aldrich*) containing 1% PenStrep (*Biochrom GmbH*, Berlin, Germany) and 10% FCS. The cells were cultured in a humidified 5% CO₂ atmosphere at 37 °C and passaged 1:15 every 2-3 days when 90% confluent. They were then counted (C-Chip disposable counting chamber, *NanoEnTek*) and subsequently transferred to gamma counter tubes (2.5 x 10⁶ cells in 900 μl medium) for *in vitro* experiments.

13.4.2 Tracer Uptake Experiments

To evaluate the uptake of [^{18}F]F-BETP in GLP-1R expressing tissues, GLP-1R/CHL cells were used as a model cell line. Additionally, a control experiment was carried out using a HEK293 cell line that did not express the GLP-1R gene. A third “blank” experiment was carried out without cells to quantify the extent to which [^{18}F]F-BETP bound to the plastic walls of the gamma counter tubes. An identical group of blocking experiments was also carried out in each cell line by doping the tracer solution with non-radioactive F-BETP (2.5 μM). All experiments were performed in triplicate.

The tracer solution (delivered from the automated synthesis) was diluted in cell culture medium to a concentration of 2 MBq/ml (2 x 10 ml) and to this solution was added either DMSO (25 μl) or a solution of non-radioactive F-BETP (25 μl , 10 mM, for blocking). 600 μl of the resulting tracer solutions were then dispensed into each tube of the relevant experimental group. The cells were incubated with the tracer for 30 minutes at 37 °C after which they were centrifuged for 5 minutes at 470 x g. The supernatant was discarded, and the cells were washed with two portions of medium (500 μl) followed by a single 1.5 ml portion. The cells were again centrifuged and the supernatant was discarded, after which the cell pellets were measured in an automatic gamma counter. The tracer uptake into each group of cells was quantified against a standard sample of the tracer.

13.4.3 SDS-PAGE experiments

Cells from a separate [^{18}F]F-BETP uptake experiment (2 MBq with 0.5×10^6 cells) were lysed using radioimmunoprecipitation assay (RIPA) buffer containing protease inhibitor. 20 μl of each cell lysate solution was then treated with 4 μl of loading buffer (Tris HCl 0.5 M, SDS 10%, glycerol 30%, bromophenol blue 0.012%, 2-mercaptoethanol 6%), incubated at 95 °C for 5 minutes, and centrifuged (5 minutes, room temperature, 4618 x g). The resulting cell lysates were then separated via sodium dodecyl sulfate polyacrylamide gel electrophoresis (SDS-PAGE) using a 5% acrylamide stacking gel (set with ten pocket comb) and a 12% acrylamide separating gel with running buffer (tris base 25 mM, glycine 200 mM, SDS 0.1%). The cell lysate solutions were loaded into the lanes of the gel. One lane was loaded with a reference protein ladder (PageRuler Prestained Protein Ladder, *Thermo Scientific*, Waltham, Massachusetts, USA). The gel was then connected to a power supply (PowerPac HC, *Bio-Rad Laboratories Inc.*, Hercules, California, USA) and run at 150 V.

13.4.4 Autoradiography

After the completion of SDS-PAGE, the gels were rinsed with water and placed in a light-shielded exposure cassette. A storage phosphor screen (*Molecular Dynamics*, Caesarea, Israel) was carefully laid over the gel, the cassette was sealed, and the screen exposed for approximately ten ^{18}F half-lives (≈ 18 hours). Finally, the phosphor screen was imaged using a Storm 840 phosphorimager (*Molecular Dynamics*).

13.4.5 Coomassie Staining

After the electrophoresis run was complete, the gel was subjected to Coomassie staining. The gel was incubated with InstantBlue (*Expedeon/Biozol GmbH, Eching, Germany*) Protein Stain solution (10 ml) on a shaker at room temperature for 1 hour. The gel was then rinsed and stored in water to prevent desiccation.

References:

1. Brom, M., Andrałojć, K., Oyen, W. J. G., Boerman, O. C. & Gotthardt, M. Development of radiotracers for the determination of the beta-cell mass in vivo. *Curr. Pharm. Des.* **16**, 1561–1577 (2010).
2. Herman, W. H. Diabetes epidemiology: Guiding clinical and public health practice: The Kelly West Award Lecture, 2006. *Diabetes Care* **30**, 1912–1919 (2007).
3. Scully, T. Diabetes in numbers. *Nature* **485**, S2–S3 (2012).
4. Riaz, S. Study of Protein Biomarkers of Diabetes Mellitus Type 2 and Therapy with Vitamin B1. *J. Diabetes Res.* **2015**, 1–10 (2015).
5. Ichise, M. & Harris, P. E. Imaging of β -Cell Mass and Function. *J. Nucl. Med.* **51**, 1001–1004 (2010).
6. Gotthardt, M., Eizirik, D. L., Cnop, M. & Brom, M. Beta cell imaging - a key tool in optimized diabetes prevention and treatment. *Trends Endocrinol. Metab.* **25**, 375–377 (2014).
7. Di Galleonardo, V. *et al.* Imaging of β -cell mass and insulinitis in insulin-dependent (Type 1) diabetes mellitus. *Endocr. Rev.* **33**, 892–919 (2012).
8. Laurent, D. *et al.* Pancreatic β -cell imaging in humans: fiction or option? *Diabetes, Obes. Metab.* **18**, 6–15 (2016).
9. Andralojc, K. *et al.* Obstacles on the way to the clinical visualisation of beta cells: looking for the Aeneas of molecular imaging to navigate between Scylla and Charybdis. *Diabetologia* **55**, 1247–1257 (2012).
10. De Herder, W. W., Van Schaik, E., Kwekkeboom, D. & Feelders, R. A. New therapeutic options for metastatic malignant insulinomas. *Clin. Endocrinol. (Oxf)*. **75**, 277–284 (2011).
11. Mathur, N. B., Sharma, M., Agarwal, A. & Kumar, A. Positron emission tomography in congenital hyperinsulinism. *Indian Pediatr.* **48**, 139–147 (2011).
12. Demirbilek, H. & Hussain, K. Congenital Hyperinsulinism: Diagnosis and Treatment Update. *J. Clin. Res. Pediatr. Endocrinol.* **9**, 69–87 (2017).
13. Kahn, S. E., Hull, R. L. & Utzschneider, K. M. Mechanisms linking obesity to insulin resistance and type 2 diabetes. *Nature* **444**, 840–846 (2006).
14. Faustman, D. L. Why were we wrong for so long? The pancreas of type 1 diabetic patients commonly functions for decades. *Diabetologia* **57**, 1–3 (2014).
15. Akirav, E., Kushner, J. A. & Herold, K. C. Beta-Cell Mass and Type 1 Diabetes: Going, Going, Gone? *Diabetes* **57**, 2883–2888 (2008).
16. Oram, R. A. *et al.* The majority of patients with long-duration type 1 diabetes are insulin microsecretors and have functioning beta cells. *Diabetologia* **57**, 187–191 (2014).
17. Jodal, A., Schibli, R. & Béhé, M. Targets and probes for non-invasive imaging of β -cells. *Eur. J. Nucl. Med. Mol. Imaging* **44**, 712–727 (2017).
18. Wang, W. *et al.* Identification of small-molecule inducers of pancreatic β -cell expansion. *Proc. Natl. Acad. Sci.* **106**, 1427–1432 (2009).
19. Cabrera, O. *et al.* The unique cytoarchitecture of human pancreatic islets has implications for islet cell function. *Proc. Natl. Acad. Sci.* **103**, 2334–2339 (2006).
20. Holmberg, D. & Ahlgren, U. Imaging the pancreas: from ex vivo to non-invasive technology.

- Diabetologia* **51**, 2148–2154 (2008).
21. Nobelprize.org. The Nobel Prize in Chemistry 1943. *Nobel Media AB* Web http://www.nobelprize.org/nobel_prizes/chemistry/laureates/1943/ (2014).
 22. Rahmim, A. & Zaidi, H. PET versus SPECT: strengths, limitations and challenges. *Nucl. Med. Commun.* **29**, 193–207 (2008).
 23. Khalil, M. M., Tremoleda, J. L., Bayomy, T. B. & Gsell, W. Molecular SPECT Imaging: An Overview. *Int. J. Mol. Imaging* **2011**, 1–15 (2011).
 24. Webb, A. *Introduction to Biomedical Imaging*. (John Wiley & Sons, Inc, 2002).
 25. Catana, C., Guimaraes, A. R. & Rosen, B. R. PET and MR Imaging: The Odd Couple or a Match Made in Heaven? *J. Nucl. Med.* **54**, 815–824 (2013).
 26. Bloch, F., Hansen, W. W. & Packard, M. The nuclear induction experiment. *Phys. Rev.* **70**, 474–485 (1946).
 27. Purcell, E., Torrey, H. & Pound, R. Resonance Absorption by Nuclear Magnetic Moments in a Solid. *Phys. Rev.* **69**, 37–38 (1946).
 28. Rorsman, P. & Hellman, B. The interaction between manganese and calcium fluxes in pancreatic beta-cells. *Biochem. J.* **210**, 307–314 (1983).
 29. Rorsman, P., Berggren, P. O. & Hellman, B. Manganese accumulation in pancreatic beta-cells and its stimulation by glucose. *Biochem. J.* **202**, 435–444 (1982).
 30. Antkowiak, P. F. *et al.* Noninvasive assessment of pancreatic β -cell function in vivo with manganese-enhanced magnetic resonance imaging. *Am. J. Physiol. Metab.* **296**, E573–E578 (2009).
 31. Antkowiak, P. F., Stevens, B. K., Nunemaker, C. S., McDuffie, M. & Epstein, F. H. Manganese-enhanced magnetic resonance imaging detects declining pancreatic β -cell mass in a cyclophosphamide-accelerated mouse model of type 1 diabetes. *Diabetes* **62**, 44–48 (2013).
 32. Antkowiak, P. F., Vandsburger, M. H. & Epstein, F. H. Quantitative pancreatic β -cell MRI using manganese-enhanced Look-Locker imaging and two-site water exchange analysis. *Magn. Reson. Med.* **67**, 1730–1739 (2012).
 33. Lamprianou, S. *et al.* High-resolution magnetic resonance imaging quantitatively detects individual pancreatic islets. *Diabetes* **60**, 2853–2860 (2011).
 34. Eter, W. A. *et al.* SPECT-OPT multimodal imaging enables accurate evaluation of radiotracers for β -cell mass assessments. *Sci. Rep.* **6**, 24576 (2016).
 35. Machulla, H.-J., Al-Momani, E. & Malik, N. *The PET Method: Tracer Principle and Radiochemistry*. (Steinbeis-Edition, 2016).
 36. Synowiecki, M. A., Perk, L. R. & Nijssen, J. F. W. Production of novel diagnostic radionuclides in small medical cyclotrons. *EJNMMI Radiopharm. Chem.* **3**, 1–25 (2018).
 37. Conti, M. & Eriksson, L. Physics of pure and non-pure positron emitters for PET: a review and a discussion. *EJNMMI Phys.* **3**, 1–22 (2016).
 38. Wester, H. J. *Pharmaceutical Radiochemistry: 1*. (Scintomics, 2010).
 39. Nobelprize.org. The Nobel Prize in Physics 1939. *Nobel Media AB* Web http://www.nobelprize.org/nobel_prizes/physics/laureates/2005/advanced.html (2014).

40. Henderson, M. C. & White, M. G. The Design and Operation of a Large Cyclotron. *Rev. Sci. Instrum.* **9**, 19–30 (1938).
41. Lawrence, E. O. & Livingston, M. S. The Production of High Speed Light Ions Without the Use of High Voltages. *Phys. Rev.* **40**, 19–35 (1932).
42. Kambali, I. *et al.* Dependence of ¹⁸F Production Yield and Radioactive Impurities on Proton Irradiation Dose. *Phys. Res. Int.* **2017**, 1–5 (2017).
43. Campbell, M. G. & Ritter, T. Modern carbon-fluorine bond forming reactions for aryl fluoride synthesis. *Chem. Rev.* **115**, 612–633 (2015).
44. Fina, B. L. & Rigalli, A. CHAPTER 3. The Chemistry of Fluorine. in *Fluorine: Chemistry, Analysis, Function and Effects* (ed. Preedy, V. R.) 41–53 (The Royal Society of Chemistry, 2015). doi:10.1039/9781782628507-00041.
45. Liang, T., Neumann, C. N. & Ritter, T. Introduction of fluorine and fluorine-containing functional groups. *Angew. Chemie - Int. Ed.* **52**, 8214–8264 (2013).
46. Campbell, M. G. *et al.* Bridging the gaps in ¹⁸F PET tracer development. *Nat. Chem.* **9**, 1–3 (2017).
47. Preshlock, S., Tredwell, M. & Gouverneur, V. ¹⁸F-Labeling of Arenes and Heteroarenes for Applications in Positron Emission Tomography. *Chem. Rev.* **116**, 719–766 (2016).
48. Furuya, T., Kuttruff, C. A. & Ritter, T. Carbon-fluorine bond formation Fluorinating reagents. *Curr. Opin. Drug Disc.* **11**, 803–819 (2008).
49. Schirmacher, R., Wangler, C. & Schirmacher, E. Recent Developments and Trends in ¹⁸F-Radiochemistry: Syntheses and Applications. *Mini. Rev. Org. Chem.* **4**, 317–329 (2007).
50. Yu, S. Review of ¹⁸F-FDG synthesis and quality control. *Biomed. Imaging Interv. J.* **2**, 1–11 (2006).
51. Bickelhaupt, F. M. & Bento, A. P. Nucleophilicity and Leaving-Group Ability in Frontside and Backside S_N2 Reactions. *J. Org. Chem.* **73**, 7290–7299 (2008).
52. Clayden, J., Greeves, Ni., Warren, S. & Wothers, P. *Organic Chemistry*. (Oxford University Press, 2001).
53. Jacobson, O., Kiesewetter, D. O. & Chen, X. Fluorine-18 radiochemistry, labeling strategies and synthetic routes. *Bioconjug. Chem.* **26**, 1–18 (2015).
54. van der Born, D. *et al.* Fluorine-18 labelled building blocks for PET tracer synthesis. *Chem. Soc. Rev.* **46**, 4709–4773 (2017).
55. Ichiishi, N., Canty, A. J., Yates, B. F. & Sanford, M. S. Cu-catalyzed fluorination of diaryliodonium salts with KF. *Org. Lett.* **15**, 5134–5137 (2013).
56. Ichiishi, N. *et al.* Copper-Catalyzed [¹⁸F]Fluorination of (Mesityl)(aryl)iodonium Salts. *Org. Lett.* **16**, 3224–3227 (2014).
57. McCammant, M. S. *et al.* Cu-Mediated C–H ¹⁸F-Fluorination of Electron-Rich (Hetero)arenes. *Org. Lett.* **19**, 3939–3942 (2017).
58. Lee, E. *et al.* A Fluoride-Derived Electrophilic Late-Stage Fluorination Reagent for PET Imaging. *Science (80-)*. **334**, 639–642 (2011).
59. Ren, H. *et al.* Synthesis and imaging validation of [¹⁸F]MDL100907 enabled by Ni-mediated fluorination. *ACS Chem. Neurosci.* **5**, 611–615 (2014).

60. Lee, E., Hooker, J. M. & Ritter, T. Nickel-mediated oxidative fluorination for PET with aqueous [18F] fluoride. *J. Am. Chem. Soc.* **134**, 17456–17458 (2012).
61. Beyzavi, M. H. *et al.* 18F-Deoxyfluorination of Phenols via Ru π -Complexes. *ACS Cent. Sci.* **3**, 944–948 (2017).
62. Neumann, C. N., Hooker, J. M. & Ritter, T. Concerted nucleophilic aromatic substitution with 19F- and 18F-. *Nature* **534**, 369–373 (2016).
63. Brooks, A. F., Topczewski, J. J., Ichiishi, N., Sanford, M. S. & Scott, P. J. H. Late-stage [18F]fluorination: New solutions to old problems. *Chem. Sci.* **5**, 4545–4553 (2014).
64. Ye, Y., Schimler, S. D., Hanley, P. S. & Sanford, M. S. Cu(OTf)₂-mediated fluorination of aryltrifluoroborates with potassium fluoride. *J. Am. Chem. Soc.* **135**, 16292–16295 (2013).
65. Qiao, J. X. & Lam, P. Y. S. Copper-promoted carbon-heteroatom bond cross-coupling with boronic acids and derivatives. *Synthesis (Stuttg.)* **6**, 829–856 (2011).
66. King, A. E., Ryland, B. L., Brunold, T. C. & Stahl, S. S. Kinetic and spectroscopic studies of aerobic copper(II)-catalyzed methoxylation of arylboronic esters and insights into aryl transmetalation to copper(II). *Organometallics* **31**, 7948–7957 (2012).
67. Tredwell, M. *et al.* A General Copper-Mediated Nucleophilic 18 F Fluorination of Arenes. *Angew. Chemie - Int. Ed.* **53**, 7751–7755 (2014).
68. Zlatopolskiy, B. D. *et al.* Copper-mediated aromatic radiofluorination revisited: Efficient production of PET tracers on a preparative scale. *Chem. - A Eur. J.* **21**, 5972–5979 (2015).
69. Preshlock, S. *et al.* Enhanced copper-mediated 18 F-fluorination of aryl boronic esters provides eight radiotracers for PET applications. *Chem. Commun.* **52**, 8361–8364 (2016).
70. Mossine, A. V *et al.* Synthesis of [18F]Arenes via the Copper-Mediated [18F]Fluorination of Boronic Acids. *Org. Lett.* **17**, 5780–5783 (2015).
71. Zischler, J., Kolks, N., Modemann, D., Neumaier, B. & Zlatopolskiy, B. D. Alcohol-Enhanced Cu-Mediated Radiofluorination. *Chem. - A Eur. J.* **23**, 3251–3256 (2017).
72. Antuganov, D. *et al.* Effect of Pyridine Addition on the Efficiency of Copper-Mediated Radiofluorination of Aryl Pinacol Boronates. *ChemistrySelect* **2**, 7909–7912 (2017).
73. Makaravage, K. J., Brooks, A. F., Mossine, A. V., Sanford, M. S. & Scott, P. J. H. H. Copper-Mediated Radiofluorination of Arylstannanes with [18F]KF. *Org. Lett.* **18**, 5440–5443 (2016).
74. Zarrad, F., Zlatopolskiy, B., Krapf, P., Zischler, J. & Neumaier, B. A Practical Method for the Preparation of 18F-Labeled Aromatic Amino Acids from Nucleophilic [18F]Fluoride and Stannyl Precursors for Electrophilic Radiohalogenation. *Molecules* **22**, 2231 (2017).
75. Mossine, A. V *et al.* Development of Customized [18F]Fluoride Elution Techniques for the Enhancement of Copper-Mediated Late-Stage Radiofluorination. *Sci. Rep.* **7**, 233 (2017).
76. Mossine, A. V. *et al.* Automated synthesis of PET radiotracers by copper-mediated 18F-fluorination of organoborons: Importance of the order of addition and competing protodeborylation. *J. Label. Compd. Radiopharm.* **61**, 228–236 (2018).
77. Riss, P. J. *et al.* Direct, nucleophilic radiosynthesis of [18F]trifluoroalkyl tosylates: Improved labelling procedures. *Org. Biomol. Chem.* **10**, 6980–6986 (2012).
78. Fawaz, M. V. *et al.* High affinity radiopharmaceuticals based upon lansoprazole for PET imaging of

- aggregated tau in alzheimer"s disease and progressive supranuclear palsy: Synthesis, preclinical evaluation, and lead selection. *ACS Chem. Neurosci.* **5**, 718–730 (2014).
79. Huiban, M. *et al.* A broadly applicable [¹⁸F]trifluoromethylation of aryl and heteroaryl iodides for PET imaging. *Nat. Chem.* **5**, 941–944 (2013).
80. van der Born, D., Herscheid, J. (Koos) D. M., Orru, R. V. A. & Vugts, D. J. Efficient synthesis of [¹⁸F]trifluoromethane and its application in the synthesis of PET tracers. *Chem. Commun.* **49**, 4018–4020 (2013).
81. Van der born, D. *et al.* A universal procedure for the [¹⁸F]trifluoromethylation of aryl iodides and aryl boronic acids with highly improved specific activity. *Angew. Chemie - Int. Ed.* **53**, 11046–11050 (2014).
82. Riss, P. J. & Aigbirhio, F. I. A simple, rapid procedure for nucleophilic radiosynthesis of aliphatic [¹⁸F]trifluoromethyl groups. *Chem. Commun.* **47**, 11873–11875 (2011).
83. Otte, A. The Role of PET in Drug Discovery — Neuropsychiatry. in *Trends on the Role of PET in Drug Development* (eds. Elsinga, P. H., Waarde, A. Van, Paans, A. M. J. & Dierckx, R. A. J. O.) 559–574 (WORLD SCIENTIFIC, 2012). doi:10.1142/9789814317740_0020.
84. Price, E. W. & Orvig, C. Matching chelators to radiometals for radiopharmaceuticals. *Chem. Soc. Rev.* **43**, 260–290 (2014).
85. Brandt, M., Cardinale, J., Aulsebrook, M. L., Gasser, G. & Mindt, T. L. An Overview of PET Radiochemistry, Part 2: Radiometals. *J. Nucl. Med.* **59**, 1500–1506 (2018).
86. Bowden, G. D., Pichler, B. J. & Maurer, A. A Design of Experiments (DoE) Approach Accelerates the Optimization of Copper-Mediated ¹⁸F-Fluorination Reactions of Arylstannanes. *Sci. Rep.* **9**, 11370 (2019).
87. Murray, P. M., Tyler, S. N. G. & Moseley, J. D. Beyond the Numbers: Charting Chemical Reaction Space. *Org. Process Res. Dev.* **17**, 40–46 (2013).
88. Leardi, R. Experimental design in chemistry: A tutorial. *Anal. Chim. Acta* **652**, 161–172 (2009).
89. Murray, P. M. *et al.* The application of design of experiments (DoE) reaction optimisation and solvent selection in the development of new synthetic chemistry. *Org. Biomol. Chem.* **14**, 2373–2384 (2016).
90. Lendrem, D. W. *et al.* Lost in space: Design of experiments and scientific exploration in a Hogarth Universe. *Drug Discovery Today* vol. 20 1365–1371 (2015).
91. Dejaegher, B. & Vander Heyden, Y. Experimental designs and their recent advances in set-up, data interpretation, and analytical applications. *J. Pharm. Biomed. Anal.* **56**, 141–158 (2011).
92. Murray, P. M. What is Experimental Design? *catalysisconsulting.co.uk* <http://www.catalysisconsulting.co.uk/what-is-experimental-design.html> (2019).
93. Tye, H. Application of statistical ‘ design of experiments ’ methods in drug discovery. *Drug Discov. Today* **9**, 485–491 (2004).
94. Box, G. E. P., Hunter, J. S. & Hunter, W. G. *Statistics for Experimenters*. (Wiley Interscience, 2005).
95. Dunn, K. *Process Improvement Using Data*. (Kevin Dunn, 2018).
96. Sweet, I. R. *et al.* Systematic screening of potential β -cell imaging agents. *Biochem. Biophys. Res. Commun.* **314**, 976–983 (2004).

97. Sweet, I. R., Cook, D. L., Iernmark, Å., Greenbaum, C. J. & Krohn, K. A. Non-Invasive Imaging of Beta Cell Mass: A Quantitative Analysis. *Diabetes Technol. Ther.* **6**, 652–659 (2004).
98. Imperiale, A. *et al.* 18F-FDOPA PET/CT imaging of insulinoma revisited. *Eur. J. Nucl. Med. Mol. Imaging* **42**, 409–418 (2015).
99. Kauhanen, S., Seppanen, M., Minn, H. & Nuutila, P. Clinical PET Imaging of Insulinoma and Beta-Cell Hyperplasia. *Curr. Pharm. Des.* **16**, 1550–1560 (2010).
100. Tessonnier, L. *et al.* Limited Value of 18F-F-DOPA PET to Localize Pancreatic Insulin-Secreting Tumors in Adults with Hyperinsulinemic Hypoglycemia. *J. Clin. Endocrinol. Metab.* **95**, 303–307 (2010).
101. Rubí, B. *et al.* Dopamine D2-like Receptors Are Expressed in Pancreatic Beta Cells and Mediate Inhibition of Insulin Secretion. *J. Biol. Chem.* **280**, 36824–36832 (2005).
102. Garcia, A., Venugopal, A., Pan, M.-L. & Mukherjee, J. Imaging Pancreas in Healthy and Diabetic Rodent Model Using [(18)F]Fallypride Positron Emission Tomography/Computed Tomography. *Diabetes Technol. Ther.* **16**, 640–643 (2014).
103. Garcia, A. *et al.* 18F-Fallypride PET of Pancreatic Islets: In Vitro and In Vivo Rodent Studies. *J. Nucl. Med.* **52**, 1125–1132 (2011).
104. Willekens, S. M. A. *et al.* Quantitative and longitudinal imaging of intramuscular transplanted islets of Langerhans with SPECT using [123I]IBZM. *Diabetes, Obes. Metab.* **19**, 604–608 (2017).
105. Simpson, N. R. *et al.* Visualizing pancreatic β -cell mass with [11C]DTBZ. *Nucl. Med. Biol.* **33**, 855–864 (2006).
106. Souza, F. *et al.* Current progress in non-invasive imaging of beta cell mass of the endocrine pancreas. *Curr. Med. Chem.* **13**, 2761–73 (2006).
107. Souza, F. *et al.* Longitudinal noninvasive PET-based β cell mass estimates in a spontaneous diabetes rat model. *J. Clin. Invest.* **116**, 1506–1513 (2006).
108. Fagerholm, V. *et al.* Assessment of Islet Specificity of Dihydropyridazine Radiotracer Binding in Rat Pancreas and Human Pancreas. *J. Nucl. Med.* **51**, 1439–1446 (2010).
109. Schäfer, M. K.-H. *et al.* Species-specific vesicular monoamine transporter 2 (VMAT2) expression in mammalian pancreatic beta cells: implications for optimising radioligand-based human beta cell mass (BCM) imaging in animal models. *Diabetologia* **56**, 1047–1056 (2013).
110. Proks, P., Reimann, F., Green, N., Gribble, F. & Frances, A. Sulfonylurea stimulation of insulin secretion. *Diabetes* **51**, 368–377 (2002).
111. Schneider, S. *et al.* In Vitro and In Vivo Evaluation of Novel Glibenclamide Derivatives as Imaging Agents for the Non-Invasive Assessment of the Pancreatic Islet Cell Mass in Animals and Humans. *Exp Clin Endocrinol Diabetes* **113**, 388–395 (2005).
112. Kazakos, K. Incretin effect: GLP-1, GIP, DPP4. *Diabetes Res. Clin. Pract.* **93**, S32–S36 (2011).
113. Graaf, C. d. *et al.* Glucagon-Like Peptide-1 and Its Class B G Protein-Coupled Receptors: A Long March to Therapeutic Successes. *Pharmacol. Rev.* **68**, 954–1013 (2016).
114. Tornehave, D., Kristensen, P., Rømer, J., Knudsen, L. B. & Heller, R. S. Expression of the GLP-1 receptor in mouse, rat, and human pancreas. *J. Histochem. Cytochem.* **56**, 841–851 (2008).
115. Cline, G. W., Zhao, X., Jakowski, A. B., Soeller, W. C. & Treadway, J. L. Islet-selectivity of G-protein coupled receptor ligands evaluated for PET imaging of pancreatic β -cell mass. *Biochem. Biophys.*

- Res. Commun.* **412**, 413–418 (2011).
116. Koole, C. *et al.* Recent advances in understanding GLP-1R (glucagon-like peptide-1 receptor) function. *Biochem. Soc. Trans.* **41**, 172–179 (2013).
117. Jazayeri, A. *et al.* Crystal structure of the GLP-1 receptor bound to a peptide agonist. *Nature* **546**, 254–258 (2017).
118. Willard, F. S. & Sloop, K. W. Physiology and Emerging Biochemistry of the Glucagon-Like Peptide-1 Receptor. *Exp. Diabetes Res.* **2012**, 1–12 (2012).
119. Donnelly, D. The structure and function of the glucagon-like peptide-1 receptor and its ligands. *Br. J. Pharmacol.* **166**, 27–41 (2012).
120. Underwood, C. R. *et al.* Crystal Structure of Glucagon-like Peptide-1 in Complex with the Extracellular Domain of the Glucagon-like Peptide-1 Receptor. *J. Biol. Chem.* **285**, 723–730 (2010).
121. Jones, B. *et al.* Targeting GLP-1 receptor trafficking to improve agonist efficacy. *Nat. Commun.* **9**, 1602 (2018).
122. Wootten, D. *et al.* Differential Activation and Modulation of the Glucagon-Like Peptide-1 Receptor by Small Molecule Ligands. *Mol. Pharmacol.* **83**, 822–834 (2013).
123. Coopman, K. *et al.* Residues within the Transmembrane Domain of the Glucagon-Like Peptide-1 Receptor Involved in Ligand Binding and Receptor Activation: Modelling the Ligand-Bound Receptor. *Mol. Endocrinol.* **25**, 1804–1818 (2011).
124. Eng, J., Kleinman, W. A., Singh, L., Singh, G. & Raufman, J. P. Isolation and characterization of exendin-4, an exendin-3 analogue, from *Heloderma suspectum* venom. Further evidence for an exendin receptor on dispersed acini from guinea pig pancreas. *J. Biol. Chem.* **267**, 7402–7405 (1992).
125. Raufman, J. P., Singh, L. & Eng, J. Exendin-3, a Novel Peptide from *Heloderma horridum* Venom, Interacts with Vasoactive Intestinal Peptide Receptors and a Newly Described Receptor on Dispersed Acini from Guinea Pig Pancreas. *J. Biol. Chem.* **266**, 2897–2902 (1991).
126. Gotthardt, M. *et al.* A new technique for in vivo imaging of specific GLP-1 binding sites: First results in small rodents. *Regul. Pept.* **137**, 162–167 (2006).
127. Kiesewetter, D. O. *et al.* 18F-radiolabeled analogs of exendin-4 for PET imaging of GLP-1 in insulinoma. *Eur. J. Nucl. Med. Mol. Imaging* **39**, 463–473 (2012).
128. Wild, D. *et al.* Exendin-4-Based Radiopharmaceuticals for Glucagonlike Peptide-1 Receptor PET/CT and SPECT/CT. *J. Nucl. Med.* **51**, 1059–1067 (2010).
129. Reiner, T. *et al.* Accurate measurement of pancreatic islet β -cell mass using a second-generation fluorescent exendin-4 analog. *Proc. Natl. Acad. Sci. U. S. A.* **108**, 12815–12820 (2011).
130. Keliher, E. J., Reiner, T., Thurber, G. M., Upadhyay, R. & Weissleder, R. Efficient 18 F-Labeling of Synthetic Exendin-4 Analogues for Imaging Beta Cells. *ChemistryOpen* **1**, 177–183 (2012).
131. Brand, C. *et al.* In Vivo Imaging of GLP-1R with a Targeted Bimodal PET/Fluorescence Imaging Agent. *Bioconjug. Chem.* **25**, 1323–1330 (2014).
132. Wild, D. *et al.* [Lys40(Ahx-DTPA-111In)NH2]exendin-4, a very promising ligand for glucagon-like peptide-1 (GLP-1) receptor targeting. *J. Nucl. Med.* **47**, 2025–2033 (2006).
133. Wicki, A. *et al.* [Lys40(Ahx-DTPA-111In)NH2]-exendin-4 is a highly efficient radiotherapeutic for glucagon-like peptide-1 receptor-targeted therapy for insulinoma. *Clin. Cancer Res.* **13**, 3696–3705

- (2007).
134. Wild, D., Mäcke, H., Christ, E., Gloor, B. & Reubi, J. C. Glucagon-like Peptide 1–Receptor Scans to Localize Occult Insulinomas. *N. Engl. J. Med.* **359**, 766–768 (2008).
 135. Brom, M. *et al.* Non-invasive quantification of the beta cell mass by SPECT. *Diabetologia* **57**, 950–959 (2014).
 136. Brom, M., Joosten, L., Oyen, W. J. G., Gotthardt, M. & Boerman, O. C. Radiolabelled GLP-1 analogues for in vivo targeting of insulinomas. *Contrast Media Mol. Imaging* **7**, 160–166 (2012).
 137. Rylova, S. N. *et al.* Approaches to improve the pharmacokinetics of radiolabeled GLP-1 receptor ligands using antagonistic tracers. *J. Nucl. Med.* **57**, 1282–1289 (2016).
 138. Mikkola, K. *et al.* 64Cu- and 68Ga-Labelled [Nle14,Lys40(Ahx-NODAGA)NH2]-Exendin-4 for Pancreatic Beta Cell Imaging in Rats. *Mol. Imaging Biol.* **16**, 255–63 (2014).
 139. Kiesewetter, D. O. *et al.* Evaluation of an [18F]AlF-NOTA analog of exendin-4 for imaging of GLP-1 receptor in insulinoma. *Theranostics* **2**, 999–1009 (2012).
 140. Mikkola, K. *et al.* Low kidney uptake of GLP-1R-targeting, beta cell-specific PET tracer, 18F-labeled [Nle14,Lys40]exendin-4 analog, shows promise for clinical imaging. *EJNMMI Res.* **6**, 1–11 (2016).
 141. Yim, C.-B. *et al.* Synthesis and preclinical characterization of [64Cu]NODAGA-MAL-exendin-4 with a Nε-maleoyl-l-lysyl-glycine linkage. *Nucl. Med. Biol.* **40**, 1006–1012 (2013).
 142. Willard, F. S., Bueno, A. B. & Sloop, K. W. Small Molecule Drug Discovery at the Glucagon-Like Peptide-1 Receptor. *Exp. Diabetes Res.* **2012**, 1–9 (2012).
 143. Yang, D., Zhou, C., Liu, Q. & Wang, M. Landmark studies on the glucagon subfamily of GPCRs : from small molecule modulators to a crystal structure. *Acta Pharmacol. Sin.* **36**, 1033–1042 (2015).
 144. Song, G. *et al.* Human GLP-1 receptor transmembrane domain structure in complex with allosteric modulators. *Nature* **546**, 312–315 (2017).
 145. Murphy, K. G. & Bloom, S. R. Nonpeptidic glucagon-like peptide 1 receptor agonists: A magic bullet for diabetes?: Fig. 1. *Proc. Natl. Acad. Sci.* **104**, 689–690 (2007).
 146. May, L. T. & Christopoulos, A. Allosteric modulators of G-protein-coupled receptors. *Curr. Opin. Pharmacol.* **3**, 551–556 (2003).
 147. Conn, P. J., Christopoulos, A. & Lindsley, C. W. Allosteric modulators of GPCRs: a novel approach for the treatment of CNS disorders. *Nat Rev Drug Discov* **8**, 41–54 (2009).
 148. Bueno, A. B. *et al.* Positive allosteric modulation of the glucagon-like peptide-1 receptor by diverse electrophiles. *J. Biol. Chem.* **291**, 10700–10715 (2016).
 149. Knudsen, L. B. *et al.* Small-molecule agonists for the glucagon-like peptide 1 receptor. *Proc. Natl. Acad. Sci.* **104**, 937–942 (2007).
 150. Teng, M. *et al.* Small molecule ago-allosteric modulators of the human glucagon-like peptide-1 (hGLP-1) receptor. *Bioorg. Med. Chem. Lett.* **17**, 5472–5478 (2007).
 151. Irwin, N., Flatt, P. R., Patterson, S. & Green, B. D. Insulin-releasing and metabolic effects of small molecule GLP-1 receptor agonist 6, 7-dichloro-2-methylsulfonyl-3-N- tert -butylaminoquinoxaline. *Eur. J. Pharmacol.* **628**, 268–273 (2010).
 152. Koole, C. *et al.* Allosteric ligands of the glucagon-like peptide 1 receptor (GLP-1R) differentially modulate endogenous and exogenous peptide responses in a pathway-selective manner:

- implications for drug screening. *Mol. Pharmacol.* **78**, 456–465 (2010).
153. Li, N., Lu, J. & Willars, G. B. Allosteric Modulation of the Activity of the Glucagon-like Peptide-1 (GLP-1) Metabolite GLP-1 9-36 Amide at the GLP-1 Receptor. *PLoS One* **7**, 1–10 (2012).
154. Owen, S. C. *et al.* Colloidal Drug Formulations Can Explain “Bell-Shaped” Concentration–Response Curves. *ACS Chem. Biol.* **9**, 777–784 (2014).
155. Sloop, K. W. *et al.* Novel Small Molecule Glucagon-Like Peptide-1 Receptor From Human Islets. **59**, 3099–3107 (2010).
156. Willard, F. S. *et al.* Small Molecule Allosteric Modulation of the Glucagon-Like Peptide-1 Receptor Enhances the Insulinotropic Effect of Oxyntomodulin. *Mol. Pharmacol.* **82**, 1066–1073 (2012).
157. Wootten, D. *et al.* Allosteric Modulation of Endogenous Metabolites as an Avenue for Drug Discovery. *Mol. Pharmacol.* **82**, 281–290 (2012).
158. Nolte, W. M. *et al.* A potentiator of orthosteric ligand activity at GLP-1R acts via covalent modification. *Nat. Chem. Biol.* **10**, 629–631 (2014).
159. Broichhagen, J. *et al.* Allosteric Optical Control of a Class B G-Protein-Coupled Receptor. *Angew. Chemie - Int. Ed.* **55**, 5865–5868 (2016).
160. Li, J. J. *et al.* Synthesis and structure-activity relationship of 2-amino-3-heteroaryl-quinoxalines as non-peptide, small-molecule antagonists for interleukin-8 receptor. *Bioorganic Med. Chem.* **11**, 3777–3790 (2003).
161. Sabra, G. *et al.* INS-1 cell glucose-stimulated insulin secretion is reduced by the downregulation of the 67 kDa laminin receptor. *J. Tissue Eng. Regen. Med.* **9**, 1376–1385 (2015).
162. Koole, C. *et al.* Minireview: Signal bias, allosterism, and polymorphic variation at the GLP-1R: implications for drug discovery. *Mol. Endocrinol.* **27**, 1234–44 (2013).
163. Pocai, A. Unraveling oxyntomodulin, GLP1’s enigmatic brother. *J. Endocrinol.* **215**, 335–346 (2012).
164. Keov, P., Sexton, P. M. & Christopoulos, A. Allosteric modulation of G protein-coupled receptors: A pharmacological perspective. *Neuropharmacology* **60**, 24–35 (2011).
165. Mathiessen, B., Jensen, A. T. I. & Zhuravlev, F. Homogeneous nucleophilic radiofluorination and fluorination with phosphazene hydrofluorides. *Chem. - A Eur. J.* **17**, 7796–7805 (2011).
166. Mathiessen, B., Jensen, M. & Zhuravlev, F. [18F] fluoride recovery via gaseous [18F]HF. *J. Label. Compd. Radiopharm.* **54**, 816–818 (2011).
167. Kopka, K. *et al.* 5-Pyrrolidinylsulfonyl isatins as a potential tool for the molecular imaging of caspases in apoptosis. *J. Med. Chem.* **49**, 6704–6715 (2006).
168. Vaidyanathan, G. *et al.* Radiolabeled guanine derivatives for the in vivo mapping of O6-alkylguanine-DNA alkyltransferase: 6-(4-[18F]fluoro-benzyloxy)-9H-purin-2-ylamine and 6-(3-[131I]iodo-benzyloxy)-9H-purin-2-ylamine. *Bioconjug. Chem.* **11**, 868–875 (2000).
169. Thonon, D., Kech, C. C., Paris, J. J., Lemaire, C. & Luxen, A. A. New Strategy for the Preparation of Clickable Peptides and Labeling with 1-(Azidomethyl)-4-[18F]-fluorobenzene for PET. *Bioconjug. Chem.* **20**, 817–823 (2009).
170. Mossine, A. V *et al.* One-pot synthesis of high molar activity 6-[18F]fluoro-l-DOPA by Cu-mediated fluorination of a BPin precursor. *Org. Biomol. Chem.* **17**, 8701–8705 (2019).
171. Zhang, X., Basuli, F. & Swenson, R. E. An azeotropic drying-free approach for copper-mediated

- radiofluorination without addition of base. *J. Label. Compd. Radiopharm.* **62**, 139–145 (2019).
172. Taylor, N. J. *et al.* Derisking the Cu-Mediated ¹⁸F-Fluorination of Heterocyclic Positron Emission Tomography Radioligands. *J. Am. Chem. Soc.* **139**, 8267–8276 (2017).
173. Eng, H. *et al.* Demonstration of the Innate Electrophilicity of 4-(3-(Benzyloxy)phenyl)-2-(ethylsulfinyl)-6-(trifluoromethyl)pyrimidine (BETP), a Small-Molecule Positive Allosteric Modulator of the Glucagon-Like Peptide-1 Receptor. *Drug Metab. Dispos.* **41**, 1470–1479 (2013).
174. Rühl, T., Rafique, W., Lien, V. T. & Riss, P. J. Cu(i)-mediated (¹⁸F)-trifluoromethylation of arenes: Rapid synthesis of (¹⁸F)-labeled trifluoromethyl arenes. *Chem. Commun.* **50**, 6056–6059 (2014).
175. Chen, S. *et al.* Poison tolerance to the selective hydrogenation of cinnamaldehyde in water over an ordered mesoporous carbonaceous composite supported pd catalyst. *ACS Catal.* **7**, 2074–2087 (2017).
176. Chen, D. S. & Huang, J. M. A mild and highly efficient conversion of arylboronic acids into phenols by oxidation with MCPBA. *Synlett* **24**, 499–501 (2013).
177. Golchoubian, H. & Hosseinpour, F. Effective oxidation of sulfides to sulfoxides with hydrogen peroxide under transition-metal-free conditions. *Molecules* **12**, 304–311 (2007).
178. Zhang, P. M. *et al.* A One-pot Facile Synthesis of 2,3-Dihydroxyquinoxaline and 2,3-Dichloroquinoxaline Derivatives Using Silica Gel as an Efficient Catalyst. *J. Heterocycl. Chem.* **55**, 1809–1814 (2018).
179. Jodal, A. *et al.* Evaluation of ¹¹¹In-Labelled Exendin-4 Derivatives Containing Different Meprin β -Specific Cleavable Linkers. *PLoS One* **10**, e0123443 (2015).
180. Eter, W. A. *et al.* Graft revascularization is essential for non-invasive monitoring of transplanted islets with radiolabeled exendin. *Sci. Rep.* **5**, 15521 (2015).
181. Eter, W. A. *et al.* Non-invasive in vivo determination of viable islet graft volume by ¹¹¹In-exendin-3. *Sci. Rep.* **7**, 7232 (2017).
182. Huang, T., Tu, H., Aibibu, Z., Hou, C. & Zhang, A. Synthesis and herbicidal activity of novel substituted 2- and 4-pyrimidinylphenoxypropionate derivatives. *Arkivoc* **2011**, 1 (2010).
183. Murphy, A. & Jones, J. Spatial resolution. *Radiopaedia.org* <https://radiopaedia.org/articles/spatial-resolution> (2018).
184. Parker, M. *Things to Make and Do in the Fourth Dimension*. (Penguin, 2014).